

ENTRAINMENT AND FLAME GEOMETRY
OF
FIRE PLUMES

Thesis by
Baki Mehmet Cetegen

In Partial Fulfillment
of the Requirements for the Degree of
Doctor of Philosophy

California Institute of Technology
Pasadena, California

1982

(Submitted May 18, 1982)

ACKNOWLEDGEMENTS

I am deeply thankful to those who contributed to the research reported here: to my advisor, Professor E. E. Zukoski not only for his close guidance and interest but also for his understanding, friendship and inspiration; to Professor Toshi Kubota whose many valuable suggestions and helpful discussions contributed immensely to this thesis; to Professors F. E. Marble and R. C. Flagan for many helpful comments and suggestions; to my friends J. Scott Patton and Michael Otto who helped in taking the flame geometry video data and my officemate Graham C. Fleming for his many helpful discussions.

The encouragement, understanding and friendship of many people contributed to making my studies most productive and enjoyable during my stay at Caltech. Among those are my friends, Ms. Dorothy Eckerman and the skillful staff of the Aeronautics shop who helped in building some of the equipment for the experiments.

Last but not least, I would like to express my gratitude to my parents who helped and encouraged me throughout my education.

This work was carried out with support from The Center for Fire Research of the National Bureau of Standards, U.S. Department of Commerce through grant number G8-9014.

ABSTRACT

This study concerns the flame structure and fire plume entrainment of natural gas diffusion flames on 0.10, 0.19 and 0.50 m. diameter burners. The heat release rates ranged from 10 kW to 200 kW. Flame heights based on high speed photography and eye averages show a transition in the dependence of flame height on a dimensionless heat addition parameter around unity. For flames taller than three burner diameters, the initial diameter of the fire does not affect the length of these flames whereas for short flames initial geometry becomes important. Another prominent feature of these flames is the presence of large scale ring vortex-like structures which are formed close to the burner surface more or less regularly. It is found that these structures are responsible for the fluctuations of the flame top.

Entrainment measurements spanned heights starting very close to the burner surface to distances about six times the average flame heights. Experiments indicate the presence of three regions; a region close to the burner surface where plume entrainment rates are independent of the fuel flow (or heat release) rates; a far field region above the flame top, where a simple point source model correlates the data reasonably well; and a not so well-defined intermediate region where entrainment seems to be similar to that of a turbulent flame with plume-like characteristics. It is also found that the disturbances in the ambient atmosphere will greatly enhance the fire plume entrainment. Finally, a theoretical study of a steady, buoyant, diffusion flame indicated the importance of the puffing in the entrainment process.

TABLE OF CONTENTS

	Title	Page
	AKNOWLEDGEMENTS	ii
	ABSTRACT	iii
	TABLE OF CONTENTS	iv
	LIST OF FIGURES	vi
	LIST OF TABLES	xii
	LIST OF SYMBOLS	xiii
1	INTRODUCTION	1
	References	7
2	EXPERIMENTAL TECHNIQUE AND APPARATUS	10
	2.1 Experimental Technique	10
	2.2 Apparatus	13
3	FLAME GEOMETRY	22
	3.1 Qualitative Description	24
	3.2 Quantitative Measures	26
	References	39
4	PLUME MASS FLUX MEASUREMENTS	53
	4.1 Far Field	53
	4.1.1 Simple Model	53
	4.1.2 Plume Mass Flux Measurements	59
	4.1.3 Heat Balance	64
	4.1.4 Fuel Heating Value	65
	4.1.5 Fuel-Air Ratio at the Flame Top	67
	4.1.6 Disturbances in the Ambient Atmosphere	69

	4.2 Near Field	70
	4.2.1 Simple Model for Initial Region	72
	4.2.2 Turbulent Flame	76
	4.2.3 Matching of the Plume Mass Fluxes	80
	4.2.4 Model Comparison with Experiments	83
	4.2.5 Fuel Rich Ceiling Layer	85
	References	89
5	INTEGRAL SOLUTION OF A LAMINAR BUOYANT DIFFUSION FLAME	113
	5.1 Governing Equations	114
	5.2 Pressure Variation and Flame Shape	116
	5.3 Equation of State	118
	5.4 Chemical Reaction	118
	5.5 Boundary Layer Integral Equations	119
	5.6 Similar Plane Case	127
	5.7 Results for Vertical Plane Flame	129
	5.8 Nonsimilar Axisymmetric Case	131
	5.9 Results for Axisymmetric Flame	136
	References	140
6	CONCLUSIONS	158
	Appendix A	161
	Appendix B	164

LIST OF FIGURES

Figure	Title	Page
1.1	Sketch of events during the early stages of a room fire	8
1.2	Entrainment contributions into the ceiling layer	9
2.1	Entrainment contributions into the ceiling layer	18
2.2	Plume mass flux measurement technique	18
2.3	Sketch of the hood showing the details of the apparatus	19
2.4	Typical temperature profile around the ceiling layer interface	20
2.5	Apparatus for chemical sampling	21
3.1	Picture and simultaneously photographed shadow-graph image of a 20 kW. fire on 0.19 m. diameter burner	40
3.2	Picture and simultaneously photographed shadow-graph image of a 20 kW. fire on 0.19 m. diameter burner	41
3.3	Successive flame shapes of a 127 kW. fire on 0.50 m. diameter burner	42
3.4	Successive flame shapes of a 42 kW. fire on 0.19 m. diameter burner	43
3.5	Motion of vortices in a fire plume	44

3.6	Intermittency of flame height for 0.10 m. diameter burner for various heat release rates	45
3.7	Intermittency of flame height for 0.19 m. diameter burner for various heat release rates	46
3.8	Intermittency of flame height for 0.50 m. diameter burner for various heat release rates	47
3.9	Flame height correlation for 0.10, 0.19 and 0.50 m. diameter burners.	48
3.10	Eye averaged flame height data correlation	49
3.11	Comparison of eye averaged and video taped flame heights.	50
3.12	Sketch for the flame height fluctuations	51
3.13	Dependence of maximum slope thickness on flame height and burner diameter for 0.10, 0.19 and 0.50 m. diameter burners	52
4.1	The sketch of buoyant turbulent plume	90
4.2	Computed nondimensional entrainment rates as a function of the ratio of interface height to flame height	91
4.3	Computed nondimensional entrainment rates as a function of the ratio of interface height to flame height	92
4.4	Computed nondimensional entrainment rates as a function of the ratio of interface height to flame height	93
4.5	Far field entrainment data for 0.10 m. diameter burner	94

4.6	Far field entrainment data for 0.19 m. diameter burner	95
4.7	Far field entrainment data for 0.50 m. diameter burner	96
4.8	Dependence of heat balance ratio on the ratio of interface height to flame height	97
4.9	Dependence of mass flux ratio on aerodynamic disturbances	98
4.10	Effect of blockage on mass flux ratio	99
4.11	Plume mass flux normalized by the far field correlation as a function of interface height divided by the flame height for 0.10 m. burner	100
4.12	Plume mass flux normalized by the far field correlation as a function of interface height divided by the flame height for 0.19 m. burner	101
4.13	Plume mass flux normalized by the far field correlation as a function of interface height divided by the flame height for 0.50 m. burner	102
4.14	Definition of scales in the initial and turbulent flame regions	103
4.15	Dependence of plume mass flux in three regions	104
4.16	Plume mass flux normalized by the far field correlation as a function of interface height divided by the flame height for 0.10 m. burner	105
4.17	Plume mass flux normalized by the far field correlation as a function of interface height divided by the flame height for 0.19 m. burner	106

4.18	Plume mass flux normalized by the far field correlation as a function of interface height divided by the flame height for 0.50 m. burner	107
4.19	Plume mass flux as a function of interface height for various heat release rates shown together with model computations for 0.10 m. diameter burner	108
4.20	Plume mass flux as a function of interface height for various heat release rates shown together with model computations for 0.19 m. diameter burner	109
4.21	Plume mass flux as a function of interface height for various heat release rates shown together with model computations for 0.50 m. diameter burner	110
4.22	Ceiling layer gas temperature profiles as a function of the height normalized by the height of the small hood	111
4.23	CO_2 , CO , unburned hydrocarbon concentrations and temperature as a function of equivalence ratio of the hood gas, φ_h	112
5.1	The sketch of the problem showing the potential fuel core and the flame sheet at the fuel oxidizer interface as well as the coordinate systems and the blow up of region close to the burner lip	141
5.2	Fuel flow in the potential core within the flame surface	141
5.3	Velocity and Schwab Zeldovich variable profiles	142
5.4	Entrainment and consumption of oxidizer around the flame region	142
5.5	Coordinate system for the plane flame sheet	142

5.6	Dimensionless entrainment of a vertical plane diffusion flame as a function of density ratio of oxidizer and fuel	143
5.7	Dimensionless characteristic velocity as a function of density ratio of oxidizer and fuel	144
5.8	Dimensionless boundary layer thickness as a function of density ratio of oxidizer and fuel	145
5.9	The ratio of fuel velocity outside the boundary layer to characteristic velocity in the boundary layer as a function of density ratio of oxidizer and fuel	146
5.10	Adiabatic flame temperature normalized by heating value per mass of combustible fuel as a function of density ratio of oxidizer and fuel	147
5.11	The shape of the fuel-air interface, where diffusion flame lies, for a 40 kW fire on three different size burners	148
5.12	Characteristic velocity in the boundary layer normalized by the buoyant velocity as a function of the distance above the burner surface normalized by the burner radius	149
5.13	Dimensionless boundary layer thickness as a function of the distance above the burner surface normalized by the burner radius	150
5.14	The ratio of fuel velocity outside the boundary layer to characteristic velocity in the boundary layer as a function of the distance above the burner surface normalized by burner radius	151

5.15	Ambient air entrained as a function of height above the burner surface	152
5.16	Entrainment normalized by that of a plane diffusion flame surrounding burner perimeter as a function of z/r_0	153
5.17	Characteristic velocity in the boundary layer normalized by the buoyant velocity as a function of the distance above the burner surface normalized by the burner radius	154
5.18	Dimensionless boundary layer thickness as a function of the distance above the burner surface normalized by the burner radius	155
5.19	The ratio of fuel velocity outside the boundary layer to characteristic velocity in the boundary layer as a function of the distance above the burner surface normalized by burner radius	156
5.20	Entrainment normalized by that of a plane diffusion flame surrounding burner perimeter as a function of z/r_0	157

LIST OF TABLES

Table	Title	Page
2.1	Burner Initial Parameters	17
3.1	Flame Shape Parameters	29
4.1	Far Field Entrainment Constants	61
4.2	Offset Example	63
4.3	Effects of Fuel Dilution on Fire Plume	66
4.4	Fuel Air Ratio at the Flame Top	68
4.5	Entrainment and Equivalence Ratios for 0.19 m. Burner	71
4.6	Transition Heights for the Intermittent Flame Region	77
5.1	Effect of Dilution on Entrainment	131

LIST OF SYMBOLS

Symbol	Description
a	Constant in equation (4.18)
A	Constant in equation (5.30)
b	Constant in equation (4.18) and transformed half width defined in equation (4.4)
B	Constant in equation (5.30)
C	Constant in equation (5.30)
C_1, C_2	Constants in equations (3.8) and (3.7) respectively
C_l, C_T, C_v	Constants in equation (4.12)
C_m	Plume mass flux constant in equation (4.17)
C_p	Specific heat at constant pressure
D	Burner diameter and constant in equation (5.31)
D	Diffusion coefficient
E	Constant in equation (5.31)
f	Frequency
F	Constant in equation (5.35)
Fr	Froude number
g	Gravitational constant
g'	Modified gravitational constant, $\frac{\Delta\rho}{\rho} g$
G	Constant in equation (5.36)
Gr	Grashof number, $\frac{g' Z^3}{\nu}$
h	Specific enthalpy, see equation (A1)
h_w	Heat of combustion per unit mass of air

h_c	Heat of combustion per unit mass of fuel
H	Height of the small hood
HB	Heat balance parameter in equation (4.21)
I	Intermittency
k	Heat conductivity
K_u, K_δ	Parameters defined in equations (5.42) and (5.43)
Le	Lewis number, $\frac{\rho D C_p}{k}$
\dot{m}	Mass flux
\dot{m}_c	Mass flux into the ceiling layer
\dot{m}_E	Mass flux entrained by the plume, see figure (2.1)
\dot{m}_i	Plume mass flux, see figure (2.1)
\dot{m}_τ	Mass flux due to plunging of the plume, see figure (2.1)
$\dot{m}_{1,2,3}$	Computed mass fluxes in initial, turbulent flame and far field regions respectively
M	Molecular weight
P	Pressure
Pr	Prandtl number, $\frac{\mu C_p}{k}$
\dot{Q}_f	Heat release rate based on $\dot{m}_f h_c$
Q_D^*	Dimensionless heat addition parameter, $\frac{\dot{Q}}{\rho_\infty C_p T_\infty \sqrt{g D} D^2}$
Q_Z^*	As above replacing D with Z
Q_{Zfl}^*	As above replacing Z with Z_{fl}
r	Radius
r_0	Burner radius
R	Gas constant
R	Universal gas constant

Re	Reynolds number, $\frac{\rho_f V_f D}{\mu_f}$
Ri	Richardson number, $\frac{\Delta \rho g D}{\rho_f V_f^2}$
Sc	Schmidt number, $\frac{\nu}{D}$
t	Time
T	Temperature
\bar{T}	Average temperature
ΔT	Temperature difference
u	Velocity in x direction
u_o	Velocity on the x axis in chapter 5
v	Velocity in y direction
V_f	Fuel velocity at the burner surface
\dot{V}	Volume flux
w, W	Velocity in z direction
W_s	Vortical structure velocity
x	Streamwise coordinate, moles of excess air in chapter 2
X	Variable in equation (3.15)
y	Transverse coordinate
Y	Mole fraction in chapter 2 and species mass fraction in chapter 5
z	Coordinate perpendicular to burner surface
Z	Height above the burner surface
Z_i	Interface height
Z_{fl}	Average flame height
Z'_{fl}	Eye averaged flame height
Z_t	Transition height
ΔZ	Offset in Z direction

Greek Symbols

α	Entrainment constant
β	Ratio of Gaussian half widths of velocity and temperature profiles
γ	Specific heat ratio, C_p / C_v
Γ	$\frac{\gamma}{\gamma - 1}$
δ	Boundary layer thickness
Δ	Maximum slope thickness
η	Similarity variable, turbulent plume diameter
θ	Angle defined in figure (5.1)
κ	Fraction of entrained mass consumed in combustion see equation (4.34)
Λ	Velocity ratio, u_f / u_o , shown in figure (5.3)
μ	Dynamic viscosity
ν	Kinematic viscosity, stoichiometric coefficient in chapter 5
ρ	Density
$\Upsilon_{1,2}$	Integration variables defined in equation (5.52)
φ	Equivalence ratio (fuel-air ratio divided by the stoichiometric value)
φ_{of}	Oxidizer-fuel mass ratio
ψ	Schwab - Zeldovich variable
$\dot{\omega}$	Species production rate
$\bar{\omega}_i$	Widths of vortical structures

Subscripts

c	ceiling layer quantities
E	entrained

f	fuel
fl	flame
h	hot or hood values
i, j	indices
m	mean or maximum
o	oxidizer
OC, OL, OE	see figure (5.4)
p	plume quantities
0	values at origin, initial values
s	structure
T	turbulent
∞	values at infinity

Chapter 1

INTRODUCTION

One of the current artifices used in constructing models of fire spread through multi-room structures is that of dividing each room into two homogeneous layers. In each room, the upper or ceiling layer is assumed to contain the hotter gas and the lower or floor region, the cooler gas (see figure (1.1)). Processes in each layer are analyzed by making use of conservation equations for energy, mass and species. In addition, a description must be given of the various transport processes for mass and energy between the layers, as well as between each layer and its walls and any openings to other volumes.

The entrainment of the lower region air into the fire plume and transport to the upper layer in these two-layer models of room fires is the major source of mass flow between the layers in the fire-involved room as shown in figure (1.1). The plunging of the fire plume into the ceiling layer, \dot{m}_r and the mixing at the interface, \dot{m}_i as shown in figure (1.2) contribute to the entrainment, but, as it will be discussed later, these two contributions are found to be small compared to the entrainment in the fire plume itself. The rate of production of hot gas and its temperature are strongly dependent on this plume entrainment. Although considerable information is presently available concerning entrainment in buoyant plumes, it has principally been obtained in plumes which have risen far above their origin and which have densities little different from that in the surrounding gas. In contrast, in building fires, we are interested in regions of the plume located very close to the origin.

The extent of the heat release zone and thus the fire geometry, is also of primary importance since we expect that the size of the fire source, the effects of

large density differences, and the presence of heat release due to combustion will greatly influence the entrainment process. When flames extend into the hot ceiling layer gas, the problem may be further complicated by greatly reduced oxygen concentrations in the ceiling layer and the possibility that unburned fuel can build up in that layer and eventually result in phenomena such as flash-over.

The previous work on fire geometry and plume entrainment is extensive. Here, we will only discuss the work which is directly related to our measurements. Early work on flame geometry was presented by Thomas et al [1.1]. More recently, flame height literature was reviewed by Steward [1.2] who also presents extensive new data which are directly pertinent to our experiments. Entrainment by plumes has been studied both experimentally and theoretically by a long line of investigators beginning with Schmidt [1.3], Rouse et al [1.4], Morton et al [1.5] and Yokoi [1.6]. Recent efforts include that of Thomas et al [1.7], work of McCaffery [1.8], Terai and Nitta [1.9] and Cox and Chitty [1.10] who are concerned with entrainment in the region of the flame itself.

The experimental work on entrainment can be divided into two types. In the first, point measurements of fluid properties such as velocity, temperature and composition are made and then are used to determine the time averaged values of upward mass fluxes of mass and enthalpy. (see for example the work of references [1.4] to [1.10]). The mass and enthalpy fluxes determined from these measurements suffer from the uncertainties caused by very large scale fluctuations in the direction of the velocity vector and in the magnitudes of all observable quantities. The magnitude of these fluctuations is often increased by the wandering of the plume axis due to small disturbances present in the atmosphere surrounding the flame. One of the examples of these difficulties is illustrated by the gas velocity measurements of Cox and Chitty [1.10] who used a

technique based on the cross correlation of random thermal fluctuations in a turbulent diffusion flame. In this technique, the time elapsed during the passage of a thermal disturbance between the two thermocouple probes and the separation distance between the probes are used to estimate the gas velocity. For this technique to be valid, we must assume that the disturbances travel with the local gas velocity. This method clearly gives erroneously large values when the direction of the traveling front is different from the alignment of the probes. These skewed disturbances are very likely to occur in turbulent flames even along the centerline due to wandering of the plume axis and the large scale puffs we discuss in this thesis.

Finally in all point measurements we know, experimenters have assumed that the time average values of vertical mass flux per unit area $\overline{\rho w}$ is equal to the product of the time average values of the vertical velocity \overline{w} and the time average value of gas density $\overline{\rho}$. That is, that $\overline{\rho w}$ is equal to $\overline{\rho} \overline{w}$. This assumption ignores the contribution of the correlation of the vertical velocity fluctuations and the density fluctuations which may be large since buoyancy is the driving force for vertical motion. Thomas et al [1.7] avoided these problems by making mass flow measurements at a cylindrical surface surrounding the flame at a distance such that density was constant. However, uncertainties concerning the selection of proper surface remain in this work.

Before starting our experiments, we considered many alternative techniques for entrainment measurements. The techniques involved with point measurements were discarded because of the problems described above. The second possible approach concerned the use of a direct measurement of entrainment rates similar to that employed by Ricou and Spalding [1.11]. Their technique was based on the idea of satisfying the entrainment appetite of the jet by supplying appropriate mass flow rate to an enclosure which surrounded the jet. The

appropriate value was found by adjusting the entrained flow rate to eliminate the pressure gradients in the axial direction. They made measurements in momentum dominated jets and for two diffusion flames in which the buoyancy was important. Our technique measures the entrainment into the ceiling layer due to a fire plume which might be slightly greater than the plume entrainment itself due to the contributions mentioned earlier and shown in figure (1.2).

Theoretical modelling of plumes without combustion started with the mixing length model used by Schmidt [1.3], Rouse et al [1.4], and Yokoi [1.6]. Morton et al [1.5] and Taylor [1.12] abstracted an ad hoc entrainment model from Schmidt's results which was used by many subsequent investigators. More recently, an improved version of $k-\varepsilon-g$ model of turbulence has been applied to a turbulent, buoyant diffusion flame by Tamanini [1.13] and Steward's [1.2] approach has been extended to include a study of the buoyant diffusion flame with radiation and more complex chemistry by Wilcox [1.14]. In all these models, difficulties arise in modelling the Reynolds stresses and similar quantities in energy and species conservation equations. The so-called closure assumptions for the time averages of the products of fluctuating quantities are semi-empirical and sometimes have to be modified from one flow configuration to the other.

In this thesis, we describe the plume mass flux measurements made in axisymmetric diffusion flames by two techniques which will be explained later. These measurements span large ranges of heat release rates and heights above the fire source level for three different size burners. The fuel was natural gas and heat release rates ranged from 10 kW to 200 kW whereas the heights were from about 0.2 m above the burner to six times the average visible flame height.

Chapter 2 concerns the description of the two techniques used for entrainment measurements. The first is based on the direct measurements of the mass

fluxes by mass conservation of the ambient air and the plume gases. The second approach based on estimating the overall air-fuel ratio of a well mixed layer of hot combustion products and air by chemical analysis of the various species in the hot ceiling layer gas is convenient for use in the near field entrainment measurements. The entrainment estimates obtained from these two different methods show good agreement in the overlapping region of the measurements.

Chapter 3 deals with investigation of the flame geometry as obtained from high speed photographs and video movies of the flames. A correlation for the average visible flame height with a dimensionless heat addition parameter was obtained from a large body of data taken in our laboratory as well as the data available in the literature. The fluctuations in the flame height were observed to be due to quasi-periodic production of ring-vortex-like structures at the base of the flame. A correlation for the heights of these vortical structures with the average flame height and burner diameter is also presented. A noticeable change in the flame structure is observed when a dimensionless heat addition parameter has values around unity.

In chapter 4, entrainment measurements are presented. It is found that the plume can be divided into three regions. An initial region close to the burner surface, where the entrainment rates are independent of the total heat release rates of the fires. In this region, the flow field is complicated by periodic pulsations of the flame surface which result in production of toroidal vortices. The second region resembles a turbulent flame with plume-like characteristics. The combustion still prevails in at least part of this second region. The third zone above the average visible flame height is well correlated by turbulent plume model for buoyant plumes. The transitions among these three regions are not sharply defined and sometimes span large distances.

The signs of existence of the initial region just described, motivated us to the study of the entrainment of a laminar, buoyant, axisymmetric and steady diffusion flame presented in Chapter 5. The work described here is an attempt to make a quantitative estimate of the entrainment of a buoyant, laminar diffusion flame under the conditions which very crudely approximate the steady features of these flames. This study showed that the theoretical entrainment rates are much lower than the experimentally obtained values and thus this calculation reinforces our concern with the influence of the unsteady vortical structures on the plume entrainment.

References

- [1.1] P. H. THOMAS, C. T. WEBSTER and M. M. RAFTERY, Some Experiments on Buoyant Diffusion Flames, *Combustion & Flame*, **5**, 359,(1961)
- [1.2] F. R. STEWARD, Prediction of the Height of Turbulent Diffusion Buoyant Flames, *Comb. Sci. & Tech.*, **2**, 203,(1970)
- [1.3] W. SCHMIDT, Turbulente Ausbreitung eines Stromes Erhitzter Luft, *Zeitschrift fuer Angewandte Mathematik und Mechanik*, **21**, Nr.5, 265,(1941), also **21**, Nr.6,351,(1941)
- [1.4] H. ROUSE, C. S. YIH and H. W. HUMPHREYS, Gravitational Convection from a Boundary Source, *Tellus*, **4**, 201,(1952)
- [1.5] B. R. MORTON, G. I. TAYLOR and J. S. TURNER, Turbulent Gravitational Convection from Maintained and Instantaneous Sources, *Proc. Roy. Soc.*, **A 234**, 1-23,(1956)
- [1.6] S. YOKOI, The Use of Models in Fire Research, Publication Nr.786, 186-206, *National Academy of Sciences, National Research Council, Washington D. C.* (1961). See also: Report 29, *Japanese Bldg. Res. Inst.*,(1959)
- [1.7] P. H. THOMAS, R. BALDWIN and A. J. M. HESELDEN, Buoyant Diffusion Flames: Some Measurements of Air Entrainment, Heat Transfer and Flame Merging, *Tenth Symposium (International) on Combustion*, 983, Academic Press, New York (1965)
- [1.8] B. J. McCAFFERY, Purely Buoyant Diffusion Flames: Some Experimental Results, NBSIR79-1910, *National Bureau of Standards, Department of Commerce, Washington D.C.* (1979)
- [1.9] T. TERAJ and K. NITTA, *Proc. Syms. Arch. Inst., Japan*,(1975)
- [1.10] G. COX and R. CHITTY, A Study of the Deterministic Properties of Unbounded Fire Plumes, *Combustion & Flame*,**39**, 191-209,(1980)
- [1.11] F. P. RICOU and D. B. SPALDING, Measurement of Entrainment by Axisymmetrical Turbulent Jets, *J. Fluid Mech.*, **11**, 21,(Aug-Dec 1961)
- [1.12] G. I. TAYLOR, The Use of Models in Fire Research, Publication Nr.786,10-31, *National Academy of Sciences, National Research Council, Washington D. C.* (1961)
- [1.13] F. TAMANINI, The Prediction Of Reaction Rates and Energy Transfers in Turbulent Fire Plumes *Factory Mutual Research, Technical Report 22360-3*, RC-B-60, May 1976.
- [1.14] D. C. WILCOX, Models for Fires with Low Initial Momentum and Nongray Thermal Radiation, *AIAA Journal*, **13**, Nr.3,381, March 1975

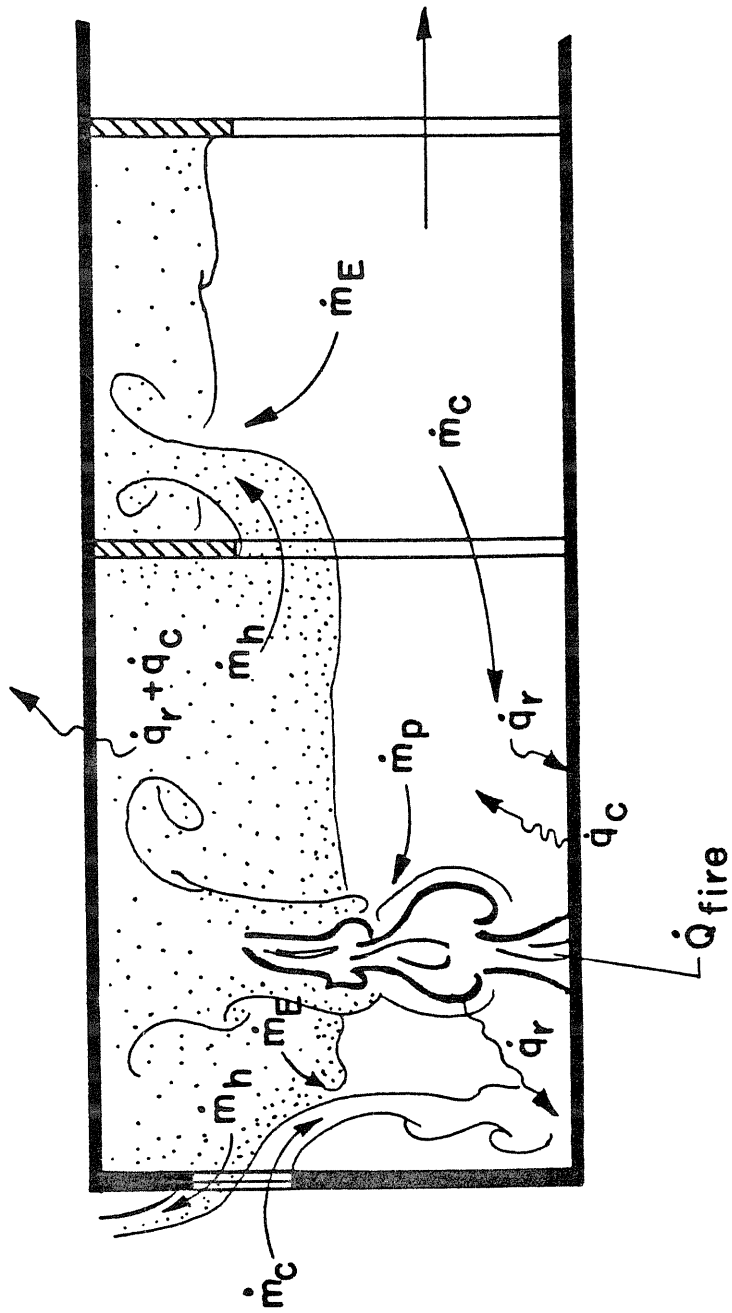


Figure (1.1) Sketch of events during the early stages of a room fire

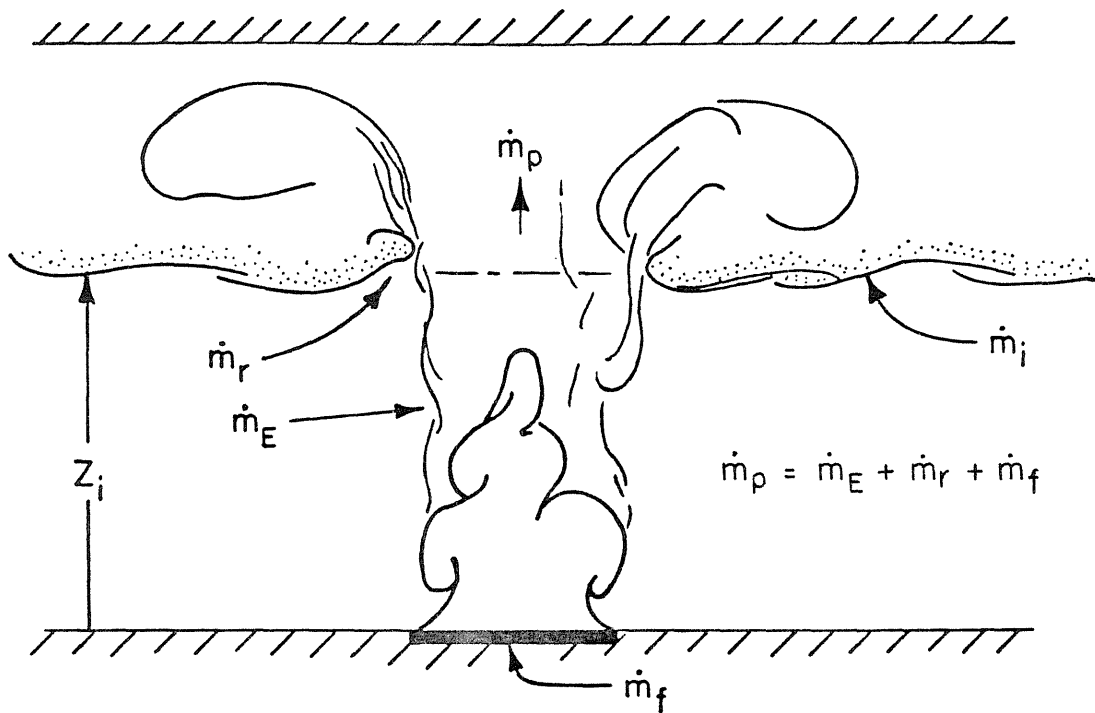


Figure (1.2) Entrainment contributions into the ceiling layer

Chapter 2

EXPERIMENTAL TECHNIQUE AND APPARATUS

2.1. Experimental Technique

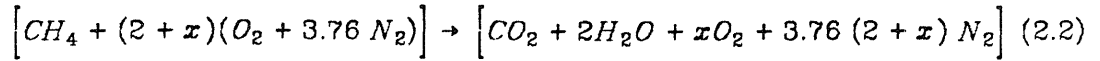
Basic idea for the technique used to make plume mass flux measurements is best illustrated by the use of the sketch shown in figure (2.1). In the early stages of a fire, the hot products of combustion produced by a flame are usually segregated in a well stirred ceiling layer whose properties are roughly homogeneous. The flame and the buoyant plume it produces entrain cool air from the room and heat it in the fire by combustion processes and in the plume by mixing with the plume gas (See figure (1.1)). If the fuel consumption rate is \dot{m}_f and the air entrainment rate is \dot{m}_E , this heated gas flows into the ceiling layer at a rate $(\dot{m}_E + \dot{m}_f)$. Other gas may flow into the ceiling layer as a result of the disturbance produced by the plume as it plunges into the ceiling layer, \dot{m}_r , or as a result of other mixing processes which may occur at the interface separating the hot ceiling layer from the cool air layer, \dot{m}_i . Thus the total mass flux to the ceiling layer, \dot{m}_C will be the sum of these contributions,

$$\dot{m}_C = (\dot{m}_E + \dot{m}_f + \dot{m}_r) + \dot{m}_i \quad (2.1)$$

The terms $(\dot{m}_E + \dot{m}_f + \dot{m}_r)$ are directly associated with the fire plume and are called the plume mass flux, \dot{m}_p . Because the interface between the hot and cold gas is stabilized by the gravitational field, we expect that the mass entrainment rate at the interface far from the fire, \dot{m}_i will often be negligible in the absence of some other mixing process such as drafts through a door or window. Observations of gas motion (made visible by adding smoke to the ambient gas) suggest

that very little entrainment occurs at the interface and that most occurs at the edges of the plume itself. Since we need to be able to describe entrainment as a part of any model which is used to predict the behavior of the early stages of a fire, the primary purpose of our experiment is to measure the plume related mass flux, \dot{m}_p as a function of height above the fire source, Z_i ; heat release rate, \dot{Q}_f and the initial fire geometry expressed as burner diameter, D . This is accomplished by use of a hood shown schematically in figure (2.2). The interface level of the ceiling layer is maintained at a constant height above the fire source by withdrawing a suitable flow of hot ceiling layer gas through an exhaust pipe. The hood was made large enough to insure that the gas in the hood is kept relatively quiescent so that it will not entrain air at the interface (\dot{m}_i of figure (2.1)). When this entrainment can be neglected, a simple conservation of mass argument shows that the mass withdrawal rate required to maintain a fixed interface height is the plume mass flux, \dot{m}_p .

When the interface lies well below the top of the flame, the gas temperature in the ceiling layer becomes too high for the apparatus described above, and a modification of the first technique was required. The method used to measure the plume mass flow rates in the near field of the fire plume is based upon measuring the fuel flow rate and the mole fractions of combustion products in the well-stirred hot gas layer in a small hood. If the complete combustion of methane, CH_4 into CO_2 and H_2O is achieved, then the measurement of the concentration of either CO_2 , or excess O_2 allows the calculation of the overall air-fuel ratio of the gas in the hot gas layer. Since the amount of fuel supplied to the burner is measured, we can then determine the entrainment rate of ambient air in the lower regions of the flame. The complete combustion of methane in the presence of x moles of **excess** air can be written as,



then for dried products,

$$x = \frac{8.52 Y_{O_2}}{1 - 4.76 Y_{O_2}} \quad \text{or} \quad x = \frac{1 - 8.52 Y_{CO_2}}{4.76 Y_{CO_2}} \quad (2.3)$$

Here Y_{O_2} and Y_{CO_2} are measured mole fractions of O_2 and CO_2 respectively. When we are only interested in the air-fuel ratio of the exhaust gases, we can ensure that all carbon is reduced to CO_2 and hydrogen to H_2O by passing the gas through a furnace in the presence of excess oxygen. The equivalence ratio (which is the stoichiometric air-fuel ratio divided by the measured air-fuel ratio) in these experiments was never greater than 0.70, and hence excess oxygen was always present in the hood gas.

Either of the two independent estimates of x , obtained from equation (2.3) can be used to estimate the entrained flow rate of air as,

$$\dot{m}_E = \left[8.58 (2 + x) - 1 \right] \dot{m}_f \equiv \dot{m}_p - \dot{m}_f \quad (2.4)$$

We have also made a photographic study of the geometry of the flames produced in these experiments. Photographs of the flame were made with a video tape recorder at a framing rate of 30 frames per second. Direct photographs of these flames were also taken with exposure times ranging from 1/250 to 1/60 seconds. A shadowgraph system was employed to allow us to compare the boundary fixed by the initial density change in the gas with the visible flame boundary. These photographs were taken by a 35 mm. camera placed at the same distance from the flame as the point light source for the shadowgraphs. This

arrangement insures that both flame and shadowgraph images are magnified almost equally.

2.2. Apparatus

The hood and the associated equipment used to make our far field entrainment measurements (interface height, Z_i greater than average flame height, Z_{fl}) are shown in figure (2.3). The hood dimensions are $2.4 \times 2.4 \times 1.56$ m. deep; it was made out of steel and insulated with 10 cm thick glasswool. The burner and the floor can be moved vertically to change the elevation of the interface height between 2.3 m. and a lower bound of roughly 1.0 m. which is set by our desire to keep the ratio of interface thickness to the interface height below $1/10$.

The location of the interface between the cool room air and the hot gas layer was determined from temperature measurements with the two vertical arrays of thermocouples which span the interface. We used 0.10 mm. iron-constantan thermocouples spaced at intervals of 0.05 m. in the longer array and 0.10 m. in the shorter one. A typical temperature profile is shown in figure (2.4). In the regions both above and below the interface the gas temperature is constant; in the interface, large temperature gradients and fluctuations are observed. These conditions are a result (a) of the real thickness of the interface in which the gas temperature rises rapidly and (b) of waves in the interface produced by the hot gas as it sloshes back and forth in the hood. The location of the interface was always taken to be the mid-point of this interface thickness. Typical interface thicknesses are 10 - 20 cm. Two layers of 16×18 mesh screens made of 0.05 cm. diameter wire were hung from the bottom rims of the hood and allowed to fall around the floor. The floor-screen arrangement was used to reduce the strength of the disturbances present in the laboratory air as this gas was sucked in to the plume by the entrainment process. Mass flow measurements of the plume gas were made in a 0.40 m. dia. pipe with a standard ASME, flat plate orifice

located 12 diameters downstream from a 90° elbow.

The near-field entrainment measurements were made in a small hood, a 1.2 m. cube, open on the bottom side, which was designed to be used at gas temperatures up to 1000 °C. The hot gas is allowed to spill out under the edges of the bottom side of the hood. The plume mass flux is deduced from the measurements made of the carbon dioxide and oxygen partial pressures in the gas samples withdrawn from the hood and from the measurements of the fuel flow rates.

The experimental set-up is shown in schematic diagram of figure (2.5). The small hood (1.2 × 1.2 × 1.2 m.), made out of steel, is lowered upon the fire by a pulley mechanism and the fires are stabilized by the 0.10, 0.19 and 0.50 m. diameter axisymmetric burners described below. A gas sample is withdrawn from the small hood through a 6.4 mm. dia. stainless-steel tube inserted to various depths in the small hood. An aspirated chromel-alumel thermocouple is placed at the entrance of the probe to monitor the gas temperature. The sample was first passed through a furnace which insures complete oxidation of incomplete combustion products (mainly CO), and is then dried and filtered to remove particulates from the gas stream. The furnace is a 84 cm. long U shaped, 0.64 cm. OD stainless-steel tube (0.025 cm. wall thickness) kept at about 1000°C by electrical heating. The CO₂ and CO contents of the sample was measured with a Beckman Model 864 Nondispersive Infrared analyzer. The O₂ concentration was monitored with a Beckman Model 741 amperometric oxygen detector and the amount of any remaining unburnt hydrocarbons was measured with a Beckman Model 400 Flame Ionization Hydrocarbon analyzer. The location of the hot-cold gas interface was determined by a shadowgraph system and the screens surrounding the large hood helped to suppress the disturbances in the ambient air. The large hood was used to remove continuously the hot gases spilled around

the edges of the small hood.

The fuel used in these experiments was city gas taken without processing from the Southern California Gas Company mains. The fuel is a mixture of hydrocarbons and its principal constituents, with their mole fractions, are methane 0.924, ethane 0.042, nitrogen 0.015 and propane 0.01. The lower heating value is about 47.5 MJ/kg and density is about 0.72 kg/m^3 at 20°C and one atmosphere. These properties are average values which do not vary more than a few percent from week to week. A Meriam laminar flowmeter was used to measure the flow rate of the fuel.

The fuel was fed into the flame after passing through a porous bed of spherical glass beads whose surface was made flat and flush with the metal edge of the burner. Three burner designs were used. One burner had a diameter of 0.50 m. and a layer of 2 mm. glass beads about 4 cm. deep. The second design was a 0.19 m. in diameter and had a 5 cm. thick bed of glass beads of diameter 6.3 mm. This burner was also used as a 0.10 m. diameter burner by fitting an insert. The third one was a 0.10 m. diameter burner having 6.3 mm. glass beads about 5 cm. deep. Experiments were performed with and without a 2.4 m square floor mounted flush with the upper surface of the burners. In the experiments without the floor, the burners resembled right circular cylinders which extended at least 2 to 3 diameters above the floor of the laboratory. This arrangement prevented strong shear interactions developing between the entrained air and the hot-cold gas interface when the interface height was less than 25 cm. above the top of the burner.

The velocity of the fuel at the surface of the burner is dependent on its temperature at that point. Because of the intense thermal radiation to the glass beads at the surface of the burner and subsequent convective heating of the fuel, the gas temperature at the surface is about $400 - 600 \text{ }^\circ\text{K}$. Table 2.1 gives

values of fuel velocity based on a 600 °K gas temperature and a fuel flow rate corresponding to a heat release of 42 and 126 kW. Also tabulated are the values of Richardson and Reynolds numbers based on burner diameter. The Richardson number is defined as,

$$Ri_f = \frac{(\rho_\infty - \rho_f)gD}{\rho_f V_f^2} \quad (2.5)$$

and is a measure of the relative magnitudes of the buoyancy force (the numerator) and the momentum flux (the denominator). In terms of the heat release rate,

$$\dot{Q}_f = \frac{\pi}{4} D^2 \rho_f V_f h_c \quad (2.6)$$

we get,

$$Ri_f = \frac{\left[\left(\frac{\pi D^2}{4} \right) \rho_f \sqrt{\frac{(\rho_\infty - \rho_f)}{\rho_f}} \sqrt{gD} h_c \right]^2}{\dot{Q}_f^2} \quad (2.7)$$

The Reynolds number is defined as,

$$Re_f = \frac{\rho_f V_f D}{\mu_f} = \left(\frac{4}{\pi D} \right) \frac{\dot{Q}_f}{h_c \mu_f} \quad (2.8)$$

Here Ri_f is proportional to $\frac{D^5}{\dot{Q}_f^2}$, the Reynolds number, to $\frac{\dot{Q}_f}{D}$, and V_f to $\frac{\dot{Q}_f}{D^2}$.

Minimum values of Ri_f (using the 10 cm. burner at 126 kW.) were around 2 and maximum velocities at the same condition approached 1 m/s. These values of

Table 2.1. Burner Initial Parameters

$\dot{Q}_f = 42 \text{ kW.}$				$\dot{Q}_f = 126 \text{ kW.}$		
$D, \text{ m.}$	$V_f \text{ m/s.}$	Ri_f	Re_f	$V_f \text{ m/s.}$	Ri_f	Re_f
0.10	0.3	21	820	0.9	2.33	2500
0.19	0.09	5.1×10^2	430	0.27	57	1300
0.50	0.013	6.4×10^4	160	0.04	7.1×10^3	480

Richardson number show that the buoyancy of the jet dominates the initial momentum at small heights of the order of burner diameter in all our experiments. These values establish a lower bound for Richardson numbers since they are evaluated at one burner diameter above the burner. The minimum values, which occur at high heat release rates on small burners, would be greatly increased if we used the flame height rather than the burner diameter since these flames are very tall. For example, 126 kW. fire on 0.10 m. burner would give a Richardson number of about 2. But the flame height is about 35 burner diameters. Typical Reynolds numbers shown in the table were not always very low and the maximum value (for 10 cm. burner at 126 kW.) was about 2500. Although these values are large, the increase in kinematic viscosity which occurs at the flame surface (due to temperature rise caused by combustion) will keep the fuel "jet" in a laminar state for at least a number of diameters. Hence, we expect that the momentum flux of the fuel is never very important in our flames and that close to the burner lip, the flow will be laminar though it may be unsteady. Here, we also note that for large diameter fires, (0.50 m. burner at 126 kW.) Richardson numbers are very large and Reynolds numbers are small. Thus, for these large diameter fires, which are typical of real fires, buoyancy is clearly dominant and laminar conditions are expected.

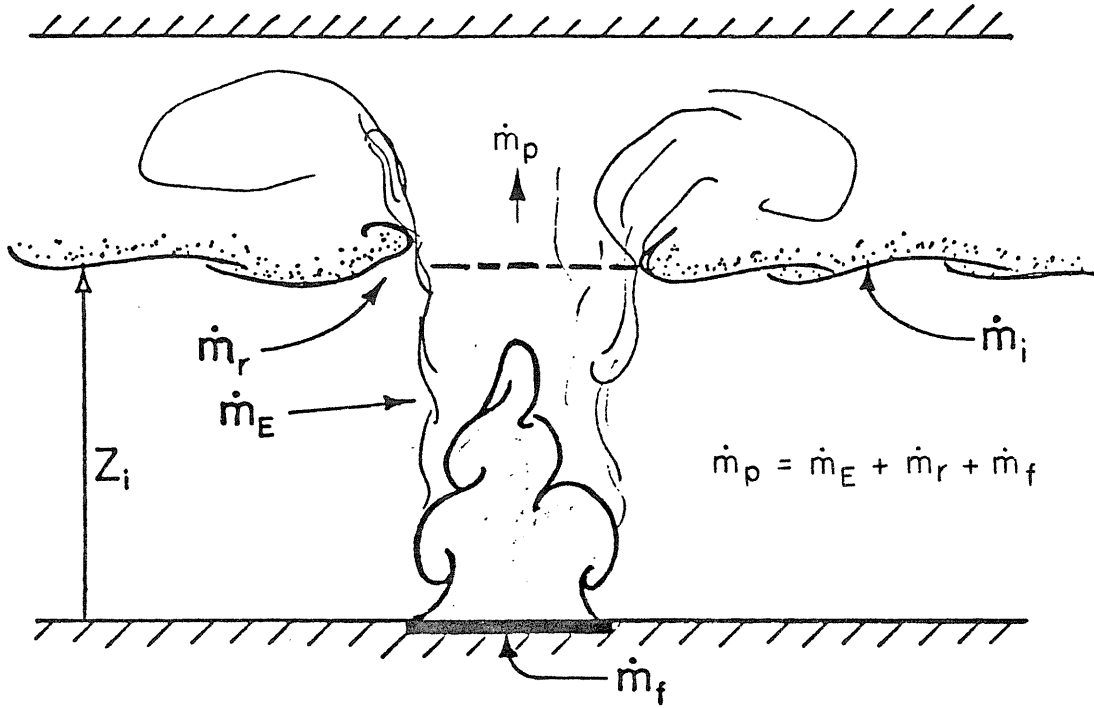


Figure (2.1) Entrainment contributions into the ceiling layer

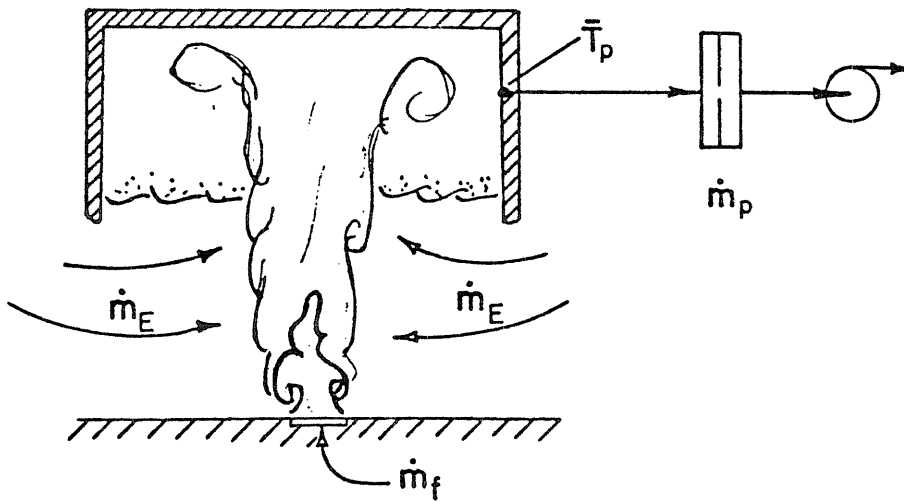


Figure (2.2) Plume mass flux measurement technique

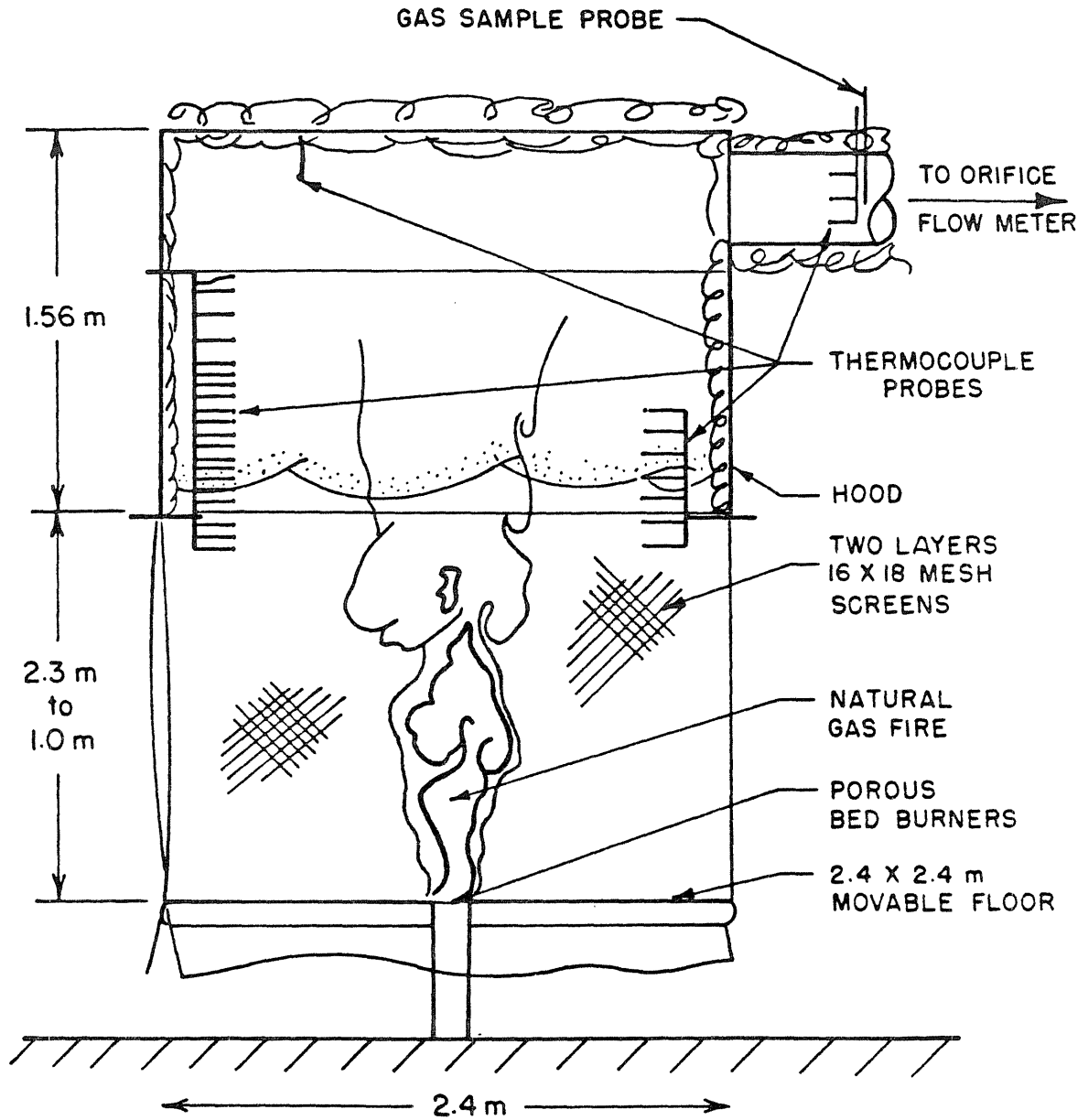


Figure (2.3) Sketch of the hood showing the details of the apparatus

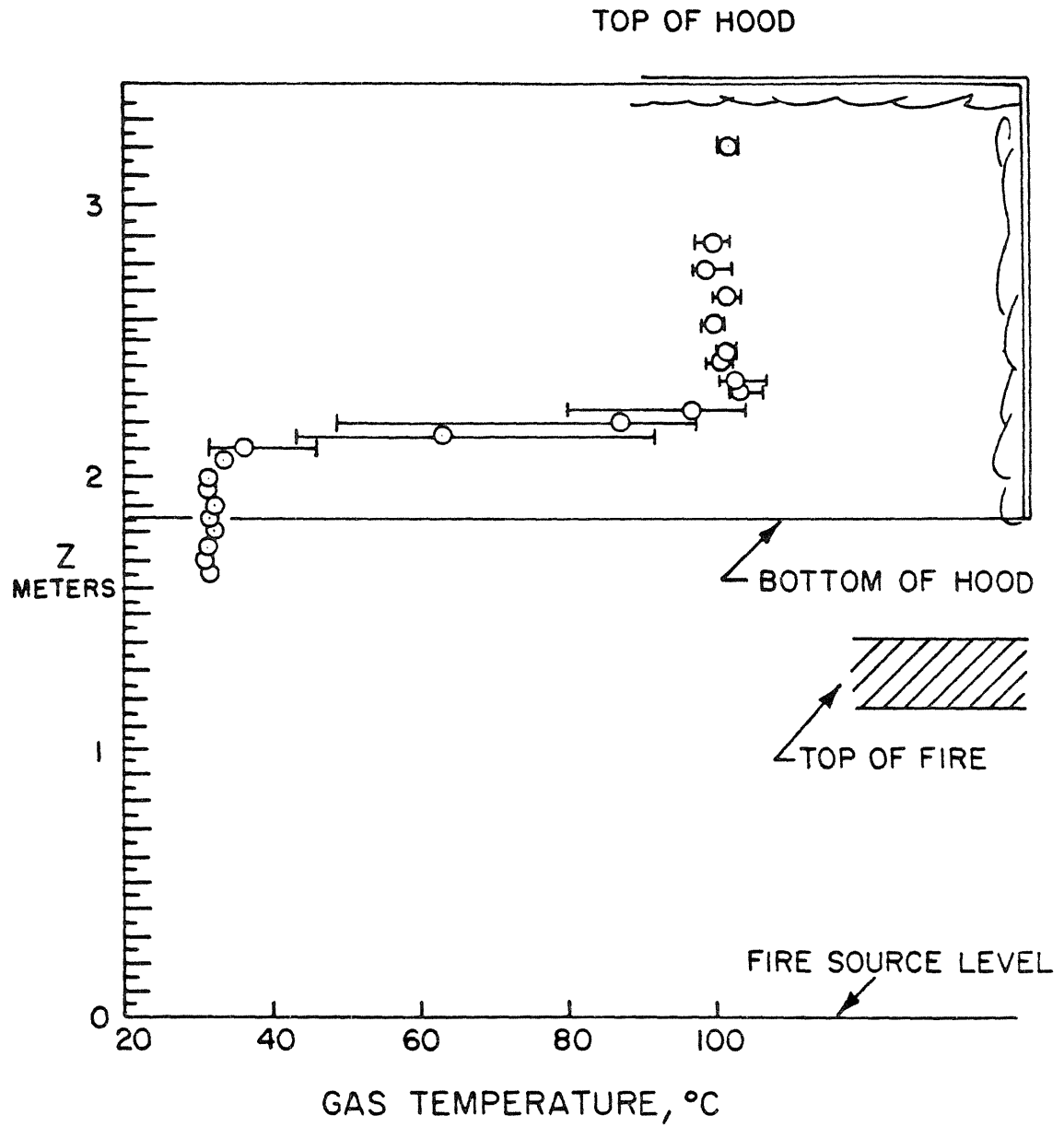


Figure (2.4) Typical temperature profile around the ceiling layer interface

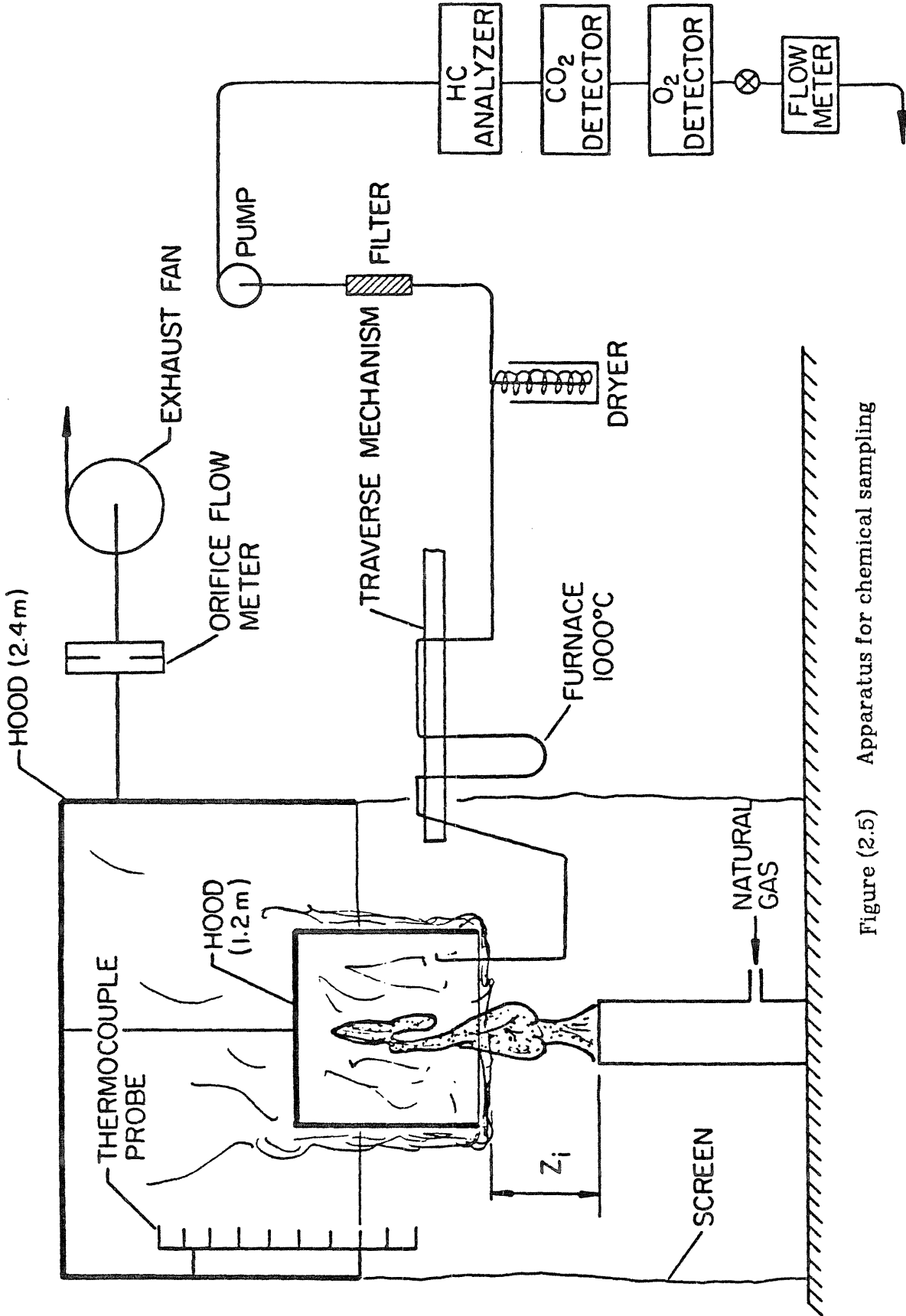


Figure (2.5) Apparatus for chemical sampling

Chapter 3

FLAME GEOMETRY

The geometry of the flame is important since flame is the origin of the plume and hence must influence its initial development. This is especially crucial for entrainment measurements in the fire plumes at elevations near the fire or heat release zone. One crude estimate of the extent of the heat release region is the average flame height which approximately marks the upper bound of heat release region. Even this measurement is not a trivial one because of the roughly periodic fluctuations of the "top" of the flame. Our measurements on flame geometry included eye-measured flame heights and the averages made from video tape recordings of a number of these flames for extended times and short time exposure photographs of these diffusion flames. The eye averaged height data were taken with a meter stick held close to the flame and the observers then made an estimate of the time averaged top of the visible flames. Several observations were made at each condition (often several weeks apart) and each estimate was made by different observers. An arithmetic average was taken from all the estimates.

Video tape recordings were made for each test condition at a framing rate of 30 frames a second, and randomly selected sequences corresponding to several hundred frames of each test were then analyzed by making measurements directly on a TV monitor screen. The video pictures were taken in the light from the flame itself and record the radiation emitted by burning soot particles which had a radiation temperature of about $1400^{\circ}K$ which was measured by an optical pyrometer. Hence, the flame height data reported here concern that part of the combustion zone made visible or marked by radiation from burning

soot.

In a normal methane-air diffusion flame, the region in which chemical reactions occur is very thin compared with the diffusive thickness of the flame region, and soot is typically formed within this diffusive thickness, on the fuel side of chemical reaction zone. and close to the region of intense chemical reaction. Because the diffusive thickness itself is usually no more than a centimeter thick, the soot and chemical reaction zones are separated by a few millimeters at most. We believe that soot production and combustion, in the flames we are studying, is by this same process and hence that the radiation from the soot does mark the regions of intense chemical reaction. This belief is supported by the following observations: Studies were made of flames in which soot production was entirely suppressed by diluting the fuel with nitrogen. These flames are made visible by radiation from chemical species formed in excited states during the chemical reactions. Qualitatively, these flames resemble the sooty flames closely and have the same eye-averaged flame length. The combustion efficiency of the methane-air flames we have studied is very high and if the soot formation and combustion occurred at substantial distances from each other, we would expect lower combustion efficiency and considerably more unburnt soot production. Thus, we feel that the radiation from the soot is a good marker for the flame zone of the diffusion flames studied here and that it gives an accurate picture of the volume of space in which vigorous heat release occurs.

In addition to the video recordings, we took simultaneous photographs of the flame and shadowgraph images of the plume. A few pictures of this type recorded on 35 mm. film at exposure times of about 0.01 second are shown in figures (3.1) and (3.2). These photographs allow us to assess the difference between the shadowgraph boundary, which is fixed by the initial temperature rise of the air surrounding the visible flame, and the visible flame boundary,

fixed by the burning soot.

The soot boundaries defined in either type of photograph are sharp, well-defined surfaces which are recorded with such a short exposure time that they are marked unambiguously. Hence, this technique although tedious, does not suffer from the uncertainties arising from the selection of the exposure time which arise when time exposure methods are used to define an average flame height.

3.1. Qualitative Description

The most prominent feature of these photographs and also of visual observation of the flames is the presence of strong periodic pulsations in the flame. They are associated with a periodic reduction of the flame diameter near the burner plane which produces a regular and more or less continuous train of puffs. Figures (3.3) and (3.4) show the typical traces of flame boundaries at successive time steps for a 127 kW fire on 0.50 m. dia. burner and 42 kW fire on 0.19 m. dia. burner. Production of these puffs can easily be traced in these types of sequences. This periodic phenomenon has been described many times and is apparently present in some form in many types of burners with gaseous, liquid and solid fuels, (e.g. references [1.10] and [3.7] to [3.9]).

In the burner flames described here, these pulsations are often very well marked and we believe that the puffs they produce play an important role in fixing the rate of entrainment and heat release in the flame, and also the flame geometry. Observation of the photographs and particularly of the shadowgraph pictures shows that each puff of the flame consists of a very roughly axisymmetric, ring-shaped, vortex-like structure, which is formed close to the burner surface and then rises through the flame. The structures often persist as identifiable entities until they reach the top of the flame where radiation stops.

At formation, the structures have a width and height approximately equal to the burner diameter. As the structures rise, their vertical spacing grows much more rapidly than their width. At the top of the visible flame, the radiation from each puff dies out throughout the whole structure almost simultaneously and we interpret this event as indicating that combustion of the fuel in the puff is completed at about the same time throughout the structure. This sudden extinction of radiation throughout the uppermost visible puff means that the top of the next lowest puff then becomes the top of the flame. Consequently, the apparent motion of the top of the flame is produced by the periodic extinction of radiation from the uppermost puff of a long line of puffs which rise from the burner under the influence of gravity. Although the production of puffs is not always regular and the extinction of the top puff is not instantaneous, this picture appears to be a useful description on the average and does emphasize the importance of these large structures in these diffusion flames.

The scales of disturbances visible in the flame photographs cover a very wide range. The largest is the scale of the puffs which is comparable to the burner diameter when the puffs are formed and subsequently they grow larger. Smaller scale disturbances are plentiful in the flame, and near the burner the flame takes on the appearance of a folded drapery. The smaller disturbances still have scales about a centimeter and the very small scales visible, for example, in the shadowgraph of a turbulent jet prior to ignition are not visible. In the simultaneously taken shadowgraph and flame pictures such as those shown in figures (3.1) and (3.2), it is interesting to note that the puffs in the visible flame have clear corresponding shadowgraph images. In these pictures, the visible flame is seen to lie within the boundary defined by the shadowgraph technique. Near the burner, this difference is a very small fraction of the flame width but the average separation grows with distance above the burner. Close to the burner, both the shadowgraph image and the visible flame image appear to be wrinkled but

laminar. In contrast, when we look above the beginning of the intermittent flame zone (above $Z_{fl} - \Delta/2$), we find that the direct photograph still has the appearance of a wrinkled laminar surface whereas the shadowgraph image of the hot gas which lies outside of the visible flame boundary now has a small grained structure which we believe is indicative of a turbulent flow. This transition lies roughly at $Z_{fl} - \Delta/2$ but has not yet been the subject of a thorough investigation. Given this change in the hot-cold gas boundary of the plume, we should anticipate a corresponding change in the entrainment processes at this elevation.

3.2. Quantitative Measures

Information obtained from the photographic study is summarized in Table 3.1 and figures (3.5) through (3.13). Analysis of a typical section of a video tape record of a 60 kW fire stabilized on a 0.19 m. diameter burner is shown in figure (3.5). The sketch shown in figure (3.5b) is a highly simplified picture of a typical photograph, such as the ones shown in figures (3.3) and (3.4). In figure (3.5b), the flame has two well-defined boundaries. These are the top of the visible flame, Z_0 and the symmetric indentation at elevation Z_1 . This indentation appears to define a toroidal shaped vortex ring which we believe is a primary source of entrainment. Examination of a number of shadowgraph pictures such as those in figures (3.1) and (3.2) show that the bottom edges of these structures just above the indentations are fairly flat and in some of these photographs, the symmetric roll-up on both sides can easily be seen (e.g. figure (3.2)). Furthermore, it was possible to observe the whole roll-up phenomenon by visual inspection of the shadowgraph images projected continuously onto a screen. These observations on the two dimensional image of nearly axisymmetric plumes suggest that these structures are toroidal vortices.

Time traces of the vertical positions of these indentations discussed above were made by measurements on successive frames of the video tapes. Data obtained in this manner is shown in figure (3.5a) in which values of Z_n are plotted for successive events as a function of time. A number of features emerge from examination of plots of this type. First, the indentations are formed much less than one burner diameter above the burner surface. Second, the boundaries defined by the indentations can often be followed all the way from a point near the burner surface to the top of the flame although at times they become ill-defined or actually vanish. These observations lead us to believe that in these flames toroidal vortices are shed by puffing of the flame near the burner surface and retain their identity as they move upward. Third, as these vortices move upward the fuel contained in each one eventually burns out and the radiation from the vortex vanishes. This causes the top of the flame to drop to the top of the next vortex in the train. From data such as the one presented in figure (3.5a), we can obtain information concerning: (1) the intermittency, I , defined as the fraction of the time during which at least part of the flame lies above a horizontal plane located at elevation, Z above the burner.; (2) time averaged flame height, Z_{fl} ; (3) time averaged puffing frequency, f ; (4) a measure of the velocity with which the puff structures rise, W_s ; (5) values of $\bar{\omega}_n$, the widths of the structures as they are first formed; and (6) the time averaged maximum widths of the first structure in the train above the indentation closest to the burner, $\bar{\omega}_{n-1}$. Most of these parameters are listed in Table (3.1) for three burners and various heat release rates, \dot{Q}_f .

A typical example of the height and width measurements and the puffing phenomena are shown in figure (3.3) for a 127 kW. fire on a 0.50 m. diameter burner. In this figure, two structures formed one after the other (labeled as I and II) are followed in time. The maximum width of structure I, $\bar{\omega}_{n-1}$ is measured at the time the indentation at Z_n has fully taken place as shown in (a). Between

the frames (a) and (c), the structure I moves up and retains its identity until it finally burns out between (c) and (d). At (d), the maximum width, $\bar{\omega}_n$ of the new structure II is measured just before the contraction of the flame surface. After necking-in at (e), the structure II becomes the uppermost structure and the whole cycle is repeated. The life time of structure I was about 0.60 seconds and in less than 0.20 seconds it was reduced from the size shown in figure (3.3c) to the small remnant at the top of structure II visible in figure (3.3d). The apparent drop in flame height between (c) and (d) is caused by the extinction of radiation in structure I.

A similar sequence of events is shown in figure (3.4) for a 42 kW. fire on 0.19 m. diameter burner. The straight bars on the right side of each sketch indicate our assesment of the boundaries of each puff. The difficulty in making this assessment is clear for this sequence in which the puffs are less well defined in the direct photographs. However, one can easily follow the demarcations which define structure II from its birth at the bottom of figure (3.4a) until it rises to the top in figure (3.4i). The *sudden decay* of radiation from structure I, the upper structure in frames (c) to (f), occurs between frame (e) and (g) and this happens in less than 0.20 seconds. The life of a structure here is about 10 frames or 1.0 second and thus the decay time is a small fraction (about $1/5^{th}$) of the life time.

Although there is a weak dependence on the fuel flow rate or \dot{Q}_f , the initial widths are not appreciably different from the burner diameter. This is an important result and is quite different from the behavior we would expect from a buoyant fuel jet rising steadily through quiescent air. In the latter case, the fuel velocity would increase with height roughly as \sqrt{Z} due to buoyancy and consequently the diameter of the fuel column would decrease as $Z^{-1/4}$. (This problem is discussed at length in Chapter 5.) Clearly the vortex structures prevent this

reduction of the fuel column diameter with height and in fact cause it to grow rather than to decrease. The fact that \bar{w}_n/D is near one will play an important role later in developing an entrainment model in Chapter 4.

Table 3.1. Flame Shape Parameters

$D, m.$	$\dot{Q}_f kW.$	$Z_{fl} m.$	$\frac{\Delta}{Z_{fl}}$	$f \sqrt{\frac{D}{g}}$	$\frac{W_s}{\sqrt{gZ}}$	$\frac{Z_{fl}}{D}$	Q_D^*	$\frac{\bar{w}_n}{D}$	$\frac{\bar{w}_{n-1}}{D}$
0.50	21.0	0.34	0.90	-	-	0.68	0.11	0.64	-
	32.0	0.44	0.80	0.23	-	0.88	0.16	-	-
	42.0	0.54	0.70	0.25	-	1.08	0.21	0.63	0.57
	63.0	0.70	0.68	0.28	-	1.40	0.32	0.71	0.60
	84.0	0.83	0.80	0.27	0.34	1.67	0.43	0.87	0.79
	127.0	1.13	0.70	0.29	-	2.26	0.65	0.91	-
	190.0	1.41	0.66	0.29	0.36	2.82	0.97	0.97	-
0.19	21.0	0.65	0.56	0.28	-	3.42	1.20	0.93	0.98
	42.0	0.90	0.56	0.26	-	4.74	2.40	1.04	1.33
	63.0	1.05	0.48	0.30	0.36	5.53	3.60	1.02	1.30
	84.0	1.16	0.46	0.26/0.29	0.32	6.11	4.80	1.16	1.49
0.10	21.0	0.64	0.42	0.28/0.24	-	6.4	5.97	0.95	1.79
	42.0	0.82	0.40	-	-	8.2	11.94	1.07	2.19
	63.0	1.09	0.38	0.21	-	10.9	17.92	1.30	1.89

All experiments with floor surround.

Typical plots for intermittency are shown in figures (3.6), (3.7) and (3.8) for 0.10 , 0.19 and 0.50 m. dia. burners and various heat release rates. The data have been normalized by the height at $I = 0.50$ which we call the average flame height, Z_{fl} , and the values of Z_{fl} are listed in Table 3.1. The normalized data are quite similar and change very slowly with the heat release rate of the fire. The extent of the intermittent region normalized by the average flame height increases with the burner diameter. A measure of the scale of the height of this intermittent region can be taken as the distance between the intercepts of the

maximum slope line at $I = 1.0$ and $I = 0.0$ and this distance is defined as the maximum slope thickness, Δ . For the three burners of diameters 0.10 , 0.19 and 0.50 m. , these values are very roughly $0.4 Z_{fl}$, $0.60 Z_{fl}$ and $0.80 Z_{fl}$ respectively. Although the numerical values of Δ depend on the chosen boundaries of intermittent region, the main features remain unchanged. For example, if we take the top and the lower end of this intermittent region to be $I = 0.05$ and $I = 0.95$ for 0.19 m. dia. burner at 42 kW, the intermittent region will extend over a distance of about $0.50 Z_{fl}$ whereas with limits $I = 0$ and $I = 1.0$, Δ is about $0.56 Z_{fl}$. Thus the intermittent region occupies a height of 40 to 60 % of Z_{fl} depending on the definition used. These values agree roughly with a value of 60 % obtained by McCaffery [3.1] for a 0.3 m. square burner. He used a technique based on time exposure photographs and eye averaging to define flame heights. Given the different definitions of length scales, this degree of agreement is good.

The values of $\frac{\Delta}{Z_{fl}}$ do depend weakly on Z_{fl} and grow smaller as Z_{fl} grows larger. For the largest burner, $\frac{\Delta}{Z_{fl}}$ approaches one for the small heat release rates. See values given in Table 3.1.

The flame height depends strongly on the definition used as well as the heat release rate of the fire and the burner diameter. The flame height obtained from video pictures which correspond to $I = 0.50$ are plotted in figure (3.9) for 0.10, 0.19 and 0.50 m. diameter burners and 10 to 200 kW fires. The data are shown in the form of a plot of Z_{fl}/D versus a dimensionless parameter $Q_D^* \equiv \dot{Q}_f / [\rho_\infty C_{p\infty} T_\infty \sqrt{g} D D^2]$ where \dot{Q}_f , is the total heat release rate (based on fuel flow rate and lower heating value) and D is the burner diameter. The lower and upper bounds of each data point correspond to the heights $(Z_{fl} - \Delta/2)$ and $(Z_{fl} + \Delta/2)$ respectively. In this plot, there are two distinct regions where flame height scales differently. If we consider the data obtained at large values of the

two parameters (e.g. $Q_D^* > 1.0$), they lie along a line with a slope of roughly 2/5. In this upper region, the diameter effect can be eliminated completely since,

$$\frac{Z_{fl}}{D} \propto \left(\frac{\dot{Q}_f}{D^{5/2}} \right)^{\frac{2}{5}} \propto \frac{\dot{Q}_f^{2/5}}{D} \quad (3.1)$$

Thus, it can be expressed for our data

$$\frac{Z_{fl}}{\dot{Q}_f^{2/5}} \approx 0.20 \text{ m} / (\text{kW})^{2/5} \quad (3.2)$$

or

$$\frac{Z_{fl}}{\left[\dot{Q}_f / \rho_\infty C_{p_\infty} T_\infty \sqrt{g} \right]^{2/5}} \equiv \frac{1}{\left(Q_{Z_{fl}}^* \right)^{2/5}} \approx 3.3 \quad (3.3)$$

Here, the normalizing group $\rho_\infty C_{p_\infty} T_\infty$ is independent of T_∞ since $\rho_\infty T_\infty$ is proportional to P_∞ (ideal gas law) which is constant in this work.

For the lower region where $Q_D^* < 1.0$, the dependence of flame height on burner diameter, D reappears. Since:

$$\frac{Z_{fl}}{D} \propto \left(\frac{\dot{Q}_f}{D^{5/2}} \right)^{\frac{2}{3}} \propto Q_D^{*\frac{2}{3}} \quad (3.4)$$

or

$$Z_{fl} \propto \left[\frac{\dot{Q}_f}{D} \right]^{\frac{2}{3}} \quad (3.5)$$

The transition between the two curves occurs around $\frac{Z_{fl}}{D} \approx 3.0$. In our subsequent analysis, we will employ the 50 % intermittency definition for the flame heights and will use the following formulae,

$$\left. \begin{aligned} Q_D^* < 1.0 \quad \frac{Z_{fl}}{D} &= 3.30 Q_D^{*\frac{2}{3}} \\ Q_D^* > 1.0 \quad \frac{Z_{fl}}{D} &= 3.30 Q_D^{*\frac{2}{5}} \end{aligned} \right\} \quad (3.6)$$

In addition to the video measurements, we recorded eye-averaged flame heights for the same burners and heat input ranges as the video data. These data are shown in figure (3.10) in the form $\frac{Z'_{fl}}{D}$ versus Q_D^* or a dimensional parameter, $\dot{Q}_f / D^{\frac{5}{2}}$ kW/m.^{5/2}. The data obtained from the work of a number of other investigators are also shown on this plot. The data at large values of Q_D^* have roughly the same slope (2/5) obtained from video measurements. This type of dependence has been obtained earlier, by Putnam and Speich [3.2] and Steward [3.3] who used a wide range of gaseous fuels including methane (natural gas) and hydrogen. We show a few of Steward's data points and a curve fitted to other data not shown on this figure and also extending out to Z_{fl} / D values of 200. Data of Putnam and Speich also lie on this curve at $100 \leq Z_{fl} / D \leq 200$. The range of agreement is truly remarkable when we consider that we are dealing with 100 kW fires stabilized on a 0.19 m. dia. burner at one end and 10 kW fires burning on a 0.003 m. dia. burner at the other end.

Other data shown here include fire heights measured by Thomas et al [3.4] who used wood cribs ; You and Faeth [3.5], who used wicks with a range of alcohol fuels; and Terai and Nitta [3.6] and McCaffery [3.1] who used natural gas flames on 0.30 m. square burners. These data and our data which lie in the left-hand side of figure (3.6) are in good agreement and show a gradual transition from $2\beta^{ths}$ power curve to a $2\beta^{ths}$ power curve in the range $2 \leq \frac{Z_{fl}}{D} \leq 4$. Similar behavior at small $\frac{Z_{fl}}{D}$ is also noted by Thomas [3.7]. The good agreement among these data indicate that the phenomena we are all observing is a general one which is not strongly dependent on burner geometry and fuel properties. The transition which occurs around $\frac{Z_{fl}}{D} = 3$ is not unexpected since it seems natural that as the flame top approaches close to the burner, the scaling parameters should change and that burner diameter should become an important scale length. In this regime, for very small values of $\frac{Z_{fl}}{D}$, the flame breaks into a number of small flamelets which are all roughly the same height. They surround the burner perimeter and move almost independently of one another. Thus, we expect that the dependence of the flame height and other parameters such as entrainment will have a markedly different dependence when Q_D^* is much less than one.

The comparison between the eye-averaged flame heights and those obtained from the video pictures is shown in figure (3.11) where data of figure (3.10) are sketched as cross-hatched. The agreement between the two is within 10 - 15 % . The eye-averaged data lie closer to the time-averaged top of the flame than the 50 % intermittency value. Here, the time-averaged top is the simple time average of the maximum height reached by each structure prior to flame extinction. This corresponds to $Z_{fl} + \Delta/2$. The eye-averaged results lay consistently 10 -15 % higher than 50 % intermittency level flame heights. For eye averaged data the

constants in equations (3.2) and (3.3) become 0.23 and 3.37 respectively.

The use of the dimensionless heat addition parameter, Q_D^* is one of the many ways of correlating the flame heights. For example, Steward [3.3] used a more complicated parameter resulting from his analytic model. His parameter depends on the heat release per mass of oxidizer which is a very weak function of the fuel type. Even though the heating value per mass of fuel varies with the fuel type, the heating value per mass of oxidizer, which fixes the gas temperature, varies less than 20 % from one fuel to the other. This makes the choice of the correlation parameter difficult. Extensive numerical analysis of Steward's data suggests that the parameter, Q_D^* did a better job of correlating his data than did his more complex parameter. A final selection of scaling parameter will require tests in which large changes are made in heating value per unit mass of the oxidizer.

Rough values of the average puffing frequency normalized by the $\sqrt{\frac{D}{g}}$ are given in Table 3.1 and these results lie in the frequency range given by,

$$f = (0.27 \pm 0.03) \sqrt{\frac{g}{D}} \quad (3.7)$$

for our test conditions. The frequency was better defined when the level of random disturbances in the ambient air was very low. In a real fire, puffing may not be very well defined because of a higher level of ambient disturbances. Note that f is also independent of fire strength (expressed as either Z_{fl} or \dot{Q}_f).

Velocity determinations from our data requires a certain amount of art and imagination, and it is one of the least well defined of the parameters of Table 3.1

The data are consistent with a value of

$$W_s = (0.34 \pm 0.02) \sqrt{gZ} \quad (3.8)$$

but the uncertainty is much larger than suggested here. This result is in sharp contrast with the observations of McCaffrey [3.1] which indicate that the gas speed on the axis of the burner increases like $2.2 \sqrt{gZ}$ for $Z < 0.4 Z_{fl}$ and is constant for $0.4 Z_{fl} \leq Z \leq Z_{fl}$. Thus, in the lower region, the gas speeds reported by McCaffrey appear to be about six times the speed of our vortex structures. This velocity is also about 1/3 of that reported by Thomas [3.7] who analyzed the data of Rasbash et al [3.8]. These differences are related to the fact that we are clearly measuring the velocity of a structure not the gas speed.

We can tie together several of these results by calculating the dependence of the fluctuation scale length, Δ on the diameter of the burner, D and the average flame height, Z_{fl} . To do this, we identify the scale Δ with the vertical size of the uppermost puff at the moment that the flame is extinguished in the puff. The fluctuations of the flame top can best be illustrated by use of figure (3.12). At instant t , the average position of the top of the puff will lie at a height of about $(Z_{fl} + \Delta/2)$ above the burner. When the top puff burns out, the top of the flame will suddenly drop from height $(Z_{fl} + \Delta/2)$ to $(Z_{fl} - \Delta/2)$.

If Z_s is the position of the top of a disturbance, that is, the indentation marking the top of a puff. Our measurements suggest that:

$$\frac{dZ_s}{dt} \equiv W_s = C_1 \sqrt{gZ_s} \quad (3.9)$$

where C_1 is given in equation (3.8). This can be integrated to give

$$Z_s = \left[\frac{C_1}{2} \right]^2 g t^2 \quad (3.10)$$

if t is picked to be zero when Z_s is zero. If this structure reaches its maximum height, just before it burns out (and the radiation from the soot stops) at time t_i , our simple model suggests that the top of the flame will lie at about $\Delta/2$ above the average flame top at Z_{fl} . Hence we can write,

$$Z_s(t_i) = \left[\frac{C_1}{2} \right]^2 g t_i^2 = Z_{fl} + \frac{\Delta}{2} \quad (3.11)$$

similarly, the top of the next puff in the train will lie at a point given by,

$$Z_s(t_i - 1/f) = \left[\frac{C_1}{2} \right]^2 g (t_i - 1/f)^2 = Z_{fl} - \frac{\Delta}{2} \quad (3.12)$$

because it will arrive at this point at time $1/f$ after the first disturbance has passed. If we subtract the last two equations and rearrange slightly, we get:

$$\Delta = \left[\frac{C_1}{2} \right]^2 g t_i^2 \left[1 - \left(1 - \frac{1}{t_i f} \right)^2 \right] \quad (3.13)$$

Now $f t_i$ can be calculated from equations (3.11) and (3.7). One obtains

$$f t_i = \left[\frac{2C_2}{C_1} \right] \sqrt{\frac{Z_{fl}}{D}} \sqrt{1 + \frac{\Delta}{2Z_{fl}}} \quad (3.14)$$

where C_2 is the numerical constant in equation (3.7). This result can be used to rewrite equation (3.13) as

$$\frac{\Delta}{Z_{fl}} = X \left(1 - \frac{X^2}{16} \right)^{\frac{1}{2}} \quad (3.15)$$

where

$$X = \frac{\left[\frac{C_1}{C_2} \right]}{\sqrt{\frac{Z_{fl}}{D}}}$$

This is an equation for $\frac{\Delta}{Z_{fl}}$ as a function of $\frac{C_1}{C_2}$ and $\frac{Z_{fl}}{D}$. Equation (3.15) is plotted in figure (3.13) for $\frac{C_1}{C_2} = 1.20$ and 1.33 which are reasonable estimates given the data of Table 3.1. The data also shown on this figure agree remarkably well with either curve given the simplicity of the model, the crude nature of the data and our identification of Δ . The disagreement when $Q_D^* < 1.0$ and $\frac{Z_{fl}}{D} \leq 3$ is to be expected since these flames no longer have the same structure described above. In this regime, the flames become small flamelets surrounding the burner perimeter and they burn independently of each other. This behavior also shows up in the flame height correlation as the transition between the two regimes.

The good agreement of measured and calculated values for $\frac{\Delta}{Z_{fl}}$ suggest that we have a self consistent picture of the large structures for the burner flames studied here. They are shed more or less regularly with an average frequency which scales as $\sqrt{\frac{g}{D}}$ and they rise with a velocity which is scaled by $\sqrt{gZ_s}$. The intermittent nature of the top of the flame is caused in large part by the

completion of combustion throughout the structure almost instantaneously. This process causes the visible top of the flame to drop rapidly to the top of the next structure when the upper one burns out. This description is idealized because the puffing is not perfectly regular and is easily perturbed by the disturbances in the ambient atmosphere.

The change in the slope of the flame height normalized by the burner diameter versus Q_D^* which occurs around $Q_D^* \approx 1.0$ represents an important change in the nature of the flame and presumably in other important processes such as entrainment. Most of the real fires fall in the range $Q_D^* < 1.0$. To give an idea, a waste basket fire of 0.1 m^2 area should get larger than 85 kW before Q_D^* exceeds unity. Similarly, a burning mattress of 1 m^2 area would have to exceed 1.5 MW. Hence, further study of flames in the region where $Q_D^* < 1$ should be made.

References

- [3.1] B. J. McCaffery, Purely Buoyant Diffusion Flames: Some Experimental Results, NBSIR79-1910, *National Bureau of Standards, Department of Commerce, Washington D.C.* (1979)
- [3.2] A. A. Putnam and C. F. Speich, A Model Study of the Interaction of Multiple Turbulent Diffusion Flames, *Ninth Symposium (International) on Combustion*, 867, Academic Press, New York (1963)
- [3.3] F. R. Steward, Prediction of the Height of Turbulent Diffusion Buoyant Flames, *Comb. Sci. & Tech.*, **2**, 203,(1970)
- [3.4] P. H. Thomas, C. T. Webster and M. M. Raftery, Some Experiments on Buoyant Diffusion Flames, *Combustion & Flame*, **5**, 359,(1961)
- [3.5] H. Z. You and G. M. Faeth, Ceiling Heat Transfer during Fire Plume and Fire Impingement, *Fire & Materials*, **3**, 140,(1979)
- [3.6] T. Terai and K. Nitta, *Proc. Syms. Arch. Inst., Japan*,(1975)
- [3.7] P. H. Thomas, The Size of Flames from Natural Fires, *Ninth Symposium (International) on Combustion*, 844, Academic Press, New York (1963)
- [3.8] D. J. Rusbash, Z. W. Rogowski and G. W. V. Stark, Properties of Fires of Liquids, *Fuel*, **35**, 94,(1956)
- [3.9] V. K. Rao and T. A. Brzustowski, Preliminary Hot-Wire Measurements on Free-Convection Zones Over Model Fires, *Comb. Sci. & Tech.*, **1**, 171-180,(1969)

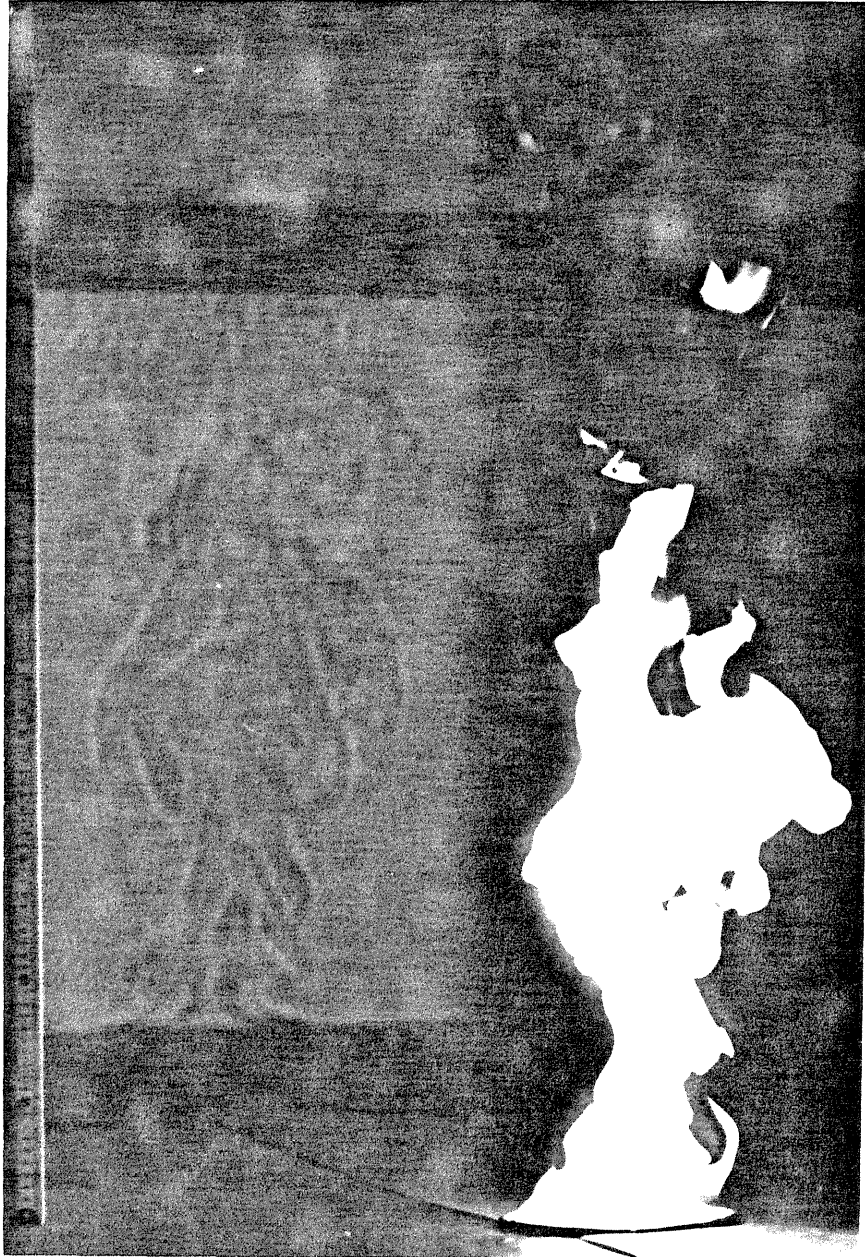


Figure (3.1) Picture and simultaneously photographed shadow-graph image of a 20 kW. fire on 0.19 m. diameter burner

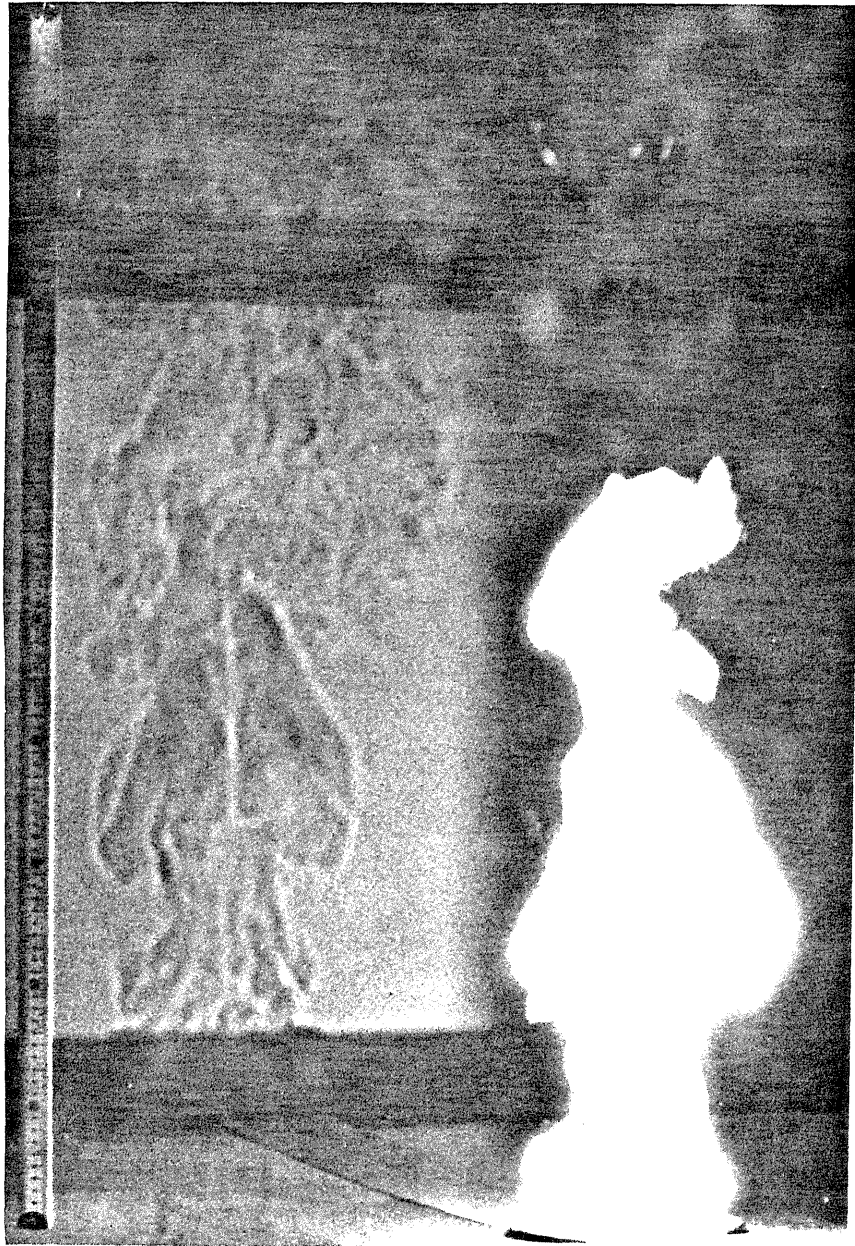


Figure (3.2) Picture and simultaneously photographed shadow-graph image of a 20 kW. fire on 0.19 m. diameter burner

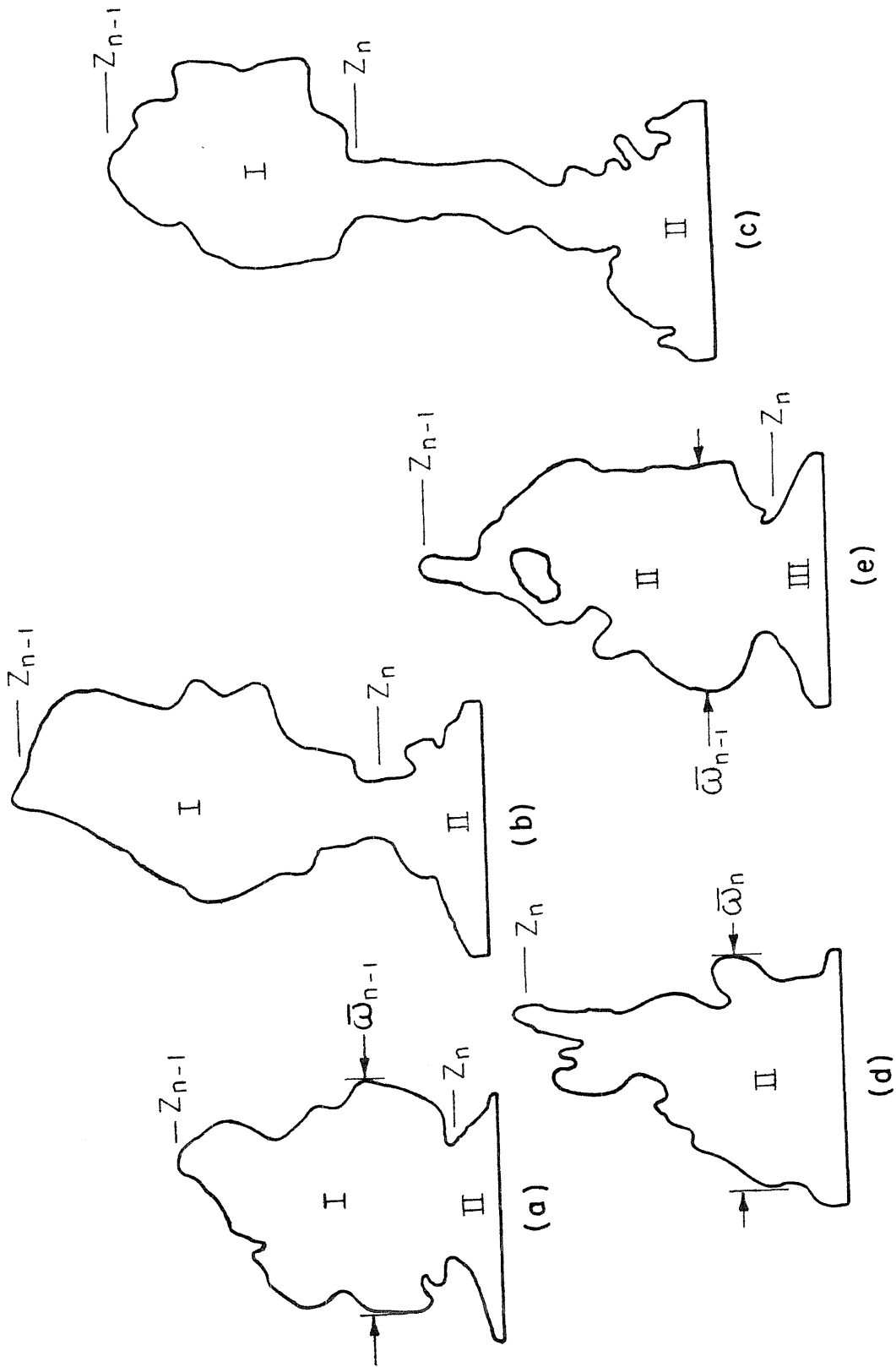


Figure (3.3) Successive flame shapes of a 127 kW. fire on 0.50 m. diameter burner with 0.2 second time steps as obtained from video tape data

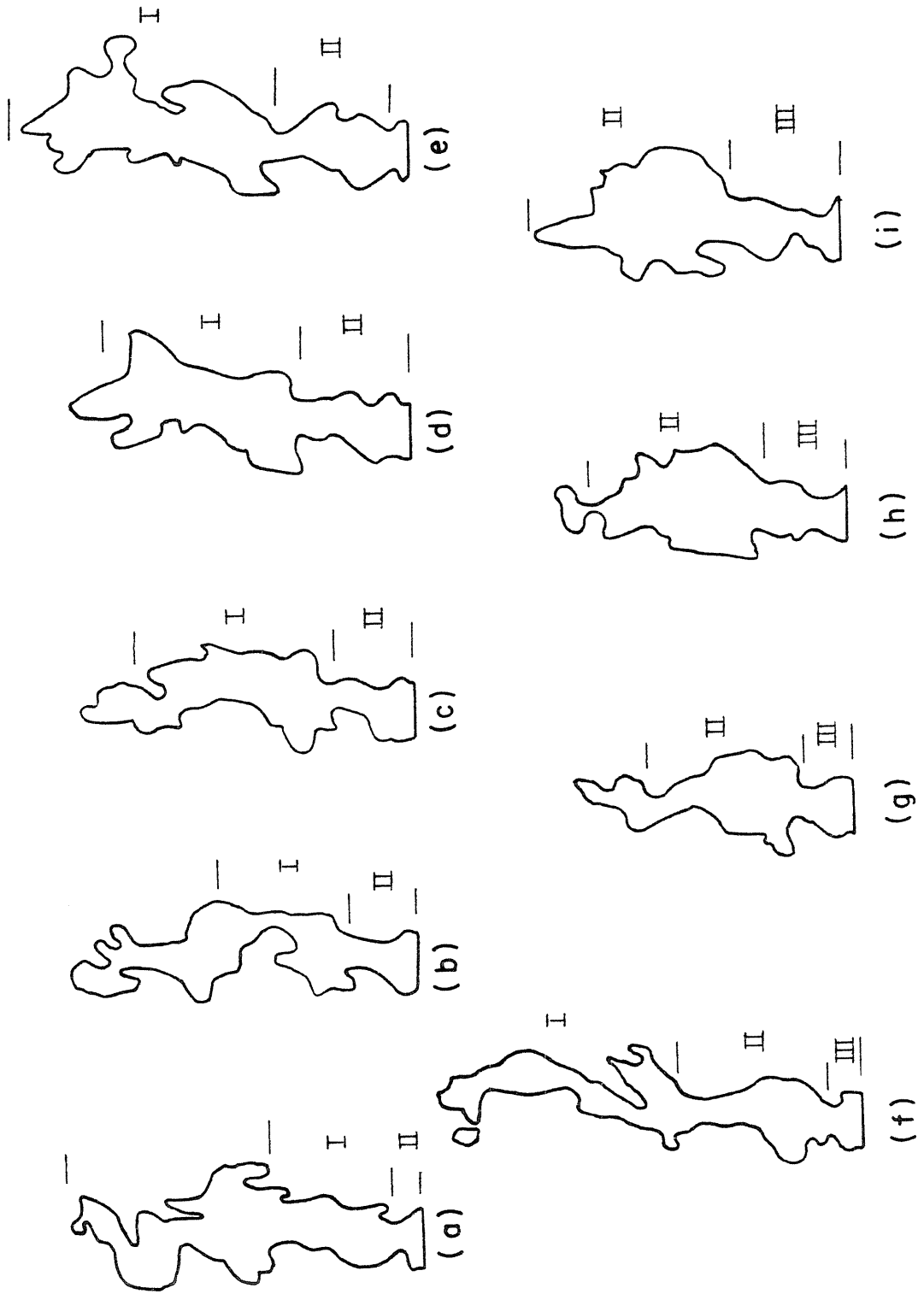


Figure (3.4) Successive flame shapes of a 42 kW. fire on 0.19 m. diameter burner with 0.1 second time steps as obtained from video tape data

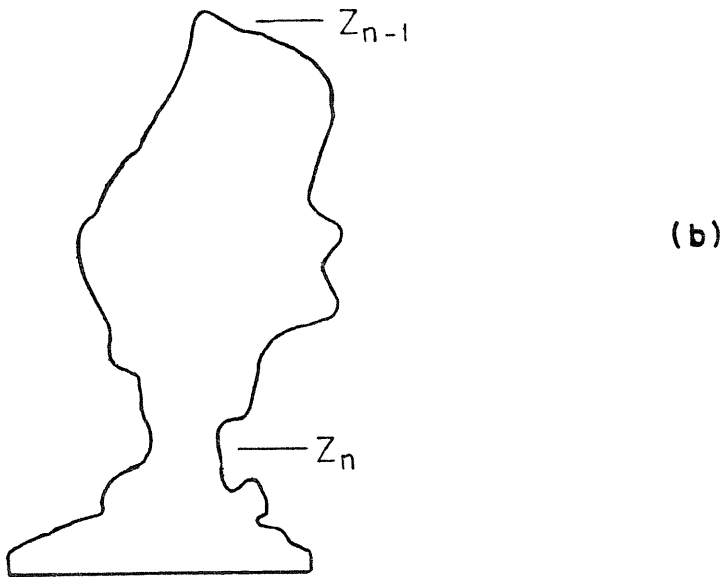
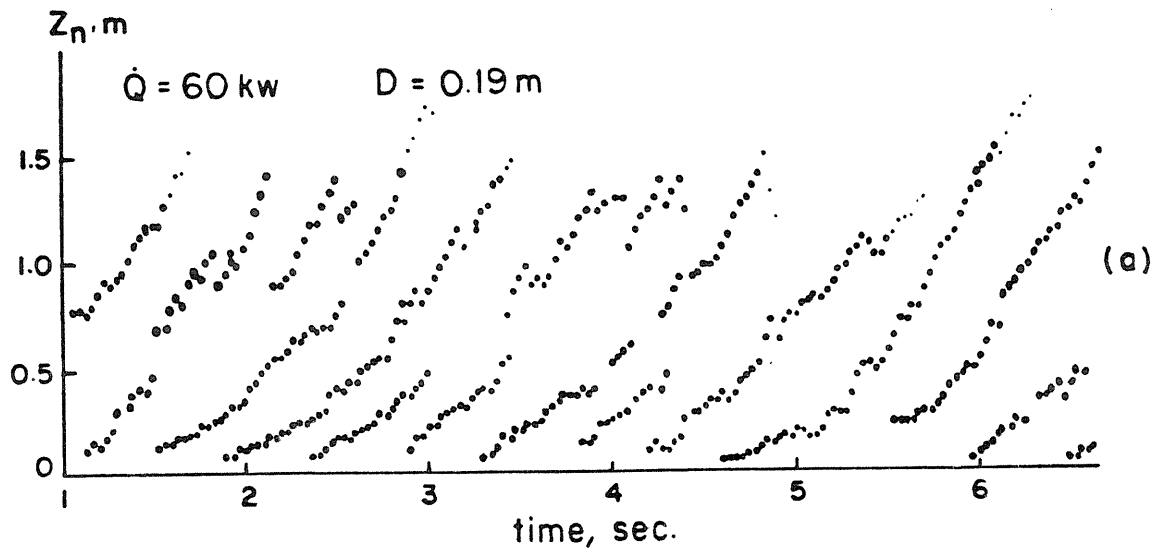


Figure (3.5) Motion of vortices in a fire plume

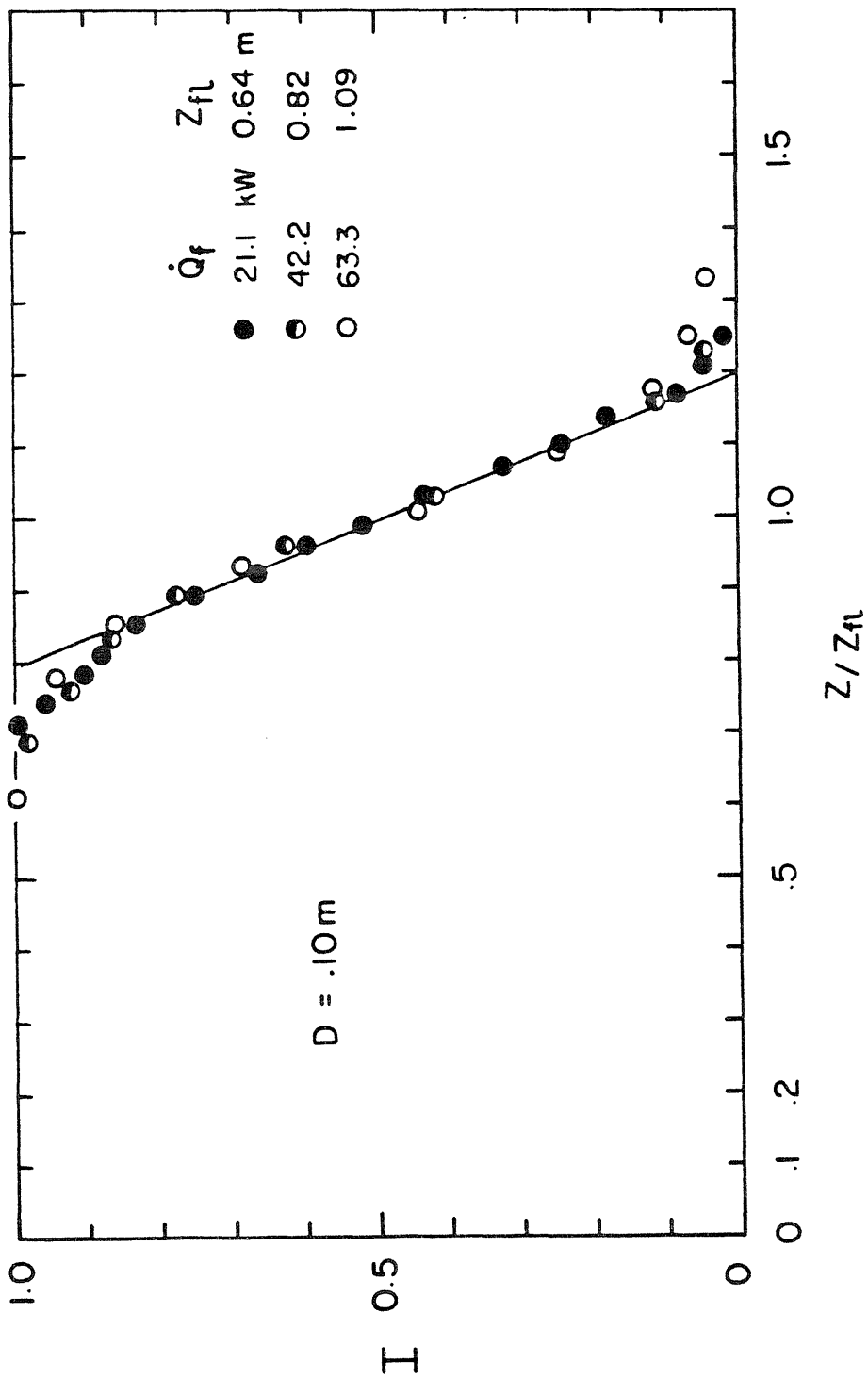


Figure (3.6) Intermittency of flame height for 0.10 m. diameter burner for various heat release rates

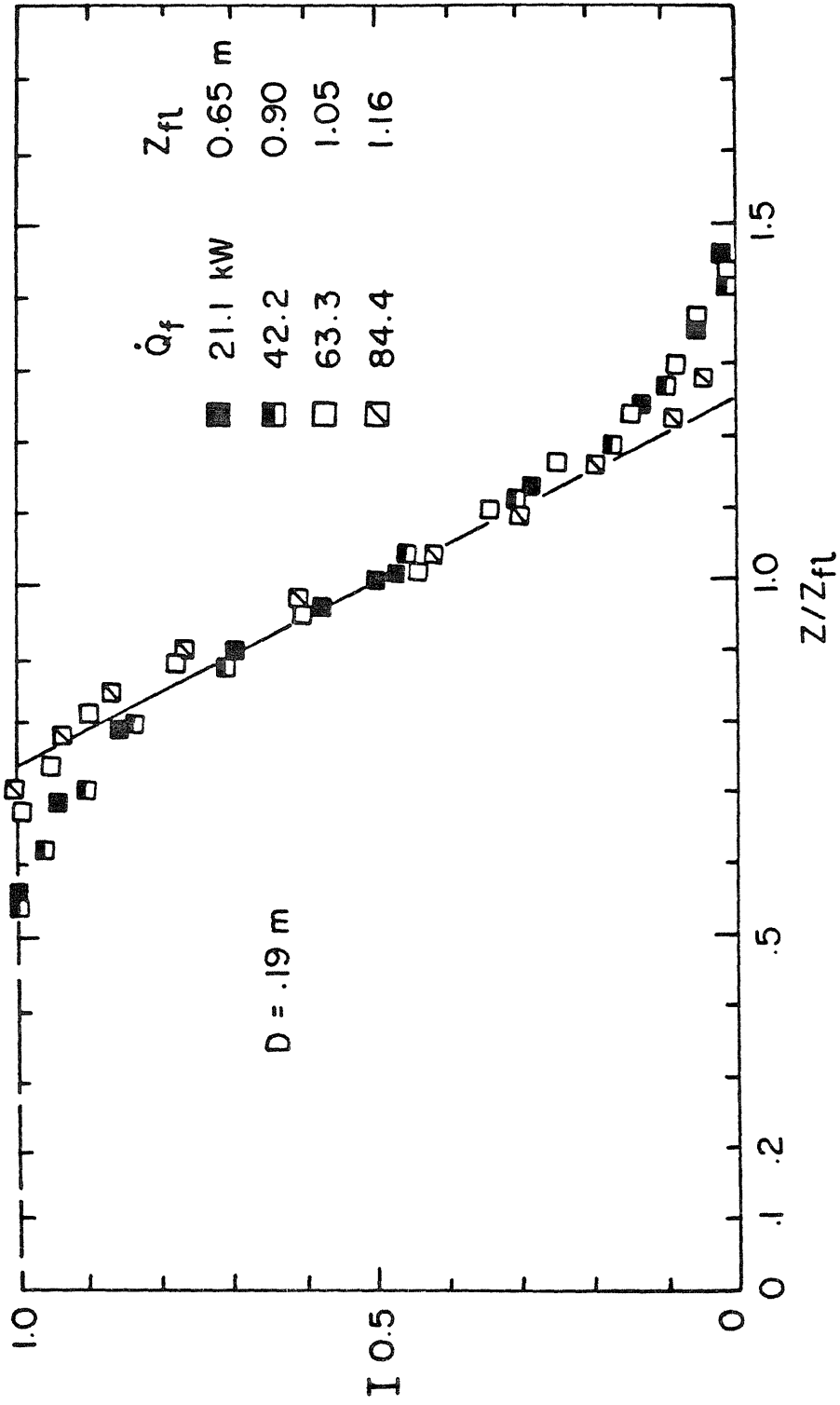


Figure (3.7) Intermittency of flame height for 0.19 m. diameter burner for various heat release rates

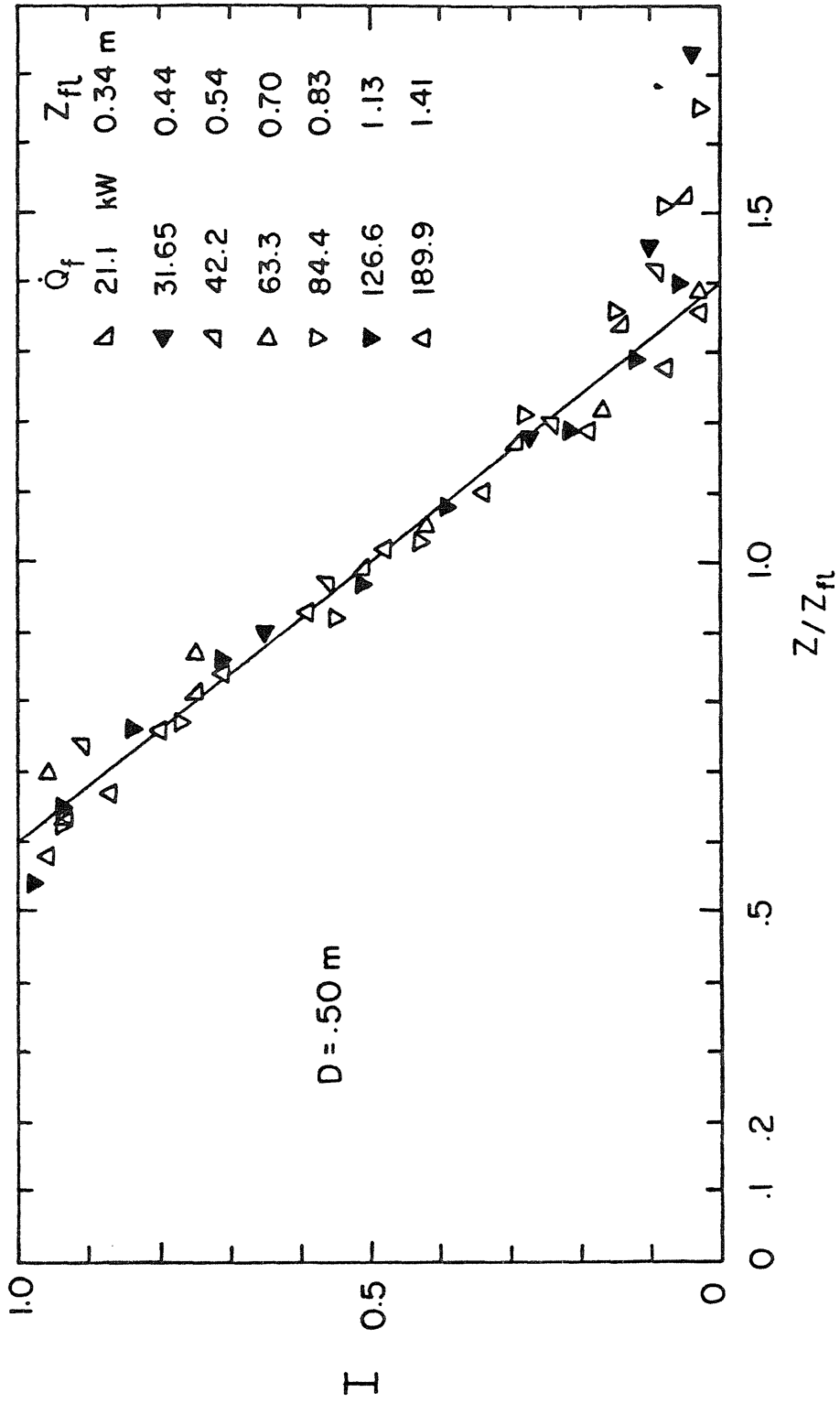


Figure (3.8) Intermittency of flame height for 0.50 m. diameter burner for various heat release rates

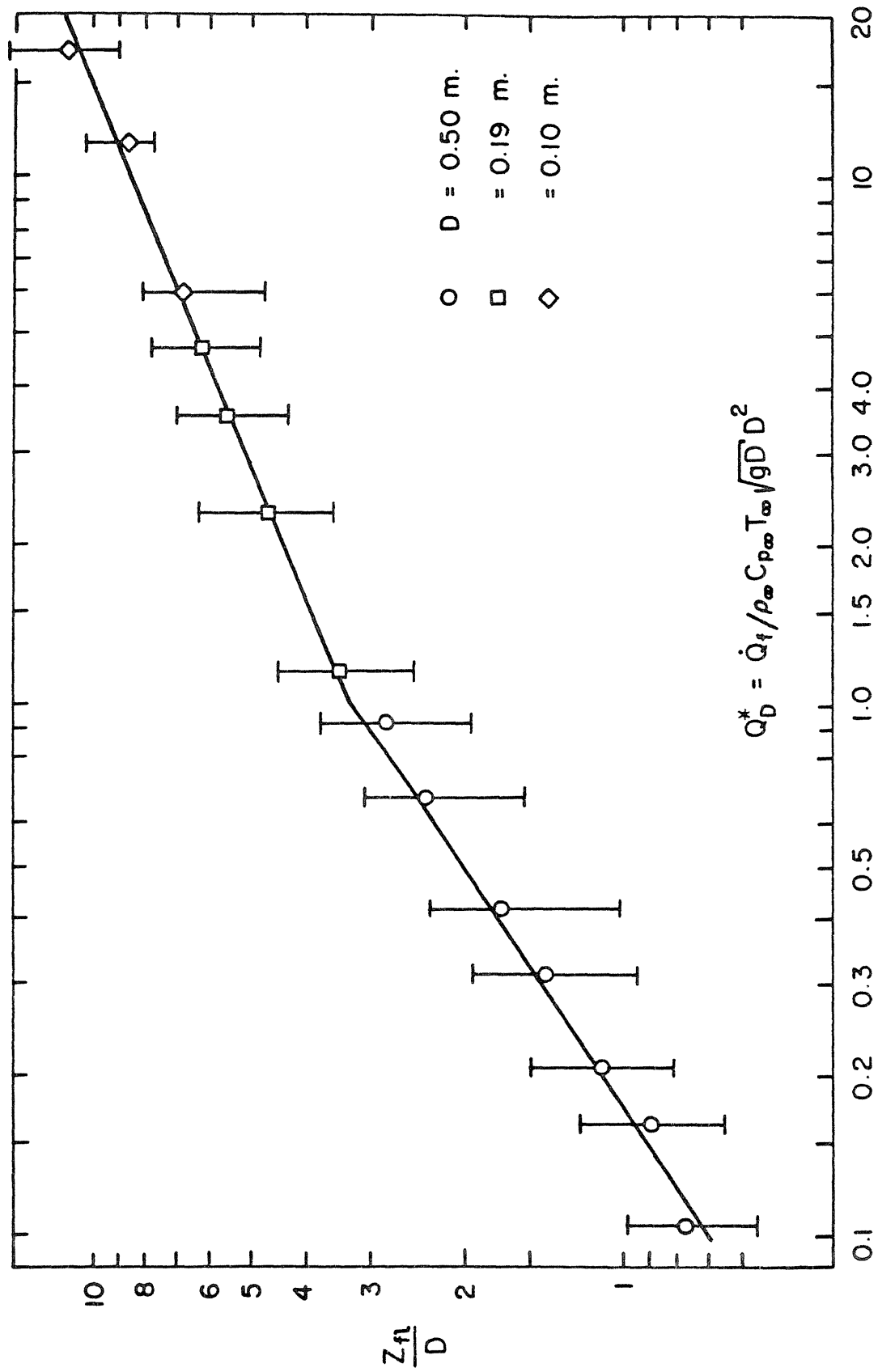


Figure (3.9) Flame height correlation for 0.10, 0.19 and 0.50 m. diameter burners. The vertical bars indicate the size of the fluctuation heights.

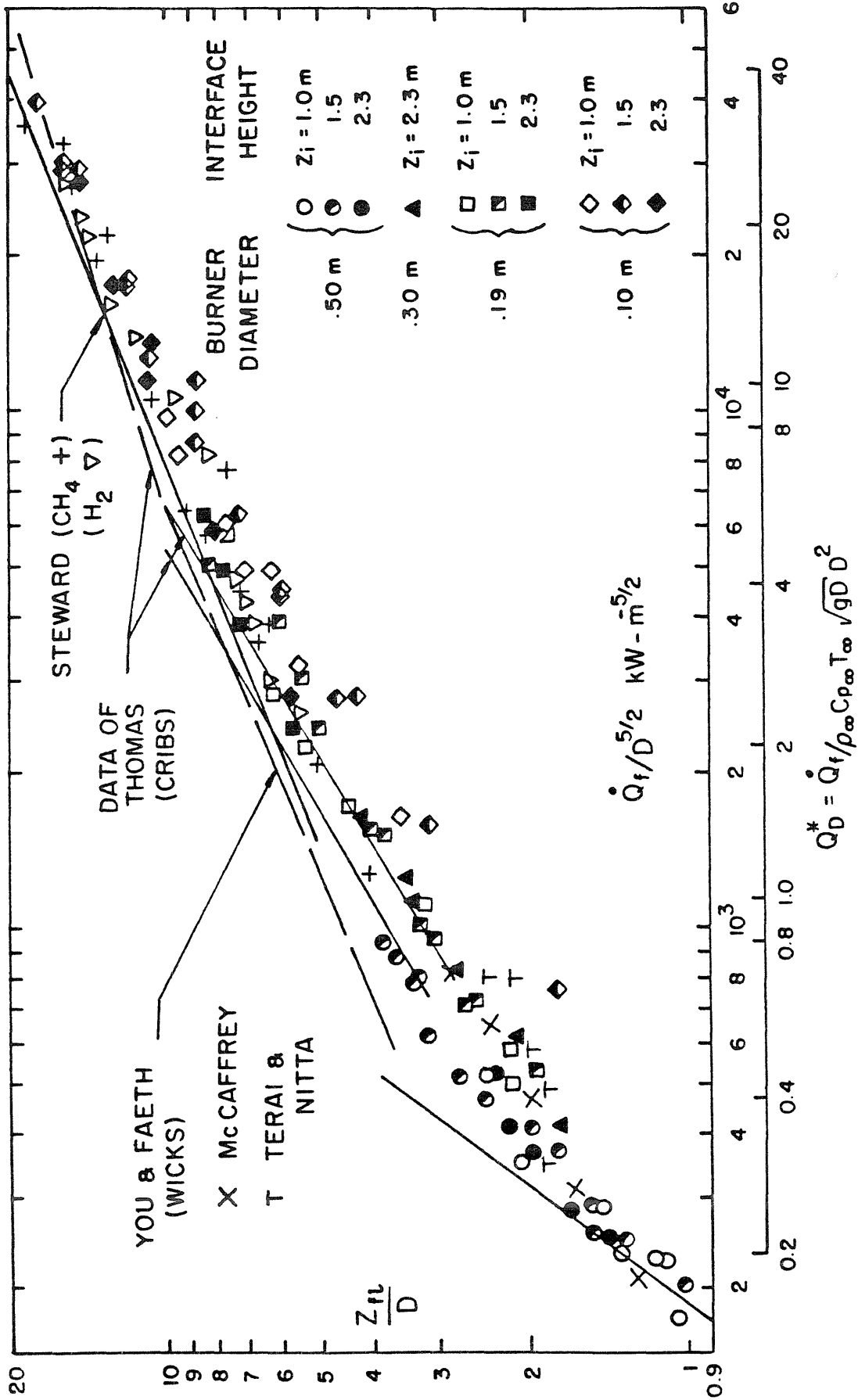


Figure (3.10) Eye averaged flame height data correlation

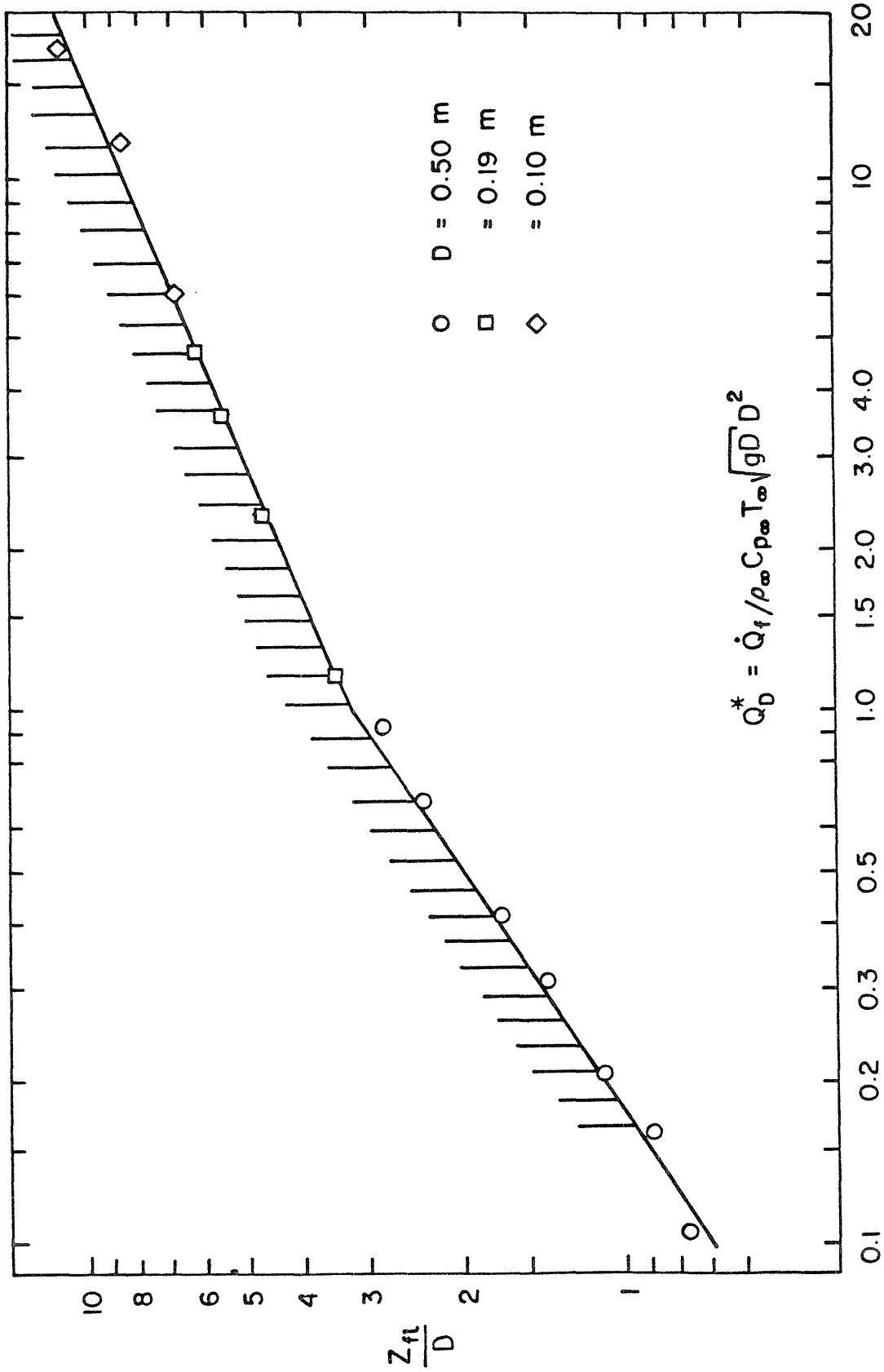


Figure (3.11) Comparison of eye averaged (cross hatched) and video taped flame heights.

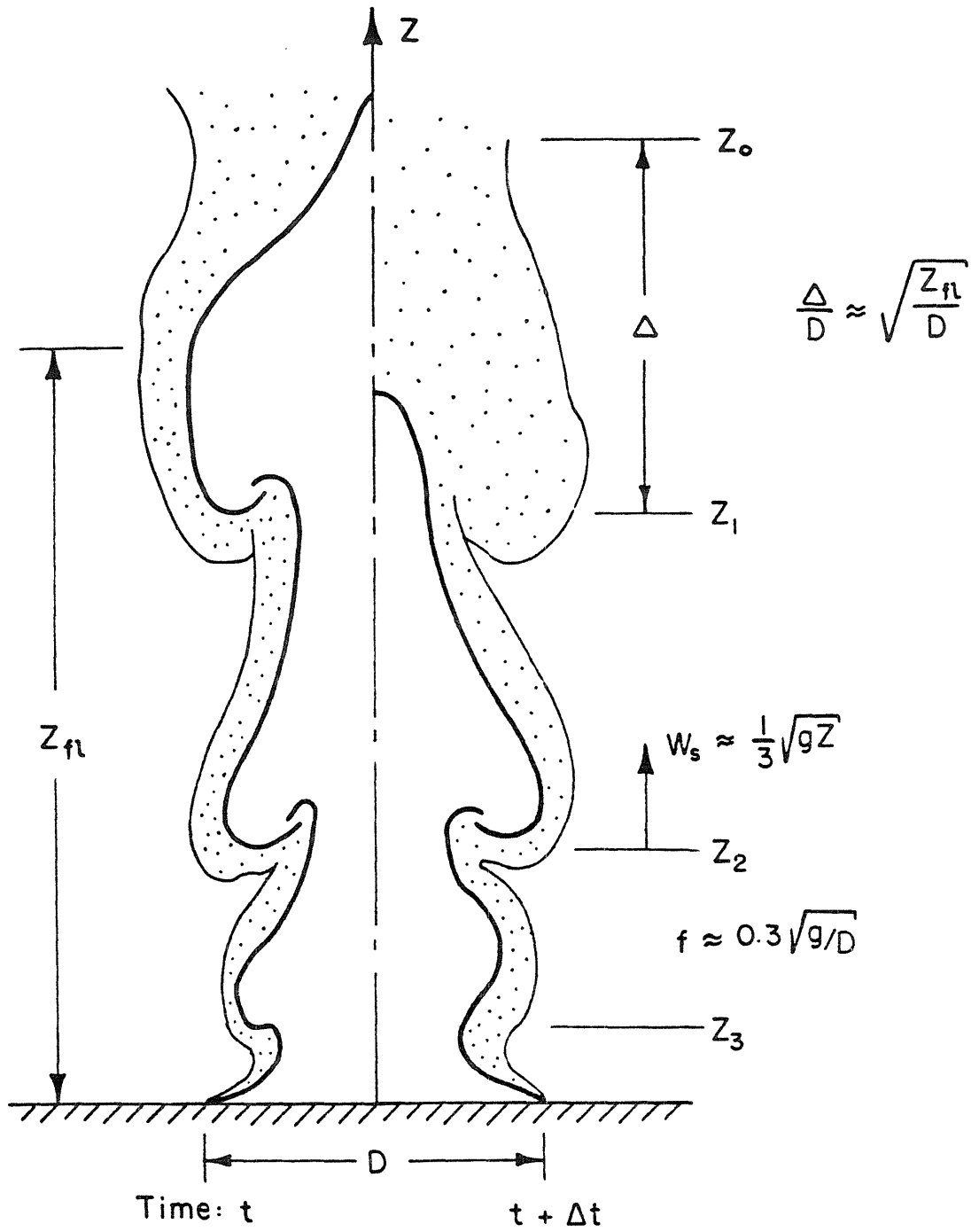


Figure (3.12) Sketch for the flame height fluctuations

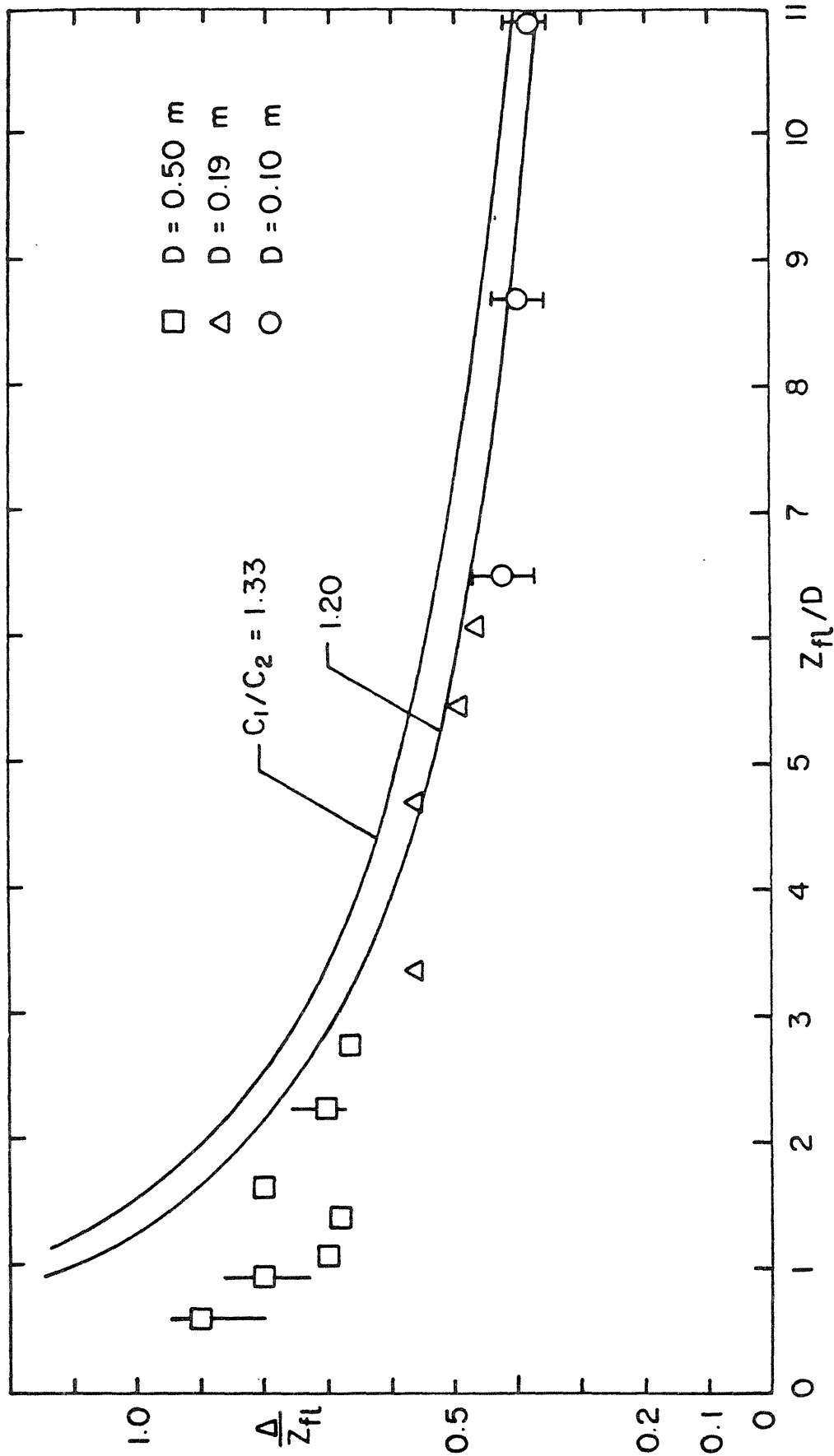


Figure (3.13) Dependence of maximum slope thickness on flame height and burner diameter for 0.10, 0.19 and 0.50 m. diameter burners

Chapter 4

PLUME MASS FLUX MEASUREMENTS

4.1. Far Field

4.1.1. *Simple Model.*

In the past, Zukoski [4.1] combined the general approach concerning entrainment suggested by Morton et al [4.2] and Taylor [4.3] with the data obtained by Yokoi [4.4]. The model is based on a point source heat addition and a Boussinesq treatment of density. Clearly neither of these approximations is appropriate for treatment of the plume near the flame and near the burner. However, we use the entrainment predicted by this model as a scaling parameter in presentation of measured plume mass fluxes. Here, we again note that in the experiments, we measure the mass flux into a ceiling layer not the plume mass flux and hence that our measurements may be slightly greater than the actual plume mass flux.

In the following treatment of the buoyant plume, we employ the procedure suggested by Kubota [4.5] and use the Howarth transformation to reduce the governing equations to incompressible forms and remove the dependence on the density variation. We also have modified the Taylor's entrainment assumption by assuming that the entrainment rate depends on the transformed half-widths rather than the physical half-widths as it was in Taylor's original formulation.

The use of the Howarth transformation and this modification of the entrainment hypothesis lead to a prediction of the entrainment rate which is exactly that reached by use of the Boussinesq approximation. The entrainment

assumption seems to be plausible one but certainly requires further investigation.

The conservation equations for an axisymmetric, buoyant plume are,

$$\text{Continuity : } \frac{d}{dZ} \left[2\pi \int_0^{\infty} \rho w r dr \right] = -2\pi \rho_{\infty} \lim_{r \rightarrow \infty} (rv) \quad (4.1)$$

$$\text{Momentum : } \frac{d}{dZ} \left[2\pi \int_0^{\infty} \rho w^2 r dr \right] = 2\pi g \int_0^{\infty} (\rho_{\infty} - \rho) r dr \quad (4.2)$$

where we have used the assumption that the pressure is everywhere given by the hydrostatic variation with z and the orientation of coordinate system is illustrated in figure (4.1).

$$\text{Energy : } \frac{d}{dZ} \left[2\pi \int_0^{\infty} \rho C_p (T - T_{\infty}) w r dr \right] = \frac{d\dot{Q}}{dZ} \quad (4.3)$$

where T_{∞} is the ambient temperature far from the plume and $\frac{d\dot{Q}}{dZ}$ is the rate of heat addition to the plume by combustion in the flame. These equations can be transformed into incompressible forms by the Howarth transformation in the r direction as

$$\rho r dr = \rho_{\infty} b^2 \eta d\eta \quad (4.4)$$

where b is the transformed half width in the r direction. The above transformation gives $r = b\eta$ in the limit $\rho/\rho_{\infty} \rightarrow 1$.

Here, we assume Gaussian profiles for vertical velocity, w and temperature difference, $(T - T_{\infty})$ in the radial direction which are expressed in transformed

coordinates as,

$$\frac{T - T_{\infty}}{T_m - T_{\infty}} = e^{-\beta^2 \eta^2} \quad (4.5)$$

and

$$\frac{w}{w_m} = e^{-\eta^2} \quad (4.6)$$

where β is the ratio of the Gaussian half widths of velocity and temperature profiles. T_m is the local temperature along the plume axis. The entrainment assumption is similar to that proposed by Taylor [4.3]

$$-\lim_{r \rightarrow \infty} (rv) = \alpha w_m b \quad (4.7)$$

where α is an empirical constant. Here, it is interesting to note that the form of the entrainment assumption used by Ricou and Spalding [4.6] is recovered from equations (4.4) and (4.7) since $\frac{r}{b} \propto \sqrt{\frac{\rho_{\infty}}{\rho}}$.

We can carry out the integrals in equations (4.1),(4.2) and (4.3) using the profiles in equations (4.5) and (4.6) to get,

$$\frac{d}{dZ} \left(\pi w_m b^2 \right) = 2\pi \alpha w_m b \quad (4.8)$$

$$\frac{d}{dZ} \left(\frac{\pi}{2} w_m^2 b^2 \right) = \frac{\pi}{\beta^2} g b^2 \frac{\Delta T_m}{T_{\infty}} \quad (4.9)$$

and

$$\frac{d}{dZ} \left(\frac{\pi}{1 + \beta^2} w_m b^2 \frac{\Delta T_m}{T_\infty} \right) = \frac{d}{dZ} \left(\frac{\dot{Q}}{\rho_\infty C_p T_\infty} \right) \quad (4.10)$$

where $\Delta T_m \equiv T_m - T_\infty$.

For point source heat addition, equation (4.10) can directly be integrated to yield,

$$\frac{\pi}{1 + \beta^2} w_m b^2 \frac{\Delta T_m}{T_\infty} = \frac{\dot{Q}_0}{\rho_\infty C_p T_\infty} \quad (4.11)$$

where \dot{Q}_0 is the total heat release at the origin. Equation (4.11) implies that the buoyancy flux remains constant and equal to the initial buoyancy due to heat addition.

The similarity solutions of equations (4.8), (4.9) and (4.11) require that

$$\left. \begin{aligned} \frac{b}{Z} &= C_1 \\ \frac{\Delta T_m}{T_\infty} &= C_T Q_Z^{*2/3} \\ \frac{w_m}{\sqrt{gZ}} &= C_V Q_Z^{*1/3} \end{aligned} \right\} \quad (4.12)$$

where $Q_Z^* \equiv \frac{\dot{Q}_0}{\rho_\infty C_p T_\infty \sqrt{gZ} Z^2}$

If we substitute these into equation (4.8), (4.9) and (4.11) we obtain the following relations among the five constants α , β , C_l , C_T and C_V .

$$\left. \begin{aligned} \alpha &= \frac{5}{6} C_l \\ \beta^2 C_V^2 &= \frac{3}{2} C_T \\ C_V C_l^2 C_T &= \frac{1 + \beta^2}{\pi} \end{aligned} \right\} \quad (4.13)$$

We can determine these five constants if we use two inputs from experiments. Yokoi [4.4] measured the temperature and velocity along the plume centerline and found that,

$$C_T = 9.115 \quad \text{and} \quad C_V = 3.87 \quad (4.14)$$

The other constants computed from equations (4.13) are,

$$\alpha = 0.11 \quad , \quad \beta^2 = 0.913 \quad , \quad C_l = 0.131 \quad (4.15)$$

The plume mass flux, \dot{m}_3 can be expressed as,

$$\dot{m}_3 = 2\pi \int_0^\infty \rho w r dr = \pi \rho_\infty w_m b^2 \quad (4.16)$$

or

$$\dot{m}_3 = C_m \rho_\infty \sqrt{gZ} Z^2 Q_Z^{*1/3} \quad (4.17)$$

where $C_m = \pi C_V C_L^2 = 0.21$.

The form of the plume mass flux correlation can be obtained from the equation suggested by Ricou and Spalding [4.6]. They proposed a constant of $C_m = 0.18$ rather than 0.21.

In the diffusion flames we are studying, the heat release takes place in a finite zone bounded by the burner surface and the top of the visible flame. Hence, it would be more appropriate to integrate equations (4.8), (4.9) and (4.10) provided that the heat release distribution in the flame region is known. Since the real heat release distribution in the flame is unknown, we have confined ourselves to the examination of the effects on entrainment rates of several simple distributions based in part on input from radiation measurements of Markstein [4.7]. A few of these computations are shown in figures (4.2), (4.3) and (4.4). as the ratio of computed entrainment to that from equation (4.17) which is the far field solution. Figure (4.2) shows the calculated entrainment for a 60 kW fire on 0.10, 0.19 and 0.50 m. dia. burners with a triangular heat release distribution. Here, $\frac{d\dot{Q}}{dZ}$ has a maximum at $Z = 0.1 Z_{fl}$ and is zero at $Z = 0$ and $Z = Z_{fl}$. Similar results are shown in figure (4.3) for the same type of heat release distribution but with a maximum located at $Z = 0.8 Z_{fl}$. If the vertex of the triangular heat release profile is changed in increments of $0.1 Z_{fl}$, we obtain the picture shown in figure (4.4). These computations stress the importance of the heat release distribution in the visible flame zone. These effects die out at large distances above the visible flame and they are surprisingly small at $Z = Z_{fl}$.

4.1.2. *Plume Mass Flux Measurements.*

Far field experiments were mostly carried out with the mass balance technique described in Chapter 2. The values of plume mass flux have been obtained for three positions of the burner corresponding to approximate interface heights of 1.0, 1.5 and 2.3 m. with three burners (0.10, 0.19 and 0.50 m. in diameter) and heat input rates of 10 to 200 kW. The data are presented in figures (4.5), (4.6) and (4.7) as the ratio of measured mass flow rate, \dot{m}_p to the ideal value, \dot{m}_3 obtained from equation (4.17) versus the interface height, Z_i divided by the average flame height, Z_{fl} .

In calculating the ideal value, \dot{m}_3 , we used the heat release rate based on the fuel flow rate and lower heating value of fuel, \dot{Q}_f . This value was used to be consistent with our near field measurements since we have no simple way of estimating heat losses (radiation and convection) for near field measurements. In addition, we have chosen to present the data as a function of the interface height, Z_i normalized by the flame height, Z_{fl} . This form of representation was chosen because the use of \dot{m}_3 to normalize the plume mass flux, \dot{m}_p substantially removes the dependence on interface height. Thus, the use of the ratio Z_i / Z_{fl} allows us to examine the influence of flame position relative to the interface.

If we consider the data obtained for 0.10 m. dia. burner with 2.4 m. square floor surrounding it, we find that the ratio \dot{m}_p / \dot{m}_3 lies around a constant value of about 0.85 for $Z_i / Z_{fl} > 2$. This implies that the actual entrainment is about 15 % less than the simple model prediction. However, if the heat release rate used in calculating, \dot{m}_3 is reduced by the radiation losses discussed in section (4.1.3), the ratio \dot{m}_p / \dot{m}_3 would increase by about 13 % and lie about a value of 0.96. In the region $1 \leq Z_i / Z_{fl} \leq 2$, entrainment decreases below the point source buoyant plume correlation indicating that the dependence of

entrainment on interface height and heat release rate changes. The scatter in this representation is less than 20 %. The effects of the floor surround were within the accuracy of the experiments.

The same general pattern is observed for 0.19 m. diameter burner. In this case, experiments were performed both with and without the floor surround. It appears that the effect of the floor surround is to lower the plume mass flux in the upper region ($Z_i / Z_{fl} > 2$) and the opposite effect is observed in the lower region. The value of \dot{m}_p / \dot{m}_3 is about 1.0 above $Z_i / Z_{fl} \approx 2$. These values would be around 1.13 if the heat release after the radiation losses were used to evaluate \dot{m}_3 .

Similar effects are observed for 0.50 m. dia. burner. The mass fluxes without the floor are approximately 30 % higher than those with the floor. The data with floor surround cluster about a value of $\dot{m}_p / \dot{m}_3 \approx 1.1$ which would be about 1.24 when the radiation losses were taken into account. These values of \dot{m}_p / \dot{m}_3 are considerably larger than the values for the other two burners.

In all our far field experiments, the scatter in the data is as high as 20 %. We believe that the diameter dependence of the entrainment ratio \dot{m}_p / \dot{m}_3 is related to the proximity of the heat release zone to the burner and thus depends on the values of Z_{fl} / D . The most of the data for 0.10 and 0.19 m. burners lie in the region where $Z_{fl} / D > 3$ (or $Q_D^* > 1$) whereas 0.50 m. burner data had Z_{fl} / D values less than 3 (or $Q_D^* < 1$). In our experiments, we see that the 0.50 m. burner data are consistently higher than the data for other two burners stressing the importance of Z_{fl} / D effect. This behavior is not surprising since we see a noticeable change in the visible flame structure around $Q_D^* \approx 1.0$ and believe that it must have an effect on entrainment. It is also interesting to note that the numerical computations shown in figures (4.3) and (4.4) give higher entrainment rates for the smallest Q_D^* .

The effects of the floor can also be tied with the proximity of the heat release region to the floor (low Z_{fl} / D). The entrainment for these short fires is much more affected by the way the entrained air gets into the plume. These effects are expected to disappear at large distances from the source as they do for 0.50 m. burner as shown in figure (4.7)

Later in our analysis of far field data, we investigated the effects of virtual plume origins and looked at the variations in the constant, C_m of equation (4.17) as well as the offsets in Z origin for the three burners. For this purpose, equation (4.17) was written as,

$$\frac{\dot{m}_p}{Q^{1/3}} = a (Z + b)^{5/3} \quad (4.18)$$

where $a = C_m \left(\frac{\rho_\infty^2 g}{C_p T_\infty} \right)^{1/3}$ is a dimensional constant and $b = \Delta Z_0$ is the offset in Z origin. We determined constants a and b by a least-mean-square analysis for the data with $Z_i / Z_{fl} \geq 1.0$ and with the floor surround for 10 to 200 kW fires. The results of this analysis are shown in Table 4.1.

Table 4.1. Far Field Entrainment Constants

$D, m.$	C_m	$\Delta Z, m.$	$\frac{\Delta Z}{D}$	$(\dot{m}_{corr} / \dot{m}_{uncorr}^*)$
0.10	0.226	-0.220	-2.20	0.71
0.19	0.208	-0.113	-0.59	0.81
0.50	0.218	+0.016	+0.03	1.07

* From equation (4.17) with $Z = 1.0$ m. and $C_m = 0.21$

Except for 0.10 m. dia. burner, offsets are relatively small. Variations in C_m are also small and we expect that for large fires $C_m \approx 0.22$ and $\Delta Z \approx 0$ would be a reasonable estimate to use in a fire plume model. The negative values of ΔZ for 0.10 and 0.19 m. burners imply that the effective origin of the plume lies **above** the plane of the burner. The last column of Table 4.1 gives the ratio of mass fluxes for the far field plume for the corrected and uncorrected models. The numerator of this ratio is evaluated from equation (4.17) with the offset taken into account, i.e. at height $Z + \Delta Z$ and with the corrected value of C_m whereas the denominator was obtained from equation (4.17) with $Z = 1.0$ m. and $C_m = 0.21$. The ratio has a scatter of about 20 %, about a value of 0.9. At a height of 2.0 m., the scatter is reduced to about 10 %.

Another ad hoc approximation sometimes proposed is to use a fictitious origin for the plume and to set this origin far below the level of the real fire source so that some measure of the plume diameter coincides with the diameter of the fire source. For example, Emmons et al [4.8] used this offset idea and then proposed to find the mass flux by subtracting the plume flow rate at the level of the fire from the value calculated at a given height above the fictitious origin from point source model. This process insures that the entrained mass flow rate starts out as zero at the fire level. Thus if $\dot{m}_p[Z + \Delta Z]$ is the flow rate \dot{m}_p at elevation $Z + \Delta Z$ above the virtual plume origin, the mass flux at elevation Z above the burner is computed as,

$$\dot{m}_p[Z] = \dot{m}_p[Z + \Delta Z] - \dot{m}_p[\Delta Z] \quad (4.19)$$

or

$$\dot{m}_p[Z] = \dot{m}_{ps}[Z] \left[\left(1 + \frac{\Delta Z}{Z} \right)^{5/3} - \left(\frac{\Delta Z}{Z} \right)^{5/3} \right] \quad (4.20)$$

since $\dot{m}_p \propto Z^{5/3}$. Here subscript (*ps*) denotes point source model. The term in the brackets corresponds to the correction of the point source model prediction. This term approaches one as Z becomes large. Some typical values are shown in Table 4.2 for an offset $\Delta Z = 1.0$ m. which corresponds to two diameters of 0.50 m. burner used in this example.

Table 4.2. Offset Example

<i>Z, m.</i>	<i>Z / D</i>	$\frac{\Delta Z}{Z}$	<i>Correction</i>
1.0	2	1.00	2.17
2.0	4	0.50	1.65
4.0	8	0.25	1.35
6.0	12	0.17	1.24

The corrections are large for elevations near the fire. But, our measurements do not show these large mass flow rates estimated from the offset idea. Given these results, there appears to be no reason to use large offsets in the origin for plume calculations involving positions in the far field of large diameter fires of the type studied here.

In summary, despite the variations in the levels of the plume mass flux ratios for different burners, the results show that a simple point source model can be used to make remarkably good estimates of plume mass fluxes when the top of the visible flame lies below the interface between the ceiling layer and cooler layer near the floor. This degree of agreement is achieved without any offset for

the origin of the plume or other device used to account for the small values of the ratio of fire height to burner diameter, the finite vertical extent of the heat addition region and the large density differences present in the flame zone. For large fires, the entrainment constant, $C_m \approx 0.22$ can be used without any origin offsets. This value of C_m is very close to that we obtained earlier from the work of Yokoi [4.4], who also found that the use of an offset was unnecessary for positions higher than two fire diameters. The plume mass fluxes produced in our experiments, \dot{m}_p are larger by about 25 % than the data reported by Ricou and Spalding [4.6] and are considerably smaller than the results of several experiments reported by Thomas et al [4.9].

In regard to our measurements, several qualifications are necessary. First, we used the heat release rate of fuel, \dot{Q}_f (fuel mass flow rate multiplied by the lower heating value of fuel) to scale the plume mass fluxes. The effects of radiation losses from the fire will be discussed later in section (4.1.3). Second, since only natural gas was used in all our experiments, we have carried out several other experiments in which we have examined the effects of the fuel heating value on entrainment process. These effects are discussed in section (4.1.4). Third, these plumes were produced in as quiet an atmosphere as we could maintain in the laboratory and we have found that small atmospheric disturbances can produce 20 to 50 % increases in plume mass flows. Some of these effects will be discussed in section (4.1.6).

4.1.3. Heat Balance.

As a part of the investigation of fire plume entrainment, we have also measured the enthalpy flux of the hood exhaust gas relative to the ambient temperature and compared it with the heat release expected from the heating value of fuel. The ratio of these two quantities is called HB and is,

$$HB = \frac{\dot{m}_p C_{pp} (\bar{T}_p - T_\infty)}{\dot{m}_f h_c} \quad (4.21)$$

where \dot{m}_f and h_c are fuel mass flow rate and lower heating value of fuel; \bar{T}_p is the average temperature of gas entering the hood exhaust and C_{pp} is the specific heat of this gas. Values of HB are shown in figure (4.8) as a function of the ratio, Z_i / Z_{fl} . The data lie about the line $HB = 0.7$ and show a slight tendency to decrease as the fire size decreases or Z_i / Z_{fl} increases. Most of the 30 % difference between the hood enthalpy flux, relative to the ambient enthalpy, and the expected fuel heat release is due to radiant energy loss from the flame and the plume. We estimate that about 1/6 or less of the 30 % difference is due to convective heat transfer to the hood walls.

This difference would cause the entrainment ratios in figures (4.5), (4.6) and (4.7) to increase by 13 % if the heat release from hood enthalpy flux had been used. The data of figure (4.8) indicate that the heat loss is independent of fire and burner size over a large variation of these parameters. This result is in agreement with the measurements of Markstein [4.7] who found that the radiant energy loss for propane flames was a constant fraction of heat release rate.

4.1.4. Fuel Heating Value. The main objective of these experiments was to determine the role of the fuel heating value on the entrainment process. In these experiments, nitrogen was added to a fixed fuel flow rate and the effects on fire height and plume mass fluxes were examined. Typical results are shown in Table 4.3. In this example, for which the mass fraction of the nitrogen diluent was about 0.83, the values of plume mass flux decreased by about 3 % when nitrogen was added and the flame height increased by about 8 %. Both changes are within the accuracy of our measurements.

Table 4.3. Effects of Fuel Dilution on Fire Plume

$D, m.$	$\dot{Q}_f kW.$	$\dot{m}_{N_2} / \dot{m}_f$	$Z_{fl}^* m.$	\dot{m}_p / \dot{m}_s	HB
0.50	50	0	0.89	1.19	0.73
		4.8	0.96	1.16	0.86

* Eye ball average values.

The heat balance ratio, HB (defined in section (4.1.3)) increases by about 14 % when nitrogen was added. This is a real effect which is a result of the fact that continuum radiation we associate with the formation and burning of soot almost vanishes at this level of nitrogen dilution. Because the heat losses due to radiation from the soot also decreases greatly, the net enthalpy of the plume gas and hence HB increases.

The results shown here are typical of a number of similar tests carried out for a range of burner diameters, heat release and dilution rates. In general, we found no effect on either plume mass flow rates or flame height (to within ± 10 %) when nitrogen mass flow rates were up to five times the fuel flow rate. Steward [4.10] reported similar insensitivity to nitrogen addition when the ratios of fuel and nitrogen mass flow rates were around one. We conclude from these results that the heating value per mass of fuel is not important in fixing entrainment or flame height. However, the important parameter which fixes the temperature increase in a stoichiometric fuel-air mixture is the heating value of fuel per mass of air at the stoichiometric ratio, h_a (i.e. the heating value of fuel per mass of fuel times the stoichiometric air-fuel ratio). In these dilution experiments, we only decrease this value by about 20 %. We also agree with Steward's

assumption that this parameter, h_a rather than h_c is the important scaling parameter related to fuel heating value. The change in h_a achieved here (about 20 %) is too small to indicate that it is or is not an important parameter in fixing entrainment rates.

4.1.5. *Fuel-Air Ratio at the Flame Top.*

One of the assumptions which is used in a number of analyses is that the combustion rate in the flame is fixed by the local entrainment rate - that is, that some fraction of the entrained air is immediately burned at the elevation where it is entrained. Our data can be used to examine this type of hypothesis to the extent we can determine the fuel-air ratio at the top of the flame.

The latter fuel-air ratio is also of interest since it throws some light on the fate of unburned fuel which enters the ceiling layer when the flame top lies above the ceiling layer interface. We can determine the fuel-air ratio at the top of the flame directly from our measurements if we assume that our measured plume mass flow rates are good estimates of the mass flows in the plume. Data for three burner diameters are shown in Table 4.4. Because a few measurements were made with the interface height very close to the visible flame top, i.e. with $Z_i / (Z_{fl} + \Delta/2) \approx 1$, we have taken the data which had values of the ratio $Z_i / (Z_{fl} + \Delta/2)$ close to one and have used the approximation $\dot{m}_p \propto Z^{5/3}$ to correct or adjust the data to the value expected when $Z_i = (Z_{fl} + \Delta/2)$.

Values of the fuel-air ratio at the top of the flame normalized by the stoichiometric value (0.058 for methane), ϕ , are represented in the fifth column of the table. They are scattered about a value of 0.056 with a variation of about 30 %. Given the sensitivity of the plume mass flux to variations in height and the crude nature of our flame height measurements, this much scatter is expected. The close agreement in the values of ϕ at the flame top suggests an underlying

similarity in the combustion process despite the changes in Q_D' from a minimum of about 0.3 to a maximum of 18.

This estimated value of the fuel-air ratio is much smaller than the value of 1/4 used by Steward [4.10] to correlate his flame height data. However, it is much closer to the value of $\phi \approx 0.1$ estimated by Thomas et al [4.9]. In addition, it is close to but lower than a value inferred from the plume centerline temperature data obtained by McCaffrey [4.11]. This comparison can be made by first using the fuel-air ratio measured here to estimate the average temperature increase in the plume flow.

Table 4.4. Fuel-Air Ratio at the Flame Top

$D, m.$	$\dot{Q}_f kW.$	$\frac{Z_i}{Z_{fl}}$	$\frac{Z_i}{Z_{fl} + \Delta R}$	ϕ^*	$\phi_{adjusted}$	$\frac{\Delta T_m^\dagger}{T_\infty}$
0.10	27	1.27	1.02	0.062	0.064	0.77
0.10	64	1.35	1.13	0.057	0.069	0.70
0.19	32	1.25	0.96	0.061	0.057	0.76
0.19	42	1.23	0.88	0.059	0.047	0.72
0.19	104	1.31	1.07	0.060	0.067	0.74
0.19	115	1.15	0.92	0.082	0.071	1.01
0.50	53	1.23	0.88	0.057	0.046	0.70
0.50	64	1.20	0.86	0.052	0.040	0.64
0.50	106	1.35	0.96	0.056	0.052	0.69
0.50	128	1.23	0.91	0.070	0.060	0.87

* ϕ is the fuel-air ratio divided by the stoichiometric value.

† These values were calculated from equations (4.11) and (4.16) taking into account the 30 % radiation losses.

If we now make the assumption that the velocity and temperature profiles in the plume are Gaussian, we can estimate the value of the maximum temperature increase ΔT_m (which occurs on the plume axis). We must correct this

calculation for the radiant energy loss of about 30 % of the total heat release rate. Calculations of this type lead to values of ΔT_m at the flame top in the range $200 \leq \Delta T_m \leq 300^\circ K$. The values of temperature, measured by McCaffrey [4.11] with large thermocouples which were not corrected for radiation from the flame or to the surroundings, were in the range $250 \leq \Delta T_m \leq 350^\circ K$ at the flame top with data from larger fires grouped around the higher value. This agreement suggests that our estimate of 0.056 for the equivalence ratio at the top of the flame is a reasonable value for this position in the flame.

The very low value of the fuel-air ratio at the top of the flame suggests that large ratios of the flame height to interface height can be allowed before the overall fuel-air ratio in the plume flow will approach the stoichiometric value. This aspect will be further discussed in the near field measurements.

4.1.6. *Disturbances in the Ambient Atmosphere.*

Early in our experimental program, we observed that disturbances in the room air could have a substantial effect on entrainment rates. For example, currents produced by an air conditioning system caused the plume mass flux rise by about 20 % above the values obtained when the system was blocked off.

This effect is best illustrated in figure (4.9), where data for the 0.19 m. burner are presented for tests in which screens were and were not used. In the latter tests, the air conditioning system was turned off and air was allowed to enter the test room through a door located at a distance of about 20 m. from the test area. The plume mass flux rates are about 15 % higher when the screens were removed. In addition, fire whirls and random deviations from the axisymmetric flow were observed in the visible flame. The disturbances in these experiments were largely due to the flow of air through the room which was produced by the entrainment process itself.

We also studied the effects of producing a more controlled disturbance by blocking the sides of the open areas below the hood where screens were hung. However, screens were present over the areas left open. The geometries used and the resultant plume mass flux ratios are shown in figure (4.10). The largest effect was produced by the corner flow configuration in which adjacent walls were blocked. These effects for the other two examples were somewhat smaller.

When the flow was blocked, the flame was blown over most strongly at the floor level and gradually turned to a vertical orientation as the distance from the floor increased, and the ceiling interface was thicker by a factor of about 2 than the corresponding unblocked case. Similar observations were recently made by Quintiere et al [4.12] who obtained 2 to 3 fold increases in entrainment over the undisturbed values for a variety of door-window opening configurations.

4.2. Near Field

Entrainment measurements in the visible flame region were made by chemical analysis of combustion products in the ceiling layer as described in Chapter 2. The plume mass fluxes have been measured for three burners (0.10, 0.19 and 0.50 m. in diameter) and heat input rates of 10 to 100 kW. In these experiments, no direct measurement of the flame height has been made, but rather the estimates made by observers looking up into the small hood at oblique angles suggested that the flame lengths in the hood were not greatly different than the free flame heights reported in Table 3.1. In some of these experiments (large heat inputs and small burners, large Q_D^*) the flames were observed to impinge on the hood intermittently.

The fuel-air ratio in the hood given as a fraction of the stoichiometric value, φ_h is presented in Table 4.5 along with the heat release rates, \dot{Q}_f ; the plume mass flux, \dot{m}_p at an interface height of $Z_i \approx 0.33 m$. and the ratio of interface

height to free flame height, Z_i / Z_{fl} for 0.19 m. burner. The values of φ_h were determined from the gas sample data and increased from about 10 % at the lowest heat input rate to almost 70 % at 81 kW. If the residence time for the gas in the hood, t_{res} is defined to be the mass of gas in the hood divided by the plume mass flux into the hood, we find that the residence time varies from about 20 seconds at 10 kW. to about 10 seconds at 81 kW. This residence time is certainly long enough to ensure that the gas in the hood will be in chemical equilibrium.

Table 4.5. Entrainment & Equivalence Ratios for 0.19 m. Burner

$\dot{Q}_f, kW.$	$\dot{m}_p, kg/s.$	φ_h	Z_i / Z_{fl}
10.5	0.035	0.11	0.71
21	0.043	0.18	0.52
42	0.043	0.35	0.36
63	0.046	0.49	0.31
81	0.042	0.70	0.29

The most important observation from Table 4.5 is that the plume mass flux is not a very strong function of heat release rate of the fire at very low elevations of the interface, Z_i . This will be discussed later in detail and will form the basis of an ad hoc model for entrainment. In all the near field experiments, the temperature of the walls of the hood and gas temperature were not controlled and the walls of the small hood were not insulated. We were forced to keep the equivalence ratio of the hood gas, φ_h below 0.70 to prevent soot formation. The results of some preliminary experiments on the composition of the fuel rich hood gas have shown that combustion efficiencies are very high provided that soot formation is suppressed by keeping the equivalence ratio of the hood gas

below 0.70. Results of these experiments are discussed in section (4.2.5).

The plume mass fluxes, \dot{m}_p normalized by the theoretical value for the far field, \dot{m}_3 as a function of interface height, Z_i normalized by Z_{fl} are shown in figures (4.11), (4.12) and (4.13) for three burners with several heat release rates. These figures suggest that there is deviation of entrainment rates from the far field correlation at low elevations. In the following paragraphs, the region close to the burner surface where entrainment rapidly changes, referred to here often as the initial region, will be discussed in detail and an ad hoc model of entrainment in this region will be developed.

Examination of data for all three burners reveals the fact that the plume mass flux is relatively insensitive to the heat release rate of the fire, \dot{Q}_f in the initial region. Even though the heat inputs change by a factor of 3 to 4 in this region, the change in entrainment is negligibly small within the accuracy with which we can make our plume mass flux measurements. Another observation is that the comparison of the entrainment data for these three burners suggests that plume mass fluxes scale linearly with the burner diameter. These observations together with the appearance of these diffusion flames in the region close to the burner surface led us to consider the simple ad hoc model for this region discussed below.

4.2.1. *Simple Model for Initial Region.*

In this simple model, the initial region is viewed as a highly wrinkled, thin, laminar diffusion flame surrounding the burner perimeter. The diffusion flame separates air on one side from fuel on the other and is in a very unsteady flow field. This picture described above may seem to be unreasonable especially for large fires. However, a review of Table 2.1 shows that a 0.50 m. diameter burner with a 126 kW. fire will have an initial Reynolds number of less than 500. Jets at

this Reynolds number are laminar for at least a number of initial diameters downstream of the jet source. Also, the photographs and shadowgraph images of the flames close to the burner surface, such as those in figures (3.1) and (3.2) show that the small scale turbulence (small compared to diffusive thickness of laminar flame sheet) are not present.

In a laminar diffusion flame, air and fuel enter the region adjacent to the flame by molecular diffusion processes and are heated by the reaction in a thin flame front and rise due to natural convection as shown in the sketch of figure (4.14a). All transport processes are assumed to be molecular. Because the temperature of the gas at the flame itself must be close to the adiabatic flame temperature, we can assume that the region near the visible flame has an average temperature which is a constant fraction of the adiabatic flame temperature. Thus, the average temperature and density in the flame zone are independent of height Z .

In this simple model, we need to estimate the surface area of the laminar diffusion flame surrounding the buoyant fuel jet. The pictures and the video movies of our flames suggest that the surface area of the flame scales like the product of the burner perimeter, πD and the height above the burner surface, Z . The width measurements in Table 3.1 indicate that the widths are of the order of the burner diameter and subsequently grow larger. Also, the minimum diameter of the flame near the burner is never much smaller than the burner diameter. Furthermore, the presence of large scale vortical structures and the wrinkling of the flame surface could easily increase the surface area estimated above, πDZ by a large factor. These observations are in contrast with what we expect for the shape of a steady, buoyant jet which accelerates due to its buoyancy and hence its diameter contracts sharply with height. The shapes of the axisymmetric, buoyant fuel jets, calculated in the second part of Chapter 5,

illustrates these large contractions which are not experimentally observed. The differences are in large part believed to be due to the periodic shedding of large scale vortical structures described above.

In the initial region, the momentum balance for the thin flame sheet (shown in figure (4.14a)) of width, δ and horizontal length proportional to burner diameter, D is

$$\frac{d}{dZ} \left(\delta D \rho_m W_m^2 \right) \propto \Delta \rho g \delta D \quad (4.22)$$

where we characterize the whole flame region by top hat profiles for velocity, W_m and density, ρ_m as well as temperature and density differences (ΔT and $\Delta \rho$). Here we also ignore the momentum contribution of the entrained air and fuel.

The energy balance is,

$$\frac{d}{dZ} \left(\delta D \rho_m W_m C_p \Delta T \right) \propto \rho_\infty D \frac{D}{\delta} h_a \quad (4.23)$$

where h_a is the heating value per **mass of air** and D is the molecular diffusion coefficient. We have taken $\frac{D}{\delta}$ as a scale for the velocity at which oxidizer is entrained by the diffusion flame. Note that only two equations are required here, because the average temperature in the layer is fixed by the chemical reaction and is constant.

If we assume that horizontal length scale is constant and equal to burner diameter, D and the average density and temperature in the flame region are independent of Z , we can rearrange these equations and write them as,

$$\frac{d}{dZ} \left(\delta W_m^2 \right) \propto \frac{\Delta \rho}{\rho_m} g \delta \quad (4.24)$$

$$\frac{d}{dZ} \left(\delta W_m \right) \propto \left[\frac{\rho_\infty}{\rho_m} \frac{h_a}{C_p \Delta T} \mathbf{D} \right] \frac{1}{\delta} \quad (4.25)$$

If a similarity solution is to exist, we can show that

$$W_m \propto Z^{1/2} \quad \text{and} \quad \delta \propto Z^{1/4} \quad (4.26)$$

Given these results, the mass flux at height Z , \dot{m}_1 , is proportional to

$$\dot{m}_1 \propto \rho_m \delta D W_m \propto Z^{3/4} D \quad (4.27)$$

and in terms of the constants, it can be written as,

$$\dot{m}_1 \propto \rho_\infty \sqrt{\frac{\rho_\infty}{\rho_m} \frac{h_a}{C_p \Delta T}} \sqrt{\mathbf{D} \sqrt{\frac{g'}{Z}}} (\pi Z D) \quad (4.28)$$

where $g' = \left(\frac{\rho_\infty}{\rho_m} - 1 \right) g$. Here it is worth noting that the plume mass flux in this region does not depend on the total heat release rate of the fire (\dot{Q}_f or Z_{fl}).

In Chapter 5, we studied a similar problem to obtain the entrainment of a steady, laminar, buoyant diffusion flame by an integral approach. First part of this involved the calculations for a plane diffusion flame separating fuel and oxidizer. The result of this calculation allowed us to evaluate the proportionality constant in equation (4.28). For a methane-air diffusion flame the integral solution gives the entrainment up to a height Z as,

$$\dot{m}_1 \approx 9.5 \rho_\infty \sqrt{D_\infty} \sqrt{\frac{g}{Z}} D Z \quad (4.29)$$

Here, the proportionality constant was evaluated based on the flame surface area equal to πDZ . But, as mentioned earlier, this constant could be greatly increased because of the area increase due to the presence of vortical structures and wrinkling of the flame surface.

4.2.2. *Turbulent Flame.*

The initial region described above later develops into an intermediate region which mostly contains the intermittent flame zone. This latter zone is important since it comprises a vertical distance which in some cases may be a large fraction of the flame height. Even though this transition is not clearly defined, there are two possible interpretations of this transition phenomenon.

The first one is related to the transition to turbulence in the plume. Here, we assume that at some height above the burner, the flame develops into a turbulent flame and that in this region entrainment occurs as it does in a turbulent buoyant plume. One interpretation of our data suggests that such a transition occurs in the Grashof number range:

$$10^9 \leq Gr \leq 10^{11} \quad \text{when} \quad Gr \equiv \frac{g Z_t^3}{\nu^2}$$

Note this implies that the transition height, Z_t , does not depend on the heat addition rate or burner diameter.

More properly, we should use g' rather than g .

$$g' = g \left(\frac{\bar{T}_m - T_\infty}{T_\infty} \right)$$

Here \bar{T}_m is an average gas temperature. The use of g' would modify our results by a constant factor of about 4.

The second interpretation is that the turbulent flame region is the intermittent flame zone which lies between $Z_{fl} - \Delta/2$ and $Z_{fl} + \Delta/2$. Table 4.6 gives some values of these quantities for the three burners with the approximate locations of transitions obtained from entrainment data.

Table 4.6. Transition Heights for the Intermittent Flame Region

$D, m.$	$\dot{Q}_f, kW.$	$Z_{fl} - \Delta/2, m.$	$Z_t, m.$
0.10	21	0.50	-
	42	0.66	0.60 - 0.70
	63	0.68	0.60 - 0.70
0.19	21	0.47	0.70
	42	0.65	0.60 - 0.70
	63	0.80	0.60 - 0.70
0.50	21	0.19	
	42	0.35	
	63	0.46	none
	127	0.73	

In contrast to the first interpretation, this suggests that the location of the transition depends on the heat release rates. Transition heights obtained by this method seems to give fair estimates of the transition heights, Z_t for the limited data of 0.10 and 0.19 m. diameter burners. The 0.50 m. burner entrainment data suggest that either this intermediate region is very small (we cannot detect

with the accuracy of our measurements) or it does not exist. This observation contradicts the second interpretation since the intermittent region occupies a large fraction of the flame height. Finally, it is interesting to note that a common ground exists for the two different interpretations of the transition. Flame photographs and shadowgraph images such as those in figures (3.1) and (3.2) suggest that the location of the transition to turbulence in the plume (identified by small grained structure in the shadowgraph pictures) coincides approximately with the beginning of the intermittent region, $Z_{fl} = \Delta/2..$

In this region, we also assume that air consumed by combustion (or heat released) per unit height in the turbulent flame is a constant fraction of the rate of ambient air entrainment per unit height at that height. This hypothesis ensures that average temperatures and densities in the buoyant flame plume remain constant. Similar to the buoyant plume entrainment, we use a turbulent diffusivity,

$$D_T = W_m \eta \tag{4.30}$$

where η is the diameter of the flame as shown in figure (4.14b). We assume that the mass is entrained per unit height at a rate given by,

$$\frac{dm}{dZ} \propto (\rho_\infty \pi \eta) \frac{D_T}{\eta} \tag{4.31}$$

and that a fraction of this mass is burned in the volume,

$$\frac{\pi}{4} \eta^2 dZ \tag{4.32}$$

Then, conservation of momentum and energy become,

$$\frac{d}{dZ} \left(\eta^2 \rho_m W_m^2 \right) \propto \Delta \rho g \eta^2 \quad (4.33)$$

$$\frac{d}{dZ} \left[\frac{\eta^2}{4} \rho_m W_m C_p \Delta T \right] \propto \rho_\infty \eta W_m \kappa h_a \quad (4.34)$$

where κ is the fraction of the entrained mass consumed in combustion. Since we assume that ΔT is fixed by the heat release process, only two equations are required. Given our assumptions equations (4.33) and (4.34) can be written as,

$$\frac{d}{dZ} \left(\eta^2 W_m^2 \right) \propto \frac{\Delta \rho}{\rho_m} g \eta^2 \quad (4.35)$$

and

$$\frac{d}{dZ} \left(\eta^2 W_m \right) \propto \left[4 \frac{\rho_\infty}{\rho_m} \frac{h_a \kappa}{C_p \Delta T} \right] W_m \eta \quad (4.36)$$

A similarity solution of these equations exists if

$$\eta \propto Z \quad \text{and} \quad W_m \propto Z^{1/2} \quad (4.37)$$

The corresponding mass flux is,

$$\dot{m}_2 \propto \rho_m \frac{\pi \eta^2}{4} W_m \propto Z^{5/2} \quad (4.38)$$

and given the constants it is,

$$\dot{m}_2 \propto \rho_m \left(\frac{\rho_\infty}{\rho_m} \right)^2 \left(\frac{\kappa h_a}{C_p \Delta T} \right)^2 \sqrt{g' Z} Z^2 \quad (4.39)$$

Under our approximations, $\frac{\kappa h_a}{C_p \Delta T}$ is about one and experimental measurements of the gas temperature suggest that in this region, the value of $\frac{\rho_\infty}{\rho_m}$ averaged over the flame is about 2 and that for $\frac{\Delta T}{T_\infty} = \frac{\Delta \rho}{\rho_m}$ is about one.

The same Z -dependence of entrainment, \dot{m}_2 can be obtained from equations (4.8) through (4.10) if ΔT is assumed to be constant. In fact, the only difference between this region and the far field is that the combustion stops at the flame top and the temperature decreases with height. The entrainment from these two regions, \dot{m}_1 , \dot{m}_2 and the far field, \dot{m}_3 should be matched to satisfy the continuity of plume mass flux.

4.2.3. Matching of the Plume Mass Fluxes.

The solutions for the three regions must now be matched at a lower transition point (t) and at the top of the flame (f). Matching conditions at (f) are simple and logical since we must conserve mass, momentum and enthalpy and because the only difference between the two regions (in this simple model) is that the combustion stops at (f) and consequently ΔT becomes a function of height. The solution at (f) is that both regions must have the same coordinate systems, i.e. the same offset.

These matching conditions require that the mass flux in the turbulent flame region, \dot{m}_2 and the far field, \dot{m}_3 be given by:

$$\dot{m}_2 = C_m \left(\rho_\infty \sqrt{gZ} Z^2 \right) Q_{Z_{fl}}^*{}^{1/3} \quad (4.40)$$

$$\dot{m}_3 = C_m \left(\rho_\infty \sqrt{gZ} Z^2 \right) Q_Z^*{}^{1/3} \quad (4.41)$$

where

$$\left. \begin{aligned} Q_Z^* &\equiv \frac{\dot{Q}}{\rho_\infty C_p T_\infty \sqrt{gZ} Z^2} \\ Q_{Z_{fl}}^* &\equiv \frac{\dot{Q}}{\rho_\infty C_p T_\infty \sqrt{gZ_{fl}} Z_{fl}^2} \end{aligned} \right\} \quad (4.42)$$

Here, Z_{fl} is the vertical distance to the time-averaged top of the flame in the coordinate system used for regions (2) and (3), and C_m is the constant given in Table 4.1.

If we normalize the mass flux in turbulent flame, \dot{m}_2 by the far field correlation, we get:

$$\frac{\dot{m}_2}{\dot{m}_3} = \left(\frac{Z}{Z_{fl}} \right)^{5/6} \quad (4.43)$$

This is shown in figure (4.15) as the curve (A) for $Z_t/Z_{fl} < Z/Z_{fl} < 1$, where Z_t is the height at which the transition to the turbulent flame occurs.

The transition at (t) between the initial region and the turbulent flame, discussed earlier, is not clearly defined in our discussion since we are treating the transition from a laminar diffusion flame surrounding a potential flow of fuel to

a turbulent flame with a plume like character. The plume mass flux measurements suggest that there is a change in the behavior of entrainment which occurs at elevations between 0.6 and 1.0 m. But, the scatter in our data prevents us from making any strong assessments on this transition. However, if we neglect, for the moment, the offsets in the vertical axis of the solutions, we find that the ratio of mass flux in the initial region, \dot{m}_1 to that in the far field, \dot{m}_3 is

$$\frac{\dot{m}_1}{\dot{m}_3} \propto D Z^{-11/12} \dot{Q}^{-1/3} \quad (4.44)$$

The lines corresponding to equation (4.44) are sketched on figure (4.15). A family of curves is obtained because of the dependence on both D and \dot{Q} .

Also if we equate the mass fluxes for the initial region and the turbulent flame at the transition height, Z_t , we get (ignoring the offsets)

$$Z_t \propto D^{4/7} \quad \text{or} \quad \frac{Z_t}{Z_{fl}} \propto \frac{D^{4/7}}{\dot{Q}^{2/5}} \quad \text{when} \quad Q_D^* > 1.0 \quad (4.45)$$

Thus, the transition height becomes a larger fraction of the flame height as the diameter increases and the heat release rate decreases. For small heat release rates and large diameter, Z_t may increase until it is of the same order as or larger than Z_{fl} . Under these conditions, the turbulent flame zone may not be present and the matching should be done at the flame top between the initial region and the far field. This is shown as curve (B) on figure (4.15) where numbers attached to the segments of the curves correspond to the three regions described above.

The simple model developed above leads to a qualitative representation for the plume mass flux measurements and a rational matching for the upper two regions (turbulent flame and far field). The comparison of the model with the experiments in the next section will show that even though the general trends predicted by the model agree with the experiments, the transitions among the three regions could span large distances.

In an attempt to test the quantitative predictions of the model, we calculated the mass fluxes for turbulent flame, \dot{m}_2 and far field, \dot{m}_3 by using the equations (4.40) and (4.41) which were corrected by the use of the offsets and variation of constant, C_m listed in Table 4.1 to match the experimental data. The comparisons of the model computations with the 0.19 m. burner entrainment data showed that a better fit was obtained when the matching at the flame top was made at $Z_{fl} + \Delta/2$ rather than at Z_{fl} . Similarly, the constant in equation (4.29) was chosen to be 65 to make this equation fit the experimental data of 0.19 m. diameter burner for which the initial region is most apparent. Finally, the transition between initial region and the turbulent flame or initial region and far field is allowed to occur whenever the calculated mass flux for initial region or far field exceeded that for initial region at the same height. These model computations are shown in figures (4.19), (4.20) and (4.21) together with the experimental data. Here, we note that no further adjustment of the constant in the initial region has been made for different burners.

4.2.4. *Model Comparison with Experiments.*

Experimental data for plume mass fluxes are presented in several forms in figures (4.16) to (4.21). In the first three of these figures (4.16), (4.17) and (4.18), the plume mass flux, \dot{m}_p normalized by the far field correlation (4.17) is shown as a function of interface height divided by the flame height, Z_i / Z_{fl} . Even though the 0.10 m. diameter burner data do not clearly show the initial

and the turbulent flame regions, the data of 0.19 m. diameter burner shows these regions for 20, 40, 60 and 80 kW data. The 20 kW data exhibit the behavior where the initial region directly approaches the the far field. This happens at a value of Q_D^* of about unity and is to be expected since we also observe a noticeable change in the flame structure (e.g. flame height, size of the vortical structures). Here, it is also apparent that the transition from the turbulent flame region to the far field spans large distances. This picture is similar to figure (4.15) which shows the model predictions. The data for 0.50 m. diameter burner show the transition from the initial region to the far field for 20, 30,40, and 60 kW fires. For all of these heat release rates, the values of Q_D^* are less than unity. Even though the scatter in the data and the simplicity of the model proposed do not allow us to make precise, quantitative estimates, the trends observed from the experiments are in agreement with the simple model.

Figures (4.19), (4.20) and (4.21) show the plume mass flux, \dot{m}_p as a function of interface height, Z_i with the heat release rate of the fire, \dot{Q}_f as a parameter. Initial region is clearly defined in these plots by the transition between it and the turbulent flame region. Comparison of the three sets of data shows that, in the initial region, \dot{m}_p scales roughly with the burner diameter and the plume mass fluxes are independent of the fuel flow rate. The values of \dot{m}_p for 0.10 m. diameter burner in the initial region are higher than the model predictions. This result may be connected with the much larger initial Reynolds numbers and smaller Richardson numbers obtained with this burner for a given heat addition rate, as compared with the corresponding values obtained with 0.19 and 0.50 m. dia. burners (see Table 2.1 for examples).

All the values of \dot{m}_p in the initial region are larger than expected from the integral calculation for a plane flame sheet. This result is probably connected with the effects of the periodically produced vortices in the flame as well as the

wrinkling of the flame surface. Neither of these effects was taken into account in the laminar flame sheet analysis described in Chapter 5.

In order to compare the model and the experimental values of the plume mass flow rates, we have calculated the plume mass flux values by the rather arbitrary method suggested at the end of section (4.2.3). The transition between the initial region and the turbulent flame is marked by a distinct change in slope of the curves whereas that between the turbulent flame and the far field is not as clear. Calculations agree reasonably well with the experiments. However, the scatter in the data is large to make any finer judgments, particularly in the intermediate turbulent flame region.

4.2.5. *Fuel Rich Ceiling Layer.*

We also carried out some preliminary experiments to investigate the flash-over phenomenon and determine the chemical composition of the fuel rich ceiling layer gas. The apparatus used for these experiments was the same as the one used for near field measurements. The only differences were: The top wall of the small hood was insulated with a 5 cm. thick layer of fiberglass; the furnace was not operated.

In these experiments, the flame extends well up into the hood and oxygen is supplied by the entrained air over the short column between the burner and the interface. Above the interface, the air entrained is heated and mixed with hot combustion products, and the fire plume continues to entrain gas in this upper region. This gas is drawn from the recirculating products of combustion produced by the plume itself. The combustion still occurs as a diffusion flame between fuel and oxygen, both of which may strongly be diluted with the combustion products.

In the near field experiments, the equivalence ratio of the hood gas, φ_h was kept below a value of 0.70 which was determined by the onset of soot formation. Due to limitations of our technique when the ceiling layer gas was sooty, we resorted to an approximate method to determine the equivalence ratios of the fuel rich ceiling layer. In the previous section, the initial region plume mass flow rates are found to be independent of the fuel flow rate as it is most apparent for 0.19 m. diameter burner. Utilizing this, we used 0.19 m. burner with an interface height of about 0.3 m. and varied the equivalence ratio of the hood gas by changing the heat release rate, assuming the entrained air flow is independent of the fuel flow rate. We used this approximate method at the expense of making detailed chemical measurements of all species in the fuel rich gas layer. Here, we note that these are preliminary measurements and we suggest that a more precise way of estimating the entrained air flow should be used for further investigations.

In these experiments, the approximate equivalence ratios were driven up to about 2.5 and the following observations were made:

As the fuel-air ratio of the hood gas increased above the stoichiometric value, $\varphi_h > 1$, the top of the flames became more diffuse in appearance and the color changed to darker yellow.

Soot was first observed around $\varphi_h \approx 0.7$ and steadily became denser as the fuel-air ratio was increased. For values of fuel-air ratio corresponding to $\varphi_h \approx 2$, we first began to see secondary flamelets propagating away from the primary fire plume. These flamelets are regions of luminous combustion with a scale of 10 to 20 cm. which are ignited near the interface and at times moved up along the outside of the hood a short distance before being extinguished. The radiation from these regions was yellow but was not nearly as bright or white as that from the flame itself. The complete flash-over of the fuel rich gas in the

hood was not observed until the equivalence ratio of the gas reached $\varphi_h \approx 2.5$.

The gas temperatures within the hood increase linearly with height for a fixed φ_h . These temperatures were measured with an unshielded, aspirated chromel-alumel thermocouple at various heights in the hood. Two examples are shown in figure (4.22) for $\varphi_h = 0.75$ and 1.0. The temperature level within the hood is far below the adiabatic flame temperature for these fuel-air ratios due to heat transfer to and radiation from the sides of the hood and the open surface at the bottom. The linear drop in temperature for lower elevations may be caused by heat loss through the uninsulated hence cooler side walls.

Measurements of concentrations of CO_2 , CO and gaseous unburned hydrocarbons were made in filtered gas samples withdrawn from a 0.6 m. level with the probe held near one corner of the hood. No attempt to make a quantitative estimate of the solid carbon particules was made because of the difficulties involved with such a measurement. The concentrations and gas temperatures are shown in figure (4.23) as functions of the estimated equivalence ratios of the hood gas, φ_h . The values of CO and unburned hydrocarbons show a sharp increase from negligible values at $\varphi_h \approx 0.5$ to values around 1 % at $\varphi_h \approx 1.1$. As the fuel-air ratio was increased above the stoichiometric value, both continued to increase and the carbon monoxide mole fraction reached a peak value of around 2 % and then became independent of φ_h . The gaseous unburned hydrocarbon mole fraction rose above 2 % at about $\varphi_h \approx 1.5$. Due to the limitation of our instrument range, we were not able to trace the quantity of this species any further. Also, above the stoichiometric fuel-air ratio, the gas temperature became almost constant. This implies that the heat release is limited by the amount of oxidizer available for combustion which is fixed by entrainment.

Finally, the results of these experiments show that the combustion efficiencies are very high provided that soot formation is avoided by keeping the

equivalence ratio of the hood gas below 0.7. This result is interesting because the mass fraction of oxygen in the hood gas could be as low as 0.06 for 81 kW fire on 0.19 m. diameter burner. This value is far below the usual value of critical oxygen index reported in the literature. The reason that we have high combustion efficiencies in cases such as those described above is that our flames entrain ambient air in the region between the burner surface and the interface of the hot gas layer. However, the critical oxygen index corresponds to the oxygen content of the ambience completely surrounding the flame.

References

- [4.1] E. E. ZUKOSKI, Development of a Stratified Ceiling Layer in the Early Stages of a Closed-room Fire, *Fire & Materials*, **2**, Nr.2, 54,(1979)
- [4.2] B. R. MORTON, G. I. TAYLOR and J. S. TURNER, Turbulent Gravitational Convection from Maintained and Instantaneous Sources, *Proc. Roy. Soc.*, **A 234**, 1-23,(1956)
- [4.3] G. I. TAYLOR, The Use of Models in Fire Research, Publication Nr.786,10-31, *National Academy of Sciences, National Research Council, Washington D. C.* (1961)
- [4.4] S. YOKOI, The Use of Models in Fire Research, Publication Nr.786, 186-206, *National Academy of Sciences, National Research Council, Washington D. C.* (1961). See also: Report 29, *Japanese Bldg. Res. Inst.*,(1959)
- [4.5] TOSHI KUBOTA, Personal Communication.
- [4.6] F. P. RICOU and D. B. SPALDING, Measurement of Entrainment by Axisymmetrical Turbulent Jets, *J. Fluid Mech.*, **11**, 21,(Aug-Dec 1961)
- [4.7] G. H. MARKSTEIN, Scaling of Radiative Characteristics of Turbulent Diffusion Flames, *Sixteenth Symposium (International) on Combustion*, 1407, Academic Press, New York (1976)
- [4.8] H. W. EMMONS, H. E. MITLER and L. N. TREFETHEN, Computer Fire Code III, Home Fire Project Technical Report Nr.25 (Harvard University, 1978)
- [4.9] P. H. THOMAS, R. BALDWIN and A. J. M. HESELDEN, Buoyant Diffusion Flames: Some Measurements of Air Entrainment, Heat Transfer and Flame Merging, *Tenth Symposium (International) on Combustion*, 983, Academic Press, New York (1965)
- [4.10] F. R. STEWARD, Prediction of the Height of Turbulent Diffusion Buoyant Flames, *Comb. Sci. & Tech.*, **2**, 203,(1970)
- [4.11] B. J. McCAFFERY, Purely Buoyant Diffusion Flames: Some Experimental Results, NBSIR79-1910, *National Bureau of Standards, Department of Commerce, Washington D.C.* (1979)
- [4.12] J. G. QUINTIERE, W. J. RINKINEN and W. W. JONES, The Effect of Room Openings on Fire Plume Entrainment, *Comb. Sci. & Tech.*, **26**, 193-201,(1981)

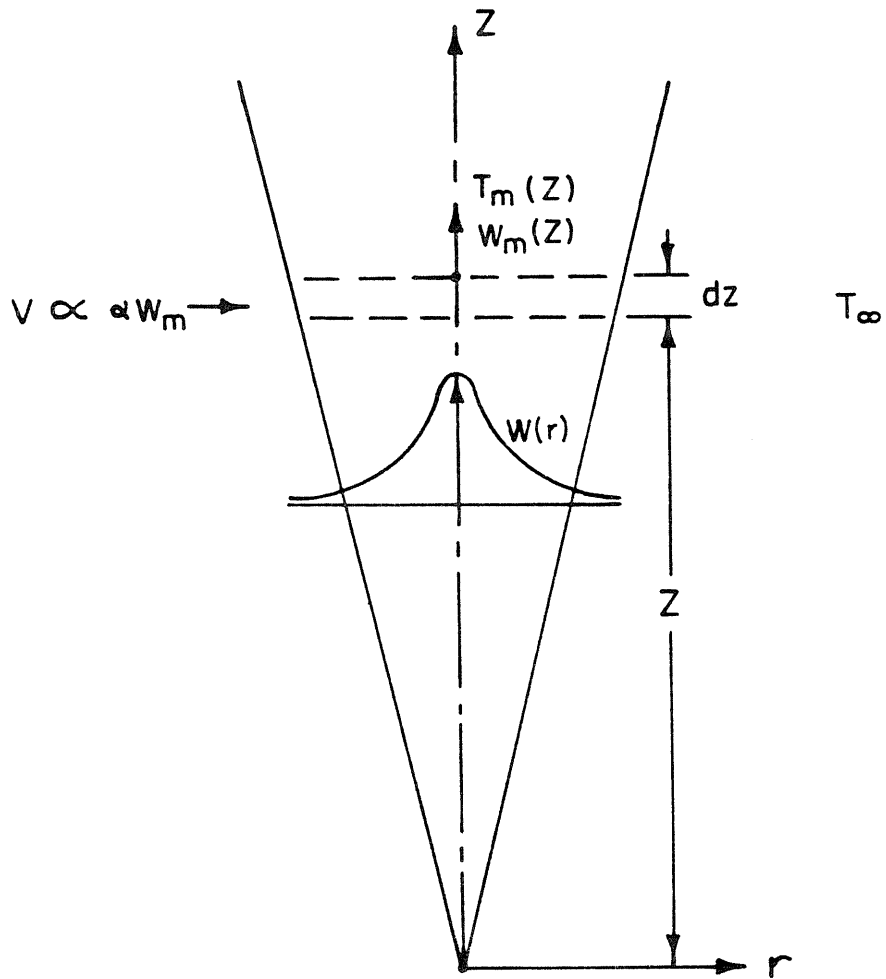


Figure (4.1) The sketch of buoyant turbulent plume

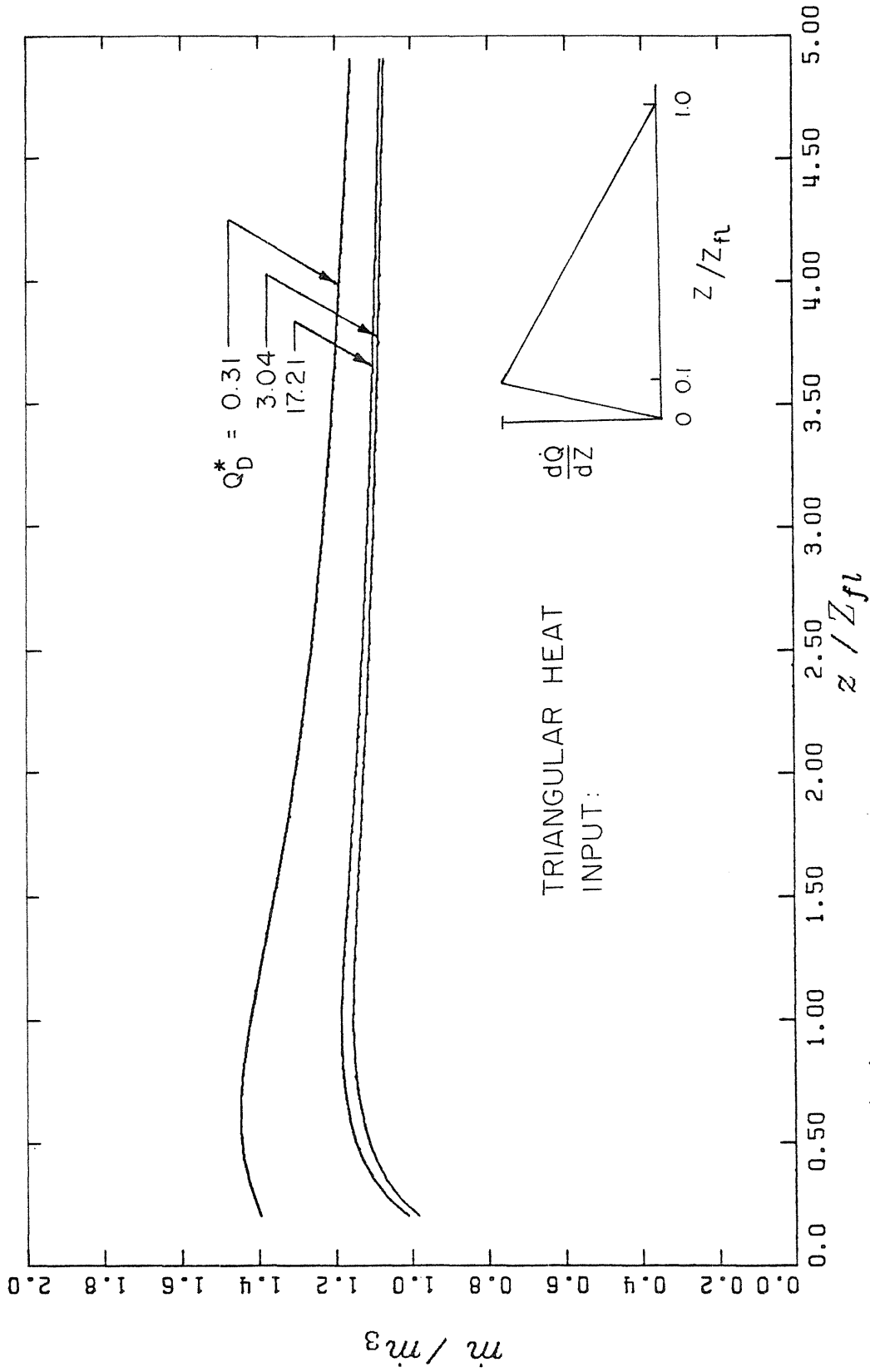


Figure (4.2) Computed entrainment rates nondimensionalized by equation (4.16) as a function of the ratio of interface height to flame height for a 60 kW, fire on 0.10, 0.19 and 0.50 m. diameter burners for a triangular heat release rate profile with maximum at $Z = 0.1 Z_{fl}$

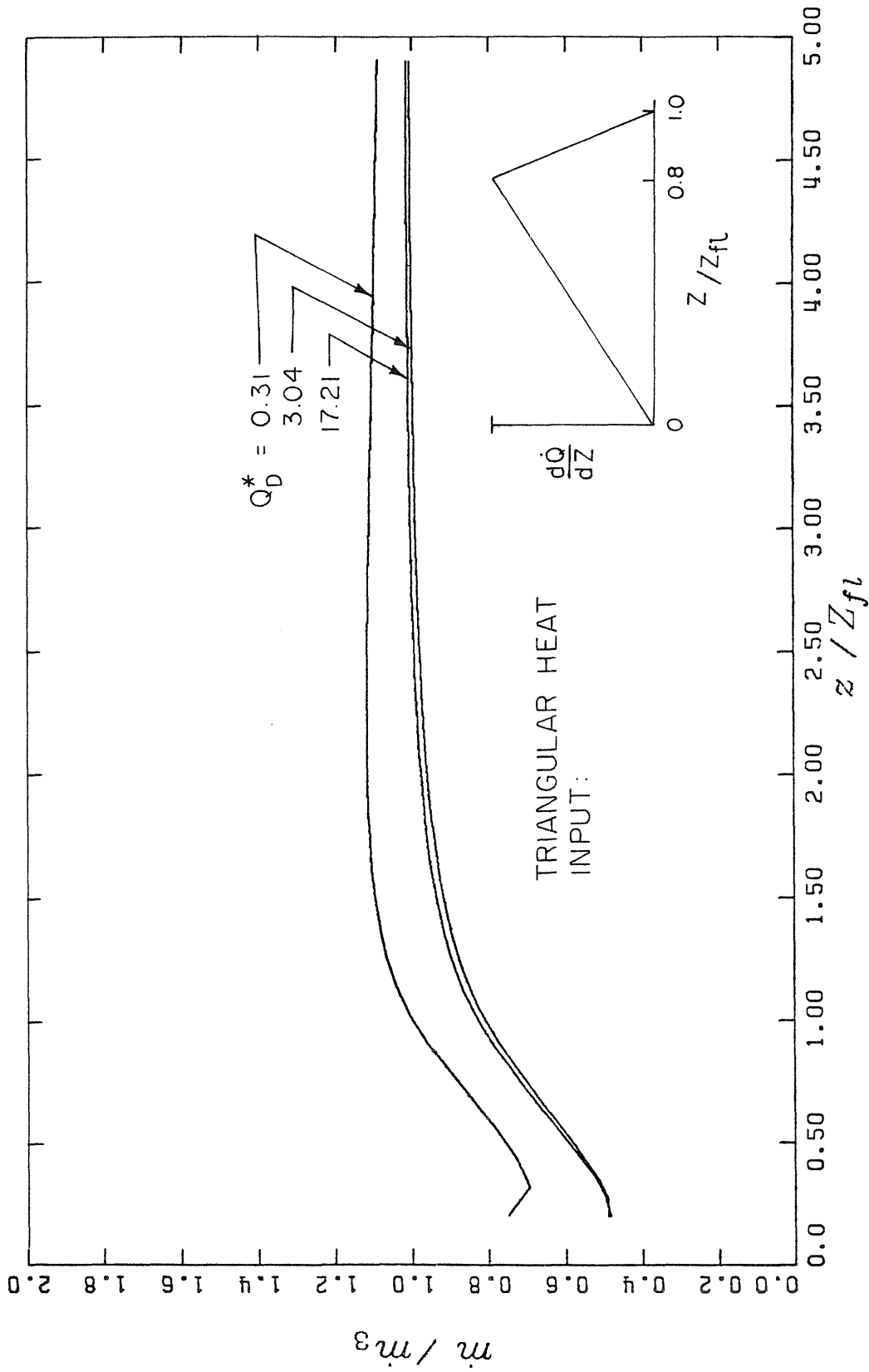


Figure (4.3) Computed entrainment rates nondimensionalized by equation (4.16) as a function of the ratio of interface height to flame height for a 60 kW. fire on 0.10, 0.19 and 0.50 m. diameter burners for a triangular heat release rate profile with maximum at $Z = 0.8 Z_{fl}$

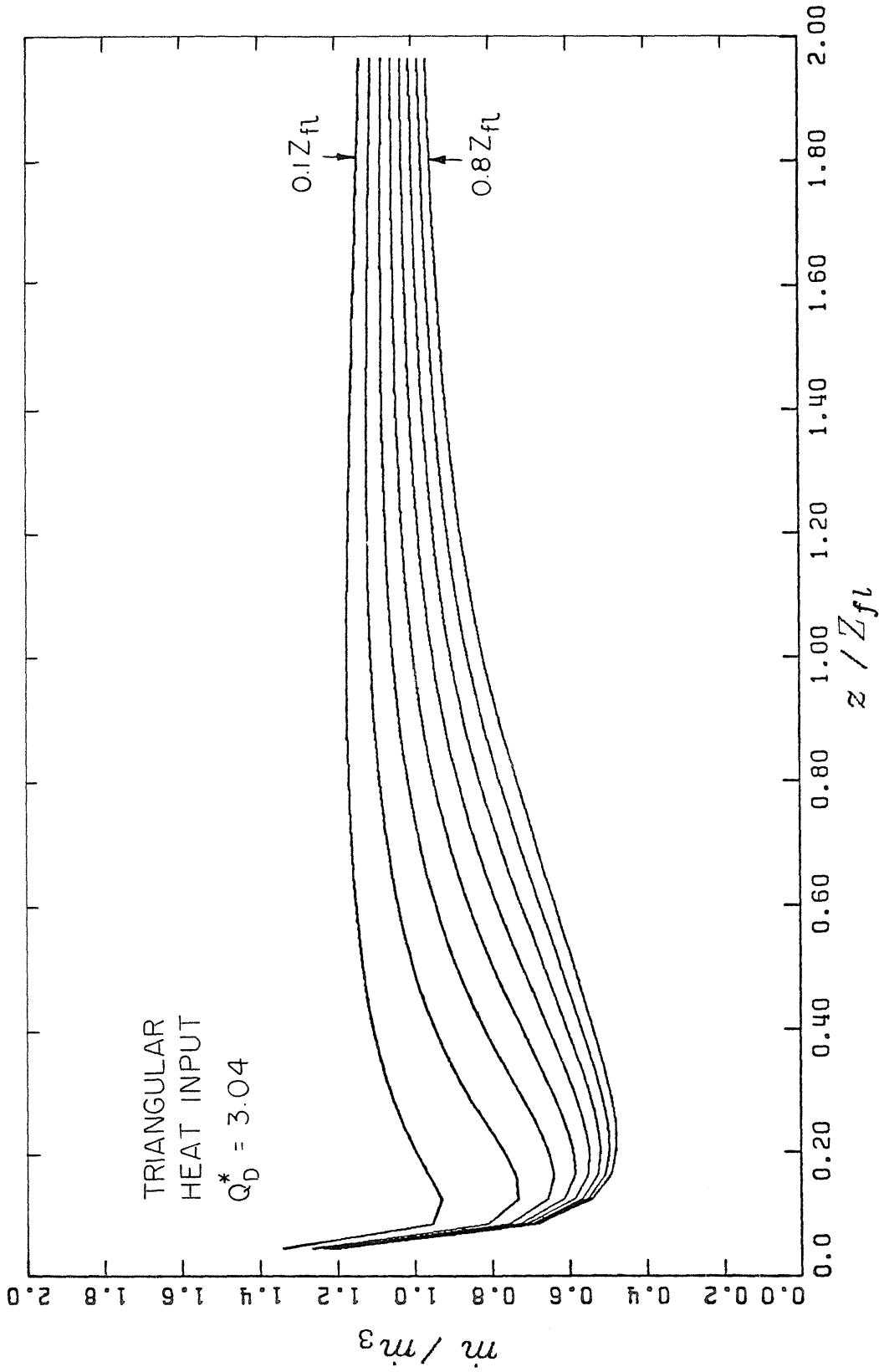


Figure (4.4) Computed entrainment rates nondimensionalized by equation (4.16) as a function of the ratio of interface height to flame height for a 60 kW, fire on 0.19 m. diameter burner for various triangular heat release rate profiles when the maximum is moved in increments of 0.1 Z_{fl}

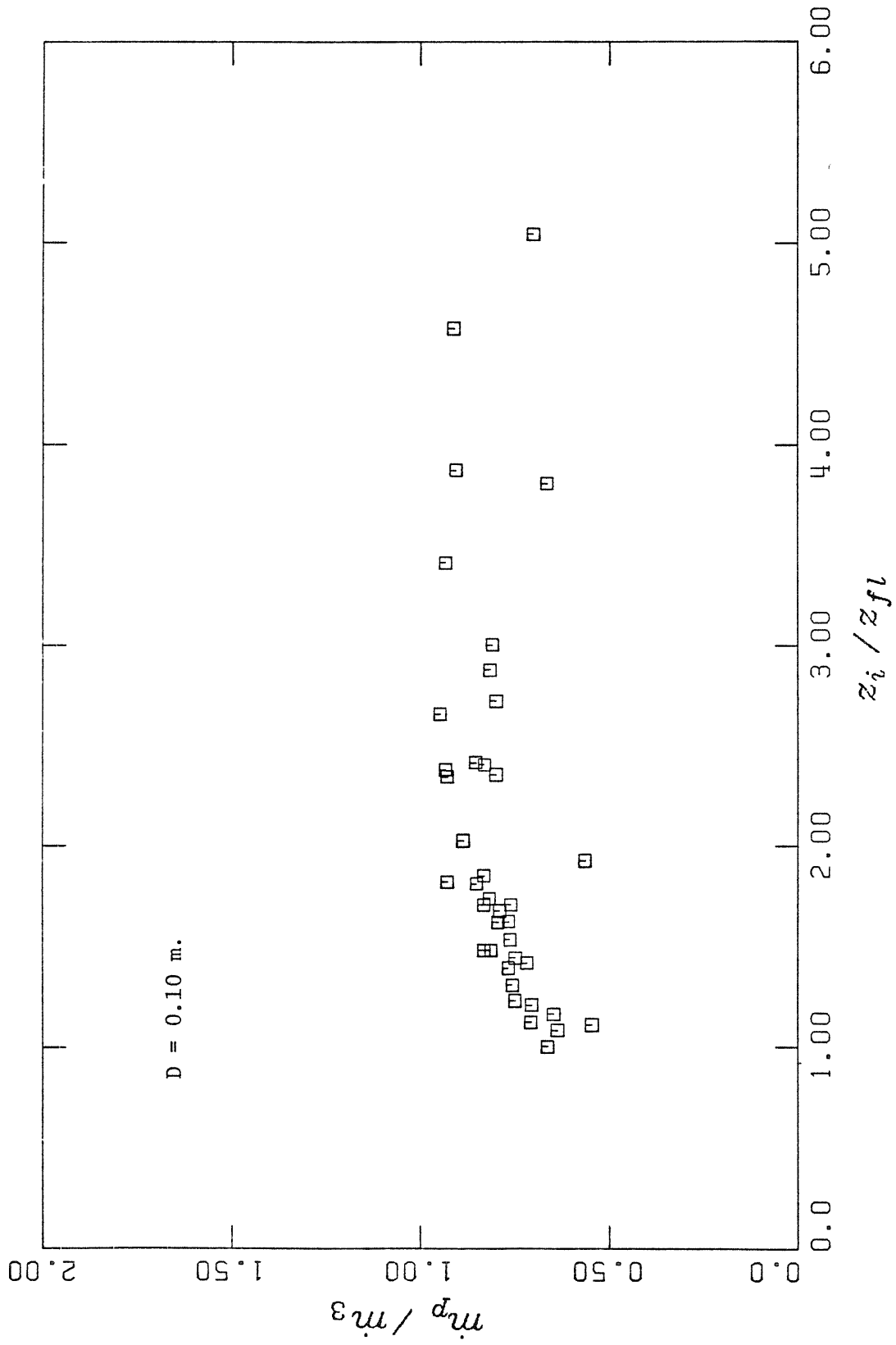


Figure (4.5) Far field entrainment data for 0.10 m. diameter burner

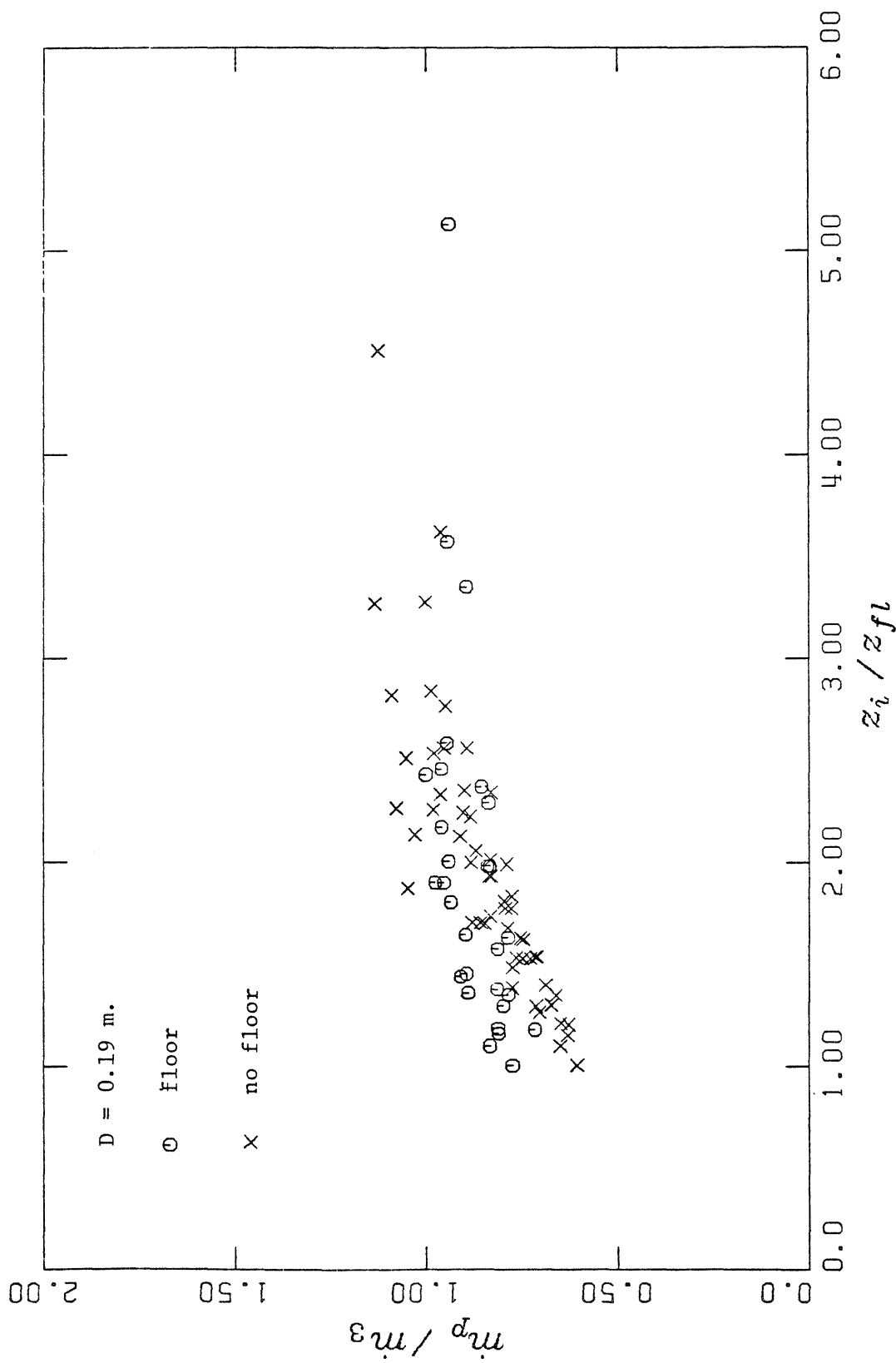


Figure (4.6) Far field entrainment data for 0.19 m. diameter burner with and without the 2.4 m. square floor surround

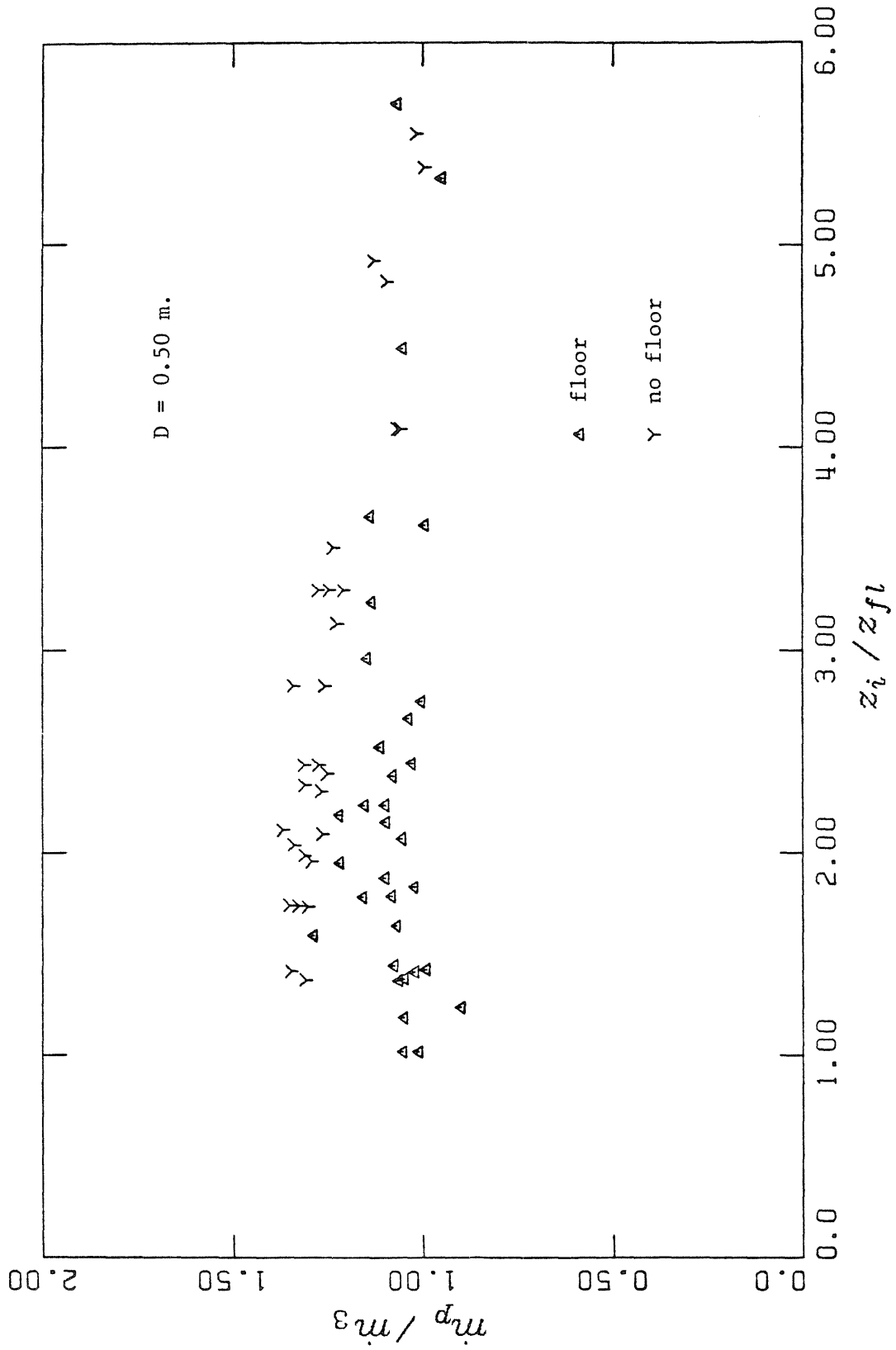


Figure (4.7) Far field entrainment data for 0.50 m. diameter burner with and without the 2.4 m. square floor surround

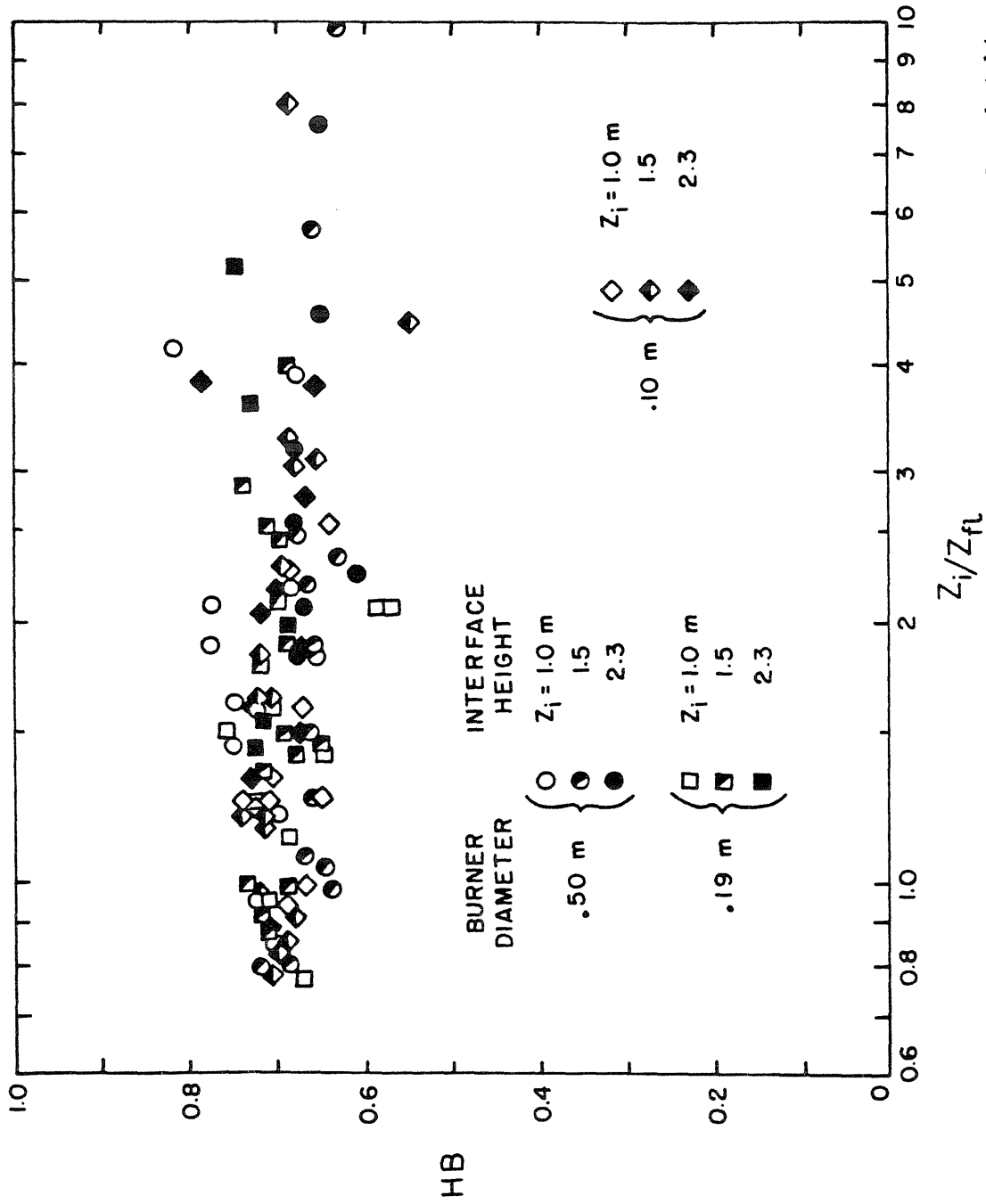


Figure (4.6) Dependence of heat balance ratio on the ratio of interface height to flame height

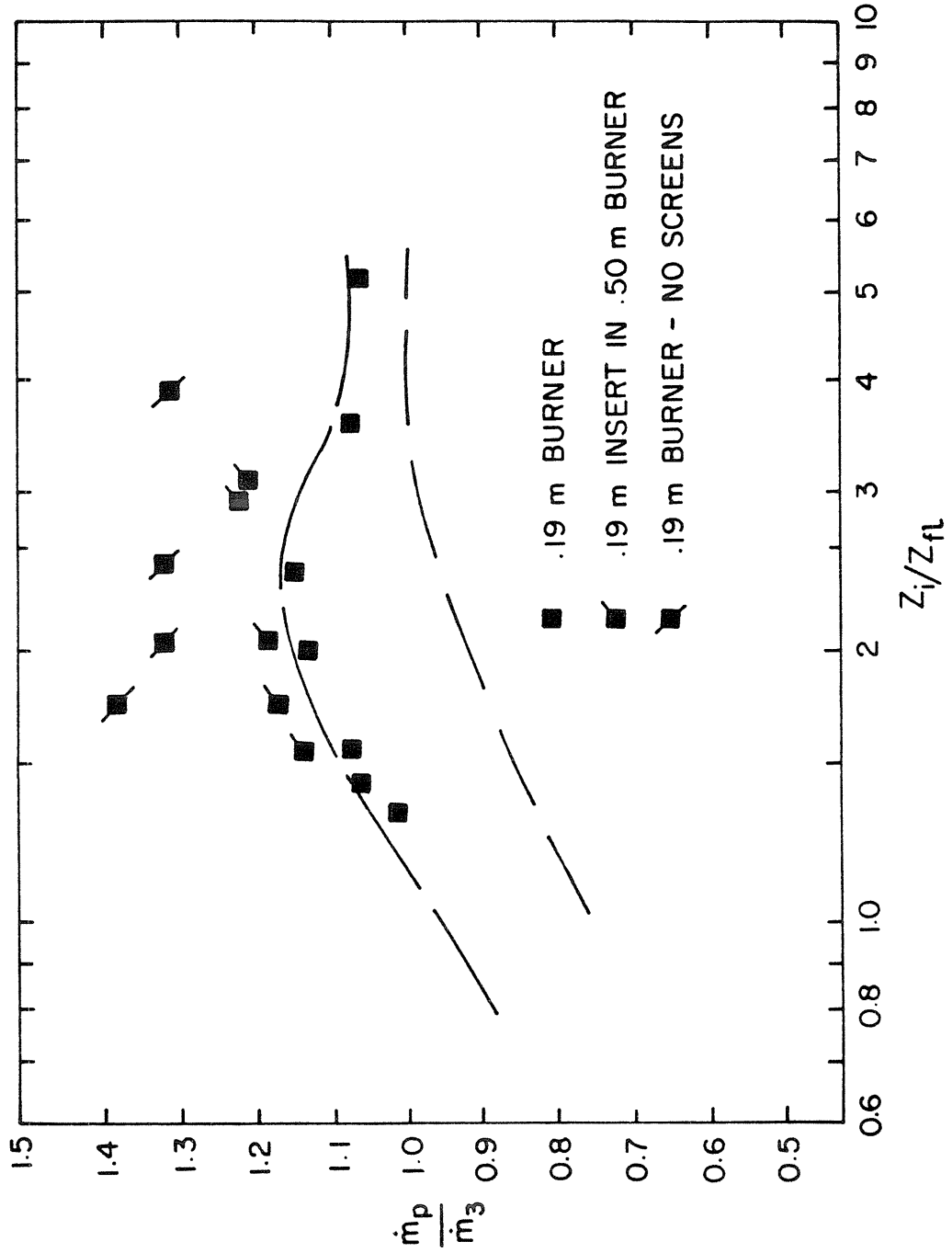


Figure (4.9) Dependence of mass flux ratio on aerodynamic disturbances

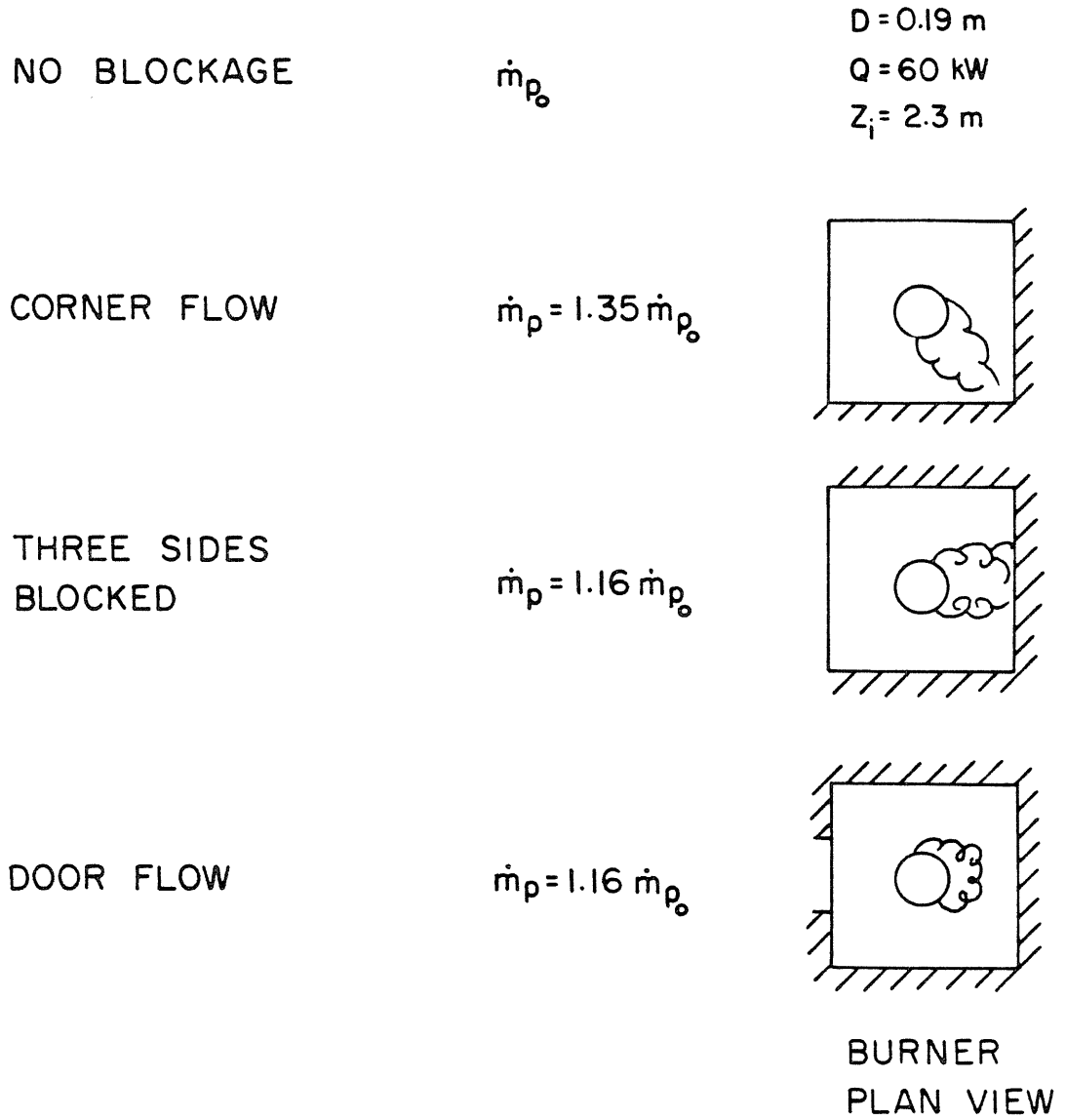


Figure (4.10) Effect of blockage on mass flux ratio

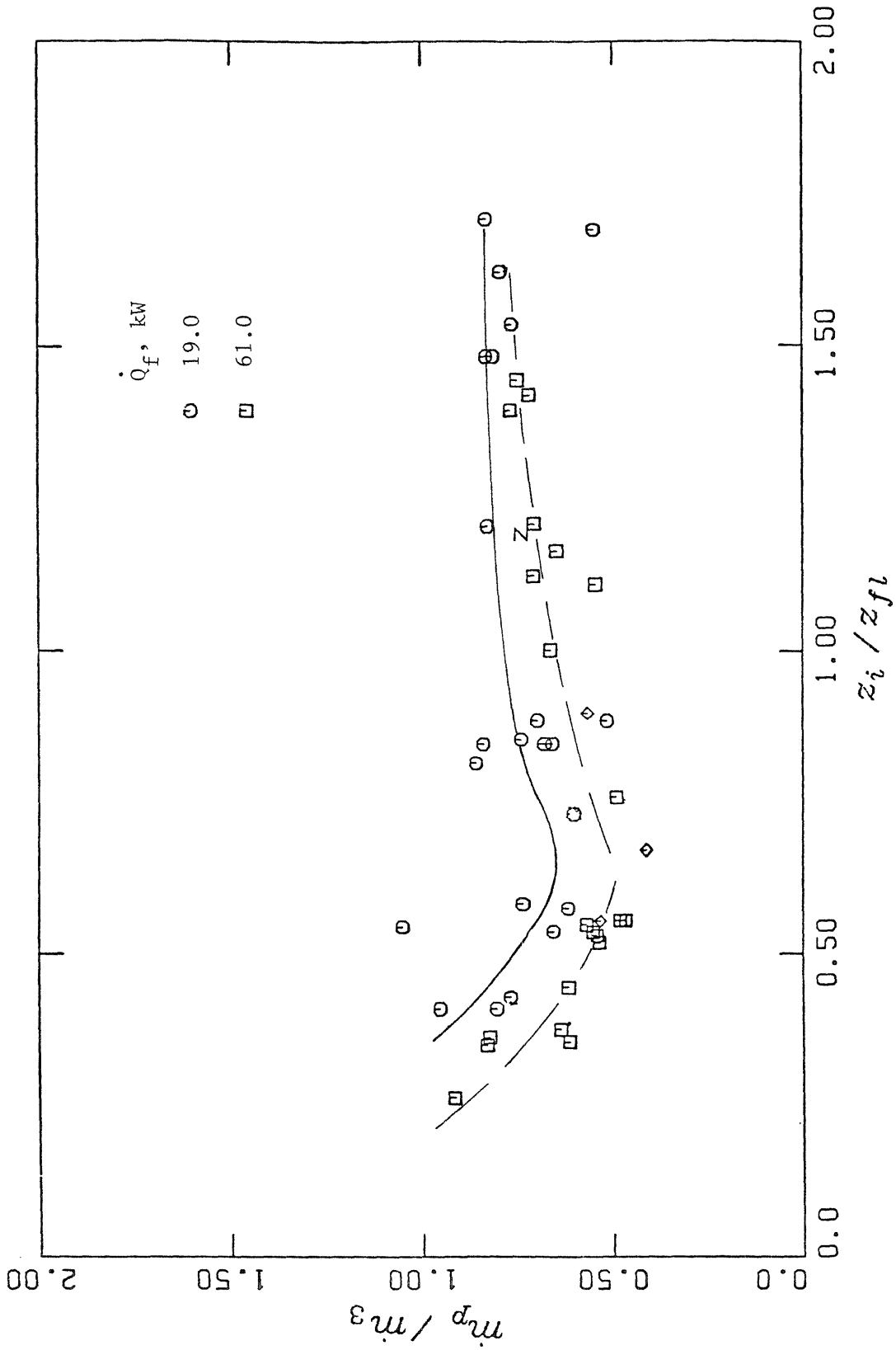


Figure (4.11) Plume mass flux normalized by the far field correlation equation (4.16) as a function of interface height divided by the flame height for various heat release rates on 0.10 m. diameter burner

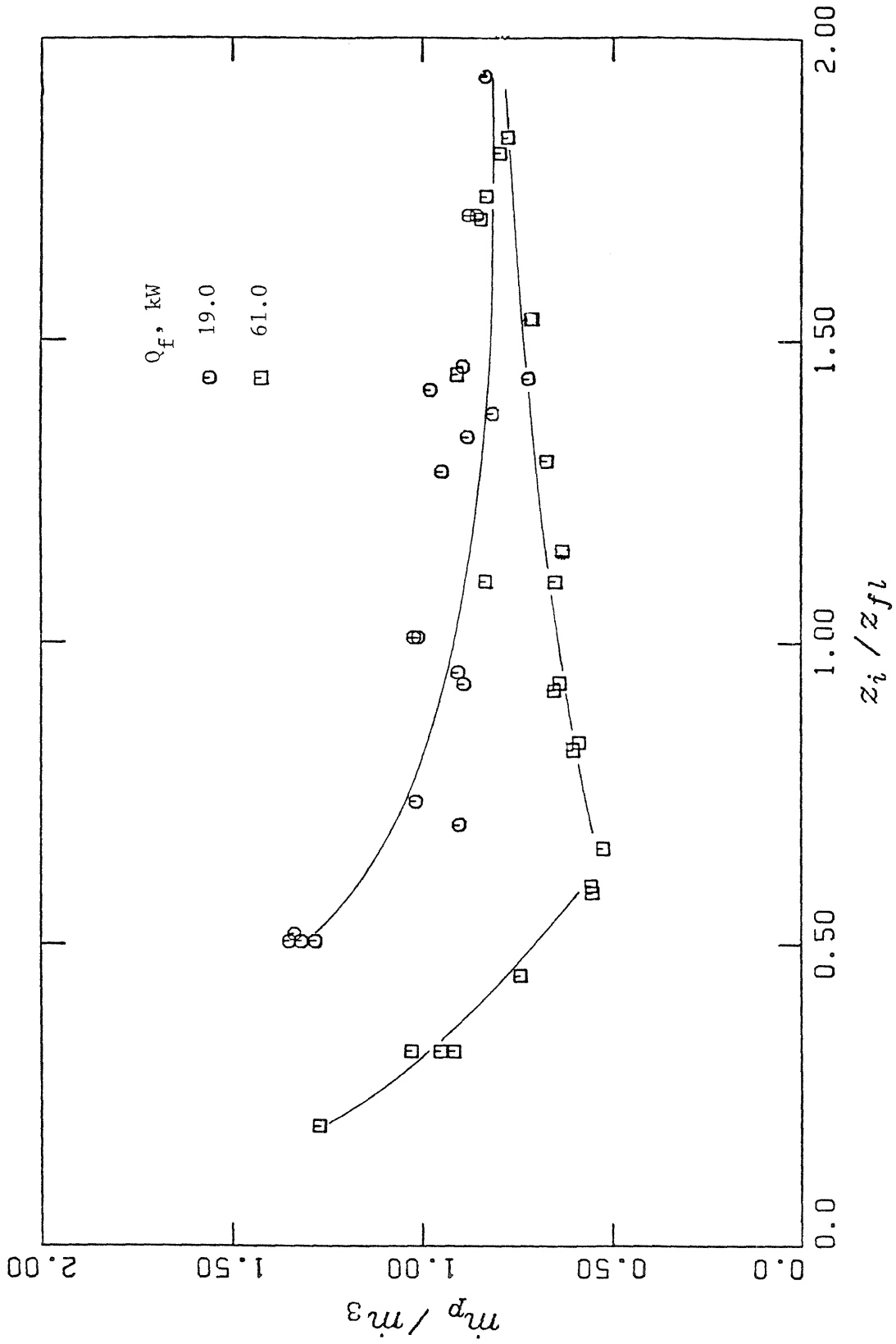


Figure (4.12) Plume mass flux normalized by the far field correlation equation (4.16) as a function of interface height divided by the flame height for various heat release rates on 0.19 m. diameter burner

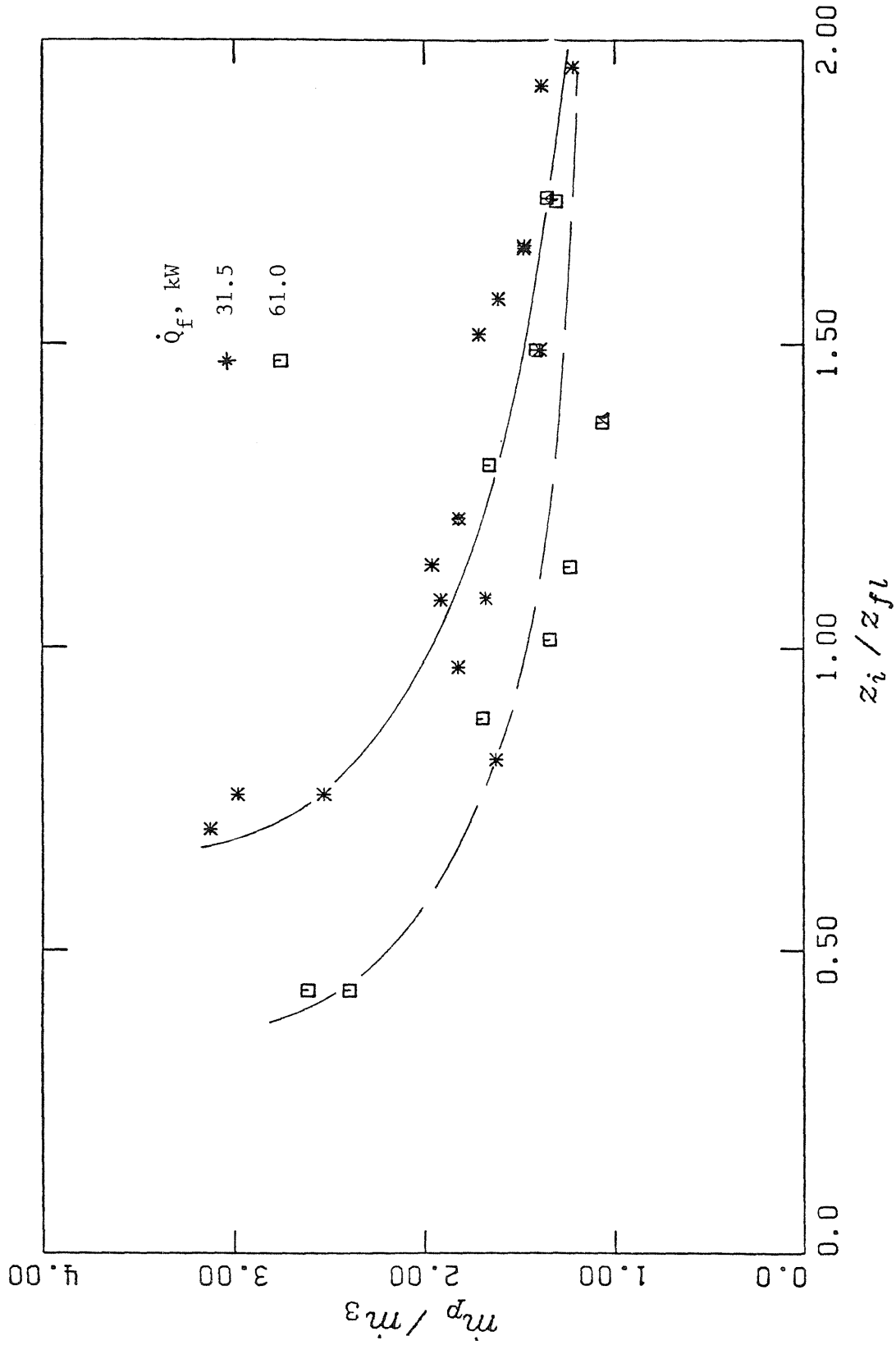


Figure (4.13) Plume mass flux normalized by the far field correlation equation (4.16) as a function of interface height divided by the flame height for various heat release rates on 0.50 m. diameter burner

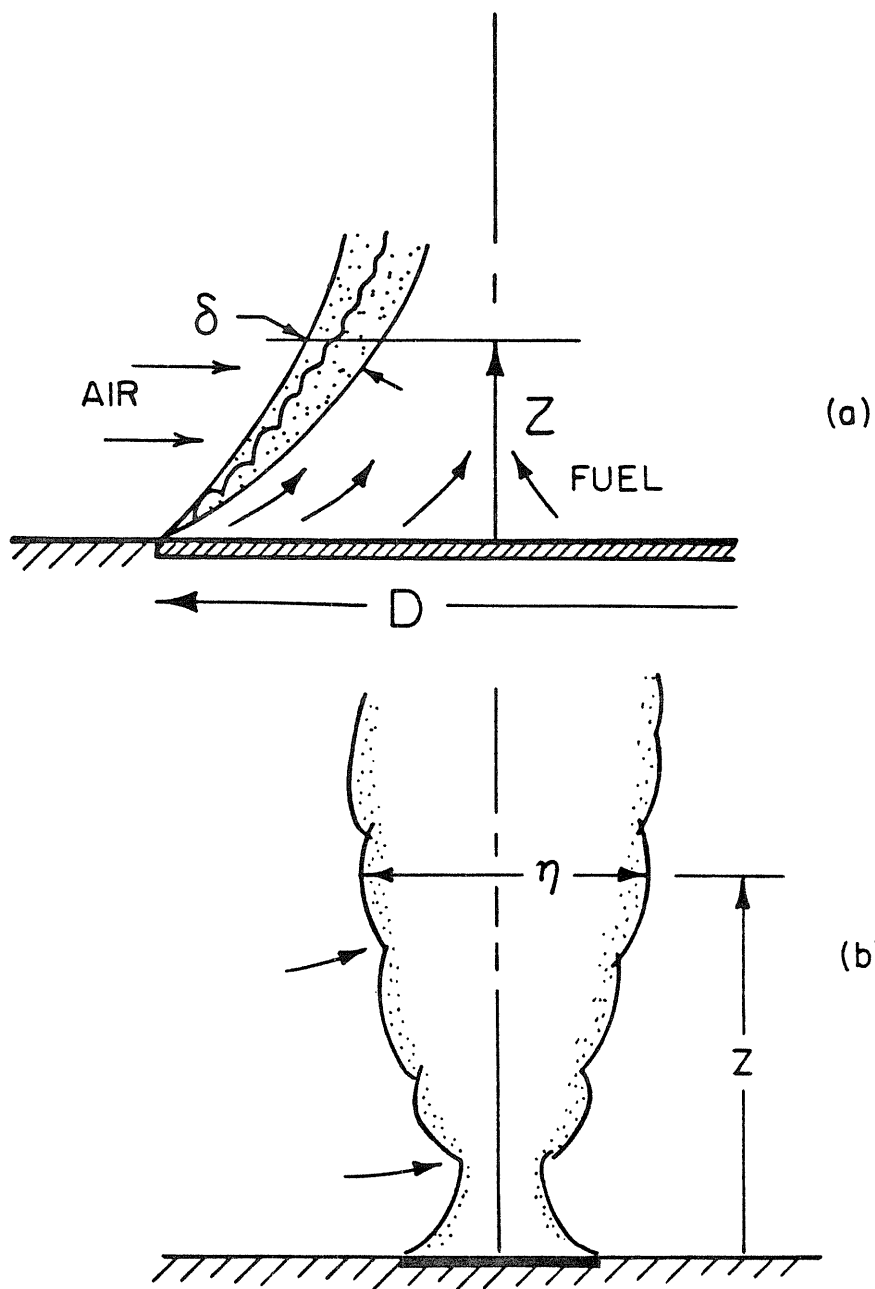


Figure (4.14) Definition of scales in the initial and turbulent flame regions

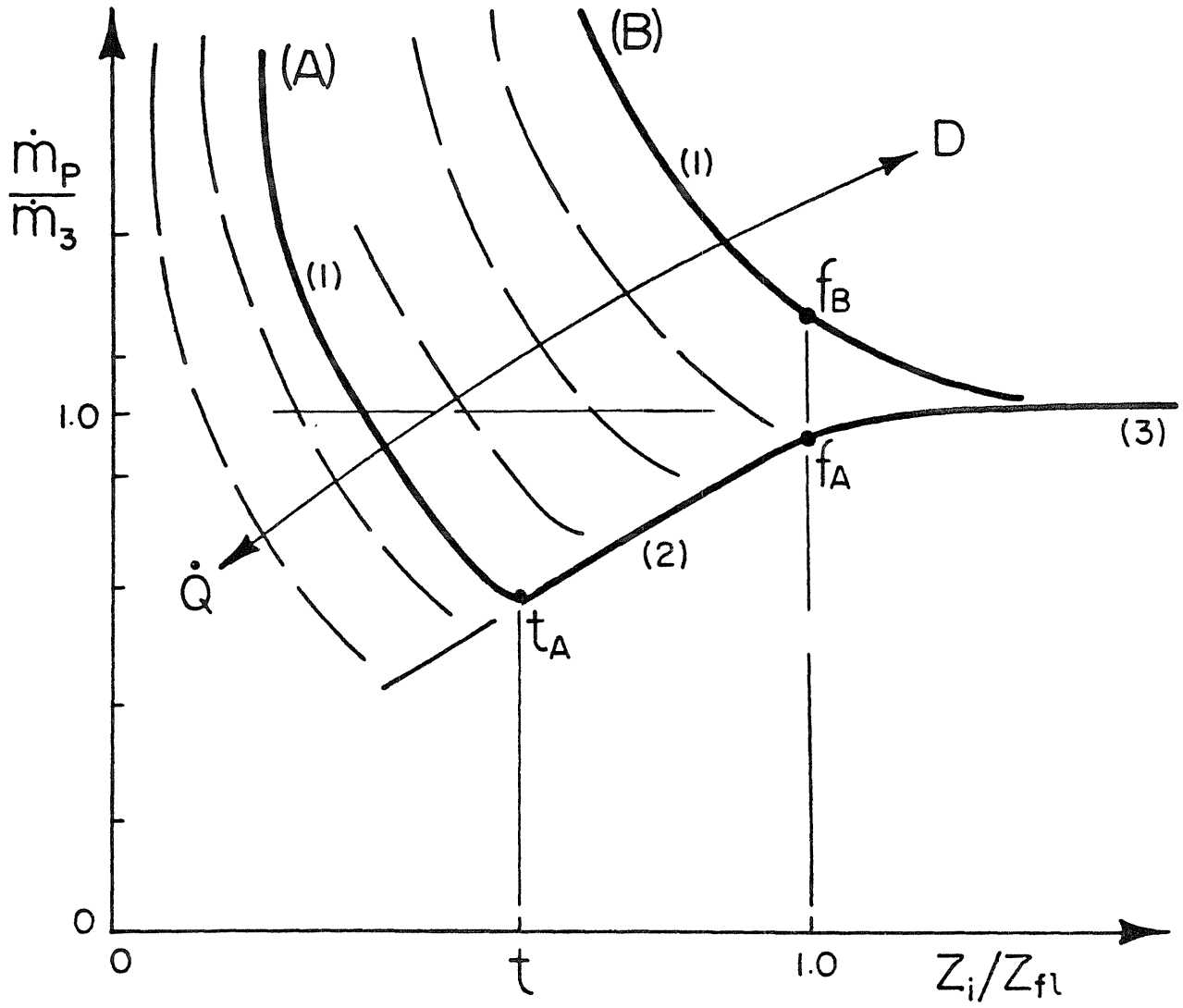


Figure (4.15) Dependence of plume mass flux in three regions. Regions (1), (2) and (3) are present for example (A); and regions (1) and (3) for (B)

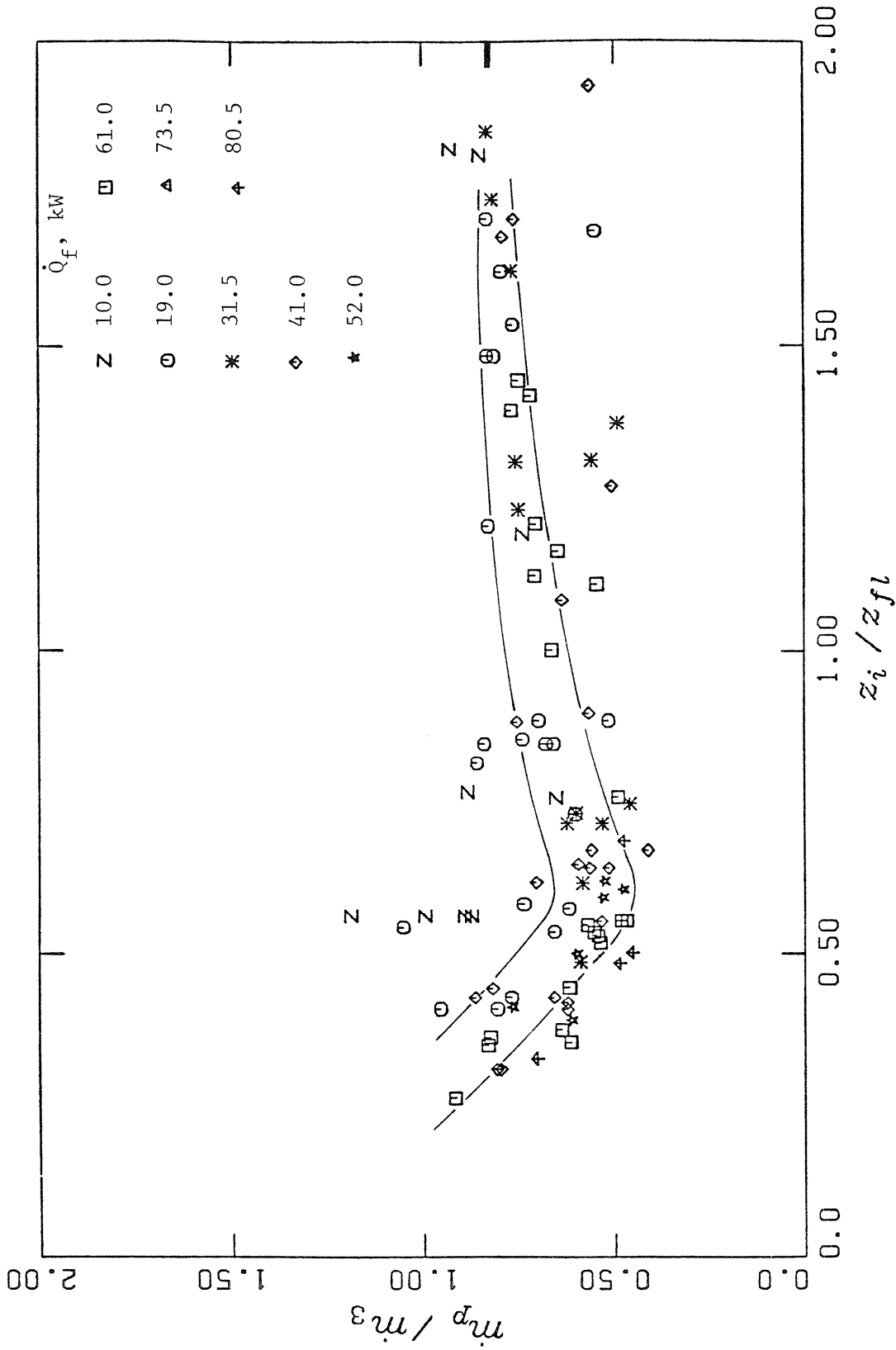


Figure (4.16) Plume mass flux normalized by the far field correlation equation (4.16) as a function of interface height divided by the flame height for various heat release rates on 0.10 m. diameter burner

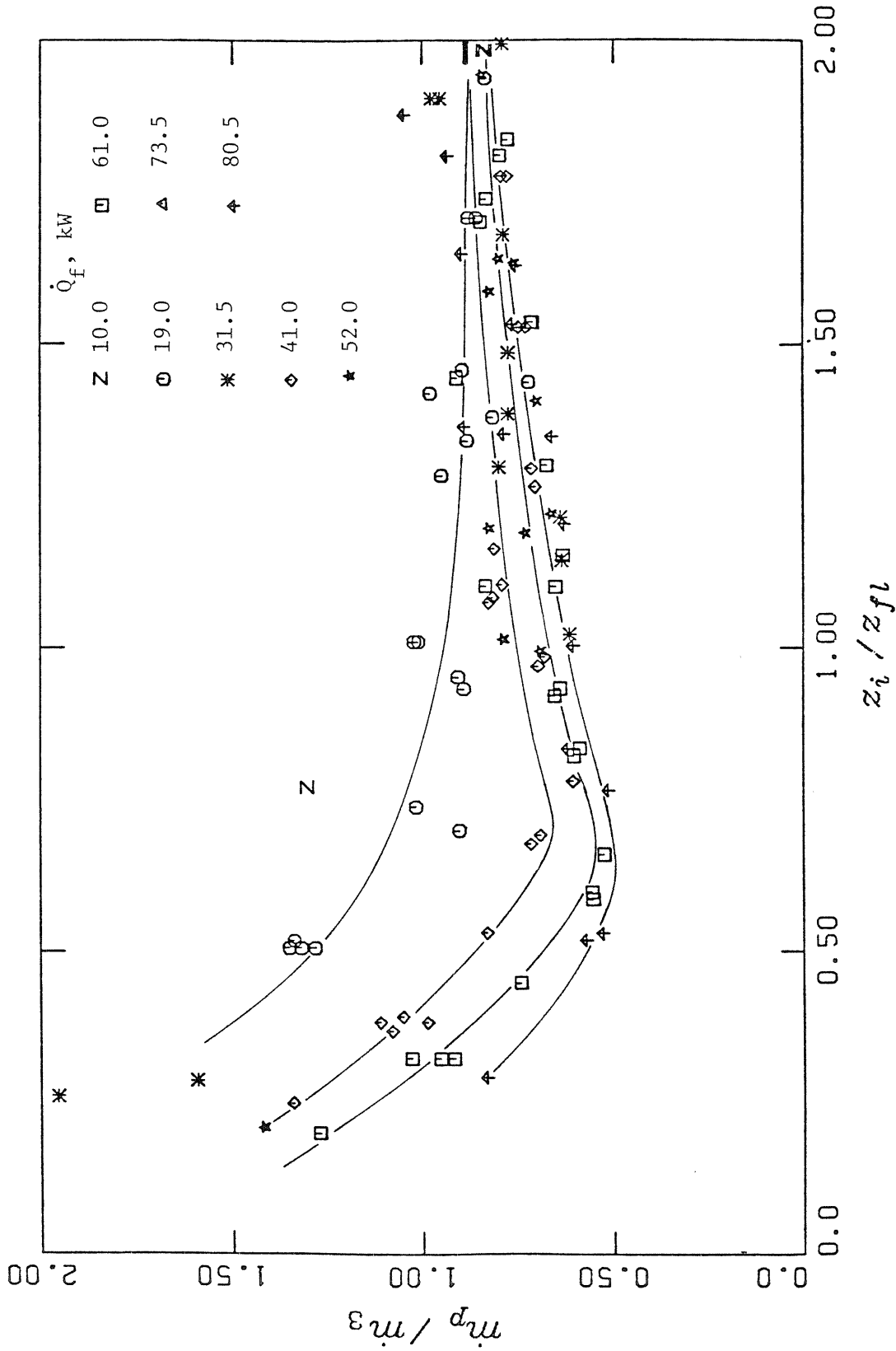


Figure (4.17) Plume mass flux normalized by the far field correlation equation (4.16) as a function of interface height divided by the flame height for various heat release rates on 0.19 m. diameter burner

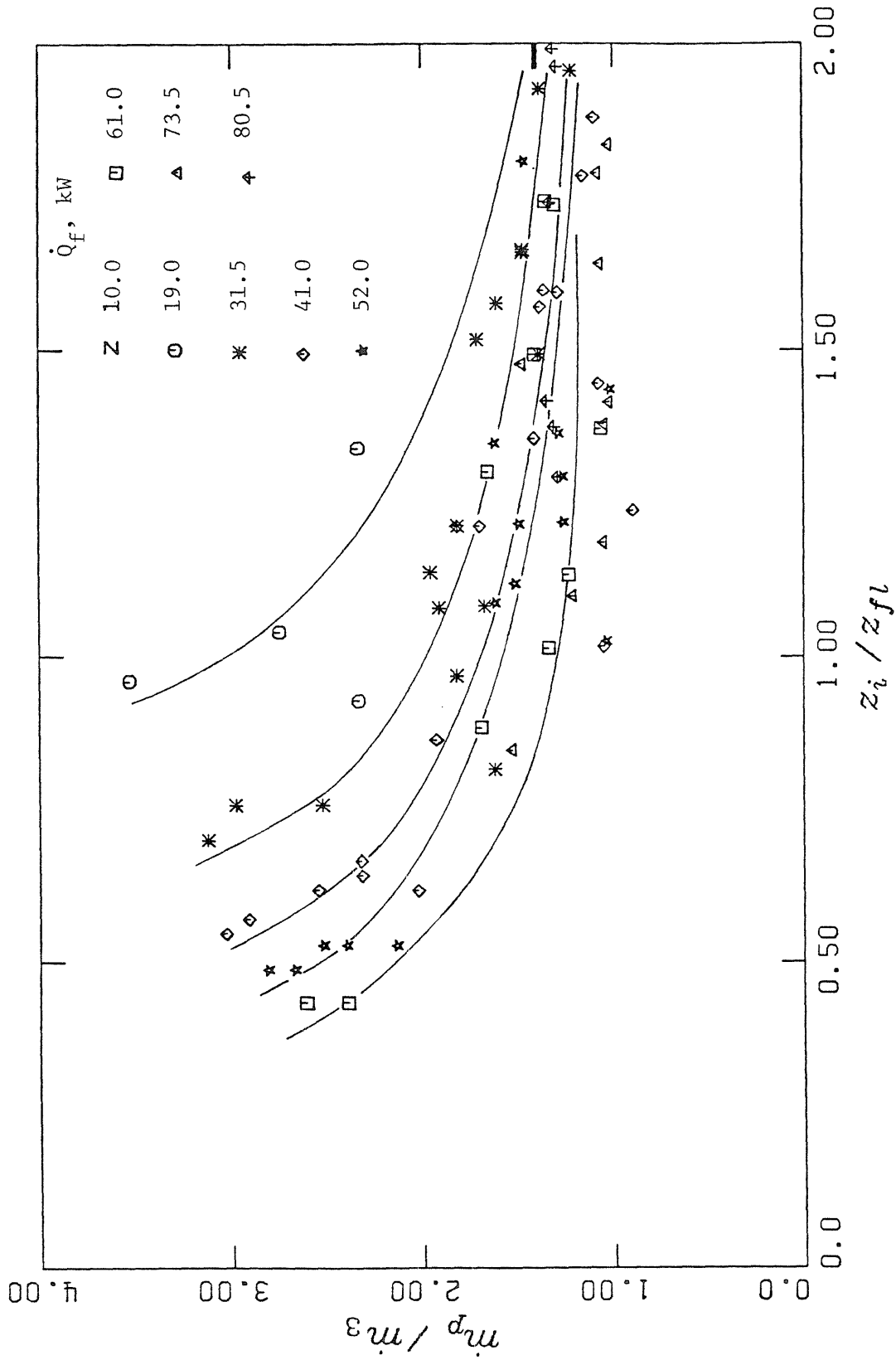


Figure (4.18) Plume mass flux normalized by the far field correlation equation (4.16) as a function of interface height divided by the flame height for various heat release rates on 0.50 m. diameter burner

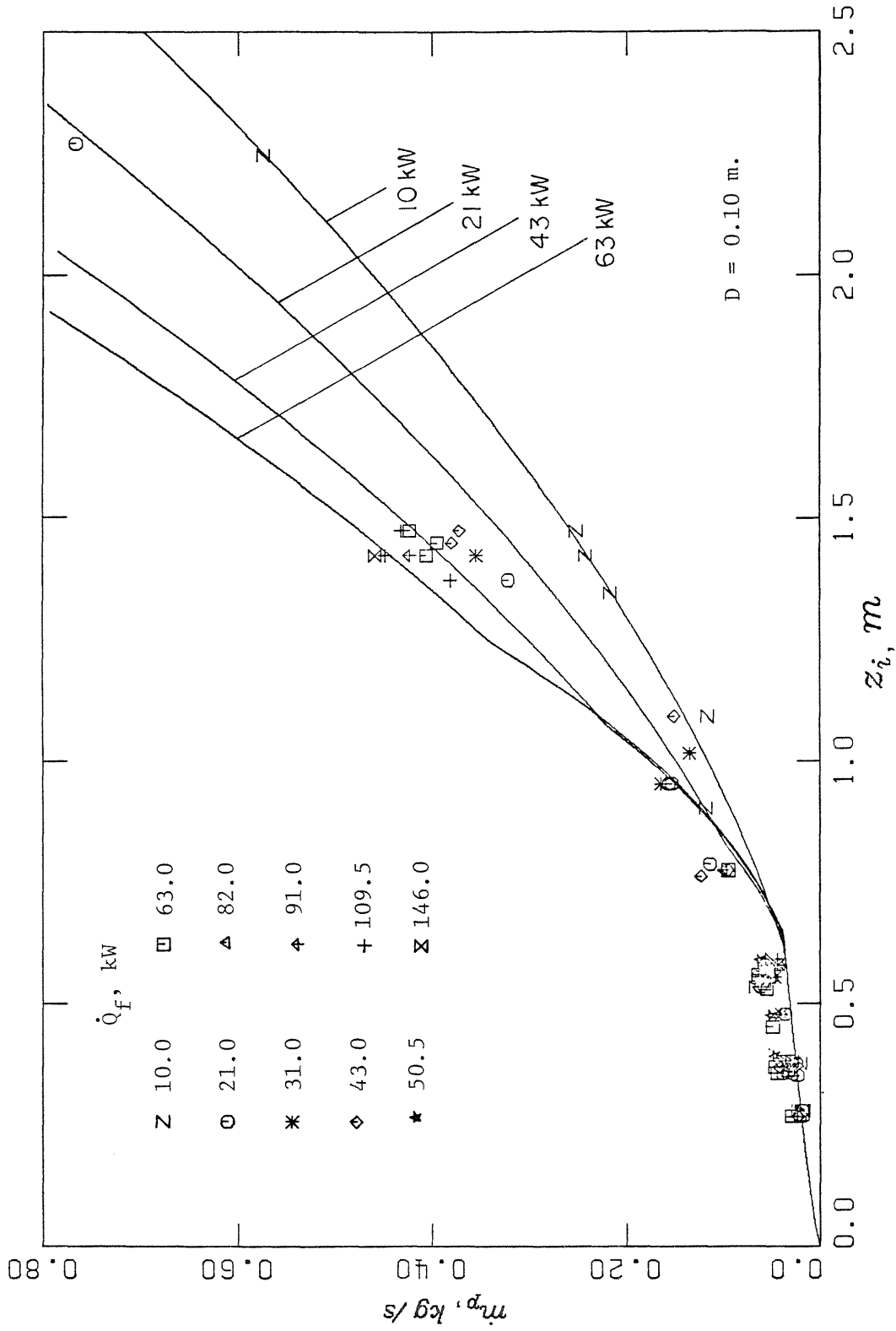


Figure (4.19) Plume mass flux as a function of interface height for various heat release rates shown together with model computations for 0.10 m. diameter burner

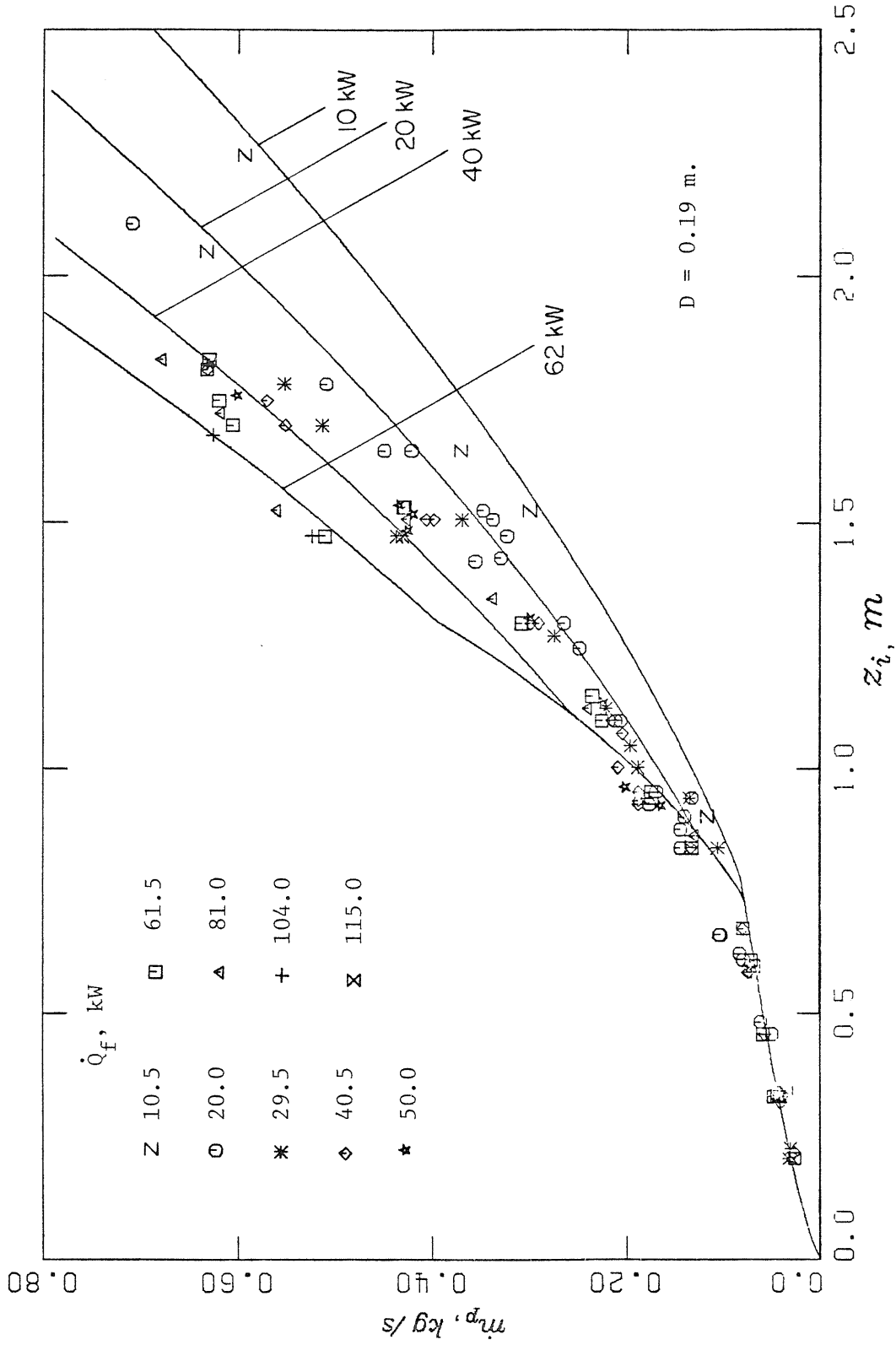


Figure (4.20) Plume mass flux as a function of interface height for various heat release rates shown together with model computations for 0.19 m. diameter burner

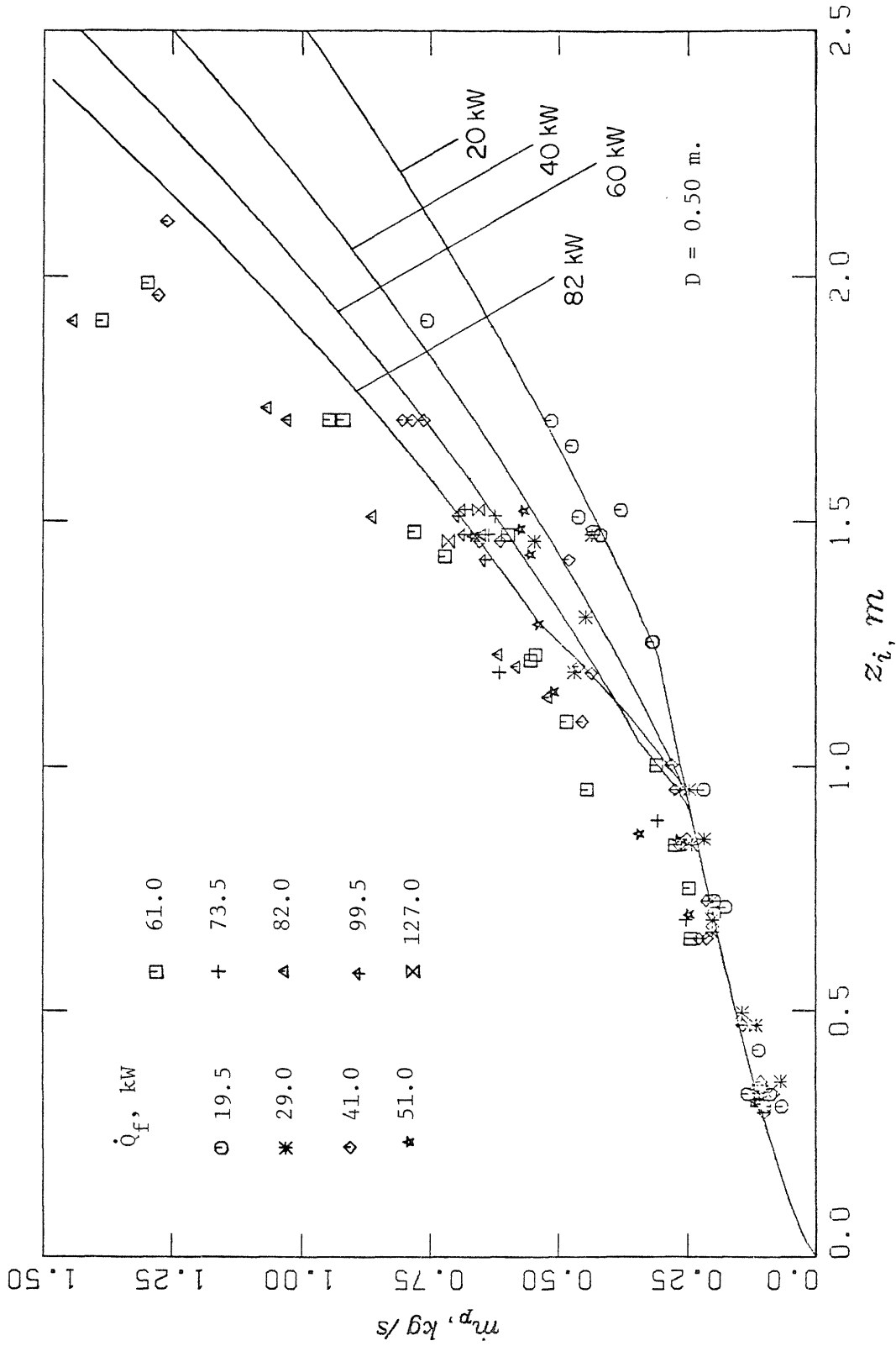


Figure (4.21) Plume mass flux as a function of interface height for various heat release rates shown together with model computations for 0.50 m. diameter burner

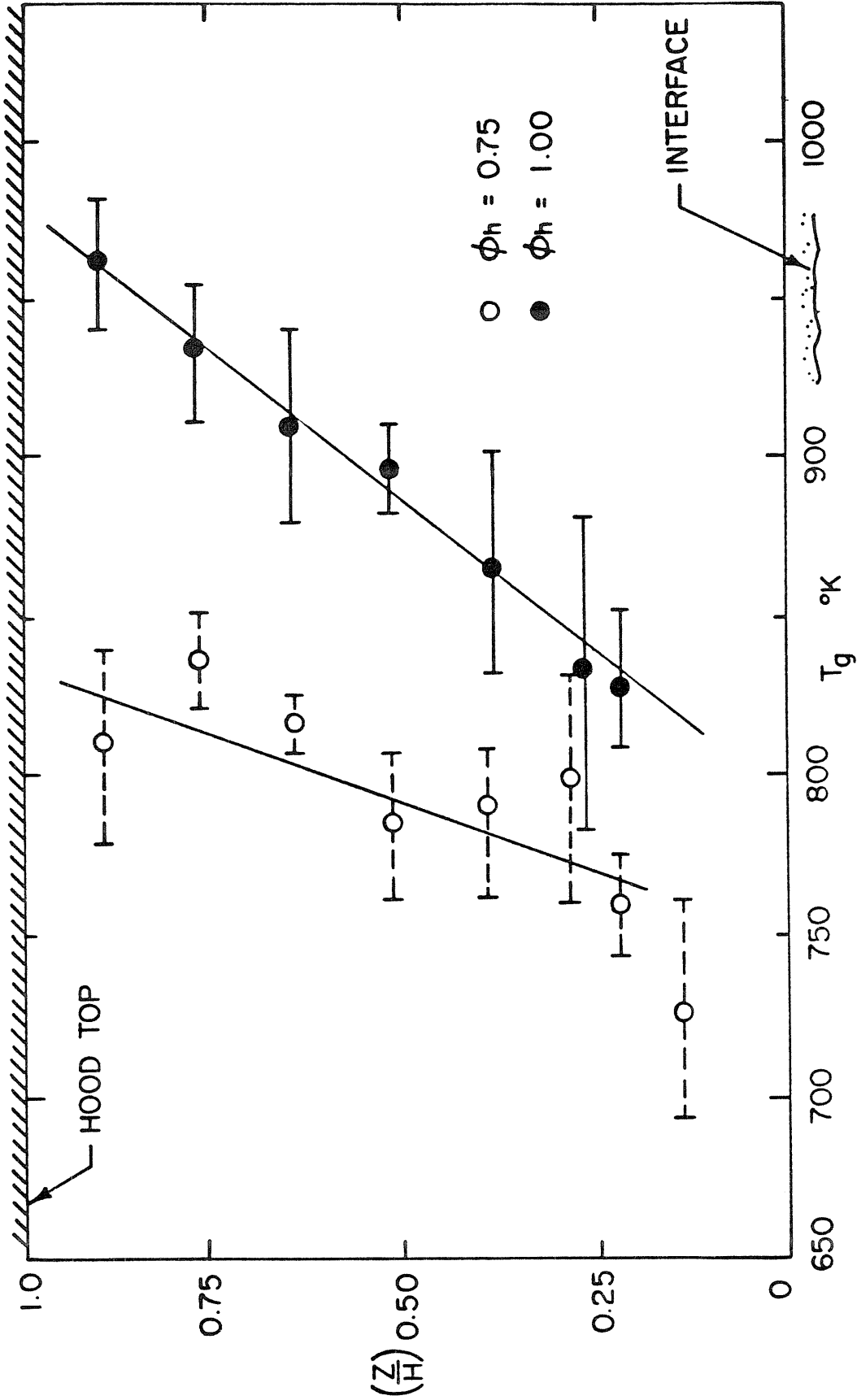


Figure (4.22) Ceiling layer gas temperature profiles as a function of the height normalized by the height of the small hood for equivalence ratios of $\phi_h \approx 0.75$ and 1.0

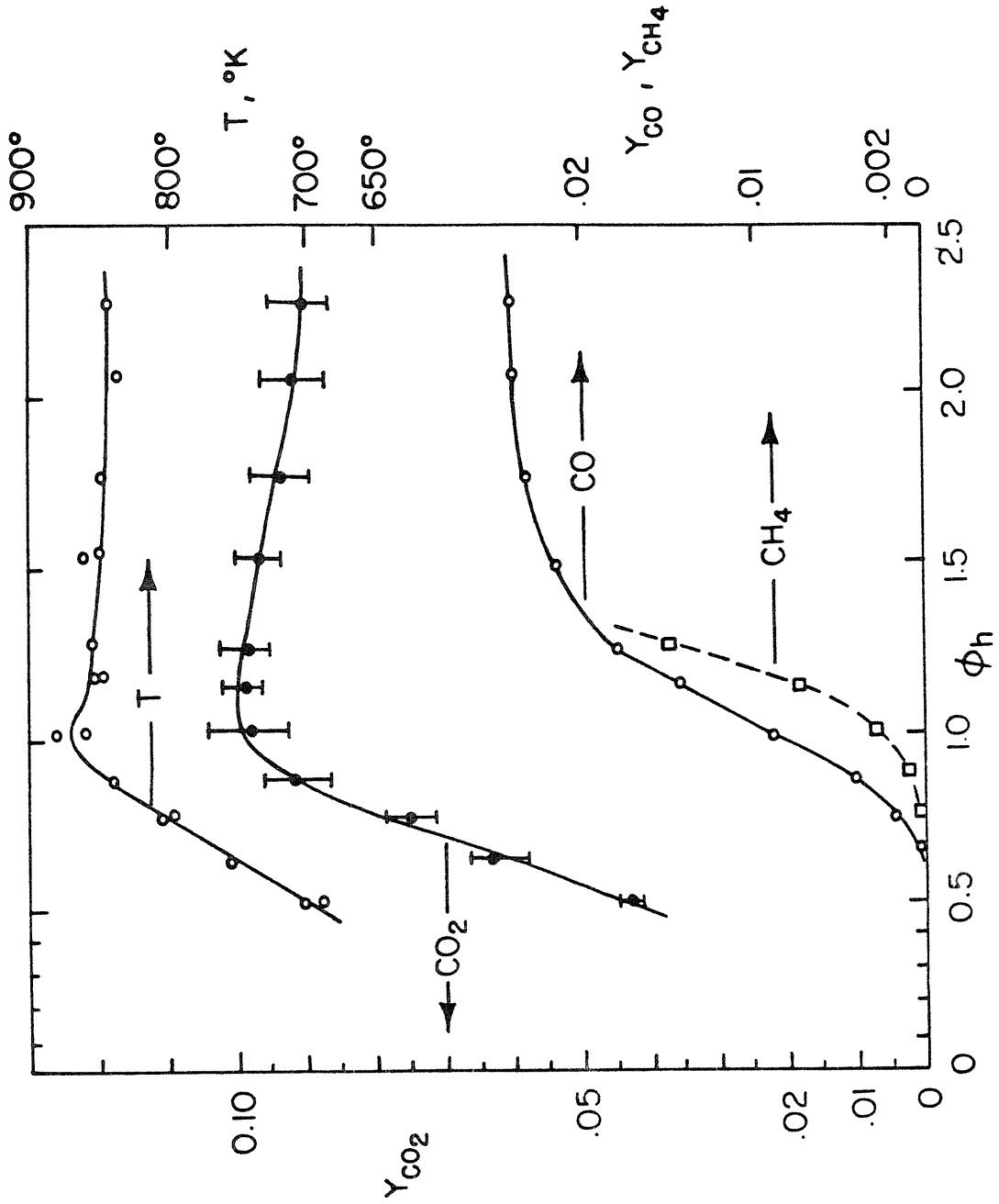


Figure (4.23) CO_2 , CO , unburned hydrocarbon concentrations and temperature as a function of equivalence ratio of the hood gas, ϕ_h

Chapter 5

INTEGRAL SOLUTION OF A LAMINAR BUOYANT DIFFUSION FLAME

Plume mass flux measurements of Chapter 4 suggested that entrainment close to the burner surface scales like that of a laminar wrinkled flame front surrounding the burner perimeter. In the experiments, the gaseous fuel flows upward through a thick bed of glass beads and emerges with very low velocities at the top of the burner. The beads are heated by radiation from the flame and enough of this energy is transferred to the gaseous fuel to increase its temperature to several hundreds of degrees Centigrade. When this low speed, hot and gaseous fuel reaches the surface of the burner, it accelerates vertically due to its buoyancy relative to the quiescent and cool air which surrounds the burner. This acceleration causes the fuel-air interface, where the diffusion flame lies, to contract sharply and close to the burner, the flame shape is roughly a hyperboloid of revolution about its vertical axis. Farther above the burner, the flow is complicated by large scale, nearly periodic pulsations and by smaller scale wrinkling of the flame surface.

The work described here is an attempt to make a quantitative estimate of the entrainment of a buoyant, laminar diffusion flame under idealized conditions which very crudely approximate the steady features of the flame described above. In this context, we solved two problems. The first and the simplest involves a vertical, plane, buoyant diffusion flame which separates stationary air on one side from buoyant fuel on the other. The second involves an axisymmetric, gaseous fuel jet which is buoyant and rises through stationary air. In both cases, the diffusion flame is superimposed on the interface between moving fuel and stationary air. The boundary layer and thin flame approximations are

used in formulating the problems. We also assume that the pressure is in hydrostatic equilibrium throughout the flow field.

In the following sections, we first develop integral equations to describe both the plane and the axisymmetric flames. The vertical plane flame yields a self-similar solution when the fuel velocity at the horizontal burner surface is zero (but the fuel is still allowed to accelerate with height due to its buoyancy). A similar problem was studied earlier by Fleming and Marble [5.1] who investigated the stability of a plane, vertical flame front with respect to periodic disturbances. Here, the planar case is discussed first in detail to exhibit information about various features of the flame which are also common to the axisymmetric case. Finally, the numerical solutions for the axisymmetric flame are obtained by taking into account the initial fuel velocity at the burner surface, acceleration of the fuel and resulting contraction of the flame surface due to the buoyancy of the fuel and the buoyancy of combustion products. We also include some examples for methane-air diffusion flames stabilized on different size burners.

5.1. Governing Equations

The basic coordinate system used in this work is (z, r) , where z is the vertical coordinate measured from the center of the burner surface and r is the radial distance measured from the z axis in axisymmetric problems (see figure (5.1)). In describing the velocity and temperature field in the diffusion zone, however, it is natural to use the orthogonal, curvilinear coordinates (x, y) for which x is the distance measured along the dividing streamline separating fuel and oxidizer regions and y is the distance measured from the dividing streamline in the direction perpendicular to it as shown in figure (5.1a). The equations of motion are simplified by use of the boundary layer approximation as well as the assumption that the radius of curvature is large in comparison with the

boundary layer thickness. The latter assumption allows us to neglect the centrifugal force terms in the momentum equation. These simplifications also require us to know only the x dependence of the core radius, $r(x,y)$. (see figure (5.1a))

Simplified equations of motion for the boundary layer region which apply to either plane or axisymmetric problems are,

$$\text{Continuity: } \frac{\partial}{\partial x} (\rho u r^n) + \frac{\partial}{\partial y} (\rho v r^n) = 0 \quad (5.1)$$

$$x\text{-momentum: } \frac{\partial}{\partial x} (\rho u^2 r^n) + \frac{\partial}{\partial y} (\rho u v r^n) =$$

$$-\tau^n \frac{\partial P}{\partial x} - \tau^n \rho g \sin \theta + \frac{\partial}{\partial y} \left(\tau^n \mu \frac{\partial u}{\partial y} \right) \quad (5.2)$$

$$y\text{-momentum: } \frac{\partial P}{\partial y} = 0 \quad (5.3)$$

Energy and species conservation equations are,

$$\frac{\partial}{\partial x} (\rho u h r^n) + \frac{\partial}{\partial y} (\rho v h r^n) = \frac{\partial}{\partial y} \left(\tau^n \frac{k}{C_p} \frac{\partial h}{\partial y} \right) - \tau^n \dot{\omega}_f h_c \quad (5.4)$$

$$\frac{\partial}{\partial x} (\rho u Y_i r^n) + \frac{\partial}{\partial y} (\rho v Y_i r^n) = \frac{\partial}{\partial y} \left(\tau^n \rho D \frac{\partial Y_i}{\partial y} \right) + \tau^n \dot{\omega}_i \quad (5.5)$$

if $n=0$ plane flow $n=1$ axisymmetric flow (For nomenclature, see list of symbols)

5.2. Pressure Variation and Flame Shape

The y-momentum equation embodies the usual boundary layer assumption that the pressure is independent of y within the boundary layer and is given by the static pressure outside the boundary layer. In our problem, we assume that the oxidizer medium is denser than the fuel and that the oxidizer mass is stationary for points far from the flame. Referring to figure (5.2), the magnitude of the fuel velocity, u_f can be obtained from Bernoulli equation, if the fuel flow is assumed to be irrotational.

$$\left. \begin{aligned} P_0 + \frac{1}{2}\rho_f u_{f0}^2 &= P + \frac{1}{2}\rho_f u_f^2 + gz \\ P_0 &= P + \rho_\infty gz \end{aligned} \right\} \quad (5.6)$$

where P_0 is the pressure at $z=0$ on oxidizer side. Since we assume also that the flow is in hydrostatic equilibrium, $dP/dr=0$, these two equations give an expression for the fuel velocity,

$$u_f = \left[2 \left[\frac{\rho_\infty - \rho_f}{\rho_f} \right] gz + u_{f0}^2 \right]^{1/2} \quad (5.7)$$

which is applicable for both plane and axisymmetric cases. The relationship between z and x is,

$$\frac{dz}{dx} = \sin \theta \quad (5.8)$$

Hence, the second of equation (5.6) combined with equation (5.8) is used to replace the pressure term in x-momentum equation (5.2) as,

$$\frac{\partial P}{\partial x} = -\rho_{\infty} g \sin \theta \quad (5.9)$$

The shape of the axisymmetric flame is obtained from continuity equation written as,

$$2\pi \int_0^r w(s, z) s ds = \pi r_0^2 u_{f0} \equiv \dot{V} \quad (5.10)$$

where w is the vertical component of fuel velocity. Since we know that w must vary from u_f at centerline to $u_f \sin \theta$ at the edge, we have chosen a parabolic variation of w , as a reasonable approximation:

$$\frac{w}{u_f} = 1 + (\sin \theta - 1) \left(\frac{s}{r} \right)^2 \quad (5.11)$$

Substituting the expression for w in equation (5.10) and performing the integration one obtains,

$$\frac{\pi}{2} u_f r^2 (1 + \sin \theta) = \dot{V} \quad (5.12)$$

this equation gives the variation of θ with z as,

$$\sin \theta = \frac{2\dot{V}}{\pi u_f r^2} - 1 \quad (5.13)$$

since $r = r(z)$ and $u_f = u_f(z)$. From geometry, the variation of r with respect to z can be expressed as,

$$\frac{dr}{dz} = -\cot \theta = -\left(\frac{1}{\sin^2 \theta} - 1\right)^{1/2} \quad (5.14)$$

This differential equation can be integrated by using equations (5.7) and (5.13) for a given fuel volume flux and initial radius r_0 .

5.3. Equation of State

The equation of state used is that for an ideal gas,

$$P = \rho RT = \rho \frac{\mathbf{R}}{M} T \quad (5.15)$$

where \mathbf{R} is the universal gas constant and M is the local molecular weight. We also assume that the specific heat ratio $\gamma = C_p/C_v$ varies so little across the flame that

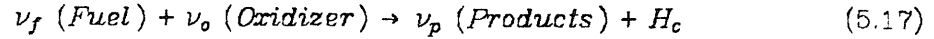
$$\rho h = \rho_f h_f = \rho_\infty h_\infty = \text{constant} \quad (5.16)$$

See Appendix A for more details.

5.4. Chemical Reaction

The fuel mixture is assumed to be composed of a gaseous fuel and a diluent gas. The term "fuel mixture" refers to the complete mixture whereas "fuel" is reserved for the combustible fuel component of the mixture. We assume that the chemical reaction rates in the diffusion flame are so fast compared with the diffusion rates of the species in the reaction zone that the reaction rates can be taken to be infinite and the reaction zone shrinks to a thin flame front with negligible thickness. A simple, one step chemical reaction is used to approximate the overall combustion process. The stoichiometric reaction between ν_0

moles of oxidizer and ν_f moles of fuel is of the form,



where ν_p is the number of moles of product formed and H_c is the heat of combustion per ν_f moles of fuel.

Conservation of mass in the reaction (5.17) leads to relations for the reaction rates of species in terms of their molecular weights, M_i and stoichiometric coefficients, ν_i . Thus,

$$\frac{\dot{\omega}_f}{\nu_f M_f} = \frac{\dot{\omega}_o}{\nu_o M_o} = - \frac{\dot{\omega}_p}{\nu_p M_p} \quad (5.18)$$

One then gets,

$$\dot{\omega}_o = \frac{\nu_o M_o}{\nu_f M_f} \dot{\omega}_f = \varphi_{of} \dot{\omega}_f \quad (5.19)$$

5.5. Boundary Layer Integral Equations

Because of the nature of the assumptions made here, we can develop equations for the boundary layer-like flame region which apply to both the axisymmetric and the plane case. The important assumption here is that the thickness of the boundary layer-like flame zone is small compared with the other important dimensions of the problem. In the axisymmetric flame, this assumption will fail far above the burner when the radius of the fuel-air interface, where diffusion flame lies, becomes very small. In both the plane and the axisymmetric cases, the approximation fails as the burner surface is approached.

The production terms in equations (5.4) and (5.5) can be eliminated by linear combination of dependent variables h and Y_i , when the Lewis number, $Le = \rho D C_p / \kappa$ is unity. The solutions of the resulting homogeneous equations may be expressed in terms of the so-called Schwab-Zeldovich variable, ψ and are given by,

$$h - h_\infty + h_c Y_f = (h_f - h_\infty + h_c Y_{f\infty})\psi(x, y) \quad (5.20a)$$

$$Y_o - Y_{o\infty} - \varphi_{of} Y_f = -(Y_{o\infty} + \varphi_{of} Y_{f\infty})\psi(x, y) \quad (5.20b)$$

Here, $\psi(x, y)$ is the solution of

$$\frac{\partial}{\partial x} (\rho u \psi r^n) + \frac{\partial}{\partial y} (\rho v \psi r^n) = \frac{\partial}{\partial y} \left(\rho D r^n \frac{\partial \psi}{\partial y} \right) \quad (5.21)$$

with $\psi(x, -\infty) = 0$ and $\psi(x, +\infty) = 1$. The Schwab-Zeldovich variables are particularly convenient to use since they are continuous and smooth through the flame sheet.

The integral momentum equation is obtained by integrating equation (5.2) with respect to y , first from $y = -\infty$ to $y = 0$ then from $y = 0$ to $y = +\infty$. Here we make use of

- i) x -axis being the dividing streamline
- ii) $r = r(x)$ only, under our small-curvature assumption
- iii) Integrated form of continuity equation
- iv) Equation (5.9) to replace the pressure term

The result is:

$$\begin{aligned} \frac{d}{dx} \left[r^n \left(\int_{-\infty}^0 \rho u^2 dy + \int_0^{\infty} \rho u (u - u_f) dy \right) \right] + r^n \frac{du_f}{dx} \int_0^{\infty} (\rho u - \rho_f u_f) dy \\ = g \sin \theta r^n \left[\int_{-\infty}^0 (\rho_{\infty} - \rho) dy + \int_0^{\infty} (\rho_f - \rho) dy \right] \end{aligned} \quad (5.22)$$

Similarly, when we integrate equation (5.4) over y , first from $y = -\infty$ to $y = y_{fl}$ then from $y = y_{fl}$ to $y = +\infty$, add the two results, rewrite the production term as the product of fuel diffusion flux into the flame sheet and the heating value per mass of fuel we get:

$$\frac{d}{dx} \left[r^n \left(\int_{-\infty}^0 \rho u (h - h_{\infty}) dy + \int_0^{\infty} \rho u (h - h_f) dy \right) \right] = r^n \rho D \left(\frac{\partial Y_f}{\partial y} \right)_{y=y_{fl}} h_c \quad (5.23)$$

In equations (5.22) and (5.23), we assume suitable profiles for velocity and ψ in terms of a width parameter $\delta(x)$ and a characteristic velocity $u_0(x)$ both of which depend on x only. No temperature parameter is required since for fast reaction case the maximum temperature is always given by the adiabatic flame temperature. Furthermore, the Howarth transformation,

$$\rho dy = \rho_{\infty} dy' \quad (5.24)$$

is used to reduce equations (5.22) and (5.23) to their incompressible forms. Selected profiles are expressed in terms of a dimensionless coordinate defined by,

$$\eta \equiv \frac{y'}{\delta} \quad (5.25)$$

The characteristic with scales for velocity and ψ profiles, δ_u and δ_ψ are assumed to be equal implying $Pr \equiv \mu C_p / \kappa$ is unity. The assumed profiles are,

$$\frac{u}{u_0} = \left[1 - \frac{\Lambda}{2} \right] e^{-\eta^2} + \frac{\Lambda}{2} (1 + \operatorname{erf} \eta) \quad (5.26)$$

and

$$\psi = \frac{1}{2} (1 + \operatorname{erf} \eta) \quad (5.27)$$

where $\Lambda = u_f / u_0$ and $\operatorname{erf} \eta$ is the error function defined by,

$$\operatorname{erf} \eta \equiv \frac{2}{\sqrt{\pi}} \int_0^\eta e^{-\xi^2} d\xi$$

As sketched in figure (5.3), the velocity profile has a bulge at $\eta = 0$ which occurs due to flame buoyancy. The second term in equation (5.26) represents mixing layer-like behavior, which exists even without combustion. To be a little more general, we should have an offset at the η origin in the exponential function in equation (5.26) to account for the flame sheet position not equal to $\eta = 0$. For the sake of simplicity, we use the present form. The flame position is fixed by the expression,

$$\operatorname{erf} \eta_{fl} = \frac{Y_{o\infty} - \varphi_{of} Y_{f\infty}}{Y_{o\infty} + \varphi_{of} Y_{f\infty}} \quad (5.28)$$

which is obtained from equations (5.20b) and (5.27). The flame may lie on either side of the x axis and its position depends on the fuel and oxidizer concentrations far from the flame and the stoichiometry of the reaction. The oxidizer and

fuel are assumed to diffuse into the flame front in stoichiometric proportions.

The ψ profile is chosen to be an approximate solution of equation (5.21) with smooth variation through the flame front. Furthermore equations (5.26) and (5.27) satisfy the boundary conditions,

$$\begin{aligned} u(\eta = -\infty) &= 0, \quad \psi(\eta = -\infty) = 0 \\ u(\eta = +\infty) &= u_f, \quad \psi(\eta = +\infty) = 1 \end{aligned}$$

Upon substitution of assumed profiles of equations (5.26) and (5.27) into the momentum and energy integral equations, integrations are performed by making use of the equations (5.24) and (5.25) as well as the assumption $\rho^2 \mathbf{D} = \rho_\infty^2 \mathbf{D}_\infty = \text{const.}$ in energy integral equation (for ideal gases, $\rho \propto T^{-1}$ and $\mathbf{D} \propto T^{7/4}$). The results contain, in addition to $\delta(x)$ and $u_0(x)$ three nondimensional constants which represent the density ratio of oxidizer and fuel media far from the flame front, χ_1 ; the heat of combustion per mass of fuel mixture, χ_2 ; and the heat of combustion per mass of the fuel mixture required for total consumption of the oxidizer (evaluated far from the flame front), χ_3 . These parameters are,

$$\chi_1 = \frac{h_f}{h_\infty} = \frac{\rho_\infty}{\rho_f}, \quad \chi_2 = \frac{h_c Y_{f\infty}}{h_\infty}, \quad \chi_3 = \frac{h_c Y_{o\infty}}{h_\infty \varphi_{of}} \quad (5.29)$$

Equations (5.22) and (5.23) take the forms,

$$\frac{d}{dx} \left[A(\Lambda) r^n \rho_\infty u_0^2 \delta \right] + B(\Lambda) r^n \rho_\infty u_0 \delta \frac{du_f}{dx} = r^n g \text{Sin } \theta \rho_\infty \delta C \quad (5.30)$$

and

$$\frac{d}{dx} \left[D(\Lambda) \tau^n \rho_\infty u_0 \delta \right] = \tau^n E \rho_\infty \frac{D_\infty}{\delta} \quad (5.31)$$

where the parameters A to E are:

$$A(\Lambda) = \left[\frac{1 - \sqrt{2}}{2\sqrt{\pi}} + \frac{1 - \sqrt{2}}{4} \sqrt{\frac{\pi}{2}} \right] \Lambda^2 - \left[1 - \frac{1}{\sqrt{2}} \right] \sqrt{\frac{\pi}{2}} \Lambda + \sqrt{\frac{\pi}{2}}$$

$$B(\Lambda) = - \left[\frac{\sqrt{\pi}}{4} + \frac{1 + \chi_3}{2\chi_3 \sqrt{\pi}} \right] \Lambda + \frac{\sqrt{\pi}}{2}$$

$$C = (\chi_2 + \chi_3) \frac{e^{-\eta_{fi}^2}}{2\sqrt{\pi}} + \frac{(\chi_1 - 1)(\chi_1 - \chi_3 - 1)}{2\chi_1 \sqrt{\pi}}$$

$$D(\Lambda) = \left\{ \frac{\chi_2}{4} \left[\eta_{fi} - \frac{\sqrt{\pi}}{4} \right] (1 + \operatorname{erf} \eta_{fi})^2 + \frac{2e^{-\eta_{fi}^2}}{\sqrt{\pi}} (1 + \operatorname{erf} \eta_{fi}) \right. \\ \left. - \sqrt{\frac{2}{\pi}} (1 + \operatorname{erf} (\sqrt{2}\eta_{fi})) \right] + \frac{\chi_3}{4} \left[-\eta_{fi} (1 - \operatorname{erf}^2 \eta_{fi}) \right. \\ \left. + \frac{2e^{-\eta_{fi}^2}}{\sqrt{\pi}} \operatorname{erf} \eta_{fi} + \sqrt{\frac{2}{\pi}} \operatorname{erfc} (\sqrt{2}\eta_{fi}) - \frac{\sqrt{\pi}}{4} (1 - \operatorname{erf} \eta_{fi})^2 \right] \Big\} \Lambda \\ + \frac{\sqrt{\pi}}{8} \left[\chi_2 (1 + \operatorname{erf} \eta_{fi})^2 + \chi_3 (1 - \operatorname{erf} \eta_{fi})^2 \right]$$

$$E = (\chi_2 + \chi_3) \frac{e^{-\eta_{fl}^2}}{\sqrt{\pi}}$$

Also equation (5.28) can be written as,

$$\text{erf } \eta_{fl} = \frac{\chi_3 - \chi_2}{\chi_2 + \chi_3} \quad (5.32)$$

Entrainment can easily be calculated by a mass balance of oxidizer as shown in figure (5.4). We define two mass flow rates of oxidizer \dot{m}_{OL} and \dot{m}_{OC} as,

$$\dot{m}_{OL} = (2\pi r)^n \int_{-\infty}^{\eta_{fl}} \rho u Y_o dy \quad (5.33)$$

and

$$\dot{m}_{OC} = \int_0^x (2\pi r)^n \rho D \left[\frac{\partial Y_o}{\partial y} \right]_{y=\eta_{fl}} dx \quad (5.34)$$

Under the assumption which led to the equations (5.30) and (5.31), we can show that,

$$\dot{m}_{OL} = (2\pi r)^n \rho_\infty u_0 \delta Y_{o\infty} F(\Lambda) \quad (5.35)$$

$$\dot{m}_{OC} = \rho_\infty D_\infty Y_{o\infty} G \int_0^x (2\pi r)^n \frac{dx}{\delta} \quad (5.36)$$

where,

$$\begin{aligned}
 F(\Lambda) = & \left\{ \left(\frac{\eta_{fl}}{2} - \frac{\sqrt{\pi}}{4} \right) (1 + \operatorname{erf} \eta_{fl}) + \frac{e^{-\eta_{fl}^2}}{2\sqrt{\pi}} - \left[1 + \frac{\chi_2}{\chi_3} \right] \left[\frac{\eta_{fl}}{4} (1 + \operatorname{erf} \eta_{fl})^2 + \right. \right. \\
 & \left. \left. \frac{e^{-\eta_{fl}^2}}{2\sqrt{\pi}} (1 + \operatorname{erf} \eta_{fl}) - \frac{1}{2\sqrt{2\pi}} (1 + \operatorname{erf} (\sqrt{2}\eta_{fl})) \right] \right\} \Lambda + \\
 & \frac{\sqrt{\pi}}{2} (1 + \operatorname{erf} \eta_{fl}) - \left[1 + \frac{\chi_2}{\chi_3} \right] \frac{\sqrt{\pi}}{8} (1 + \operatorname{erf} \eta_{fl})^2 \\
 G = & \left[1 + \frac{\chi_2}{\chi_3} \right] \frac{e^{-\eta_{fl}^2}}{\sqrt{\pi}}
 \end{aligned}$$

Since no oxidizer is generated in the control volume, we can balance the oxidizer mass flow rates by the equation,

$$\dot{m}_{OE} = \dot{m}_E Y_{O_\infty} = \dot{m}_{OC} + \dot{m}_{OL} \quad (5.37)$$

Using equations (5.35) and (5.36) we get,

$$\dot{m}_E = (2\pi r)^n \rho_\infty u_0 \delta F(\Lambda) + \rho_\infty \mathbf{D}_\infty G \int_0^x (2\pi r)^n \frac{dx}{\delta} \quad (5.38)$$

This equation gives the entrainment up to position x . Entrainment is per unit depth of the flame in the plane case ($n=0$). At this point, to proceed any further we must specialize to examine either plane or axisymmetric case.

5.6. Similar Plane Case

This is the case of the plane vertical flame sheet with zero initial fuel velocity, u_{f0} at the origin which is illustrated in figure (5.5). By properly adjusting the horizontal velocity component on the fuel side far from the flame, we maintain the dividing streamline, the x -axis vertical and the flame zone nearly vertical. Even though the initial velocity of fuel is taken as zero, the fuel is allowed to accelerate with height as,

$$u_f = \left[2 \left(\frac{\rho_\infty - \rho_f}{\rho_f} \right) g x \right]^{1/2} \quad (5.39)$$

which is obtained from equation (5.7) by replacing z with x . (see figure (5.5)). Also setting $n = 0$ and $\theta = \frac{\pi}{2}$ for the plane vertical flame, equations (5.30) and (5.31) become,

$$\frac{d}{dx} \left[A(\Lambda) \rho_\infty u_0^2 \delta \right] + \rho_\infty u_0 \delta \frac{du_f}{dx} B(\Lambda) = g \rho_\infty \delta C \quad (5.40)$$

and

$$\frac{d}{dx} \left[D(\Lambda) \rho_\infty u_0 \delta \right] = \rho_\infty D_\infty \frac{E}{\delta} \quad (5.41)$$

Above equations have a similarity solution if $u_0 \sim x^{1/2}$ and $\delta \sim x^{1/4}$. Then, these equations reduce to a simple set of algebraic equations. Here, we define,

$$u_0 = K_u \sqrt{g x} \quad (5.42)$$

and

$$\delta = K_{\delta} x \left[\frac{D_{\infty}^2}{gx^3} \right]^{1/4} \quad (5.43)$$

with constants K_u and K_{δ} . Then equations (5.39) and (5.42) imply $\Lambda \equiv u_f/u_0 = \text{constant}$. Substituting these relations into equations (5.40) and (5.41) we get,

$$K_u = \left[\frac{4C}{5A+2\Lambda B} \right]^{1/2} \quad (5.44)$$

and

$$K_{\delta} = \left[\frac{4E}{3DK_u} \right]^{1/2} \quad (5.45)$$

Rewriting equation (5.39) in terms of the dimensionless quantities gives

$$\Lambda K_u = \sqrt{2(\chi_1 - 1)} \quad (5.46)$$

Substituting K_u from equation (5.44) into equation (5.46) and squaring both sides, gives a quadratic equation in Λ whose coefficients are known functions of χ_1 , χ_2 and χ_3 . Only the positive root is meaningful and it is used to evaluate K_u and K_{δ} . Entrainment is calculated from equation (5.38)

$$\dot{m}_E = \left[FK_u K_{\delta} + \frac{4G}{3K_{\delta}} \right] \rho_{\infty} D_{\infty}^{1/2} g^{1/4} x^{3/4} \quad (5.47)$$

per unit depth of the flame

5.7. Results for Vertical Plane Flame

In figures (5.6) through (5.10), the quantities of primary interest, entrainment, characteristic velocity and width scales, velocity ratio $\Lambda = u_f/u_0$, adiabatic flame enthalpy are plotted as functions of the density ratio of the oxidizer and fuel mixture for three values of the parameters χ_2 and χ_3 . The values $\chi_2 = 120$ and $\chi_3 = 6.96$ correspond to the case of pure methane as fuel and air as oxidizer with $Y_{o_\infty} = 0.232$ *. The other two curves show the variation in all quantities when values of χ_2 and χ_3 are both changed by a factor of 2.

It is clear from figures (5.6) to (5.10) that the quantities used to normalize the variables presented in these figures as functions of the density ratio contain the major scaling parameters for these variables. This nondimensionalization involved the introduction of a modified gravitational constant $g' = g \left(\frac{h_{fl}}{h_\infty} - 1 \right)$ in the normalizing entrainment, velocity and width scales. The adiabatic flame temperature was nondimensionalized by the heating value per mass of fuel (combustible component) as shown in figure (5.10). The change in the adiabatic flame temperature is then only due to the differences of enthalpies of fuel and oxidizer media.

The nondimensional entrainment parameter (Figure (5.6)) and characteristic width scale (Figure (5.8)) are not sensitive functions of the other two parameters, χ_2 and χ_3 . They have almost constant values of 1.85 and 2.13 respectively up to oxidizer densities six times that of the fuel mixture. The dimensionless characteristic velocity which is taken to be the velocity at $y=0$, normalized by the buoyant velocity $\sqrt{g'x}$ is shown in figure (5.7). The fuel mixture velocity far from the flame sheet, u_f normalized with the characteristic velocity u_0 is plotted

* The lower heating value for CH_4 is 47.5 MJ/kg.

in figure (5.9).

The divergence in entrainment and characteristic width scales for low heating values and large density ratios (e.g. $h_c Y_{f\infty}/h_\infty = 60$, $h_c Y_{o\infty}/h_\infty \varphi_{of} = 3.48$, $\rho_\infty/\rho_f > 5$) can be explained as follows: For large values of density ratio (when the fuel mixture density is much lower than that of the oxidizer), the velocity profile approaches that of a free shear layer with a small modification around the flame sheet due to flame buoyancy. The fuel mixture density far from the flame can be decreased by either increasing the temperature of the mixture or diluting the combustible fuel component with a lower density diluent. In the first case, if the fuel mixture temperature exceeds the flame temperature by a large amount, the left hand side term in equation (5.23) can become zero resulting in a singularity in equation (5.45). This is an extreme case of a fuel mixture at a higher temperature than the flame temperature. In the second case, the decrease in the mass fraction of fuel, $Y_{f\infty}$ forces the flame front to move towards the fuel mixture. Thus, the left hand side of equation (5.23) does not vanish since the contribution from the second integral becomes smaller compared with the first term. Then, the variables χ_1 and χ_2 are not independent because of the variation in $Y_{f\infty}$ due to dilution.

Some numerical values of the quantities discussed above are shown in Table 5.1 for methane-air and hydrogen-air flames. In the examples given here, the fuel was diluted with nitrogen. The effect of dilution on entrainment is small for both methane and hydrogen flames. The dilution has an effect on the transformed boundary layer thickness for hydrogen flame but not for the methane flame. The characteristic velocities are not very different for methane flame as this velocity represents the maximum in the velocity profile. Pure hydrogen air flame has a shear layer-like velocity profile due to very low density of H_2 . The values of the ratio of expanded, physical boundary layer thickness to

Table 5.1. Effect of Dilution on Entrainment

	<i>CH₄ & Air</i>		<i>H₂ & Air</i>	
	<i>Y_{f∞} = 1.00</i>	<i>Y_{f∞}[†] = 0.50</i>	<i>Y_{f∞} = 1.00</i>	<i>Y_{f∞}[†] = 0.50</i>
<i>χ₁</i>	1.81	1.31	14.42	1.92
<i>χ₂</i>	120	60	120	60
<i>χ₃</i>	6.96	6.96	3.48	3.48
<i>m_E, kg / m / s</i>	$0.0243x^{3/4}$	$0.0220x^{3/4}$	$0.0163x^{3/4}$	$0.0207x^{3/4}$
<i>u₀, m / s</i>	$8.330x^{1/2}$	$7.500x^{1/2}$	$12.238x^{1/2}$	$6.259x^{1/2}$
<i>δ, m</i>	$0.0029x^{1/4}$	$0.0029x^{1/4}$	$0.0049x^{1/4}$	$0.0034x^{1/4}$
<i>δ_e[‡]/δ</i>	3.383	3.019	11.866	2.580

All quantities calculated with $D_{\infty} = 1.5 \cdot 10^{-5} \text{ m}^2/\text{s}$ and $\rho_{\infty} = 1.17 \text{ kg}/\text{m}^3$, *x* in meters.

(†) Dilution with *N₂*

(‡) δ_e/δ is the ratio of expanded boundary layer thickness, δ_e to the transformed boundary layer thickness, δ , given by the Howarth transformation. The expression is,

$$\frac{\delta_e}{\delta} = \frac{1}{2}(\chi_1 + \chi_3 + 1) + \frac{1}{2}(\chi_1 - \chi_3 - 1) \left(\text{erf}(1) + \frac{e^{-1} - 1}{\sqrt{\pi}} \right)$$

the reduced boundary layer thickness are also listed in Table 5.1.

5.8. Nonsimilar Axisymmetric Case

This represents the more realistic case of a diffusion flame stabilized on an axisymmetric burner where fuel is introduced with a finite initial velocity as shown in figure (5.1a). A simple similarity solution cannot be obtained because of the complexity of the flow. However, a numerical solution can be obtained by integration of the differential equations for flame radius, momentum and energy. These equations for the axisymmetric problem ($n=1$, $\theta = \theta(x)$) are,

$$\frac{dr}{dx} = -\cos \theta = -(1 - \sin^2 \theta)^{1/2} \quad (5.48)$$

where $\sin \theta$ is given by equation (5.13),

$$\frac{d}{dx} \left[A(\Lambda) r \rho_\infty u_0^2 \delta \right] + B(\Lambda) r \rho_\infty u_0 \delta \frac{du_f}{dx} = r g \sin \theta \rho_\infty \delta C \quad (5.49)$$

and

$$\frac{d}{dx} \left[D(\Lambda) r \rho_\infty u_0 \delta \right] = r \rho_\infty E \frac{D_\infty}{\delta} \quad (5.50)$$

Here, du_f/dx is calculated from equation (5.7) as

$$\frac{du_f}{dx} = \frac{(\rho_\infty - \rho_f) g \sin \theta}{\rho_f u_f} \quad (5.51)$$

For numerical integration purposes, it is convenient to introduce two variables, Υ_1 and Υ_2 defined by,

$$\Upsilon_1 \equiv A u_0^2 \delta r \quad \text{and} \quad \Upsilon_2 \equiv (D u_0 \delta r)^2 \quad (5.52)$$

Expressions for u_0 and δ are then,

$$u_0 = \frac{D \Upsilon_1}{A \Upsilon_2^{1/2}} \quad \text{and} \quad \delta = \frac{A \Upsilon_2}{D^2 \Upsilon_1 r} \quad (5.53)$$

Equations (5.49) and (5.50) become,

$$\frac{d\Upsilon_1}{dx} = \left[g \sin \theta C - B \frac{du_f}{dx} u_0 \right] \delta r \quad (5.54)$$

$$\frac{d\Upsilon_2}{dx} = 2D_\infty E D u_0 r^2 \quad (5.55)$$

The numerical integration involves computation of the value of Λ at each successive step since it is no longer constant as it was in the similar plane case. The expression for Λ is obtained from the definition of Λ ,

$$\Lambda \equiv \frac{u_f}{u_0} = u_f \frac{A \Upsilon_2^{1/2}}{D \Upsilon_1} \quad (5.56)$$

where,

$$A = a_2 \Lambda^2 + a_1 \Lambda + a_0$$

$$D = d_1 \Lambda + d_0$$

are obtained from expressions associated with equations (5.30) and (5.31). After some manipulation, these equations can be written as,

$$\left[a_2 - \frac{\Upsilon_1 d_1}{\Upsilon_2^{1/2} u_f} \right] \Lambda^2 + \left[a_1 - \frac{\Upsilon_1 d_0}{\Upsilon_2^{1/2} u_f} \right] \Lambda + a_0 = 0 \quad (5.57)$$

The equation for Λ is a quadratic equation with variable coefficients. Only the positive root is meaningful and is used to evaluate the other quantities. Ordinary differential equations (5.48), (5.54) and (5.55) can numerically be

integrated by marching in the x direction provided that initial conditions are specified. The initial condition for equation (5.48) is obviously $\tau(x) = \tau_0$, but the origin is a singular point for equations (5.54) and (5.55) since $\Upsilon_1(x=0) = 0$ and $\Upsilon_2(x=0) = 0$ from $\delta(x=0) = 0$.

In the region very close to the origin, the effect of buoyancy on the velocity profile is negligible so that this region resembles that of a shear layer as shown in Figure (5.1b). If, for small x , we have $u_0 \sim \text{const.}$, $\delta \sim x^{1/2}$, $\tau \sim \text{const.}$, then equation (5.49) leads to the conclusion that $A \sim x$ in order to balance the terms on both sides of the equation. So at $x=0$, we must have $A=0$, and this gives us the initial value of Λ , Λ_0 . The computed value of Λ_0 is 1.6297. If we let $A \approx A_1 x$ and $\delta \approx \delta_1 x^{1/2}$ as $x \rightarrow 0$, and denote $B_0 = B(\Lambda_0)$, $C_0 = C$, $D_0 = D(\Lambda_0)$, $E_0 = E$, A_1 and δ_1 can be obtained from equations (5.54) and (5.55) as,

$$A_1 = \frac{2 \Lambda_0^2 g}{3 u_{f0}^2} \left[C_0 - \frac{\rho_\infty - \rho_f}{\rho_f} \frac{B_0}{\Lambda_0} \right] \quad (5.58)$$

$$\delta_1 = \left[\frac{2 D_\infty E_0 \Lambda_0}{D_0 u_{f0}} \right]^{1/2} \quad (5.59)$$

The integration of differential equations (5.54) and (5.55) is started by computing u_0 and δ at a very small value of x using equations (5.58) and (5.59). The sensitivity of solutions to the smallness of this value of x was investigated for methane-air diffusion flame computations. The values experimented ranged from 10^{-10} to 10^{-8} m. It was observed that the initial transient disappeared before x (streamwise coordinate) exceeded 10 % of the initial radius of the burner, τ_0 . The integration scheme used was a fourth order Runge-Kutta algorithm with Adams-Moulton predictor-corrector. The initial step size was taken to be 10^{-8} m in x which after 500 integration steps was increased to 10^{-6} m. This

procedure was necessary to handle the calculations when very large initial curvatures of the flame occurred. This typically happens when r_0 is large and the volume flux \dot{V} is small. This condition also corresponds to the very low values of Froude number where $Fr \equiv \frac{u_{f0}^2}{2gr_0}$.

It is also possible to check the numerical results against the asymptotic values of the quantities since we expect that the effects of the initial fuel velocity will disappear at large distances from burner surface. In the limit as $x \rightarrow +\infty$

$$\left. \begin{aligned} \sin \theta &\rightarrow 1 \\ \frac{r}{r_0} &\rightarrow \left[2 \left(\frac{\rho_\infty - \rho_f}{\rho_f} \right) \frac{gx}{u_{f0}^2} \right]^{-1/4} \\ u_f &\rightarrow \left[2 \left(\frac{\rho_\infty - \rho_f}{\rho_f} \right) gx \right]^{1/2} \end{aligned} \right\} \quad (5.60)$$

Under these conditions, equations (5.49) and (5.50) have a similarity solution if $u_c \sim x^{1/2}$ and $\delta \sim x^{1/4}$. Using the same definitions for K_u and K_δ as in equations (5.42) and (5.43), we get equations for Λ_∞ , K_u and K_δ . These are,

$$\left[a_2 + \frac{1}{2}b_1 - \frac{C_0}{2(\chi_1 - 1)} \right] \Lambda_\infty^2 + \left[a_1 + \frac{1}{2}b_0 \right] \Lambda_\infty + a_0 = 0 \quad (5.61)$$

$$K_u = \frac{\sqrt{2(\chi_1 - 1)}}{\Lambda_\infty} \quad (5.62)$$

and

$$K_6 = \left(\frac{2}{\chi_1 - 1} \right)^{1/4} \left[\frac{E_0 \Lambda_\infty}{d_0 + d_1 \Lambda_\infty} \right]^{1/2} \quad (5.63)$$

where

$$A = a_2 \Lambda^2 + a_1 \Lambda + a_0$$

$$B = b_1 \Lambda + b_0$$

$$D = d_1 \Lambda + d_0$$

$$E = E_0$$

The numerical values of the asymptotic quantities can be obtained from equations (5.61) through (5.63) when the values of combustion parameters χ_1 , χ_2 and χ_3 are given. These asymptotic values were then used to check the numerical results.

5.9. Results for Axisymmetric Flame

The numerical computations were carried out for three burner sizes of 0.10, 0.19 and 0.50 m. in diameter, and three heat release rates of 40, 80, 200 kW for methane-air diffusion flames. In these calculations, the fuel temperature was taken to be 600°K due to radiative heating of the fuel by the flame. The density ratio of ambient air to hot gaseous fuel was 3.62 for methane and air, ambient air density was 1.17 kg/m³. The binary diffusion coefficient of all species was

taken to be $1.5 \cdot 10^{-5} \text{ m}^2/\text{s}$ at 300°K . The values of the combustion parameters χ_2 and χ_3 were 120 and 6.96 respectively.

Figure (5.11) shows the shape of the fuel-air interface, where diffusion flame lies, for a 40 kW fire on 0.10, 0.19 and 0.50 m. dia. burners. Since the fuel is assumed to be introduced with a uniform velocity at the burner top, the interface starts vertically and then contracts due to the acceleration of the light gaseous fuel caused by buoyancy. The contraction is very sharp for large burners and low heat inputs (e.g. 40 KW fire on 0.50 m. dia. burner). The validity of the computations are restricted by two limits. Failure of the solution may occur close to the burner surface, when the contraction of the interface is so sharp that the thickness of the boundary layer superimposed on this interface exceeds the vertical distance from the burner surface. The other limiting region is far above the burner where failure will occur when the boundary layer thickness, δ grows large compared to the local radius of the flame from the z -axis, r .

Figures (5.12) and (5.13) show the characteristic velocity and boundary layer thickness in dimensionless form for a 40 kW fire on burners of 0.10, 0.19 and 0.50 m. diameter. The velocity was nondimensionalized by the buoyant velocity $\sqrt{g'z}$ where $g' = (\frac{h_{fl}}{h_\infty} - 1)g$ is the modified gravitational constant. Similarly, the boundary layer thickness was normalized by the same group used in the vertical plane flame using the streamwise coordinate x . The asymptotic values of nondimensional velocity and thickness scales are 1.22 and 2.44 respectively. Figure (5.14) is a plot of the velocity ratio u_f/u_0 as a function of z/r_0 for three different burner diameters. The asymptotic value computed for u_f/u_0 is 0.722 . Except very close to the burner, all of these parameters are never very different from their asymptotic values and are within 10 % of these values at about four

radii above the burner surface. In figure (5.15), integrated ambient air mass flux entrained by the flame is shown for a 40 kW fire on the three burners. The mass consumption rate of the fuel scales in the same way as the ambient air entrainment and about 95 % of the total entrained ambient air is consumed in chemical reaction at the flame front. Ambient air entrainment when normalized by that of an vertical plane flame surrounding the burner perimeter is shown in Figure (5.16). Entrainment of the axisymmetric flame is less than that of the vertical plane flame of constant radius r_0 due to the decrease in flame area caused by the contraction of the flame surface.

Similar quantities are shown for 40, 80 and 200 kW fires on a 0.19 m. diameter burner in figures (5.17) through (5.20). We see again that the quantities such as characteristic velocity, boundary layer thickness and velocity ratio u_f/u_c are never very different from their asymptotic values and that the normalized parameters are almost independent of heat release rates. The order in which these quantities approach their asymptotic values is determined by the growth of these quantities in the region close to the burner surface.

Comparison of calculated ambient air entrainment for methane-air diffusion flames with the plume mass flux measurements of Chapter 4 indicates that the calculated entrainment rates are much lower than the experimental values. The computations do not show the diameter dependence of entrainment as obtained from ad hoc model and experiments. The dependence of entrainment on the height above the burner is also different from the experiments (e.g. for 0.50 m. diameter burner).

These results indicate that the simple model developed here does not give a good estimate of the entrainment. A few of the reasons for this discrepancy are the following: First and most important, this model does not account for the vortical structures produced near the burner surface. These vortices prevent

the contraction of the flame surface as calculated in section (5.3), thus making the calculations less representative of the actual flames. Second, the comparison with the experiments bears the inconsistency that in the experiments we measure the entrainment into the ceiling layer rather than the entrainment of the plume itself (see Figure (2.1)). Third, the wrinkling of the flame surface observed in the experiments will increase the entrainment simply due to the increase in the surface area of the flame.

References

- [5.1] G. C. FLEMING and F. E. MARBLE, Personal Communication
- [5.2] G. C. FLEMING, Structure and Stability of Buoyant Diffusion Flames, *Ph.D. Thesis, California Institute of Technology*, (1982)

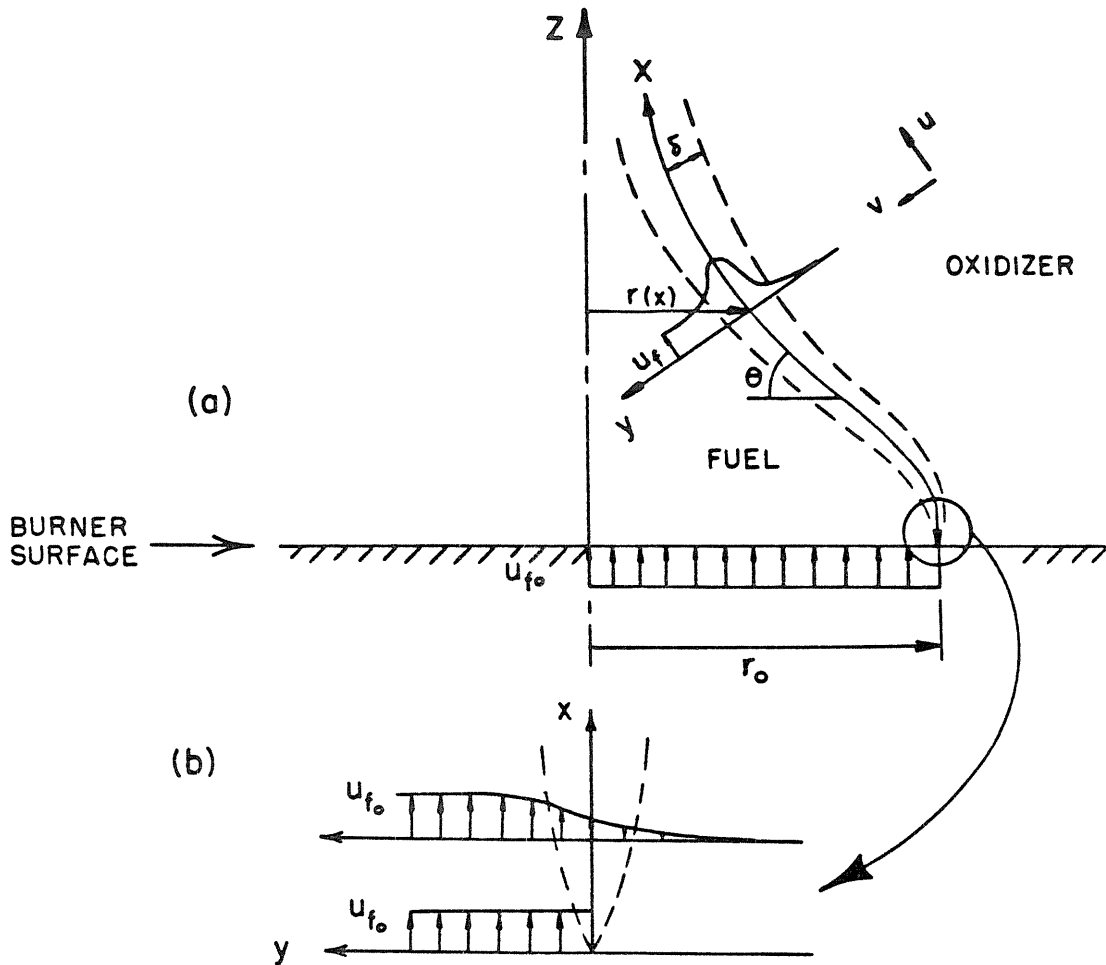


Figure (5.1) The sketch of the problem showing the potential fuel core and the flame sheet at the fuel oxidizer interface as well as the coordinate systems and the blow up of region close to the burner lip

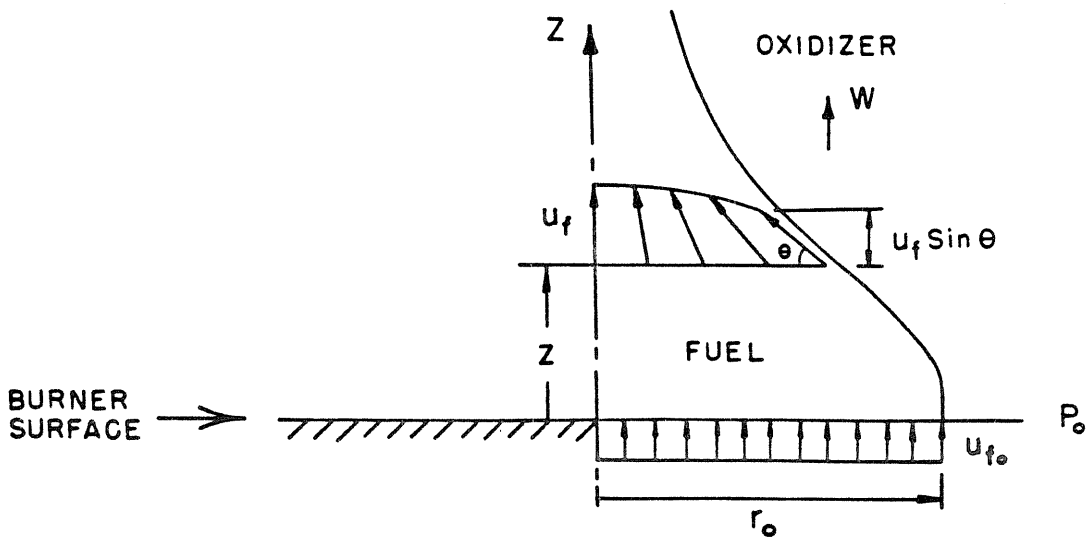


Figure (5.2) Fuel flow in the potential core within the flame surface

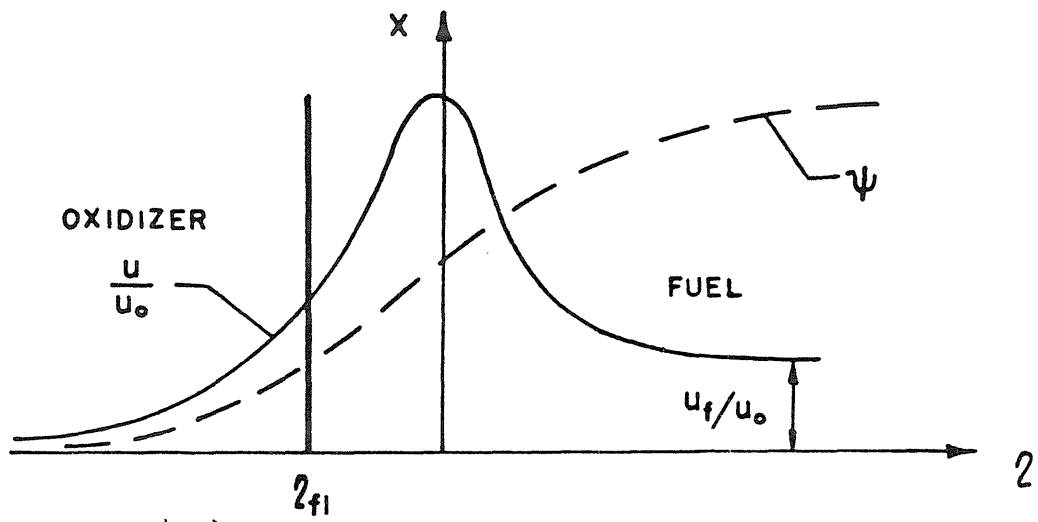


Figure (5.3) Velocity and Schwab Zeldovich variable profiles

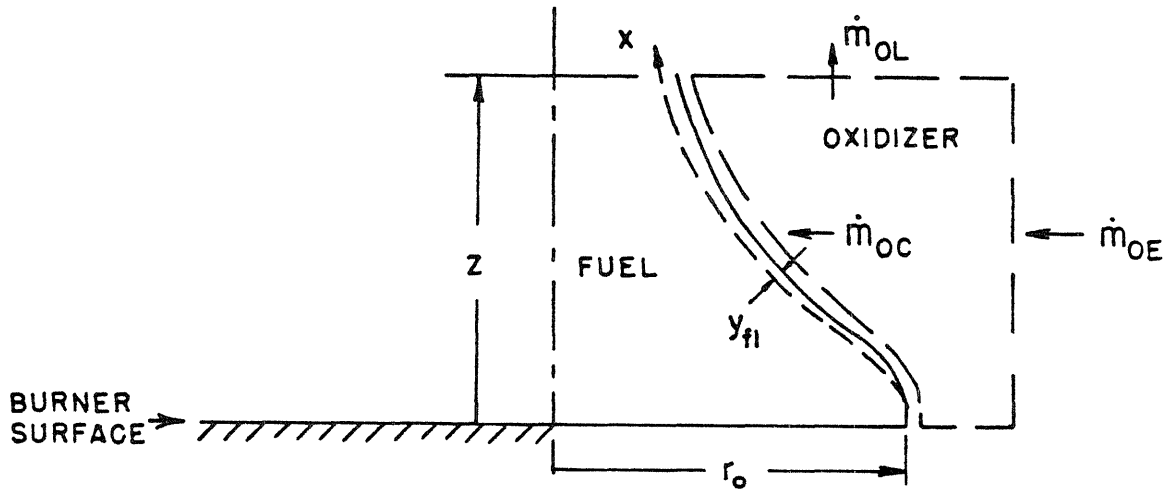


Figure (5.4) Entrainment and consumption of oxidizer around the flame region

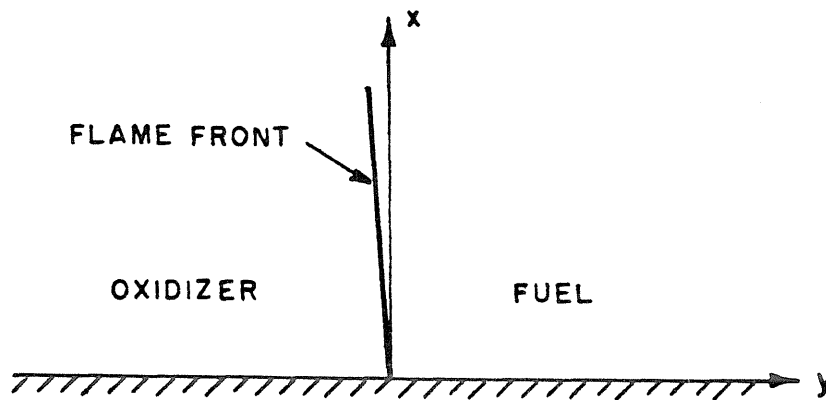


Figure (5.5) Coordinate system for the plane flame sheet

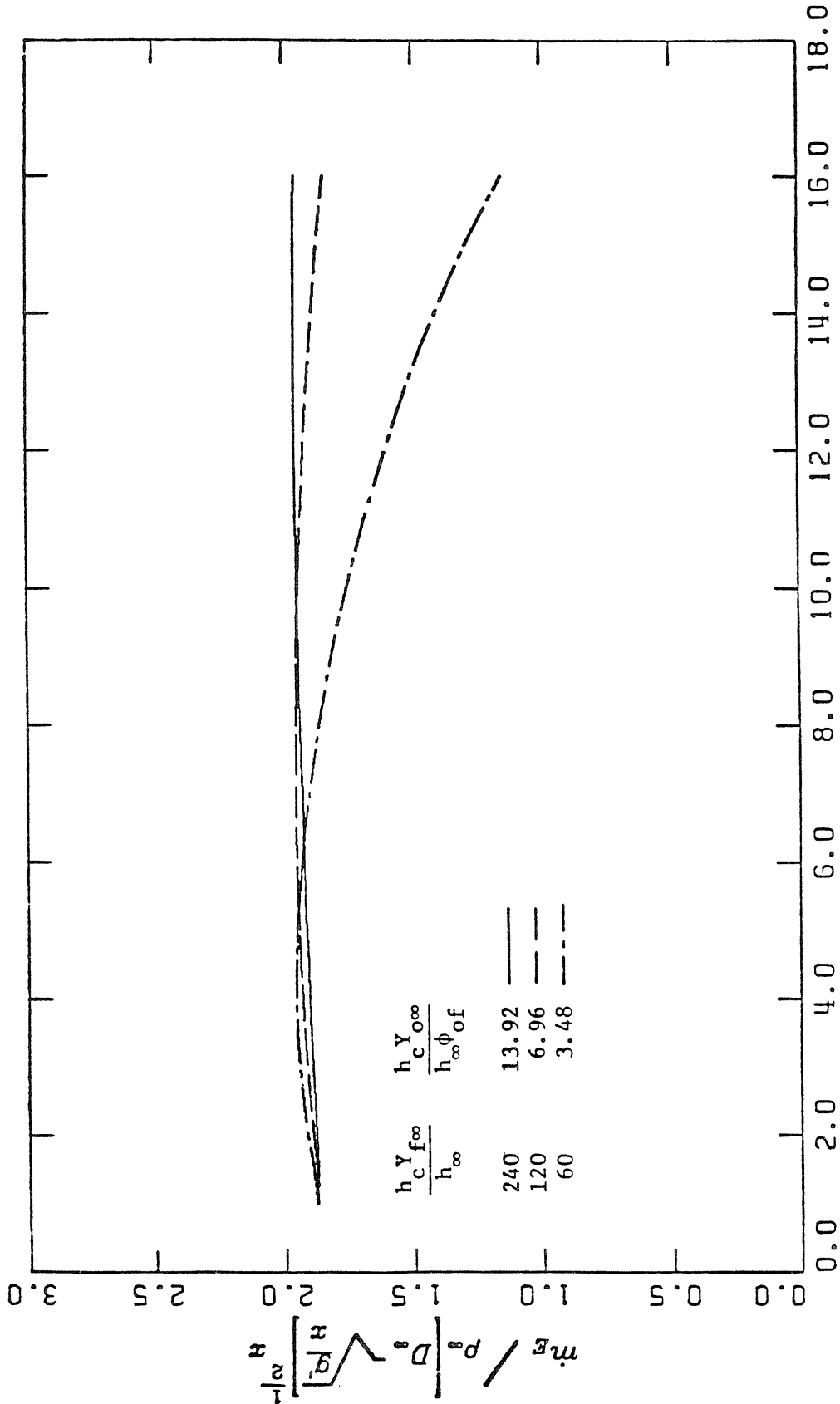


Figure (5.6) Dimensionless entrainment of a vertical plane diffusion flame as a function of density ratio of oxidizer and fuel for three values of X_2 and X_3

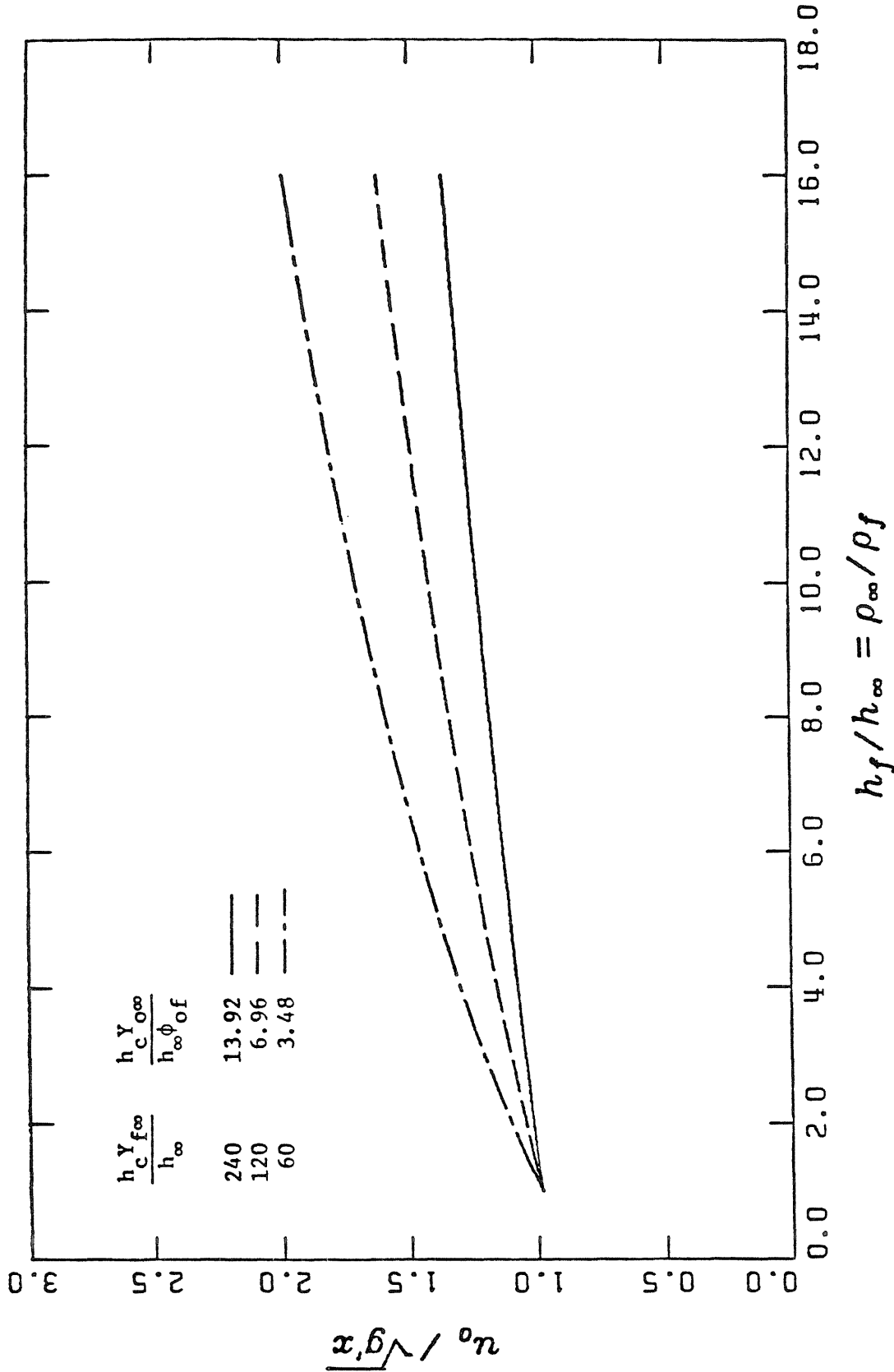


Figure (5.7) Dimensionless characteristic velocity as a function of density ratio of oxidizer and fuel for three values of X_2 and X_3

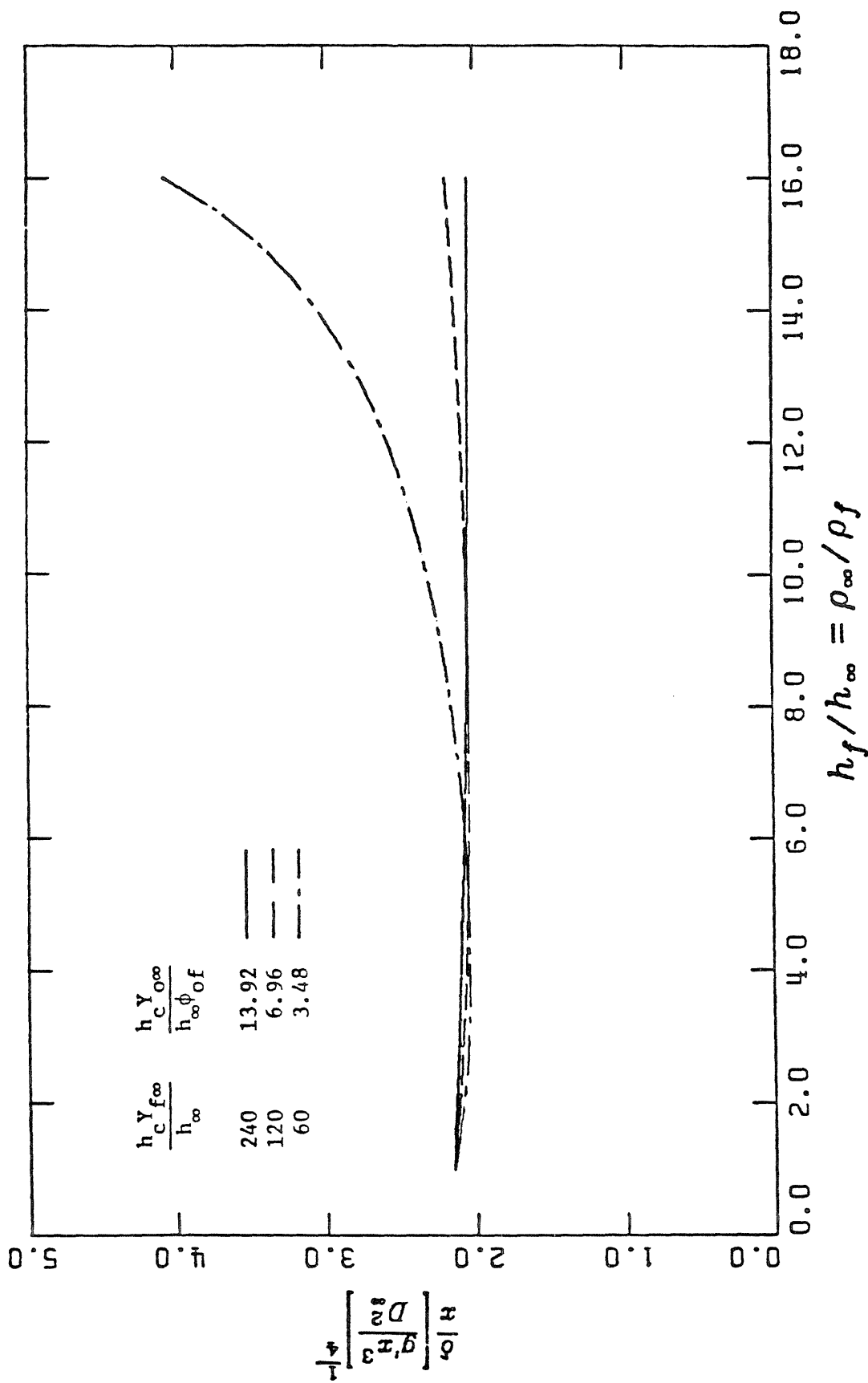


Figure (5.8) Dimensionless boundary layer thickness as a function of density ratio of oxidizer and fuel for three values of X_2 and X_3

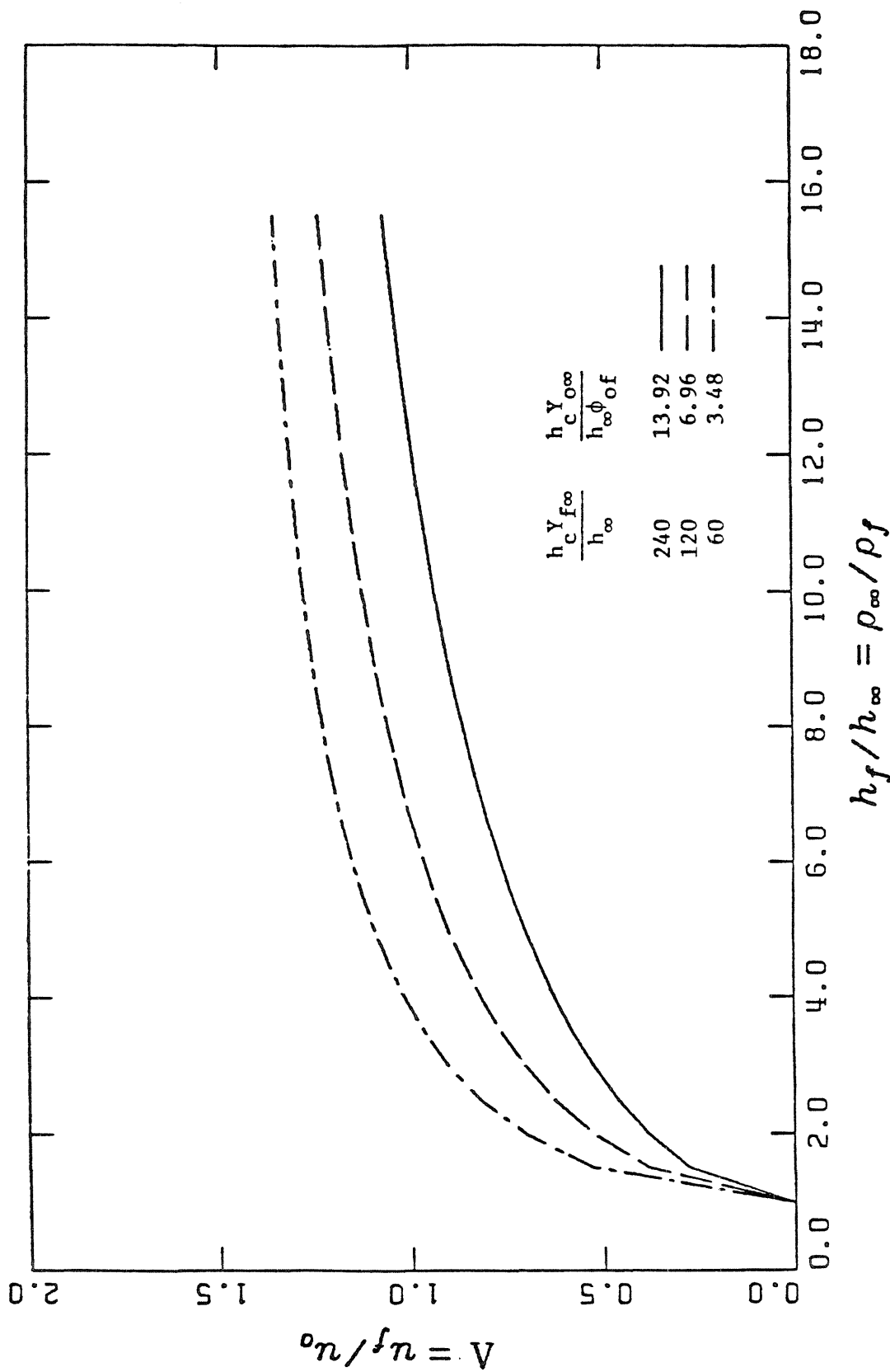


Figure (5.9) The ratio of fuel velocity outside the boundary layer to characteristic velocity in the boundary layer as a function of density ratio of oxidizer and fuel for three values of X_2 and X_3

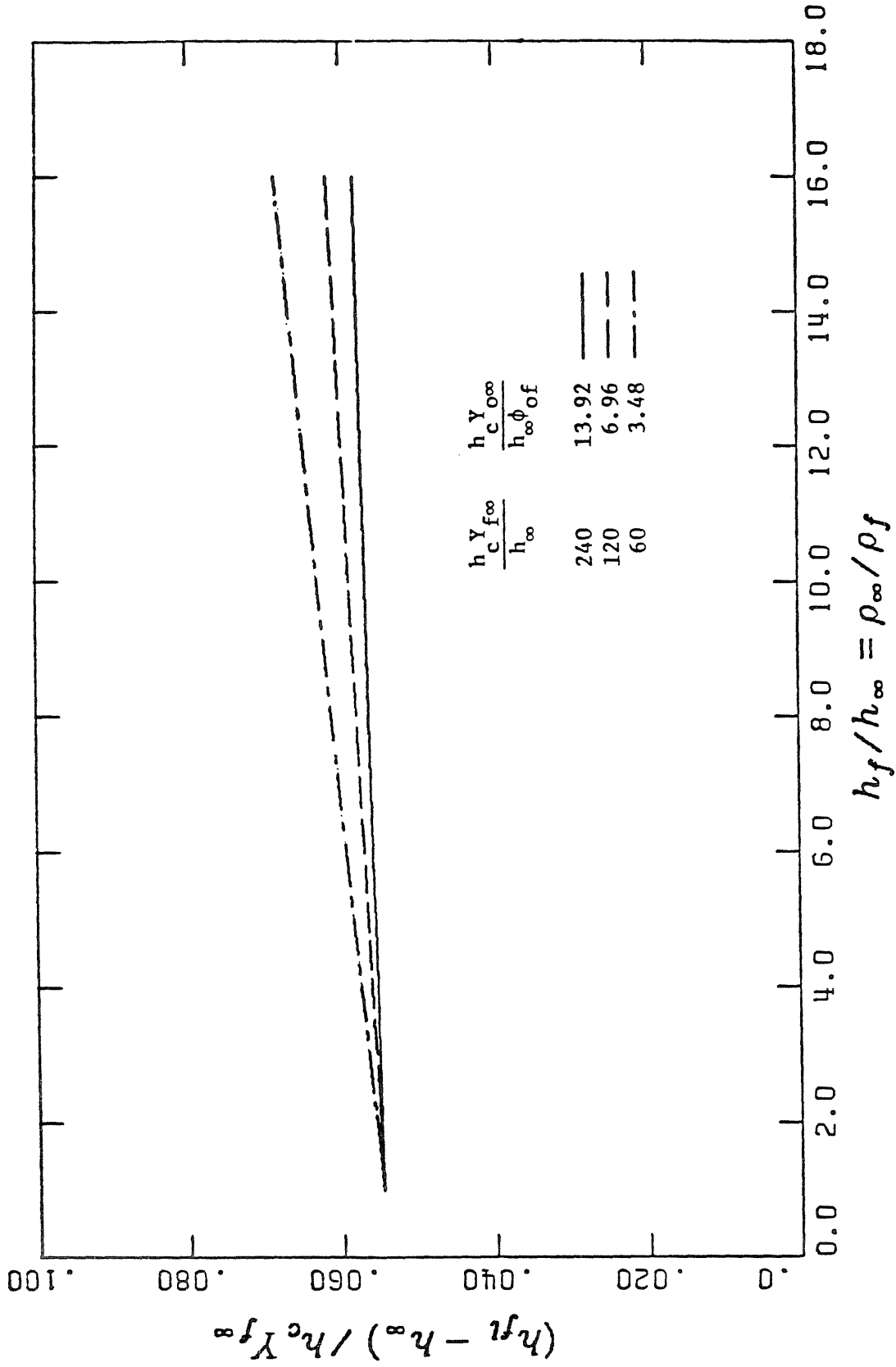


Figure (5.10) Adiabatic flame temperature normalized by heating value per mass of combustible fuel as a function of density ratio of oxidizer and fuel for three values of χ_2 and χ_3

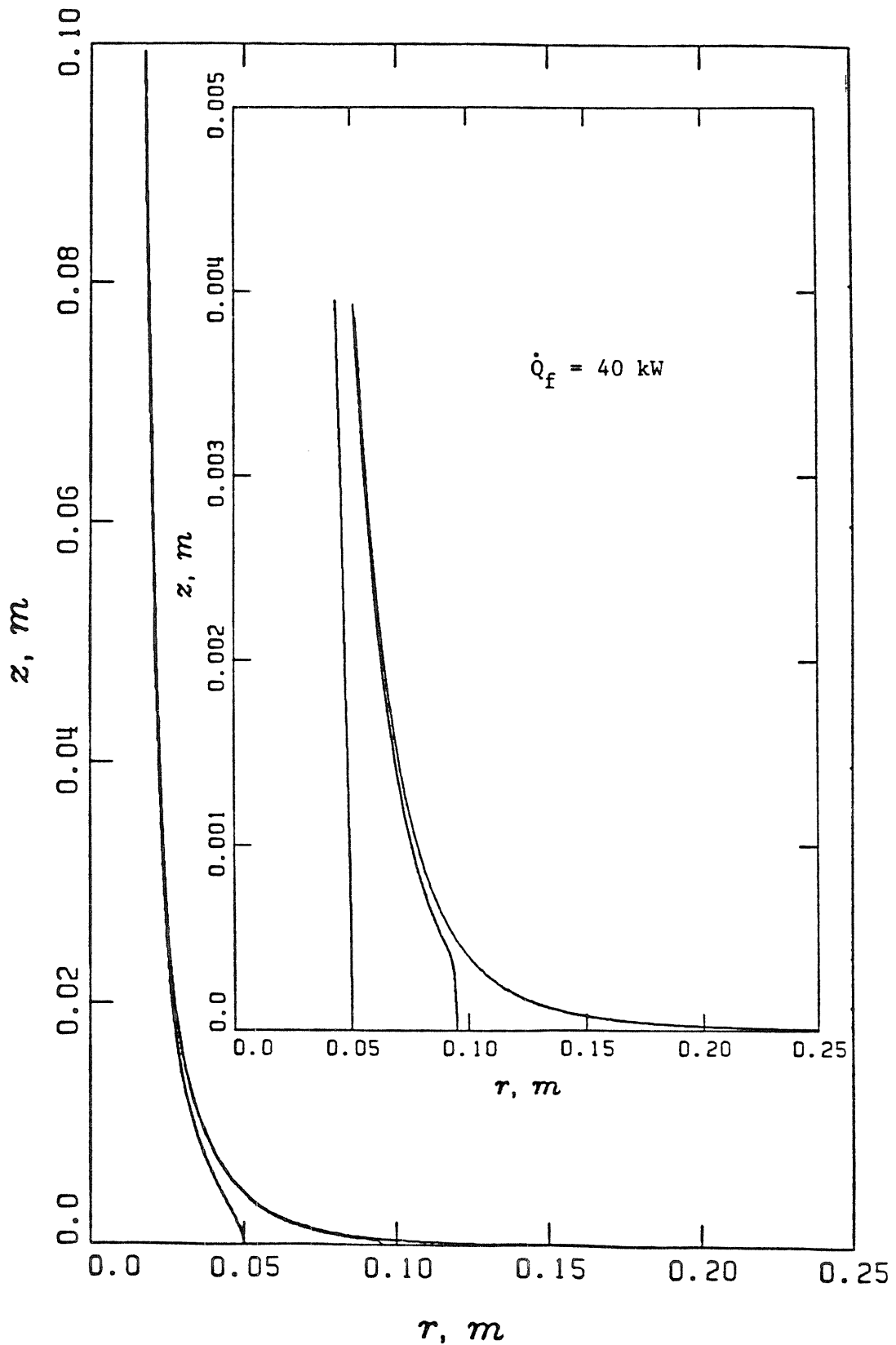


Figure (5.11) The shape of the fuel-air interface, where diffusion flame lies, for a 40 kW fire on three different size burners of $r_0 = 0.050, 0.095$ and 0.250 m.

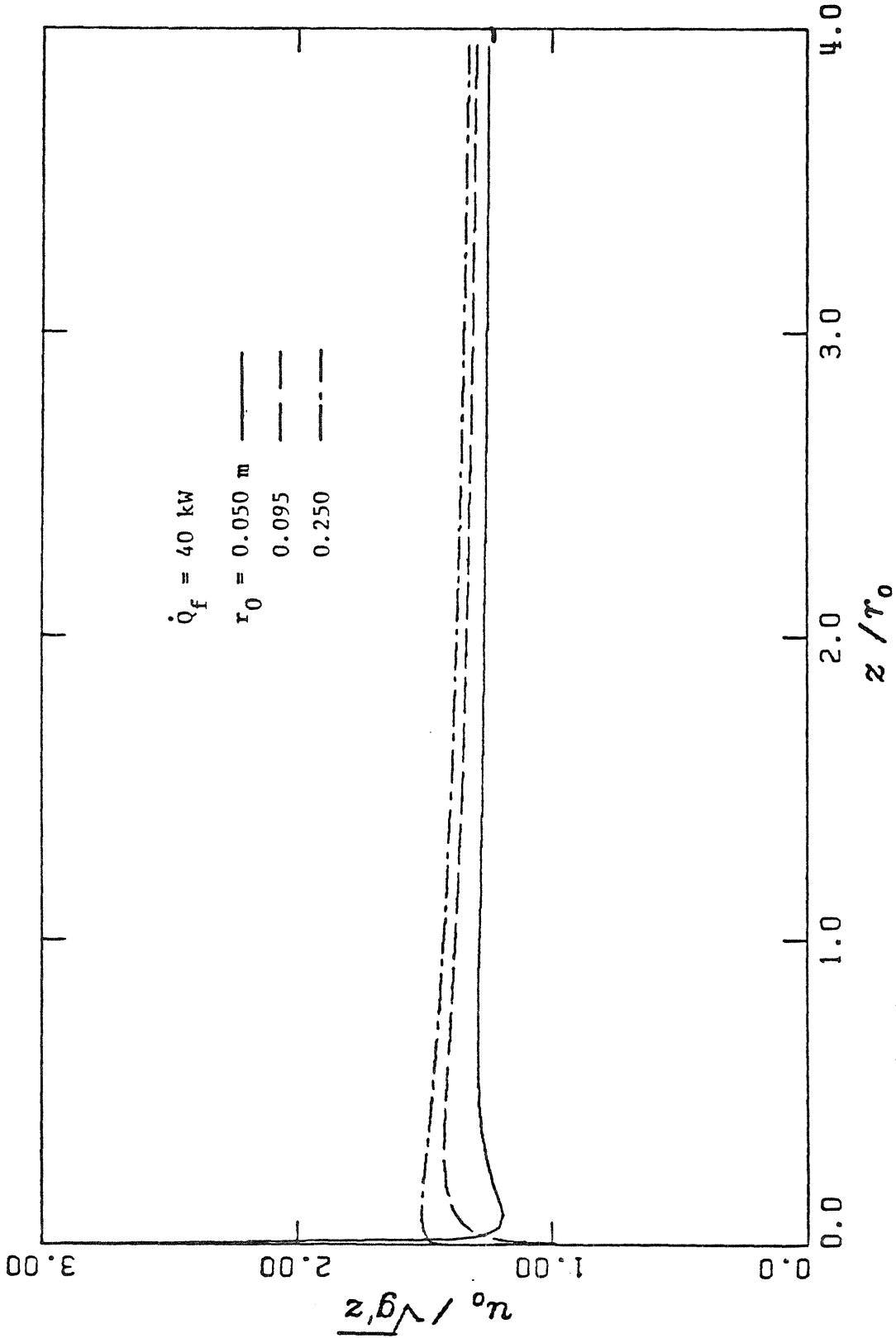


Figure (5.12) Characteristic velocity in the boundary layer normalized by the buoyant velocity, $\sqrt{\beta} z / \sqrt{g} z$ as a function of the distance above the burner surface normalized by the burner radius for a 40 kW fire and $r_0 = 0.005, 0.095$ and 0.250 m .

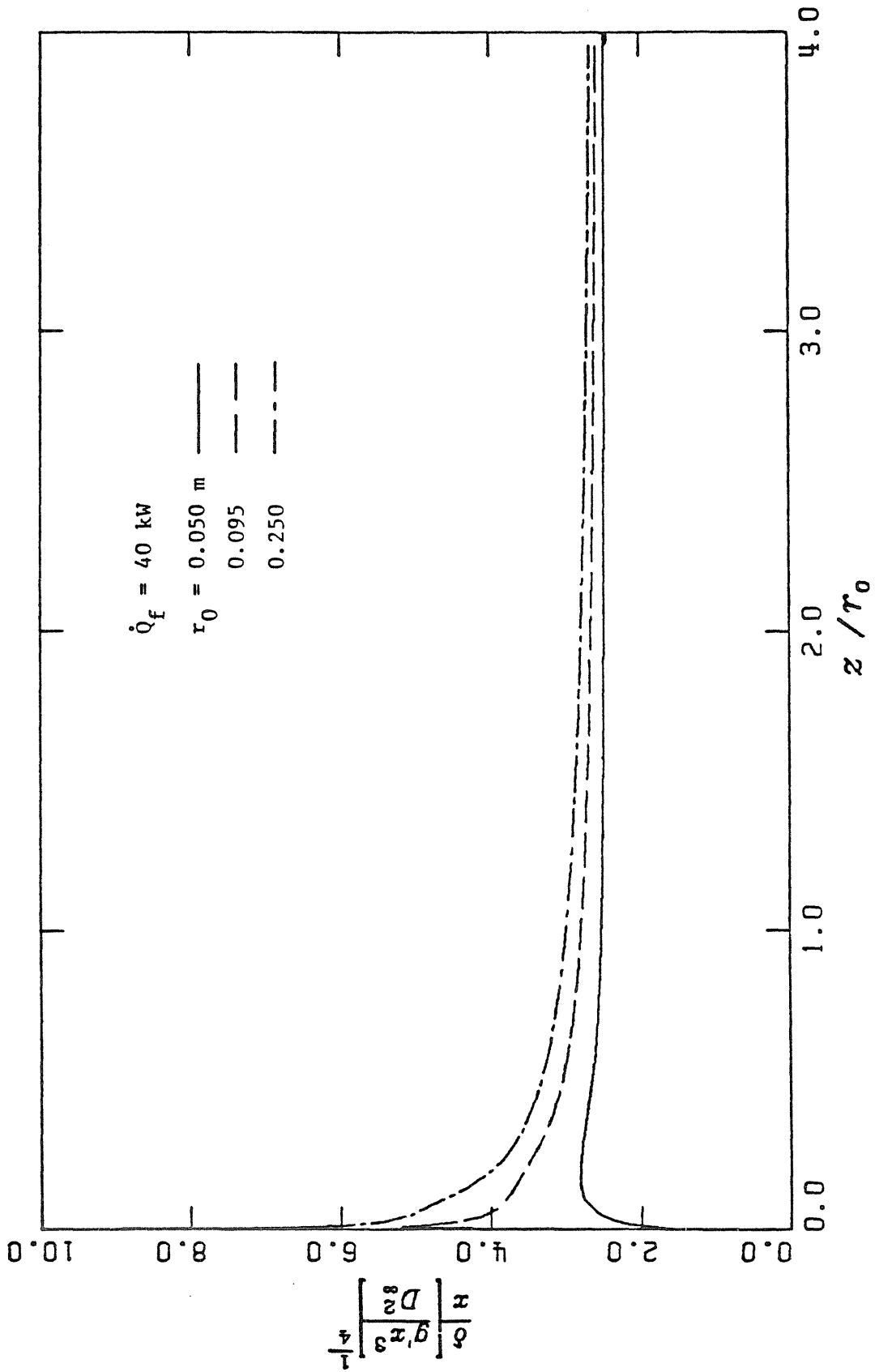


Figure (5.13) Dimensionless boundary layer thickness as a function of the distance above the burner surface normalized by the burner radius for a 40 kW fire and $r_0 = 0.005, 0.095$ and 0.250 m .

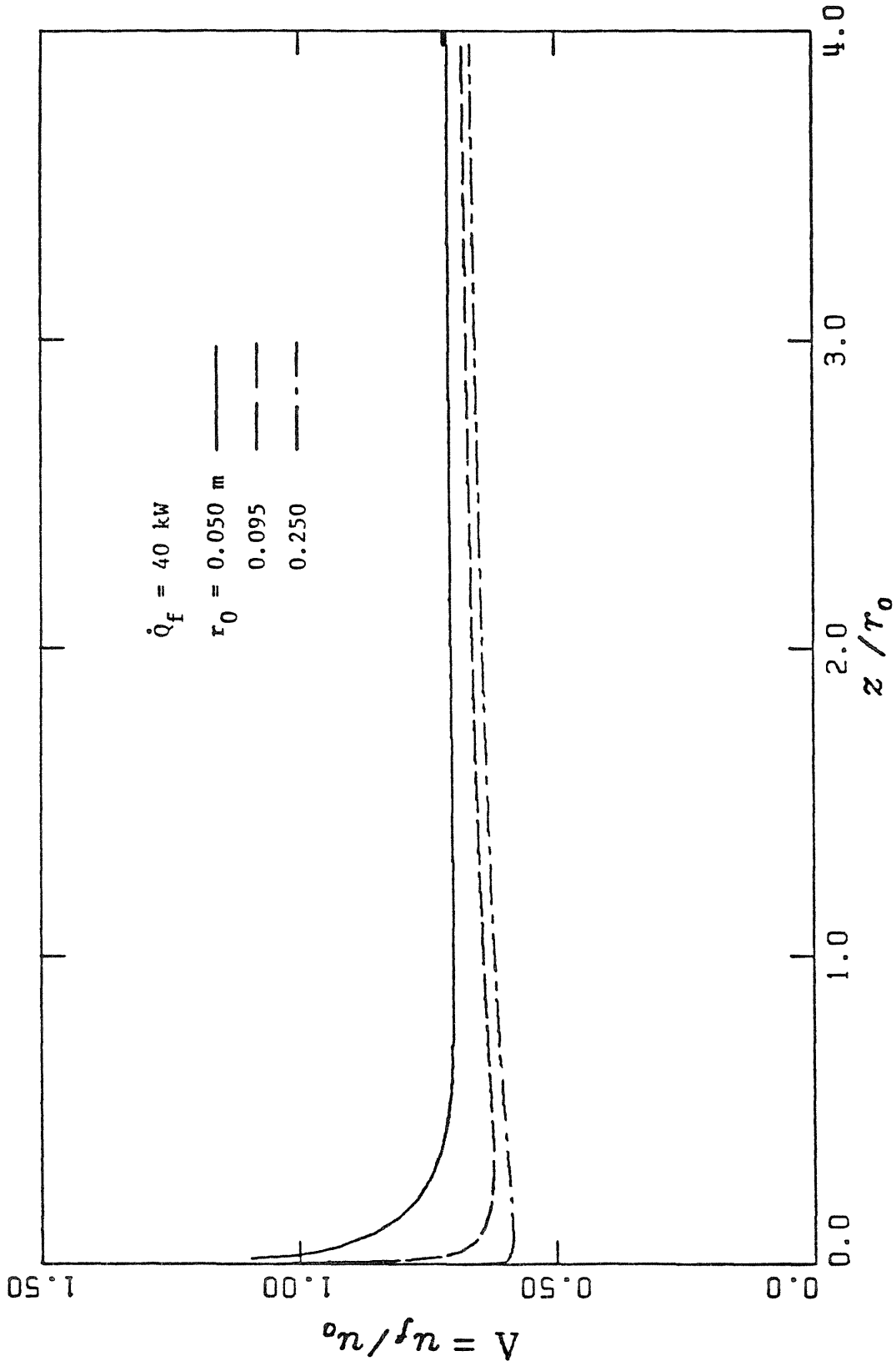


Figure (5.14) The ratio of fuel velocity outside the boundary layer to characteristic velocity in the boundary layer as a function of the distance above the burner surface normalized by burner radius for a 40 kW fire and $r_0 = 0.005, 0.095$ and 0.250 m .

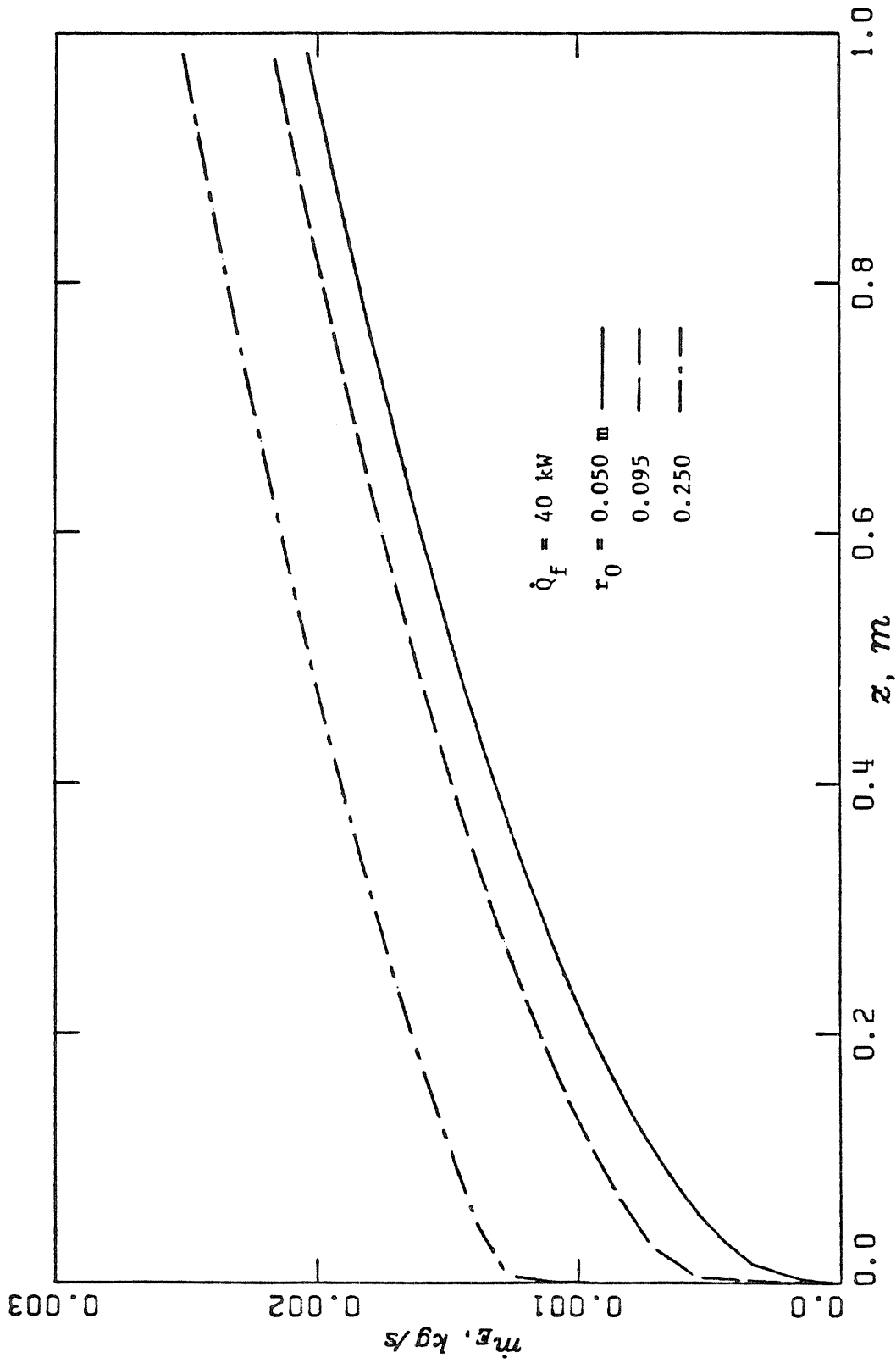


Figure (5.15) Ambient air entrained as a function of height above the burner surface for a 40 kW fire on burners with $r_0 = 0.005, 0.095$ and 0.250 m.

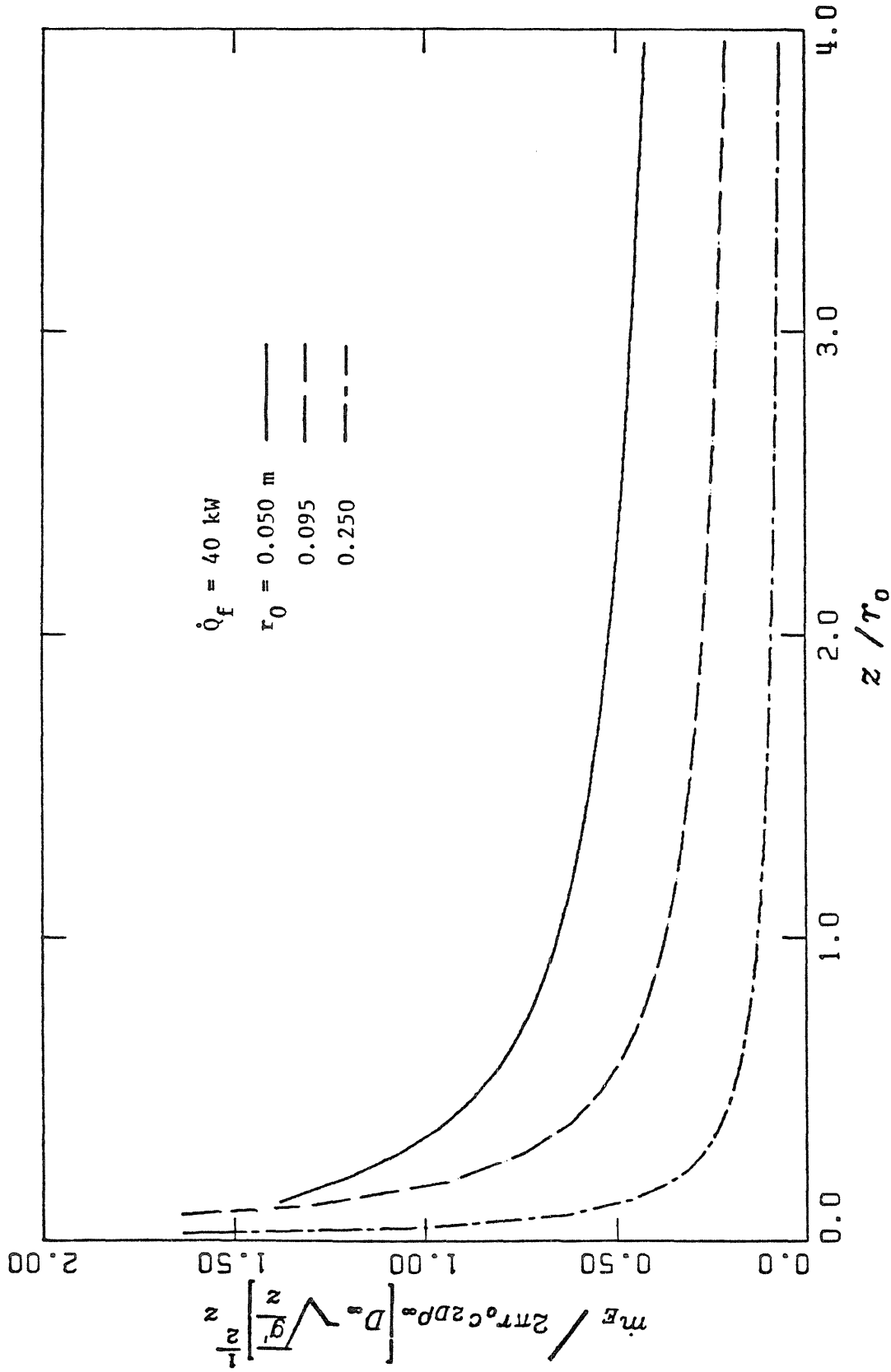


Figure (5.16) Entrainment normalized by that of a plane diffusion flame surrounding burner perimeter as a function of z/r_0 for a 40 kW fire on burners with $r_0 = 0.005, 0.095$ and 0.250 m .

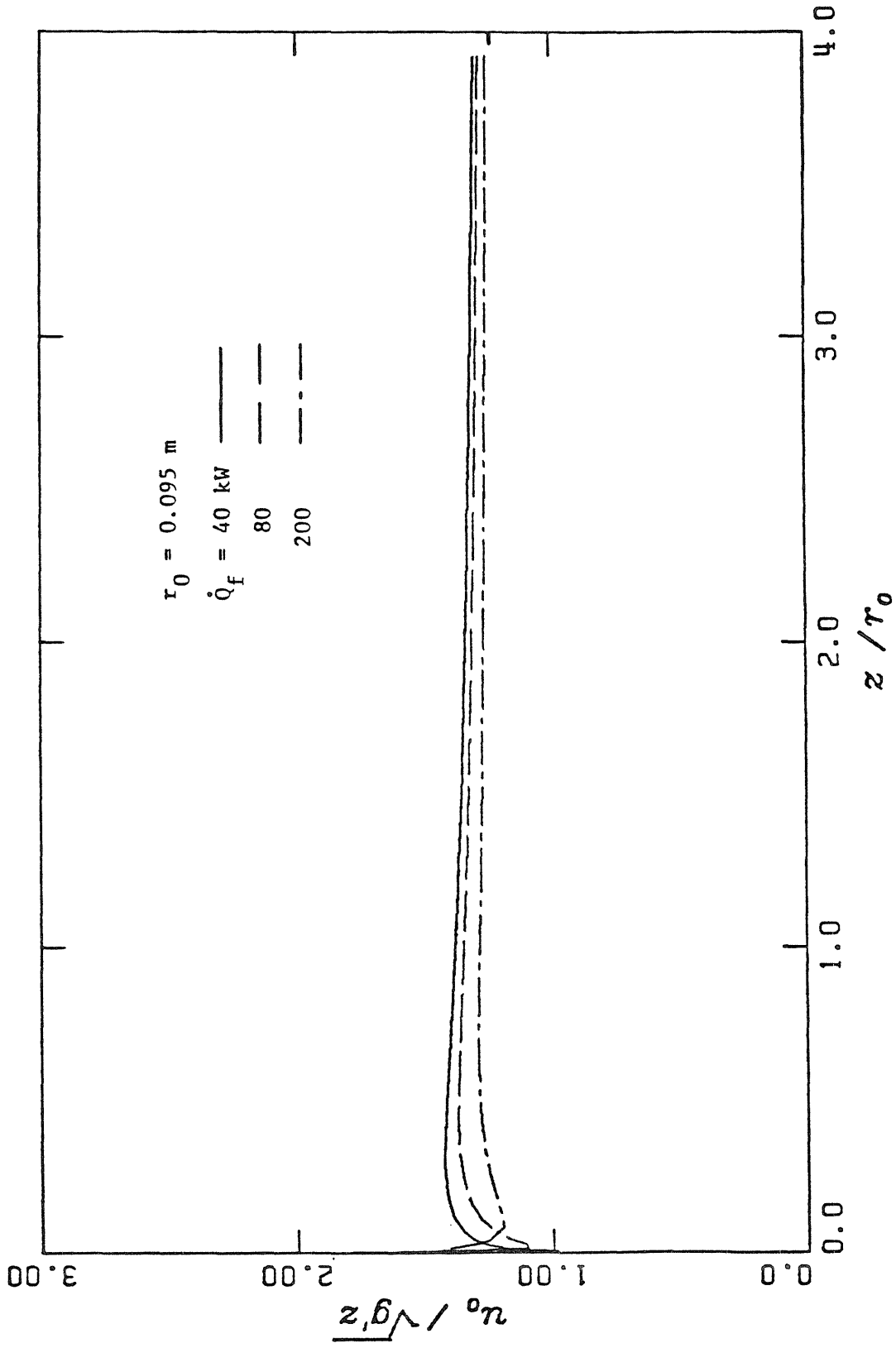


Figure (5.17) Characteristic velocity in the boundary layer normalized by the buoyant velocity, $\sqrt{(h_f/h_\infty - 1)gz}$ as a function of the distance above the burner surface normalized by the burner radius for $r_0 = 0.095 \text{ m}$. and heat release rates of 40, 80, 200 kW.

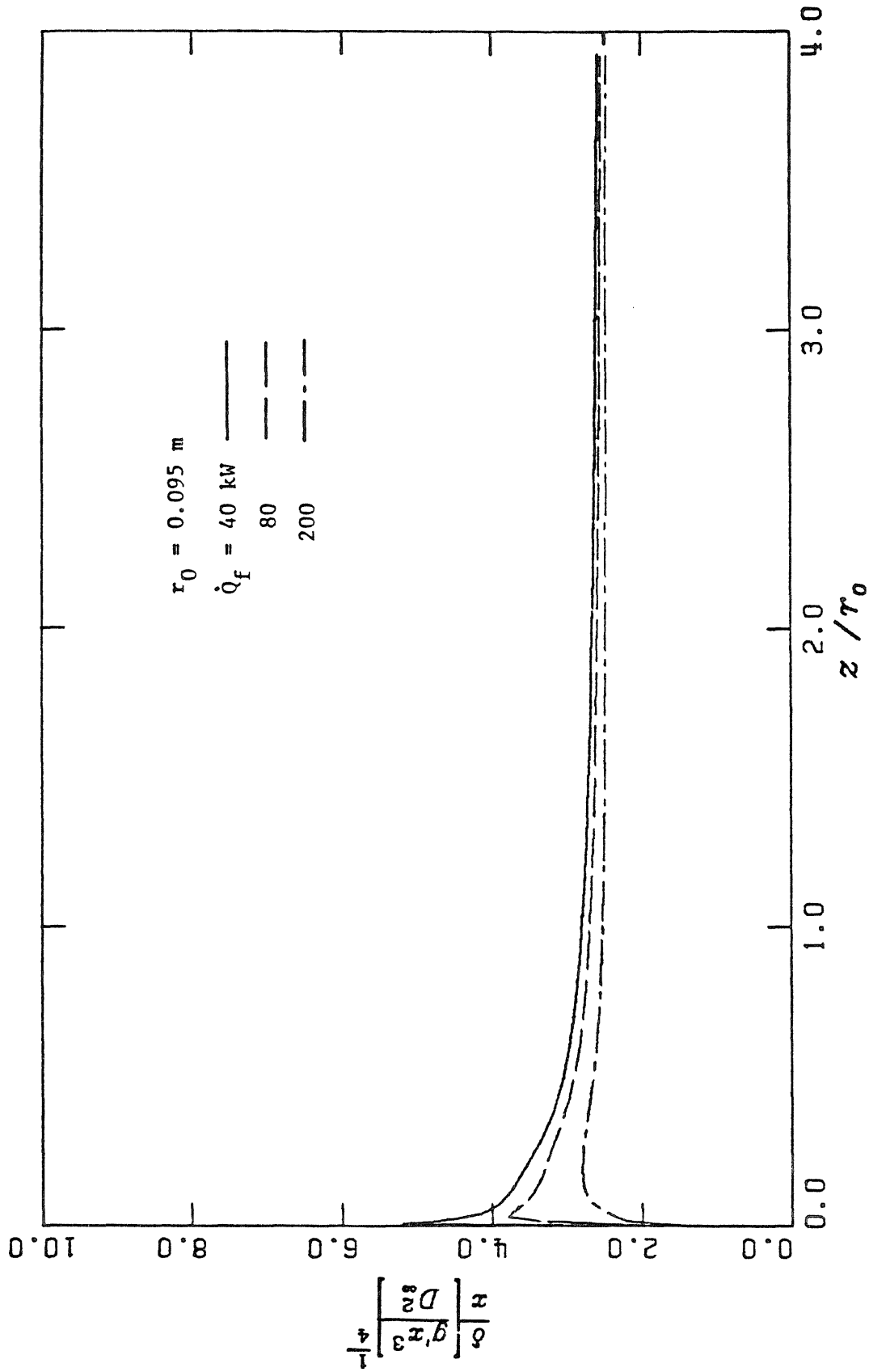


Figure (5.18) Dimensionless boundary layer thickness as a function of the distance above the burner surface normalized by the burner radius for $r_0 = 0.095 \text{ m}$. and heat release rates of 40, 80, 200 kW.

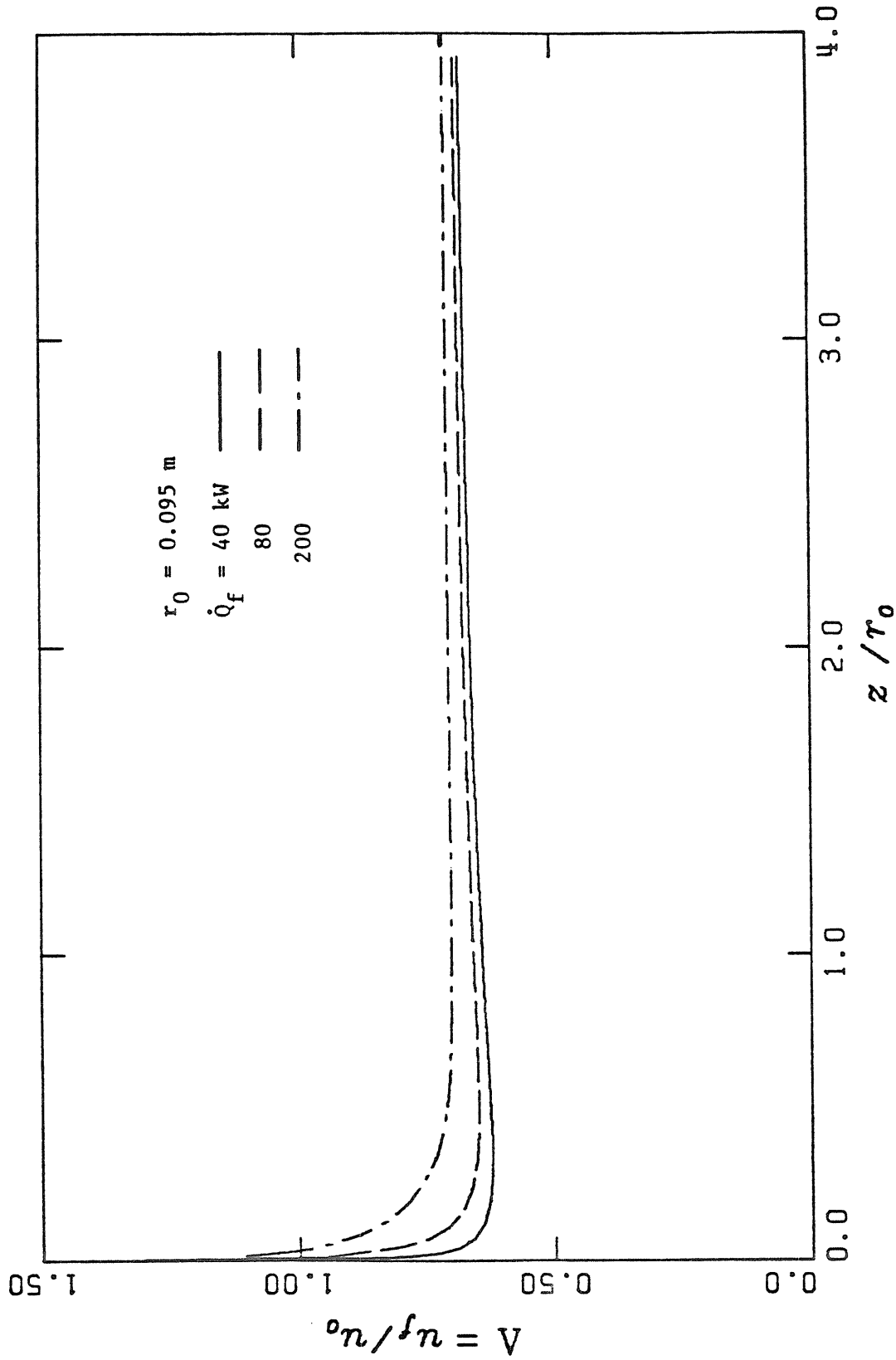


Figure (5.19) The ratio of fuel velocity outside the boundary layer to characteristic velocity in the boundary layer as a function of the distance above the burner surface normalized by burner radius for $r_0 = 0.095 \text{ m.}$ and heat release rates of 40, 80, 200 kW.

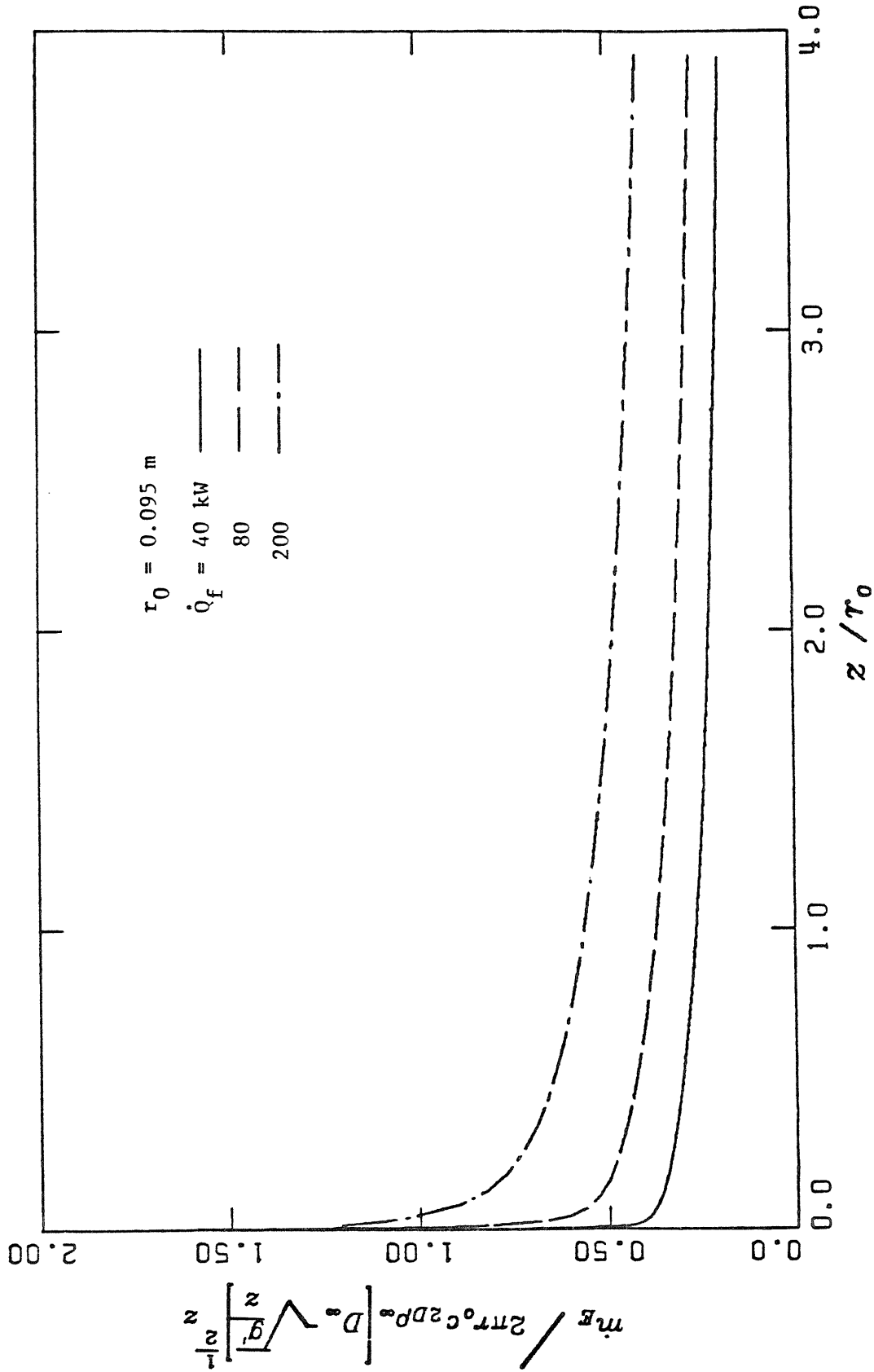


Figure (5.20) Entrainment normalized by that of a plane diffusion flame surrounding burner perimeter as a function of z/r_0 for $r_0 = 0.095$ m. and heat release rates of 40, 80, 200 kW.

Chapter 6

CONCLUSIONS

In our study of flame geometry, we found out that a prominent feature of the natural gas diffusion flames studied here is the presence of large, more or less regularly shed vortex-like structures in the flame. These structures, which we believe are toroidal vortices, are produced in a roughly regular manner with a frequency which scales as $\sqrt{g/D}$. The periodic completion of combustion of all of the fuel in the topmost puff produces the periodic motion observed in the top of the flame. It is observed that the scaling of flame heights and other flame geometry parameters change near Q_D^* values of 1.0 and Z_{fl}/D of about 3. For large values of $Q_D^* > 1.0$, the dependence of flame height on the initial geometry of the fire source (in our experiments, expressed as burner diameter, D) disappears and flame heights become proportional to $\dot{Q}_f^{2/5}$ where \dot{Q}_f is the heat release rate based on fuel heating value. In the lower regime ($Q_D^* < 1.0$), the flames are short and thus the initial geometry of the fire influences the characteristics of the flame.

In the entrainment measurements of the fire plumes, it was found that the entrainment occurs in three distinct modes. In the initial region near the base of the fire, the measured plume mass fluxes are independent of the fuel flow rate (heat release rate) and scale with height above the burner raised to a power near 3/4. In this region, the entrainment is rapid enough to produce overall fuel-air ratios below stoichiometric even when the interface height is far below the top of the flame. Under these conditions, the combustion of the fuel is complete as long as the overall fuel-air ratio of the ceiling layer gas is below 70 % of the stoichiometric value. At higher values of fuel-air ratio in the ceiling layer,

soot and unburned hydrocarbons are formed.

In the far field, above the top of the visible flame, plume mass flux data can be correlated by a simple, point source model with reasonable accuracy. No large offsets in the plume origin are necessary for large heights above the burner. However, an offset will improve the accuracy of the entrainment predictions for interface heights near the top of the flame.

The intermediate region connecting the initial region and the far field is not very clear due to the scatter in our data. But, this region resembles a turbulent diffusion flame with plume like characteristics. The transitions among these three regions do span fairly large distances which sometimes can be as high as flame height itself. The important change in the flame structure at values of Q_D^* around unity shows up in the plume mass flux measurements (transition of the initial region directly to far field) and higher far field entrainment constants when Q_D^* is less than unity. This region is important since many of the real fires are in this range.

A simple model developed for entrainment can be used to give fairly good estimates of plume mass fluxes and seems to explain some of the basic features of the fire plumes. The predictions from this model can be used in computer model calculations of fire spread.

The effects of ambient disturbances which may be present in real fire situations are to enhance the entrainment of fire plumes up to 50 % in some cases. It is also observed that about 30 % of the heat release, based on fuel heating value, is lost by radiation to the surroundings independent of the fuel flow rate.

Studies of the effects of fuel heating value on entrainment by nitrogen dilution of fuel seems to show that the important parameter is the heating value per unit mass of **air** which fixes the gas temperature.

Some preliminary experiments on the characteristics of fuel rich ceiling layers show that the combustion is complete provided that the fuel-air ratio of the ceiling layer gas is kept below 70 % of the stoichiometric value. At higher values, the concentrations of the incomplete combustion products, soot, unburned hydrocarbons increase until the flash-over of the ceiling layer. This does not happen till the fuel-air ratios exceed twice the stoichiometric values. Since these are the results of some preliminary experiments, we recommend that further detailed investigation of the properties of fuel rich ceiling layer should be undertaken.

Appendix A

SPECIFIC HEAT VARIATION THROUGH THE FLAME FRONT

The sensible enthalpy of an ideal gas can be written as,

$$h(T) = \int_{T_{ref}}^T C_p(T) dT \quad (A1)$$

where T_{ref} is the reference temperature at which the enthalpy of formation is evaluated. For calorically perfect gas, if T_{ref} is taken to be $0^\circ K$ then

$$h = C_p T \quad (A2)$$

Using equation of state for ideal gas,

$$P = \rho RT \quad (A3)$$

the density ratio can be written as,

$$\frac{\rho_\infty}{\rho} = \frac{C_{p_\infty}}{C_p} \frac{R}{R_\infty} \frac{h}{h_\infty} \quad (A4)$$

where it is known that $P = P_\infty$ across the flame front.

Specific heat for a mixture of fuel, oxidizer and products (assuming C_p for products and air are approximately equal, e.g. for Paraffin family, $C_n H_{2n+2}$ $1 \leq n \leq 15$ $27.62 \leq M_p \leq 28.66$ and for Olefin family, $C_n H_{2n}$, $M_p = 28.78$ for complete combustion) is,

$$\frac{C_p}{C_{p\infty}} = \left(\frac{C_{pf}}{C_{p\infty}} - 1 \right) Y_f + 1 \quad (\text{A5})$$

Since $C_p = \Gamma_i R_i$ where $\Gamma = \frac{C_p}{C_p - C_v}$ and $R_i = \frac{R}{M_i}$, equation A5 can also be written as,

$$\frac{C_p}{C_{p\infty}} = 1 + \left(\frac{\Gamma_f M_\infty}{\Gamma_\infty M_f} - 1 \right) Y_f \quad (\text{A6})$$

Assuming the mixture of products have the same molecular weight as air, we can write

$$\frac{R}{R_\infty} = 1 + \left(\frac{M_\infty}{M_f} - 1 \right) Y_f \quad (\text{A7})$$

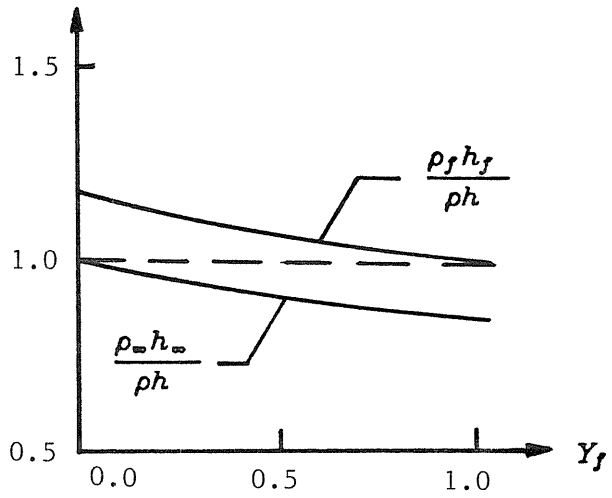
Combining A4, A6, and A7 one gets,

$$\frac{\rho_\infty h_\infty}{\rho h} = \frac{1 + \left(\frac{M_\infty}{M_f} - 1 \right) Y_f}{1 + \left(\frac{\Gamma_f M_\infty}{\Gamma_\infty M_f} - 1 \right) Y_f} \quad (\text{A8})$$

Similarly,

$$\frac{\rho_f h_f}{\rho h} = \frac{\frac{M_f}{M_\infty} + \left(1 - \frac{M_f}{M_\infty} \right) Y_f}{\frac{\Gamma_\infty M_f}{\Gamma_f M_\infty} + \left(1 - \frac{\Gamma_\infty M_f}{\Gamma_f M_\infty} \right) Y_f} \quad (\text{A9})$$

For methane-air $\Gamma_f/\Gamma_\infty = 1.179$ and $M_\infty/M_f = 1.813$



In our treatment we used,

$$\frac{\rho_f}{\rho} = \frac{h}{h_f} \text{ and } \frac{\rho_\infty}{\rho} = \frac{h}{h_\infty}$$

Appendix B

TABULATED ENTRAINMENT DATA

In the following pages, the entrainment data obtained by mass balance and chemical sampling techniques are tabulated.

Pages 165 to 168 contain the data obtained by mass balance technique for three burners and various heat release rates. The first eight columns give the values of: (1) Burner diameter, D ; (2) Heat release rate based on fuel heating value and fuel mass flow rate; (3) Interface height, Z_i ; (4) Eye averaged flame height, Z'_{fl} ; (5) Ambient room temperature, T_∞ ; (6) Average gas temperature at the hood exit, \bar{T}_h ; (7) Gas temperature at the orifice plate; \bar{T}_{OR} and (8) Measured plume mass flux, \dot{m}_p . The last column indicates the experiments done without the 2.4 m. square floor surround by an asterisk *.

Similarly, the chemical sampling data is tabulated where the first three columns show the burner diameter, D ; heat release rate, \dot{Q}_f and interface height, Z_i . The next two columns give the mole fractions of the two species; carbon dioxide, CO_2 and oxygen, O_2 . The last two columns are the plume mass flux estimates obtained from these species mole fractions.

D, m	\dot{Q}_f, kW	Z_i, m	Z_R, m	$T_w, ^\circ C$	$\bar{T}_h, ^\circ C$	$\bar{T}_{OR}, ^\circ C$	$\dot{m}_p, kg/s$	No fr
0.10	5.5	0.90	0.38	24.0	63.0	54.0	0.089	
0.10	10.6	0.90	0.50	24.5	84.0	73.0	0.118	
0.10	16.1	0.90	0.59	25.0	110.0	92.0	0.122	
0.10	16.1	1.00	0.59	25.0	98.0	91.0	0.158	
0.10	16.1	0.95	0.59	25.0	104.0	95.0	0.139	
0.10	20.1	0.95	0.64	25.5	120.0	108.0	0.156	
0.10	20.1	0.95	0.64	25.5	118.0	110.0	0.153	
0.10	27.4	0.95	0.73	26.0	142.0	126.0	0.157	
0.10	31.9	0.95	0.77	26.0	159.0	142.0	0.164	
0.10	10.2	1.47	0.49	24.5	52.0	50.0	0.252	
0.10	16.2	1.42	0.59	25.0	64.0	62.0	0.284	
0.10	42.0	1.45	0.86	27.0	106.0	102.0	0.379	
0.10	63.9	1.47	1.02	29.0	140.0	133.0	0.423	
0.10	157.9	1.63	1.47	35.0	262.0	240.0	0.482	
0.10	36.7	1.42	0.82	26.5	97.0	95.0	0.365	
0.10	42.9	1.68	0.87	27.0	117.0	111.0	0.348	
0.10	109.5	1.37	1.27	30.0	228.0	202.0	0.381	
0.10	5.7	1.47	0.39	22.0	40.0	38.0	0.171	
0.10	2.7	1.42	0.28	20.0	34.0	34.0	0.135	
0.10	10.4	1.35	0.49	22.5	54.0	52.0	0.217	
0.10	10.4	1.42	0.49	22.5	52.0	51.0	0.242	
0.10	16.1	1.42	0.59	23.0	61.0	58.0	0.292	
0.10	22.8	1.37	0.68	23.5	74.0	72.0	0.321	
0.10	31.4	1.42	0.77	25.0	89.0	86.0	0.354	
0.10	45.6	1.45	0.89	26.0	111.0	108.0	0.380	
0.10	63.9	1.45	1.02	28.0	144.0	139.0	0.395	
0.10	91.3	1.42	1.18	29.0	184.0	175.0	0.423	
0.10	109.5	1.42	1.27	31.0	204.0	200.0	0.448	
0.10	146.0	1.42	1.42	33.0	258.0	249.0	0.459	
0.10	42.0	1.47	0.86	30.0	110.0	104.0	0.372	
0.10	63.9	1.42	1.02	31.0	142.0	134.0	0.406	
0.10	109.5	1.47	1.27	33.0	204.0	186.0	0.432	
0.10	16.4	2.30	0.59	25.5	41.0	40.0	0.690	
0.10	21.9	2.27	0.67	26.0	45.0	44.0	0.766	
0.10	42.0	2.30	0.86	28.0	58.0	58.0	0.978	
0.10	63.9	2.40	1.02	31.0	68.0	65.0	1.173	
0.10	10.2	2.25	0.49	24.0	38.0	38.0	0.574	
0.10	49.3	2.19	0.92	28.5	66.0	64.0	0.940	
0.10	102.2	2.25	1.23	34.0	91.0	91.0	1.218	
0.19	11.0	0.90	0.45	26.5	79.0	65.0	0.117	
0.19	11.0	0.90	0.45	26.5	82.0	71.0	0.116	
0.19	21.0	0.90	0.65	28.0	124.0	104.0	0.141	
0.19	31.9	1.00	0.77	30.0	146.0	132.0	0.188	
0.19	42.0	1.00	0.86	31.0	172.0	155.0	0.209	
0.19	52.9	0.95	0.95	32.0	210.0	185.0	0.197	
0.19	21.0	0.95	0.65	28.0	122.0	130.0	0.169	
0.19	11.0	1.52	0.45	27.0	52.0	50.0	0.299	
0.19	20.1	1.52	0.64	29.0	69.0	66.0	0.348	
0.19	51.1	1.52	0.93	34.0	116.0	111.0	0.429	
0.19	80.3	1.52	1.12	37.0	141.0	137.0	0.560	

D, m	\dot{Q}_f, kW	Z_t, m	Z_R, m	$T_w, ^\circ C$	$\bar{T}_h, ^\circ C$	$\bar{T}_{OR}, ^\circ C$	$\dot{m}_p, kg/s$	No fr
0.19	104.0	1.68	1.24	40.0	162.0	156.0	0.625	
0.19	31.9	1.47	0.77	27.0	80.0	78.0	0.431	
0.19	63.9	1.47	1.02	31.0	120.0	120.0	0.510	
0.19	115.0	1.42	1.29	37.0	194.0	184.0	0.526	
0.19	14.8	1.47	0.57	27.0	60.0	60.0	0.330	
0.19	14.6	1.37	0.56	26.0	59.0	56.0	0.310	
0.19	21.0	1.42	0.65	27.0	68.0	66.0	0.355	
0.19	31.9	1.47	0.77	30.0	80.0	78.0	0.437	
0.19	20.1	1.47	0.64	28.0	70.0	67.0	0.323	
0.19	51.1	1.47	0.93	33.0	112.0	106.0	0.421	
0.19	104.0	1.47	1.24	38.0	178.0	168.0	0.524	
0.19	115.0	1.52	1.29	38.0	195.0	186.0	0.505	
0.19	10.4	2.25	0.44	25.0	38.0	39.0	0.593	
0.19	20.1	2.30	0.64	26.0	45.0	43.0	0.768	
0.19	51.1	2.30	0.93	29.0	62.0	61.0	1.056	
0.19	80.3	2.25	1.12	31.0	81.0	79.0	1.150	
0.19	104.0	2.25	1.24	33.0	94.0	91.0	1.239	
0.19	131.4	2.25	1.36	36.0	111.0	107.0	1.271	*
0.19	20.1	2.11	0.64	23.0	42.0	42.0	0.713	*
0.19	29.6	2.13	0.75	23.0	50.0	49.0	0.815	*
0.19	39.2	2.13	0.84	23.0	58.0	57.0	0.889	*
0.19	48.4	2.13	0.91	23.0	69.0	68.0	0.935	*
0.19	55.7	2.18	0.97	23.0	72.0	72.0	1.039	*
0.19	20.1	1.78	0.64	23.0	48.0	47.0	0.509	*
0.19	30.1	1.78	0.76	23.0	61.0	59.0	0.552	*
0.19	40.2	1.81	0.85	23.0	69.0	68.0	0.631	*
0.19	51.1	1.81	0.93	23.0	82.0	81.0	0.624	*
0.19	60.2	1.83	1.00	23.0	92.0	91.0	0.630	*
0.19	81.2	1.83	1.12	23.0	110.0	109.0	0.677	*
0.19	60.2	1.81	1.00	23.0	95.0	94.0	0.631	*
0.19	20.1	1.30	0.64	22.0	66.0	61.0	0.264	*
0.19	30.1	1.27	0.76	22.0	86.0	80.0	0.277	*
0.19	40.2	1.30	0.85	22.0	107.0	102.0	0.290	*
0.19	50.2	1.30	0.93	22.0	127.0	120.0	0.296	*
0.19	60.2	1.30	1.00	22.0	145.0	136.0	0.308	*
0.19	80.3	1.35	1.12	22.0	175.0	166.0	0.337	*
0.19	60.2	1.30	1.00	22.0	152.0	149.0	0.308	*
0.19	40.2	1.30	0.85	22.0	116.0	119.0	0.299	*
0.19	20.1	1.24	0.64	22.0	85.0	90.0	0.248	*
0.19	20.1	1.51	0.64	23.0	57.0	54.0	0.337	*
0.19	30.1	1.51	0.76	23.0	73.0	71.0	0.368	*
0.19	40.2	1.51	0.85	23.0	87.0	85.0	0.398	*
0.19	50.2	1.51	0.93	23.0	104.0	100.0	0.412	*
0.19	60.2	1.53	1.00	23.0	117.0	114.0	0.428	*
0.19	80.3	1.51	1.12	23.0	147.0	142.0	0.426	*
0.19	60.2	1.53	1.00	23.0	119.0	119.0	0.430	*
0.19	40.2	1.51	0.85	23.0	94.0	94.0	0.406	*
0.19	20.1	1.43	0.64	23.0	70.0	74.0	0.330	*
0.19	20.1	1.10	0.64	22.0	80.0	72.0	0.212	*
0.19	30.1	1.12	0.76	22.0	105.0	99.0	0.221	*

D, m	\dot{Q}_f, kW	Z_i, m	Z_f, m	$T_w, ^\circ C$	$\bar{T}_h, ^\circ C$	$\bar{T}_{OR}, ^\circ C$	$\dot{m}_p, kg/s$	No fr
0.19	40.2	1.10	0.85	22.0	135.0	126.0	0.216	*
0.19	50.2	1.12	0.93	22.0	162.0	151.0	0.220	*
0.19	60.2	1.15	1.00	22.0	183.0	172.0	0.236	*
0.19	80.3	1.12	1.12	22.0	225.0	211.0	0.240	*
0.19	60.2	1.10	1.00	22.0	190.0	185.0	0.225	*
0.19	40.2	1.07	0.85	22.0	148.0	148.0	0.205	*
0.19	30.1	1.05	0.76	22.0	124.0	125.0	0.197	*
0.19	20.1	1.10	0.64	22.0	94.0	98.0	0.207	*
0.19	11.0	1.65	0.45	23.0	40.0	39.0	0.370	*
0.19	20.1	1.65	0.64	23.0	52.0	50.0	0.449	*
0.19	30.1	1.70	0.76	23.0	62.0	60.0	0.513	*
0.19	40.2	1.74	0.85	23.0	73.0	71.0	0.570	*
0.19	61.1	1.74	1.00	23.0	97.0	94.0	0.627	*
0.19	81.2	1.72	1.12	23.0	120.0	116.0	0.619	*
0.19	60.2	1.70	1.00	23.0	99.0	98.0	0.605	*
0.19	40.2	1.70	0.85	23.0	78.0	79.0	0.551	*
0.19	20.1	1.65	0.64	23.0	61.0	63.0	0.421	*
0.19	11.0	2.05	0.45	20.0	32.0	32.0	0.632	*
0.19	20.1	2.10	0.64	20.0	39.0	38.0	0.811	*
0.19	30.1	2.13	0.76	20.0	46.0	45.0	0.915	*
0.19	40.2	2.13	0.85	20.0	53.0	52.0	0.972	*
0.19	50.2	2.10	0.93	20.0	59.0	58.0	1.047	*
0.19	60.2	2.13	1.00	20.0	66.0	65.0	1.088	*
0.19	80.3	2.10	1.12	20.0	75.0	75.0	1.191	*
0.30	21.2	2.20	0.50	24.0	42.0	42.0	0.769	
0.30	42.0	2.25	0.84	27.0	51.0	50.0	1.100	
0.30	63.9	2.25	1.02	28.0	61.0	60.0	1.273	
0.30	84.0	2.25	1.14	30.0	72.0	72.0	1.334	
0.30	58.4	2.25	0.98	26.0	59.0	58.0	1.244	
0.30	31.9	2.20	0.68	23.0	43.0	43.0	1.058	
0.50	31.9	0.85	0.44	31.0	130.0	120.0	0.218	
0.50	42.0	0.85	0.53	32.0	152.0	140.0	0.251	
0.50	52.9	0.85	0.64	34.0	150.0	144.0	0.334	
0.50	63.9	1.00	0.73	35.0	182.0	170.0	0.311	
0.50	63.9	0.95	0.73	35.0	152.0	152.0	0.444	
0.50	31.0	0.95	0.43	32.0	130.0	128.0	0.246	
0.50	42.0	1.00	0.53	33.0	144.0	139.0	0.281	
0.50	21.4	0.95	0.32	28.0	108.0	102.0	0.218	
0.50	31.9	0.95	0.44	30.0	124.0	120.0	0.264	
0.50	42.0	0.95	0.53	31.0	146.0	138.0	0.273	
0.50	18.3	1.52	0.29	25.0	55.0	53.0	0.379	
0.50	29.2	1.47	0.41	27.0	72.0	70.0	0.436	
0.50	51.1	1.47	0.62	30.0	90.0	89.0	0.565	
0.50	58.4	1.47	0.68	31.0	98.0	96.0	0.598	
0.50	74.8	1.47	0.82	33.0	112.0	111.0	0.636	
0.50	84.0	1.47	0.90	35.0	122.0	120.0	0.649	
0.50	105.9	1.47	1.07	37.0	140.0	137.0	0.684	
0.50	21.9	1.47	0.33	27.0	61.0	60.0	0.420	
0.50	42.0	1.42	0.53	30.0	89.0	87.0	0.480	

D, m	\dot{Q}_f, kW	Z_i, m	Z_f, m	$T_w, ^\circ C$	$\bar{T}_h, ^\circ C$	$\bar{T}_{OR}, ^\circ C$	$\dot{m}_p, kg/s$	No fr
0.50	94.9	1.42	0.98	35.0	137.0	133.0	0.642	
0.50	127.8	1.52	1.23	39.0	162.0	160.0	0.656	
0.50	158.8	1.47	1.45	42.0	184.0	179.0	0.773	
0.50	52.9	1.42	0.64	32.0	96.0	93.0	0.545	
0.50	105.9	1.52	1.07	38.0	140.0	139.0	0.682	
0.50	158.8	1.47	1.45	43.0	192.0	186.0	0.740	
0.50	51.1	1.51	0.62	32.0	89.0	86.0	0.558	
0.50	74.8	1.51	0.82	35.0	114.0	110.0	0.624	
0.50	105.9	1.51	1.07	37.0	138.0	132.0	0.695	
0.50	127.8	1.46	1.23	39.0	155.0	147.0	0.714	
0.50	51.1	2.27	0.62	29.0	57.0	56.0	1.225	
0.50	74.8	2.27	0.82	31.0	68.0	66.0	1.218	
0.50	105.9	2.21	1.07	34.0	86.0	84.0	1.370	
0.50	18.3	2.32	0.29	26.0	40.0	40.0	0.845	
0.50	29.2	2.32	0.41	27.0	46.0	46.0	0.996	
0.50	58.4	2.21	0.68	30.0	62.0	62.0	1.225	
0.50	84.0	2.27	0.90	32.0	72.0	70.0	1.398	
0.50	20.1	1.70	0.31	23.0	49.0	48.0	0.508	*
0.50	40.2	1.70	0.52	23.0	60.0	59.0	0.803	*
0.50	80.3	1.70	0.87	23.0	80.0	79.0	1.026	*
0.50	60.2	1.70	0.70	23.0	72.0	72.0	0.919	*
0.50	40.2	1.70	0.52	23.0	63.0	64.0	0.762	*
0.50	20.1	1.65	0.31	23.0	55.0	55.0	0.473	*
0.50	40.2	1.70	0.52	23.0	60.0	59.0	0.785	*
0.50	60.2	1.70	0.70	23.0	71.0	70.0	0.946	*
0.50	80.3	1.73	0.87	23.0	81.0	79.0	1.066	*
0.50	20.1	1.48	0.31	23.0	52.0	50.0	0.433	*
0.50	40.2	1.46	0.52	23.0	68.0	65.0	0.653	*
0.50	60.2	1.48	0.70	23.0	80.0	78.0	0.781	*
0.50	80.3	1.51	0.87	23.0	92.0	90.0	0.862	*
0.50	60.2	1.43	0.70	23.0	86.0	85.0	0.721	*
0.50	50.2	1.46	0.61	23.0	82.0	81.0	0.657	*
0.50	40.2	1.46	0.52	23.0	75.0	74.0	0.613	*
0.50	30.1	1.46	0.42	23.0	67.0	66.0	0.547	*
0.50	20.1	1.51	0.31	23.0	58.0	59.0	0.462	*
0.50	20.1	1.26	0.31	23.0	59.0	57.0	0.319	*
0.50	30.1	1.31	0.42	23.0	69.0	67.0	0.450	*
0.50	40.2	1.21	0.52	23.0	83.0	81.0	0.464	*
0.50	50.2	1.28	0.61	23.0	89.0	88.0	0.533	*
0.50	61.1	1.23	0.71	23.0	103.0	99.0	0.548	*
0.50	81.2	1.20	0.88	23.0	119.0	117.0	0.584	*
0.50	60.2	1.22	0.70	23.0	101.0	101.0	0.558	*
0.50	40.2	1.19	0.52	23.0	90.0	89.0	0.439	*
0.50	20.1	1.26	0.31	23.0	70.0	70.0	0.321	*
0.50	80.3	1.23	0.87	23.0	114.0	112.0	0.620	*

D, m	Q_f, kW	Z_t, m	Y_{CO_2}	Y_{O_2}	$\dot{m}_{p_{CO_2}}, kg/s$	$\dot{m}_{p_{O_2}}, kg/s$
0.10	10.55	0.38	0.014	0.186	0.029	0.030
0.10	20.99	0.38	0.027	0.168	0.030	0.034
0.10	41.99	0.37	0.052	0.115	0.032	0.031
0.10	63.93	0.38	0.068	0.076	0.038	0.035
0.10	82.18	0.37	0.078	0.056	0.043	0.039
0.10	63.93	0.36	0.058	0.094	0.044	0.040
0.10	52.96	0.38	0.050	0.114	0.042	0.039
0.10	41.99	0.38	0.039	0.138	0.042	0.041
0.10	20.99	0.36	0.021	0.170	0.038	0.036
0.10	41.99	0.37	0.039	0.138	0.042	0.041
0.10	63.93	0.37	0.055	0.098	0.046	0.041
0.10	10.55	0.28	0.023	0.164	0.017	0.016
0.10	10.55	0.28	0.024	0.170	0.017	0.018
0.10	20.99	0.28	0.044	0.126	0.019	0.018
0.10	41.99	0.27	0.075	0.056	0.023	0.020
0.10	63.93	0.27	0.087	0.002	0.030	0.023
0.10	41.99	0.27	0.074	0.058	0.023	0.020
0.10	20.99	0.27	0.045	0.126	0.018	0.018
0.10	20.99	0.27	0.038	0.138	0.022	0.020
0.10	10.55	0.28	0.021	0.160	0.019	0.015
0.10	10.55	0.28	0.018	0.164	0.023	0.016
0.10	10.55	0.53	0.006	0.194	0.067	0.045
0.10	20.99	0.53	0.013	0.184	0.062	0.055
0.10	41.99	0.53	0.026	0.163	0.064	0.062
0.10	63.93	0.56	0.039	0.132	0.064	0.058
0.10	82.18	0.55	0.057	0.106	0.057	0.056
0.10	63.93	0.55	0.042	0.128	0.060	0.055
0.10	41.99	0.56	0.028	0.148	0.058	0.047
0.10	20.99	0.56	0.014	0.174	0.057	0.040
0.10	82.18	0.77	0.032	-	0.100	-
0.10	63.93	0.77	0.026	-	0.095	-
0.10	41.99	0.77	0.017	-	0.095	-
0.10	20.99	0.79	0.007	-	0.114	-
0.10	41.99	0.76	0.013	-	0.123	-
0.10	10.55	0.59	0.008	0.180	0.050	0.024
0.10	20.99	0.58	0.014	0.167	0.057	0.034
0.10	31.97	0.57	0.022	0.155	0.055	0.040
0.10	41.99	0.58	0.039	0.140	0.043	0.042
0.10	52.96	0.57	0.042	0.122	0.050	0.043
0.10	63.93	0.57	0.047	0.110	0.054	0.046
0.10	82.18	0.57	0.058	0.090	0.056	0.049
0.10	63.93	0.57	0.045	-	0.055	-
0.10	52.96	0.58	0.036	-	0.057	-
0.10	41.99	0.58	0.028	-	0.058	-
0.10	31.97	0.58	0.029	-	0.043	-
0.10	20.99	0.58	0.019	-	0.042	-
0.10	10.55	0.38	0.020	0.164	0.021	0.016
0.10	20.99	0.38	0.033	0.140	0.025	0.021
0.10	31.97	0.38	0.046	0.112	0.027	0.023
0.10	41.99	0.36	0.057	0.084	0.029	0.024

D, m	\dot{Q}_f, kW	Z_i, m	Y_{CO_2}	Y_{O_2}	$\dot{m}_{PCO_2}, kg/s$	$\dot{m}_{PO_2}, kg/s$
0.10	52.96	0.36	0.070	0.058	0.031	0.025
0.10	63.93	0.36	0.078	0.036	0.033	0.027
0.10	41.99	0.35	0.060	0.094	0.028	0.026
0.10	20.99	0.35	0.035	0.146	0.023	0.023
0.10	20.99	0.48	0.022	0.170	0.036	0.036
0.10	31.97	0.48	0.031	0.154	0.040	0.040
0.10	41.99	0.48	0.041	0.130	0.040	0.037
0.10	52.96	0.46	0.046	0.110	0.045	0.038
0.10	63.93	0.45	0.052	0.098	0.049	0.041
0.10	20.99	0.55	0.012	0.185	0.064	0.057
0.10	20.99	0.55	0.016	0.180	0.052	0.048
0.10	31.97	0.55	0.026	0.165	0.047	0.049
0.10	41.99	0.55	0.033	0.150	0.050	0.049
0.10	52.96	0.55	0.039	0.135	0.054	0.050
0.10	63.93	0.53	0.046	0.125	0.055	0.053
0.10	20.99	0.55	0.016	0.170	0.050	0.036
0.10	31.97	0.55	0.022	0.165	0.055	0.049
0.10	41.99	0.55	0.030	0.145	0.054	0.045
0.10	63.93	0.54	0.043	0.125	0.058	0.053
0.10	10.76	1.09	0.004	-	0.116	-
0.10	19.20	1.07	0.006	-	0.121	-
0.10	34.18	1.09	0.010	-	0.137	-
0.10	41.57	1.09	0.010	-	0.151	-
0.10	31.97	1.02	0.009	-	0.135	-
0.19	32.39	0.22	0.041	0.145	0.031	0.035
0.19	42.43	0.22	0.063	0.110	0.027	0.030
0.19	52.93	0.19	0.088	0.068	0.025	0.027
0.19	63.88	0.20	0.100	0.032	0.026	0.027
0.19	32.39	0.20	0.039	0.135	0.032	0.030
0.19	20.99	0.66	0.008	0.200	0.104	0.141
0.19	20.99	0.66	0.008	0.195	0.105	0.095
0.19	41.99	0.67	0.020	0.180	0.081	0.096
0.19	63.93	0.67	0.031	0.160	0.080	0.088
0.19	20.99	0.48	0.013	0.190	0.062	0.071
0.19	41.99	0.46	0.028	0.165	0.058	0.065
0.19	63.93	0.46	0.042	0.135	0.060	0.060
0.19	41.99	0.46	0.028	0.163	0.058	0.062
0.19	20.99	0.46	0.016	0.185	0.050	0.057
0.19	20.99	0.34	0.018	0.180	0.045	0.048
0.19	41.99	0.33	0.036	0.145	0.045	0.045
0.19	63.93	0.33	0.053	0.105	0.048	0.044
0.19	41.99	0.34	0.037	0.145	0.044	0.045
0.19	20.99	0.33	0.019	0.180	0.043	0.048
0.19	20.99	0.33	0.018	0.176	0.044	0.042
0.19	41.99	0.32	0.040	0.135	0.041	0.039
0.19	63.93	0.33	0.057	0.091	0.045	0.039
0.19	41.99	0.33	0.041	0.130	0.040	0.037
0.19	20.99	0.33	0.020	0.170	0.041	0.036
0.19	63.93	0.33	0.060	0.085	0.043	0.037
0.19	82.18	0.33	0.079	0.042	0.042	0.036

D, m	$Q_f, kW.$	Z_i, m	Y_{CO_2}	Y_{O_2}	$\dot{m}_{PCO_2}, kg/s.$	$\dot{m}_{PO_2}, kg/s.$
0.19	10.44	0.34	0.012	0.176	0.035	0.021
0.19	41.99	0.93	0.009	0.195	0.188	0.189
0.19	41.99	0.95	0.009	0.195	0.188	0.189
0.19	20.99	0.93	0.004	0.200	0.177	0.141
0.19	63.93	0.94	0.014	0.185	0.174	0.174
0.19	82.18	0.94	0.018	0.180	0.180	0.187
0.19	63.93	0.95	0.014	0.185	0.174	0.174
0.19	41.99	0.93	0.009	0.195	0.188	0.189
0.19	20.99	0.93	0.004	0.200	0.177	0.141
0.19	20.99	0.84	0.006	0.196	0.145	0.101
0.19	42.09	0.84	0.012	0.188	0.134	0.130
0.19	63.93	0.85	0.018	0.176	0.133	0.128
0.19	82.18	0.86	0.024	0.168	0.130	0.134
0.19	63.93	0.84	0.018	0.176	0.133	0.128
0.19	42.09	0.85	0.012	0.188	0.134	0.130
0.19	20.99	0.88	0.006	0.196	0.145	0.101
0.19	20.99	0.62	0.010	0.187	0.084	0.064
0.19	41.99	0.58	0.022	0.173	0.075	0.077
0.19	63.93	0.60	0.036	0.148	0.069	0.071
0.19	82.18	0.60	0.045	0.132	0.072	0.074
0.19	63.93	0.61	0.034	0.150	0.072	0.074
0.19	41.99	0.60	0.022	0.170	0.075	0.072
0.19	20.99	0.61	0.010	0.187	0.080	0.064
0.19	82.18	0.58	0.043	0.135	0.075	0.077
0.19	20.99	0.94	0.006	-	0.133	-
0.19	31.97	0.94	0.009	-	0.135	-
0.19	50.22	0.91	0.012	-	0.160	-
0.19	36.92	0.84	0.012	-	0.113	-
0.19	27.85	0.84	0.010	-	0.106	-
0.50	20.99	0.71	0.005	-	0.177	-
0.50	31.97	0.66	0.006	-	0.202	-
0.50	41.99	0.65	0.008	-	0.213	-
0.50	31.97	0.66	0.006	-	0.202	-
0.50	20.99	0.70	0.004	-	0.199	-
0.50	31.97	0.69	0.006	-	0.202	-
0.50	41.99	0.65	0.007	-	0.228	-
0.50	52.96	0.69	0.009	-	0.237	-
0.50	63.93	0.65	0.010	-	0.243	-
0.50	73.01	0.69	0.011	-	0.253	-
0.50	20.99	0.33	0.006	0.180	0.133	0.048
0.50	31.97	0.33	0.011	0.175	0.111	0.063
0.50	41.99	0.33	0.020	0.168	0.082	0.069
0.50	52.96	0.33	0.019	0.162	0.110	0.076
0.50	63.93	0.32	0.022	0.158	0.114	0.085
0.50	52.96	0.33	0.020	0.162	0.104	0.076
0.50	41.99	0.34	0.016	0.168	0.101	0.069
0.50	31.97	0.36	0.018	0.176	0.068	0.064
0.50	20.99	0.30	0.008	0.192	0.100	0.079
0.50	31.97	0.30	0.012	0.186	0.102	0.091
0.50	41.99	0.30	0.016	0.178	0.104	0.090

D, m	Q_f, kW	Z_i, m	Y_{CO_2}	Y_{O_2}	$\dot{m}_{CO_2}, kg/s$	$\dot{m}_{O_2}, kg/s$
0.50	52.96	0.30	0.019	0.170	0.107	0.091
0.50	63.93	0.32	0.023	0.164	0.105	0.096
0.50	52.96	0.30	0.020	0.168	0.102	0.087
0.50	41.99	0.29	0.016	0.172	0.101	0.078
0.50	31.97	0.33	0.013	0.174	0.094	0.061
0.50	20.99	0.33	0.009	0.180	0.089	0.048
0.50	41.99	0.33	0.016	0.170	0.104	0.072
0.50	21.94	0.30	0.013	0.180	0.067	0.050
0.50	41.99	0.36	0.015	0.168	0.107	0.069
0.50	52.96	0.33	0.022	0.168	0.093	0.087
0.50	31.02	1.19	0.003	-	0.469	-
0.50	41.99	1.09	0.004	-	0.454	-
0.50	52.96	1.14	0.004	-	0.501	-
0.50	63.93	1.09	0.005	-	0.484	-
0.50	73.01	1.19	0.005	-	0.614	-
0.50	82.18	1.14	0.006	-	0.519	-
0.50	63.93	1.09	0.005	-	0.484	-
0.50	31.97	0.84	0.005	-	0.242	-
0.50	41.99	0.84	0.006	-	0.265	-
0.50	51.06	0.84	0.008	-	0.259	-
0.50	54.75	0.84	0.008	-	0.260	-
0.50	64.78	0.84	0.009	-	0.274	-
0.50	73.01	0.89	0.009	-	0.309	-
0.50	54.75	0.79	0.008	-	0.277	-
0.50	41.04	0.84	0.006	-	0.259	-
0.50	20.57	0.42	0.007	0.195	0.112	0.093
0.50	31.97	0.50	0.008	0.190	0.143	0.109
0.50	36.50	0.52	0.010	0.190	0.139	0.124
0.50	42.94	0.47	0.011	0.185	0.142	0.117
0.50	36.92	0.47	0.011	0.185	0.128	0.101
0.50	31.97	0.47	0.010	0.187	0.128	0.097
0.50	27.32	0.47	0.009	0.187	0.115	0.083
0.50	20.99	0.72	0.004	-	0.199	-
0.50	31.97	0.72	0.006	-	0.202	-
0.50	36.92	0.72	0.007	-	0.200	-
0.50	41.99	0.72	0.008	-	0.213	-
0.50	53.38	0.77	0.009	-	0.226	-
0.50	64.78	0.75	0.010	-	0.247	-
0.50	54.75	0.72	0.009	-	0.245	-
0.50	41.99	0.72	0.008	-	0.213	-
0.50	32.07	0.72	0.006	-	0.203	-